Accurate Visual Metrology from Single and Multiple Uncalibrated Images

Antonio Criminisi

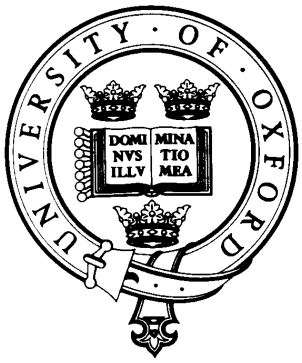

Robotics Research Group
Department of Engineering Science
University of Oxford

Michaelmas Term, 1999

Antonio Criminisi
The Queen's College

Doctor of Philosophy
Michaelmas Term, 1999

Accurate visual metrology from single and multiple uncalibrated images

A thesis submitted to the Department of Engineering Science at the
UNIVERSITY OF OXFORD
in partial fulfillment of the requirements for the degree of
DOCTOR OF PHILOSOPHY

Abstract

The work described in this thesis develops the theory of computing world measurements from photographs of scenes and reconstructing three-dimensional models of the scene. The main tool used is *Projective Geometry* which forms the basis for accurate estimation algorithms.

The techniques presented employ *uncalibrated images*; no knowledge of the camera internal parameters (such as focal length and aspect ratio) or its pose (position and orientation) is required at any time. Extensive use is made of geometric characteristics of the scene, thus there is no need for specialized calibration devices. A hierarchy of novel, accurate and flexible techniques is developed to address a number of different situations ranging from where no scene metric information is known to cases where some distances are known but there is not sufficient information for a complete camera calibration.

The geometry of *single* views is explored and monocular vision shown to be sufficient to obtain a partial or complete three-dimensional reconstruction of a scene. To achieve this the properties of planar homographies and planar homologies are extensively exploited. The geometry of *multiple* views is also investigated, particularly the use of a parallax-based approach for structure and camera recovery. The duality between two-view and three-view configurations is described in detail.

Measured distances must be associated with a measurement *accuracy* to be meaningful. Therefore, an uncertainty propagation analysis is developed in order to take account of the possible sources of error and how they affect the uncertainty in the final measurements.

The general techniques developed in this thesis can be applied to several areas. Examples are presented of commercial, industrial and artistic use.

William Hogarth, *Perspective absurdities,* engraved frontispiece to John Joshua Kirby, *Dr Brook Taylor's method of perspective made easy in both theory and practice,* Ispwitch, 1754.

Ai miei genitori

Acknowledgements

I have enjoyed very much to work in the Robotics Research Group and live in this marvellous town. It has been a fantastic experience, extremely useful for my learning and my personal growth. Many people have been close to me in these three years and I am deeply indebted to all of them.

First of all I would like to thank my two supervisors Prof. Andrew Zisserman and Dr. Ian Reid. Their tireless fervour, encouragements and constant pursuit of the best possible solution to the problems met have been fundamental in the achievement of the results presented in this thesis. I also want to thank them for being such good friends.

I am immensely grateful to my cousin and friend Dr. Roberto Cipolla. Without his passion for good science and his enthusiastic exhortations I would not have begun my D.Phil. Thanks for the help and support received during these three years.

Many thanks to Prof. Martin Kemp. Working in a field where science and art can meet and cooperate has enriched my personal culture, improved my understanding of visual perception and switched on millions of "art-oriented" neurons in remote areas of my brain.

I am indebted to Dr. Andrew Fitzgibbon who has been incredibly helpful with the software development and enthusiastic conversations about Computer Vision. David Liebowitz, with his passionate attitude towards geometric problems, has been of great help in creating many three-dimensional models and animations as well as proofreading part of this dissertation. Philip Pritchett, Frederik Schaffalitzky, Geoffrey Cross, David Capel, Richard Smith, Caroline Bailard, Karen McGaul in the Visual Geometry Group have all contributed to enriching my understanding of Projective Geometry. Thanks to Lourdes, Josephine and Claudia (Portuguese) for bearing to see my face at home as well as in the office every day; they never complained. Thank you Josephine for proofreading.

I would also like to give thanks to Professors A. Blake, L. van Gool, M. Brooks, D. Murray, P. Anandan, S. Carlsson, R. Hartley, J. Mundy for contributing, with stimulating discussions to the development of many of the ideas presented in this thesis.

In these three years I have also been supported by many friends who, especially at the beginning of my stay, have helped me to overcome any language problem and enjoy my time in Oxford. Among all I would like to thank Claudia (Mexicana), Zam, Frank, Rory, Arnd, Francesca (Ciccia), Ronan, Anna, Hester, Arnoud, Mark (another victim of the proofreading disease), Rebekah, Yaeli and little Michael, Liz, Graham, Tobias and many others. Believe it or not, going to the pub and on holiday with them has had extremely positive repercussions on my work. Many thanks also to the people who have accepted to appear in pictures of this thesis.

I should not forget my many Italian friends, colleagues and professors scattered all over the world, always ready to provide suggestions and help.

Many thanks also to the group secretary Annette Gingell and to the computer administrators Christopher Rabson and Neil Townsend; they have done a fantastic work.

Dulcis in fundo, huge thanks to my parents, my sister and Nicola. From the opposite side of the continent they have always supported my choices and my ideas and provided me with lots of love.

Grazie!

“There are three branches of perspective:
the first deals with the reason of the diminution of objects as they recede from the eye, and is known as perspective of diminution;
the second contains the way in which colours vary as they recede from the eye;
the third and last explains how objects should appear less distinct in proportion as they are more remote.
And the names are as follows: linear perspective, the perspective of colour, the perspective of disappearance.”

Leonardo da Vinci, C.A.175v

Contents

Chapter 1

Introduction

1.1 Accurate measurements from images

Images or sequences of images potentially carry a tremendous amount of geometrical information about the scene represented. The aim of the work presented in this thesis is to extract this information in a quantifiable, accurate way.

General techniques are developed which find their engineering motivation in the realization of a flexible, fast and robust visual measuring device, capable of reconstructing a three-dimensional digital model of a scene from interpreting photographs (see fig. 1.1). The leading idea is:

- an operator takes some images of the scene (or object) to be measured;
- a computer by interpreting those images creates a 3D metric model of the viewed scene [5];
- the model is stored in a database which may be queried at any time for measurements via a graphical user interface;

Such a device possesses several interesting features: (i) it is user friendly. In fact, once the images are taken and the model built an operator can virtually walk through it, view the scene from different locations, take measurements querying the software interface and store them in a database, interact with the objects of the scene, place new, consistent virtual objects in the scene (*augmented reality*) and create animations; (ii) the capture process is rapid, simple and minimally invasive since it only involves a camera to take pictures of the environment to be measured; (iii) the acquired data are stored digitally on a disk ready for reuse at any time negating the need to go back to the original

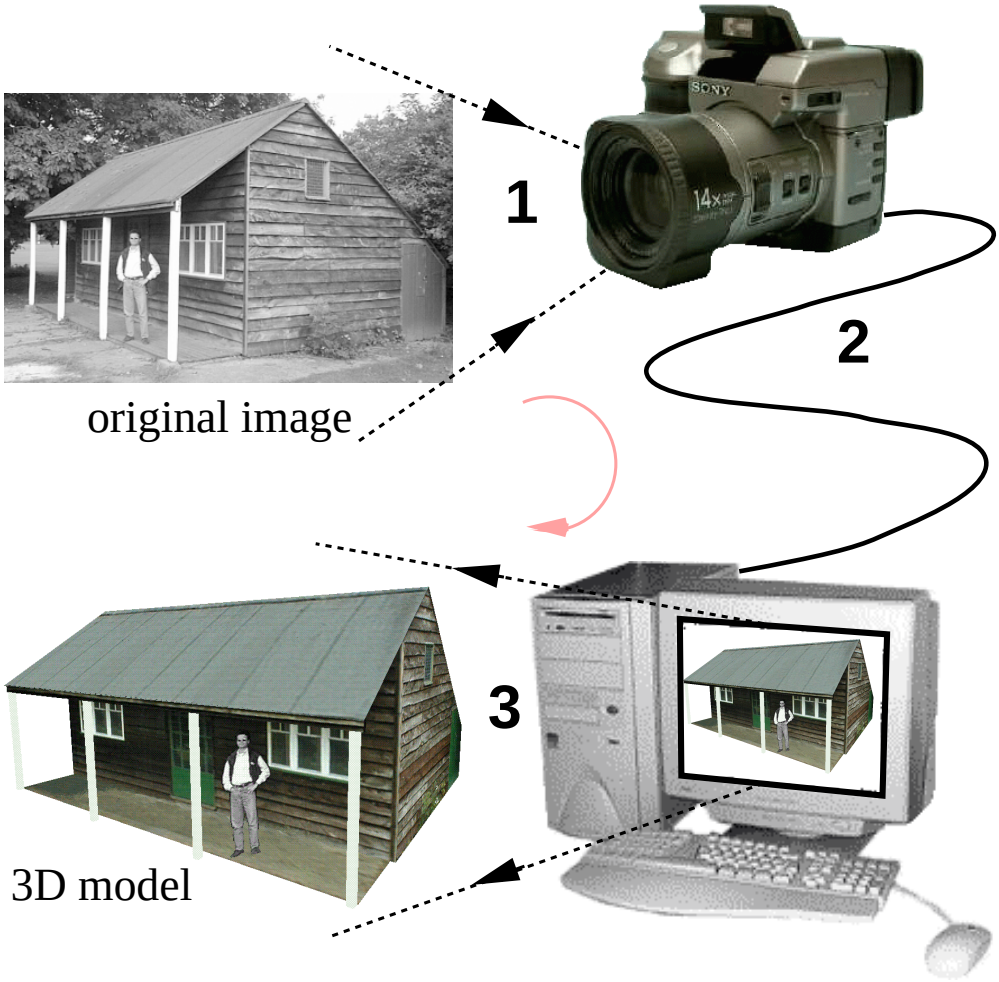

Figure 1.1: **A three-dimensional visual measuring device:** (1) a photograph of a scene is taken; (2) the image is transferred into a computer and interpreted; (3) a 3D model of the viewed scene is reconstructed and interactively queried for measurements.

scene when new measurements are needed; (iv) the hardware involved is cheap and easy to use. No new, dedicated hardware is necessary.

All the work presented here is motivated by the necessity of understanding the mathematical theory underlying such a visual measurement device.

The mathematical basis. The theory developed in this thesis proceeds from a strong and reliable mathematical basis, *Projective Geometry* [36]. In particular, 2D-2D homographic transformations and more general 3D-2D projectivities are investigated and used extensively. While much of the

underlying theory already existed, in order to achieve the goal of this thesis, a number of research areas had to be addressed.

The algorithms developed require no knowledge of the camera's internal parameters (focal length, aspect ratio, principal point) or external ones (position and orientation); i.e. no internal or external camera calibration is needed. Camera calibration is replaced by the use of scene constraints (often referred to as *scene calibration*) such as planarity of points and parallelism of lines and planes. These geometric cues are inferred directly from the images; no scene markers or specialized sensors are required.

A hierarchy of novel geometric techniques to calculate distance measurements is investigated to address a range of different cases. The techniques span situations where no metric information is known about the world (*completely uncalibrated camera*), through to cases where some reference distances are known but they are not sufficient for a complete camera calibration (*partial calibration*). This leads to extremely flexible algorithms which can be applied to a wide range of images such as: photographs of buildings and interiors, aerial images, archived images, photographs of crime scenes and even paintings.

Both single and multiple view configurations are employed. *Stereo vision* has in the past been used to compute depth, but, in this thesis, *monocular vision* proves to be sufficient, in many cases, to obtain partial or complete 3D reconstruction. The use of multiple views in a *parallax*-based framework is also considered in the cases where single view metrology cannot be applied.

Accuracy on measurements. The process of taking measurements is traditionally an engineering task, and like all the engineering tasks, must be accurate and robust. World measurements are obtained from input data (e.g. image points) by a geometric transformation (e.g. a homography). Data and transformation are affected by error and so is the output measurement (fig. 1.2). A proper treatment of error and its propagation through the chain of computations is therefore necessary.

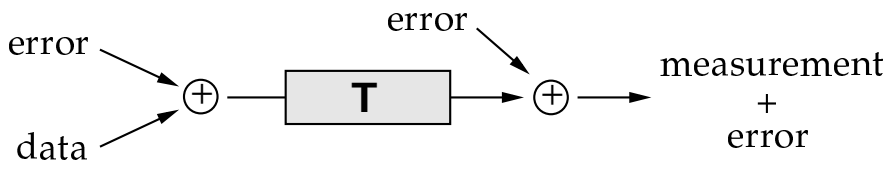

Figure 1.2: **Error propagation:** the input data are processed by the transformation `T` to obtain the required output measurement. Input data and transformation are affected by error, leading to error in the output measurement.

The uncertainty analysis developed in this thesis takes into account all the possible sources of error (the accuracy of the device used, the error affecting the data acquisition process and the operator) and predicts how these affect the accuracy on the final measurement. Thus an uncertainty estimate is associated with each output measurement.

This is achieved by using a *first order error propagation.* But first order analysis involves a linear approximation of the non-linear transformations relating input data to output measurements. Therefore the validity of the approach has to be assessed. This is done employing *Monte Carlo* statistical tests.

1.2 Why use vision?

Several different types of distance measurement devices have been used in the past. They can be categorized as *active* and *passive.* Active and passive devices differ in that active devices send signals into the environment and receive them back. Information related to distances is retrieved by analysing and comparing the outgoing and the returned signals.

1.2.1 Active devices

Ultrasonic devices. Many distance measuring systems have been based on ultrasonic technology. It is possible to buy relatively cheap ultrasonic devices capable of measuring the distance of the operator from an object (such as a wall) relying on an echo reflection time measurement system.

Ultrasonic scanners have, for instance, been successfully used in medical imaging for 3D reconstruction of the structure of bones [114] or other internal tissues. They have also been employed

in robotics problems such as autonomous vehicle navigation [45], where the accuracy and speed of the localisation system are vital. The main problem with such an approach is that the measurement returned is affected by strange and almost unpredictable phenomena like multiple reflections of the ultrasound waves on various objects, thus leading to wrong estimation of the reflection time.

Laser range finders. A second approach for measuring depths is the use of laser range finders. These devices work by directing laser beams onto the object to be measured and analysing the phase or echoing time of the reflected beams.

Laser range finders are being successfully applied to metric shape reconstruction of relatively small objects [8]. They have been successfully employed in the Michelangelo Project [73] to create three-dimensional models of ancient statues. Laser devices have also been applied to solve other common Computer Vision problems such as autonomous navigation [60]. Those systems are extremely accurate but they suffer problems similar to those of ultrasonic devices. Laser-based devices are usually tuned to detect a specific range of distances and they can be quite expensive and, sometimes, dangerous.

Structured light. Other active devices employ cameras to acquire images of an object illuminated by a regular light pattern. Some auxiliary devices (a laser emitter or just a slide projector) project a light pattern or a set of patterns onto an object. The shape of the object is computed from the deformation of the projected grid.

Structured light-based approaches have been used for accurate measurement of surfaces of close range objects which do not possess enough texture [78]. Those methods have also been used to capture facial expressions [33, 92]. The need for auxiliary light projective devices leads to a loss in the flexibility of the measuring tool.

The measurements obtained from active devices can be badly affected by unexpected reflec-

tions or interferences and therefore need to be used with extreme care. Furthermore, such devices can only be applied to measure objects which are accessible, i.e. applied in situ, and they are no use to measure scenes of which only images exist.

1.2.2 Passive devices

Passive devices such as cameras do not suffer from the above problems and are characterized by a wider range of application.

They can be applied to measure the distance of the device from an object (like range finders) as well as the distance between two other points in space, areas of surfaces and angles. Cameras return bi-dimensional data (rather than mono-dimensional ones) characterized by dense sampling within the field of view. They can measure objects which are far as well as close ones. Speed is not an issue for such devices. Furthermore, since images are the only input data, passive visual devices, unlike active ones, can successfully be applied to reconstructing objects from archived images, old footage, postcards and paintings.

1.3 Why is visual metrology hard ?

In the previous section the advantages of using cameras as opposed to other measuring devices were described. However, taking measurements of the world from images is complicated by the fact that in the imaging process the 3D space is projected onto a planar image, with some unavoidable loss of information. Reconstructing the scene means retrieving that information from the images.

In particular, perspective distortions occur during the acquisition stage. For instance, objects which are far away from the eye (or camera) look smaller than objects which are close [1]. Examples of perspective distortion on real images are shown in figure 1.4.

In the past photogrammetrists have addressed the problem of taking world measurements using images. Their techniques rely on knowing the internal parameters of the camera, its position

[1] This basic intuition has been formalized first by Euclid in his *Optica* [34] and then employed by mathematicians and artists in the Italian Renaissance among which Leonardo da Vinci is one of the outstanding examples (see fig. 1.3).

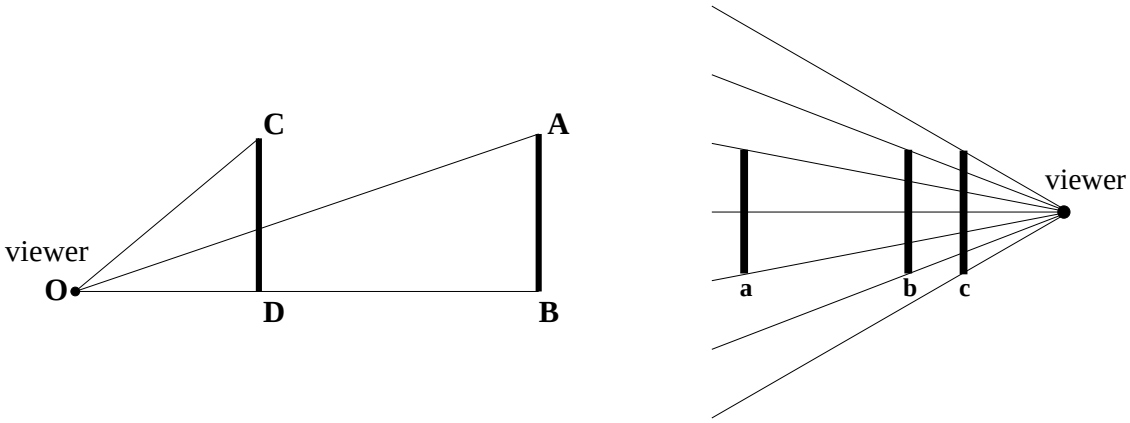

a b

Figure 1.3: **First proofs of perspective effect:** (a) Euclid's proof (ca. 300 B.C.); (b) Leonardo's proof: *"Among objects of equal size that which is most remote from the eye will look smallest."* Leonardo da Vinci (1452-1519), B.M.19r.

a b

Figure 1.4: **Perspective distortion in the image acquisition process:** (a) A photo of a wall of Keble College in Oxford: the windows are foreshortened differently depending on their distance from the camera. (b) The four pillars have the same height in the world, although their images clearly are not of the same length due to perspective effects.

with respect to the viewed scene or the position of marker points in the scene (*georeferenced images*). Unfortunately, photogrammetric algorithms work well only if those values are known with great accuracy, and even a very small deviation can cause large errors in the final measurements. Furthermore, camera internal parameters are quite sensitive to changes of temperature and mechanical shock. Photogrammetric techniques cannot be applied to archived images and are no use with paintings.

In this thesis Projective Geometry is employed in a flexible way to model the perspective distortion and recover full or partial 3D information from uncalibrated images and inferred scene geometric cues.

1.4 Applications and examples

The theory presented here can be applied to solving many of the engineering and architectural problems which involve measuring objects. For instance, it is useful to photogrammetry researchers for measuring dimensions of buildings from aerial images as well as in video compression techniques. In fact, if a 3D model of a scene is known then it is possible to eliminate all the unnecessary and redundant information and obtain a high rate compression of the data space to be stored or transfered.

This section analyses three of the many possible uses, which will be described in detail in the following chapters.

1.4.1 Architectural and indoor measurements

An important application is in taking measurements of man-made scenes (measuring objects like: furniture, doors and windows).

Geometry-based approaches are used here to compute distances on scene planar surfaces [24] (chapter 4). For example, the edge of a window can be transformed from the image into the world by a geometric transformation thus computing its real length (see figure 1.5). The accuracy of the measurements is also estimated.

Perspective distortions on planar surfaces are therefore removed and rectified (*fronto-parallel*) views created (see figure 1.6). Once two images of a world plane have been corrected for projective distortion, they can also be stitched together to make a mosaic image (see figure 1.7).

Furthermore, using the metric information retrieved for each planar surface and combining it with that computed for the others an indoor environment can be modelled as a simple shoe-box room. Protrusions from planar surfaces (columns, pipes, windows sills) can be measured using two

a b

Figure 1.5: **Measuring distances and estimating their accuracy:** (a) original image, a photograph of the facade of the Crystallography Laboratories, Oxford; (b) the height of different windows has been computed and the accuracy estimated.

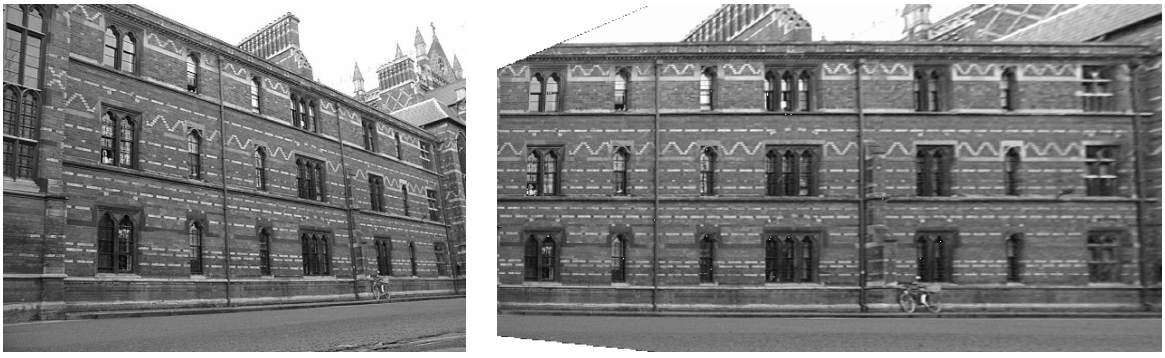

a b

Figure 1.6: **Rectification of a planar surface:** (a) original image, Keble College, Oxford; (b) rectified image. Perspective distortion has been removed.

or more views [23].

1.4.2 Forensic measurements

An important application of this theoretical framework is in forensic science, to measure metric dimensions of objects and people in images taken by surveillance cameras [26].

Because of the very bad quality of the images taken by cheap security cameras, it is not possible to recognize the face of the suspect or distinct features on his/her clothes. The height of the person becomes, therefore, an extremely useful identification feature.

Heights of people can be estimated from a single view using the techniques developed in

a

b

c

Figure 1.7: **Mosaicing two images:** (a) and (b) two images of The Queen's College MCR in Oxford; (c) mosaic image; the images have been perspectively corrected and stitched together.

chapter 5 (see figure 1.8). The main problem is that the suspect has usually departed the scene of crime or the scene has changed; therefore, in order to compute his/her height we can rely only on the actual image. This is complicated by the fact that usually only one view of the scene is available. Good results have been achieved here, some of which have been already applied in the forensic science community [26].

1.4.3 Reconstructing from paintings

Much interest is attracted by the possibility of building colourful 3D models and create beautiful animations of painted scenes [24, 74]. The mathematical theory developed here applies particularly well to paintings and drawings following the geometric rules of *Linear Perspective.*

Linear Perspective was invented at the beginning of the fifteenth century in Florence by the Italian architect Filippo Brunelleschi [64] and mathematically formalized by Leon Battista Alberti in

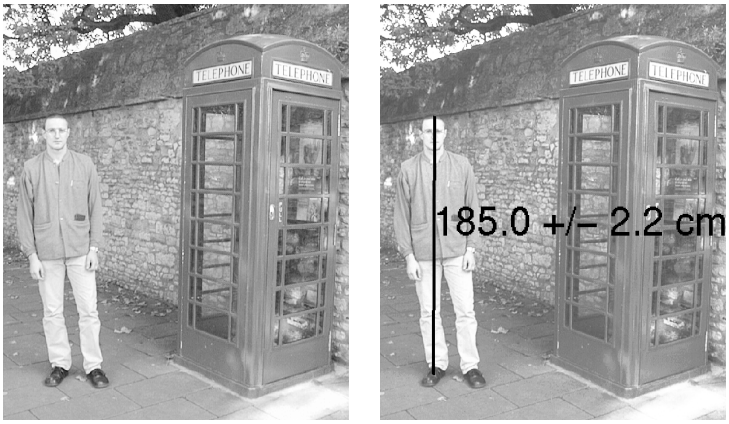

a b

Figure 1.8: **The height of a person standing by a phone box is computed**: (a) original image; (b) the computed height of the person and the estimated uncertainty are shown.

a b

Figure 1.9: **3D reconstruction from a painting**: (a) *St Jerome in His Study* (1630, Joseph R. Ritman Collection) by Henry V Steinwick (1580-1649); (b) a view of the reconstructed 3D model.

1435 [1]. Immediately after its invention Linear Perspective was applied by the masters of the Italian Renaissance (e.g. Masaccio, Piero della Francesca, Leonardo, Raffaello) to paintings, drawings and engravings, providing them with new expressions of depth and space.

A painting which follows the geometric rules of perspective behaves as a *perspective image* (like a photograph) and therefore the projective techniques in this thesis can be successfully applied (see fig. 1.9). A preliminary check on the correctness of the perspective (location of vanishing points, perspective effect etc.) is, of course, necessary.

1.5 Summary

1.5.1 Contributions

This thesis improves on the state of the art on various aspects of Computer Vision and understanding of photographs and visual art:

- a hierarchy of novel, accurate and flexible techniques is developed to make measurements and reconstruct three-dimensional scenes from uncalibrated images. They range from cases where no scene information is known to situations where only partial calibration is available;
- affine and metric reconstruction is made possible from single views as well as pairs or sequences of images;
- an analysis of the accuracy of the reconstruction is developed which predicts how errors affect the final measurements. The analytical theory is validated by means of statistical tests;
- the general algebraic techniques developed here open new ways to interpreting and understanding classical and modern works of art.

1.5.2 Thesis outline

This thesis begins in chapter 2 with a literature survey of the most relevant research conducted in the fields of: video metrology, 3D reconstruction, error analysis and art history.

In chapter 3 some background material is presented: an introduction to the basic geometry employed (3D-2D and 2D-2D projective mappings); the notation used; fundamental image processing algorithms (edge detection, radial distortion correction); the basics of error propagation theory.

Chapter 4 starts to bring the underlying mathematics to life by developing algorithms to perform metrology on planar surfaces. Different methods to accurately estimating *plane-to-plane homographies* are investigated. Planar homographies are then used to measure distances between points or parallel lines on a world plane. In order to estimate uncertainties in those measurements a first order error analysis has been developed where all major sources of error are taken into account.

A working application is also presented.

Chapter 5 extends measurements on planar surfaces to the three-dimensional case. Algorithms for recovery of partial and complete three-dimensional structure from single uncalibrated images are explored. The techniques make extensive use of planar projective transformations like *homographies* and *homologies* thus avoiding traditional problems like matching corresponding features over multiple views of a scene. Particular attention is paid in this chapter to: (i) measuring distances between two parallel planes; (ii) measuring on parallel planes and comparing these measurements to those obtained in any other parallel plane; (iii) determining the camera position. Uncertainties on the computed measurements are estimated too. This work is generalized to a parametrization of the 3D space as a collection of three pencils of parallel planes in three different directions.

Chapter 6 deals with multi-view geometry and describes the advantages of this approach over the single view. The geometry of two and three views gives rise to an elegant algebraic description of the 3D space employing planar homologies. It is shown that homologies encapsulate the fundamental geometric constraints: the epipolar constraint in the two-view case and the structure constraint in the three-view configuration. The elegance of this approach is highlighted by the duality relationship which arises naturally between the two-view and three-view configurations. Furthermore, a new interpretation of the space based on a *plane-plus-parallax* approach leads to simple formulations for computing structure and camera location.

Several examples on real images are provided in each chapter. Further examples are presented in the colour plates in chapter 7. They show images of the models computed by applying the described techniques to photographs and paintings.

Chapter 8 concludes this thesis with: a summary of the presented problems and the solution methods; a discussion on advantages and disadvantages of employing such approaches; a list of possible ways to improve the analysed techniques and future directions of research.

Chapter 2

Related work

2.1 Introduction

This chapter presents a survey of the most significant work in the field of three-dimensional reconstruction from two-dimensional images, and uncertainty estimation.

The papers are arranged from mono-view systems to bi- and multi-view ones. The works related to parallax-based approaches, estimation of the accuracy in metric reconstruction and geometric analysis of perspective paintings are also examined.

2.2 Using images for measuring and reconstruction

Visual metrology and three-dimensional reconstruction of scenes from images have been, in the past few years, amongst the main aims of Computer Vision. Much effort has been put into pursuing such goals and three main difficulties have been encountered:

- reconstructing from multiple images fundamentally involves solving the “correspondence” problem, i.e. which set of features in the images is genuinely the projection of a feature in the world;
- reliable and well defined geometric structure of the scene needs to be seen if a single view approach is applied;
- errors inevitably propagating along the computation chain cause a loss of accuracy in the measurements and thus the final structure.

Several researchers have been interested in *Euclidean* or more simply *affine* or *projective* reconstruction. Most of them have employed multi-view approaches but only a few have investigated the problem of conducting a proper uncertainty analysis to assess the accuracy of the final structure.

In this section different ways of recovering structure by using one or more views are analysed as well as various methods to estimate the associated uncertainty.

2.2.1 Using one view

In general one view alone does not provide enough information for a complete 3D reconstruction. However some metric quantities can be computed from the knowledge of some geometrical information such as the relative position of points, lines and planes in the scene. But in order to do so, in general, the intrinsic parameters of the camera need be known. These are: *focal length, principal point, skew, aspect ratio* [36].

A number of visual algorithms have been developed to compute the intrinsic parameters of a camera in the case that they are not known. This task is called *camera calibration.* Usually, calibration algorithms assume some of the camera internal parameters to be known and derive the remaining ones. Common assumptions are: unit aspect ratio, zero skew or coincidence of principal point and image centre. The calibration techniques described in this section are based on a single-view approach.

The work of Tsai [120] has been one of the most popular in the field of camera calibration. From a single image of a known, planar calibration grid (see fig. 2.1) it estimates the focal length of the camera and its external position and orientation assuming known principal point. An attempt to analyse the accuracy of the estimated parameters is also reported.

Caprile and Torre, in their classical work [12], develop an algorithm to compute the internal and external parameters of the camera (they assume unit aspect ratio and zero skew) from single views. They make use of simple properties of vanishing points; these can be extracted directly from the image by intersecting images of parallel lines. A simple calibration device consisting of a cube

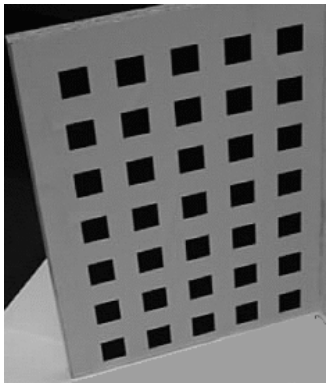

Figure 2.1: **Tsai grid:** camera parameters can be calibrated from the known pattern on the grid.

with sets of parallel lines drawn on its faces is employed. In particular the authors demonstrate that the principal point of the camera coincides with the orthocentre of the triangle whose vertices are the three vanishing points for three orthogonal directions. An earlier work on this subject can be found in the photogrammetry literature [48].

The problem of calibrating a camera is discussed in [36] by Faugeras. He presents algorithms to compute the projection matrix (*external calibration*) and eventually the camera internal parameters from only one view of a 3D known grid. He analyses linear and non linear methods for estimating the 3D-2D projection matrix, the robustness of the estimate and the best location of the reference points.

In Liebowitz and Zisserman's work [75] camera *self-calibration* is obtained simply from images of planar structures like building facades or walls, with distinguishable geometric structure. Use is made of scene constraints such as parallelism and orthogonality of lines and ratios of lengths. No specifically designed calibration object is required.

An interesting problem is addressed in [65] by Kim *et al.* In this paper the authors compute the position of a ball from single images of a football game. By making use of shadows on the ground plane and simple geometric relationships based on similar triangles the ball can be tracked throughout the sequence.

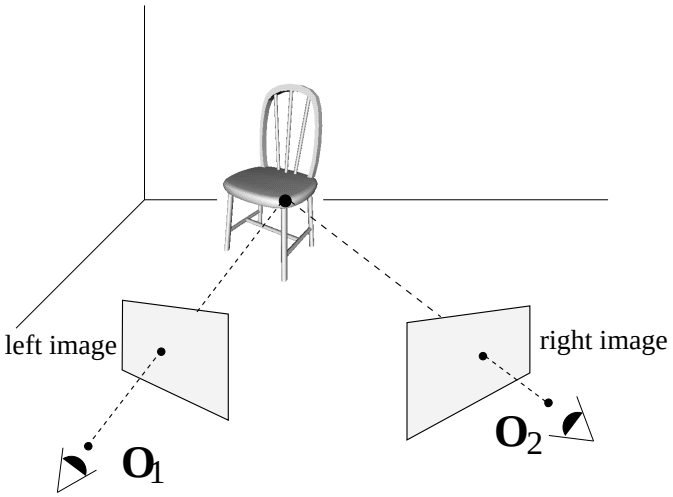

Figure 2.2: **Stereo acquisition system scheme:** two images of the same scene are captured. Three-dimensional structure can be computed from the analysis of those images.

This thesis develops a new approach to reconstruct 3D scenes from single images which does not need full camera calibration (chapter 5).

2.2.2 Using two views

The classical algorithms for 3D reconstruction use *stereo vision* systems [35]. Stereo vision consists of capturing two images of a scene, taken from different viewpoints and estimating the depth of the scene from analysing the disparity between corresponding features (see fig 2.2). This methodology finds its basis in trigonometry and triangulation and is employed by the human binocular vision system.

The basic steps in reconstructing a scene from two images are:

- Finding corresponding points on the two images.
- Intersecting the corresponding rays in the 3D space.

The following shows a comparison of how a reconstruction can be achieved using calibrated or uncalibrated images.

Calibrated route

The typical route for structure computation from pairs of calibrated images is as follows. Once two images of a scene with a calibration grid in it are captured by a fixed stereo rig, the 3D-2D projection matrices for each camera [41, 119] are computed (*external calibration*), and so is the *epipolar geometry* [36]. Some interesting features are extracted in both images, mainly corners and edges of objects in the scene. Popular approaches to feature detection include the Harris detector [49] for retrieving corners and the Canny detector [9] for edges. Then the process of matching features in the two images is performed by using the computed epipolar constraint [88]. Computing the 3D depth is now straightforward [36]. In fact the scene structure is computed via a ray triangulation task, achieved using an optimal algorithm such as the one described by Hartley and Sturm [54].

A classic work in this area is the one by Longuet-Higgins. In [76] the author presents an algorithm for computing the three-dimensional structure of a scene from a pair of perspective projections. If the images of eight world points can be located in both projections, then the three-dimensional location of other points and the relative geometry between the two viewpoints is obtained by solving a set of eight simultaneous linear equations. A fundamental application of this result is in scene reconstruction from two calibrated views.

A method for 3D reconstruction based on homography mapping from calibrated stereo systems is described in [132]. Zhang and Hanson investigate the problem of recovering the scene metric structure by mapping one image into the other using homographies inducted by planar surfaces in the scene. Using at least four coplanar correspondences the 3D structure can be achieved in Euclidean space up to a scale factor (*scaled Euclidean structure*) and two real solutions. In order to disambiguate the two solutions a third view is required.

However, using a calibrated stereo rig has some disadvantages since the camera internal parameters may not always be constant. It might be necessary to adjust the focal length; or accidental mechanical and thermal events can affect it. In order to overcome those problems new algorithms

to compute 3D structure from images with unknown camera calibration have been developed in the past few years (uncalibrated route).

Uncalibrated route

If the two cameras used during the acquisition process are uncalibrated (unknown internal parameters), then only a *projective structure* can be obtained [35]. Corresponding points on the two images can be matched and thus the *epipolar geometry* estimated. The two projection matrices are computed from the *fundamental matrix* but only up to a projectivity.

However, in order to use a pair of cameras as world measuring device a complete metric reconstruction is required. In order to extend a projective structure to an Euclidean one some more geometric information about the viewed scene is necessary. Several algorithms have been developed [37] to deal with this problem.

Given a pair of uncalibrated images, the two cameras can be calibrated from the analysis of the point matches in the two views. A self-calibration, non-iterative algorithm, based on matrix factorization has been developed by Hartley [50]. In this paper the camera intrinsic parameters are assumed to be constant. They are all known apart from the focal length which is computed, together with the relative pose of the cameras. No specialized calibration device is necessary.

Koenderink and van Doorn in [66] introduce the notion of *affine structure* from two uncalibrated views. The authors present a method for recovering structure from motion in a stratified manner. The results can be reformulated in terms of motion parallax.

In [84] Moons *et al.* present an algorithm for recovery of 3D affine structure from two perspective views taken by a camera undergoing pure translation (equivalently: translating object and stationary camera). The images of five points in two views need to be seen. The algorithm is further specialized towards single views of regular objects, such as objects containing parallel structures.

In [104] Shapiro *et al.* define the epipolar geometry between pairs of *affine cameras* and describe a robust algorithm to compute its special fundamental matrix. Least squares formulations

are employed in a noise-resistant fashion. A statistical noise model is employed to estimate the uncertainty on the computed cameras' relative pose.

In [134] Zisserman *et al.* describe a technique to determine affine and metric calibration for a stereo rig that does not involve calibration objects but a single, general motion of the whole rig with fixed parameters. The internal camera parameters and the relative orientation of the cameras are retrieved robustly and automatically (see also [32]). This approach does not require solving the non linear Kruppa equations [39, 67].

Related to the previous work is the paper by Zhang *et al.* [133]. It describes an algorithm for the self-calibration of a stereo rig and metric scene reconstruction using, again, the motion of the entire stereo rig but in this case a simplified camera model is used (the principal point is known). Because of the exploitation of information redundancy in the stereo system, this approach yields to a more robust calibration result than only considering a single camera.

In [38] Faugeras *et al.* investigate a method to upgrade from projective to affine and finally metric structure from pairs of images by making use of scene constraints such as parallelism, orthogonality and known ratios of line segments. This work applies well to reconstructing architectural and aerial views from long sequences. A similar approach is used by Liebowitz *et al.* in [74] wherein extensive use is made of *circular points* to elegantly upgrade from affine to metric structure.

2.2.3 Using three or more views

Two views suffice to reconstruct a scene, but adding one more image, taken from a third point of view can constrain more the reconstruction problem reducing the uncertainty in the estimated structure. This is particularly true if a line matching process is used rather than a point matching one (line matching is not possible in two views). Furthermore, the use of three or more views allows a check on the consistency of the features matched using the first two views.

Faugeras has been one of the first to investigate the problem of using more than two images. In [39] Faugeras *et al.* present a method for self-calibrating a camera using triplets of images from a

sequence. The authors demonstrate that it is possible to calibrate a camera just by pointing it at the environment, selecting points of interest and then tracking them in the image sequence as the camera moves (the camera internal parameters are assumed constant throughout the sequence). The camera motion does not need to be known. The solution is obtained by solving the Kruppa equations.

Work in reconstruction from multiple views has been conducted by Shashua in [4, 107, 108], where the geometry involved in a 3D reconstruction task from 2D images is analysed in a very systematic and algebraic way. The concept of *trifocal tensor* which encapsulates the geometric relationship between three views is used [53, 111]. This theory is also found useful for solving the "rendering" problem, i.e. from the knowledge of two images predicting what a third one will be if the camera is placed in a new position [40].

The problem of calibrating the camera and estimating the Euclidean structure of the scene using three or more uncalibrated images has been investigated also by Armstrong *et al.* in [2, 3]. The authors, using only point matches between images, compute the internal camera parameters and the Euclidean structure of the viewed scene. The camera undergoes a planar motion. This method presents the advantage that it can be applied in active vision tasks, the Euclidean reconstruction can be obtained during normal operation with initially uncalibrated cameras; i.e. the cameras do not need to be calibrated off-line. The trifocal tensor is used here too.

In [52] another approach for camera calibration using three or more images from a rotating camera is presented by Hartley. This method does not require the knowledge of the camera orientation and position and does not involve the epipolar geometry. In fact the images are taken from the same point of view and therefore the epipolar geometry is useless. The calibration process is based on image correspondences only and the internal parameters are assumed constant.

In [89] Pollefeys *et al.* investigate the problem of self-calibration and reconstruction from sequences with varying camera parameters. By employing a linear approximation followed by a non-linear refinement step they achieve an accurate three-dimensional metric structure of the viewed

scene while computing the internal parameters in each frame.

More recently many commercial products have been developed which reconstruct 3D architectural scenes from images. In particular *Facade* [29] has been one of the most successful systems for modelling and rendering architectural buildings from photographs. It consists of a hybrid geometric- and image-based approach. Realistic rendering is obtained by using "view-dependent texture mapping". Unfortunately the model building process involves considerable time and effort for the user.

Canoma [1] is a fast, interactive system to create 3D scenes from single or multiple images which makes extensive use of 3D templates. Another example is provided by *PhotoModeler* [2] where a 3D model of the viewed scene is computed from the knowledge of some control points.

An easy to use system is *PhotoBuilder* developed by Cipolla *et al.* [16]. The user interactively selects corresponding points on two or more photographs. The system, making use of parallelism and orthogonality constraints, computes the intrinsic and extrinsic parameters of the cameras and thus recovers metric models of architectural buildings.

2.2.4 Partial calibration

Not much work is present, in the literature, about metric reconstruction from partial calibration. A partially calibrated scene can provide only partial metric information.

In [91] Proesmans *et al.* use a minimal information about the scene (vanishing points and known vertical reference heights) to compute heights of people from forensic photographs. The authors make extensive use of the properties of cross-ratios and address the possibility of employing geometric information extracted from shadows. They also propose the Cascaded Hough Transform algorithm for the automatic computation of vanishing points.

In [124] Weinshall *et al.* make use of partial scene calibration, inferred directly from multiple

[1] `http://www.metacreations.com`
[2] `http://www.photomodeler.com`

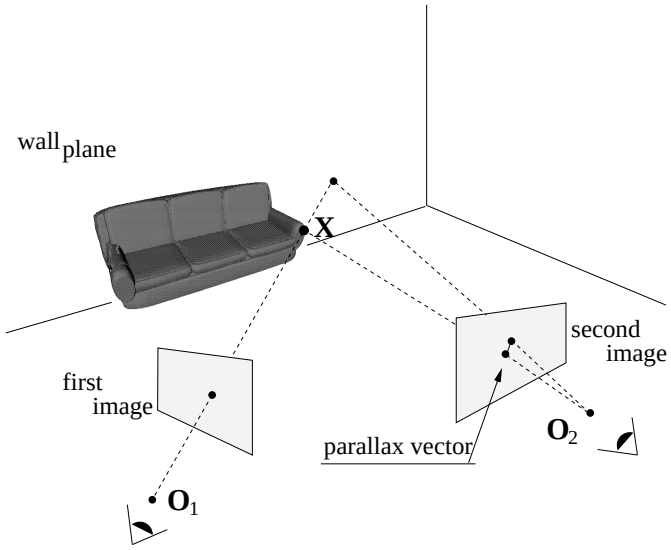

Figure 2.3: **Parallax geometry:** the parallax vector detected on the second view is related to the distance of the 3D point **X** from the wall plane.

images to obtain ordinal distances. A stratified approach is presented to upgrade the reconstruction to affine and finally Euclidean using the available scene information. This technique employs two views and a plane-plus-parallax approach.

The ideas presented in the above papers are explored and generalized in the novel, single- and multi-view reconstruction techniques developed in this thesis.

2.2.5 Parallax-based approaches

Some of the reconstruction methods make use of the concept of *parallax.*

One view only constrains each image point to lie on its projection ray, but, in order to obtain the depth of a 3D point with respect to a reference plane (or a generic surface) a second view is, in general, necessary. The parallax vector seen in the second image (see fig. 2.3) is, in fact, a function of the depth of the point from the reference plane.

The parallax approach has been used by Cipolla in [15, 17] as a way to estimate robustly curvature of surfaces. He shows that in order to recover depth from motion, usually, the rotational velocity must be known accurately. But this dependence can be removed if, instead of using raw

motion, the difference of the image motions of points (parallax) is used. The deletion of the rotational component of the motion field from the process of depth estimation can improve considerably the accuracy of the reconstruction.

Cipolla *et al.* employed *affine parallax* also in [71] for epipolar geometry computation using the parallax field; in [72] for the estimation of the ego-motion of a mobile robot and in [18] for 3D structure estimation; assessing once more the validity and effectiveness of this approach.

In his thesis [110] Sinclair discusses a method to analyse sequences of images and identify points which do not lie on the same planar surface. This work makes extensive use of planar projectivities (homographies). The parallax effect shown by points not lying on the same plane is employed for obstacle detection purposes. An analysis of the point localization error is developed to assess the limit to which noisy points can be considered to belong to the same plane.

In [100] Sawhney presents a formulation for the 3D motion and structure recovery that employs the parallax concept with respect to an arbitrary plane in the environment (real or virtual dominant plane). He shows that if an image coordinate system is warped using a plane-to-plane homography with respect to a reference view, then the residual image motion depends only on the epipoles and has a simple relation to the 3D structure.

Directly related to the work of Sawhney is the one of Kumar *et al.* [68] where the authors show that the magnitude of the parallax vector associated with a point is directly proportional to its distance from a reference plane and inversely proportional to its depth from the camera. Furthermore in [69] they show how scenes can be represented implicitly as a collection of images. In this paper a parallax-based approach is very effective for independent motion detection, pose estimation and construction of mosaic representations.

The geometry of the reconstruction problem has been deeply discussed and used by several researchers. In fact, understanding well the geometric properties of the acquisition system can be very useful for computing invariant quantities which increase the robustness and accuracy of the

process [36, 55, 86].

The idea of using parallax to compute geometric invariants, has been investigated by Irani and Anandan in [58, 59]. They present an analytical relationship between the image motion of pairs of points and several invariant quantities which can be derived from that relationship. This is shown to be useful for 3D scene structure recovery from more than two images as well as for the detection of moving objects and synthesis of new camera views.

In this thesis a *plane-plus-parallax* approach is developed in chapter 6 for computing scene structure and camera location and recovering motion and structure constraints.

2.2.6 Investigation of accuracy

The above sections have presented an overview of the relevant work done in reconstructing three-dimensional models of a scene from the analysis of planar images.

But metric information is no use without an appropriate estimation of the uncertainties on the computed distances. In fact, visual metrology must be treated as a precision engineering task; i.e. in a reliable, efficient and accurate way [36].

Faugeras [36] and Kanatani [61] have presented general analytical methods for error analysis propagation based on analysis of covariances and how these are affected by the chain of computations. Formulae to compute uncertainties of matrices, vectors and points are discussed and the powerful *implicit function theorem* introduced.

The problem of error estimation is discussed in [126] by Weng *et al.* In this paper the authors present an algorithm to estimate motion parameters and 3D scene structure from two perspective images. They also investigate how the noise corrupting the perspective projections of feature points affects the computed motion parameters. This is achieved by means of a first order *matrix perturbation theory* [47, 115].

In [102] Shapiro and Brady analyse an outlier rejection algorithm based on a *principal component regression* framework. An error estimation method is conducted using the matrix perturbation

theory and employed to identify and reject outliers. The authors also provide an error analysis for the optimal solution once the outliers have been removed. The validity of the proposed scheme is demonstrated by applying it to a structure-from-motion (SFM) problem where only affine cameras are considered.

Csurka *et al.* in [27, 129] compute the uncertainty related to the epipolar geometry between two cameras. They use the eight-point algorithm to compute the fundamental matrix and then estimate the associated covariance matrix. Two approaches are used to compute the uncertainty in the fundamental matrix: the first one is statistical and therefore as accurate as required but time consuming, the second is analytical and much simpler.

The first order estimation theory is analysed and used extensively in this thesis, including examples of propagating uncertainty through explicit transformations, transformations defined by implicit functions and even implicit functions with constraints. Working examples are presented showing how the developed theory can be applied to well known reconstruction problems.

In [70] Kumar and Hanson, using the parallax approach try to estimate robustly the camera location and orientation (*camera pose*) from a matched set of 3D model and 2D landmark features. Robust techniques for pose determination are developed to handle data contaminated by fewer than 50% outliers. The sensitivity of pose determination to incorrect estimates of camera parameters is analysed.

Mohr *et al.* in [83] discuss methods for accurate reconstruction from multiple images. The cameras internal parameters are unknown. The projective reconstruction is upgraded to Euclidean by identifying the plane at infinity and then imposing metric constraints. A simple theory for analysing the accuracy of the reconstructed scene is presented. The need for a sub-pixel image point detection is proven necessary to obtain accurate 3D structure.

2.2.7 Projective Geometry and Art History

This thesis also presents contributions in understanding Visual Arts. Since Art History has always been perceived as a non-scientific area little attempt has been made to analyse paintings in a mathematical way and, possibly, reconstruct the represented scenes.

In [64] Kemp investigates western art from a scientific point of view. In particular he describes the theory of *Linear Perspective* and its usage in the Renaissance period. The application of perspective rules to paintings is described in this book by analysing (by construction) shapes and location of painted objects. It is quite interesting to approach the same problems from an algebraic, Projective Geometry-based, point of view. The author also investigates the theory of light and colour until the French movements of nineteenth century.

Kemp's book demonstrates that Art History would benefit from the powerful tools offered by Computer Vision. On the other hand, Vision researchers, in an attentive analysis of the relevant paintings, would find new explanations and better understanding of the perception of the three-dimensional space.

In [44] Field *et al.* meticulously describe the geometric technique they have employed to analyse the perspective in Masaccio's fresco *La Trinitá* (1426, Firenze, Santa Maria Novella; see fig. 7.2a). Masaccio's florentine masterpiece is recognized by many as the first painting where Brunelleschi's perspective rules have been applied. Probably that is the first perspective image in history.

The same fresco has been investigated also by De Mey [28]. By analysing the construction lines, he has computed (with the help of CAD systems) a three-dimensional model of the painted chapel and created animations. The location of the eye point is computed too.

Much interest has also been captured by masterpieces by Piero della Francesca (1416 - 1492), a very skilled artist and mathematician [30] from the Renaissance period. In particular, his ability with perspective drawings and his "religious" care of details have made his masterpiece *La Flagel-*

lazione di Cristo (1460, Urbino, Galleria Nazionale delle Marche) one of the most studied perspective paintings [42].

Field in his recent book [43] presents an history of the evolution of the mathematics and optics, and their usage in visual arts from the Middle-age to the seventeenth century. He also describes how, after the seventeenth century, a number of mathematicians (e.g. Desargues, Pascal, Taylor) become increasingly interested in Linear Perspective [117], thus setting the foundations of modern *Projective Geometry*.

In this thesis, Projective Geometry-based methods for computing structure of painted scenes and creating convincing animations are presented in chapter 5. Results and examples are also shown (in colour) in chapter 7.

Chapter 3

Background geometry and notation

3.1 Introduction

Projective Geometry [7, 36, 101] provides this thesis with the basic mathematical background on top of which an effective and robust metrology framework is developed. This chapter presents the notation conventions and specific details of Projective Geometry which will be employed in the later chapters.

3.2 Notation

This thesis employs quite a standard notation convention:

- 3D points in general position are denoted by upper case bold symbols (e.g. $\mathbf{X}$);
- image positions and vectors by lower case bold symbols (e.g. $\mathbf{x}$, $\boldsymbol{\mu}_p$);
- scalars by normal face symbols (e.g. d, Z_p);
- matrices by typewriter style capitals (e.g. `P`, `H`);
- the line through two points $\mathbf{x}_1$ and $\mathbf{x}_2$ is denoted by $< \mathbf{x}_1 \mathbf{x}_2 >$.

When necessary, further notation choices are described in each chapter.

3.3 Camera models and perspective mappings

The image formation process must be modelled in a rigorous mathematical way. This section describes the camera models and the projective transformations which are relevant in the remainder of the thesis.

3.3.1 Pinhole camera model

The most general linear camera model is the well known central projection (*pinhole camera*).

Description

A 3D point in space is projected onto the image plane by means of straight visual rays. The corresponding image point is the intersection of the image plane with the visual ray connecting the optical centre and the 3D point (*cf.* Leonardo's Perspectograph in figure 3.1 and the schematic pinhole camera model in figure 3.2).

Algebraic interpretation

The projection of a world point $\mathbf{X}$ onto the image point $\mathbf{x}$ (fig. 3.2) is described by the following equation:

$$\mathbf{x} = \mathtt{P}\mathbf{X} \tag{3.1}$$

where $\mathtt{P}$ is the projection matrix, a 3×4 homogeneous matrix, and "=" is equality up to scale. The world and image points are represented by homogeneous vectors as $\mathbf{X} = (X, Y, Z, W)^\top$ and $\mathbf{x} = (x, y, w)^\top$. The scale of the matrix does not affect the equation, so only the eleven degrees of freedom corresponding to the ratio of the matrix elements are significant.

The camera model is completely specified once the matrix $\mathtt{P}$ is determined. The matrix can be computed from the relative positioning of the world points and camera centre, and from the camera internal parameters; however, it can also be computed directly from image-to-world point correspondences.

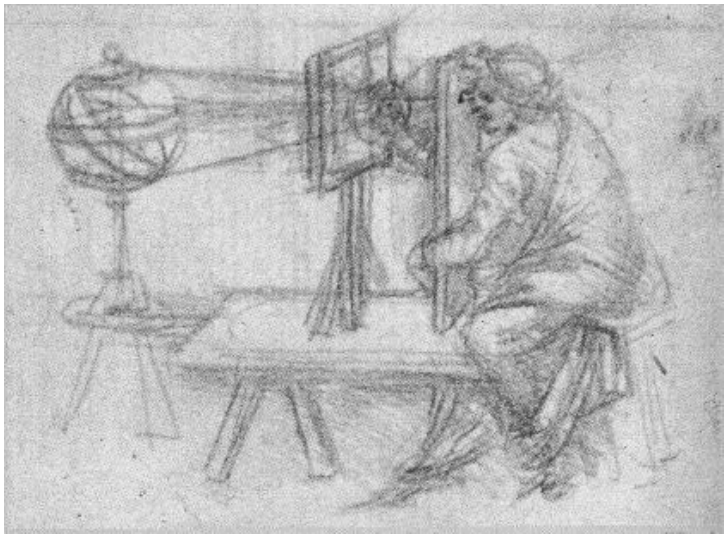

Figure 3.1: **Leonardo's perspectograph:**
"The things approach the point of the eye in pyramids, and these pyramids are intersected on the glass plane." Leonardo da Vinci (1452-1519), A.1v.

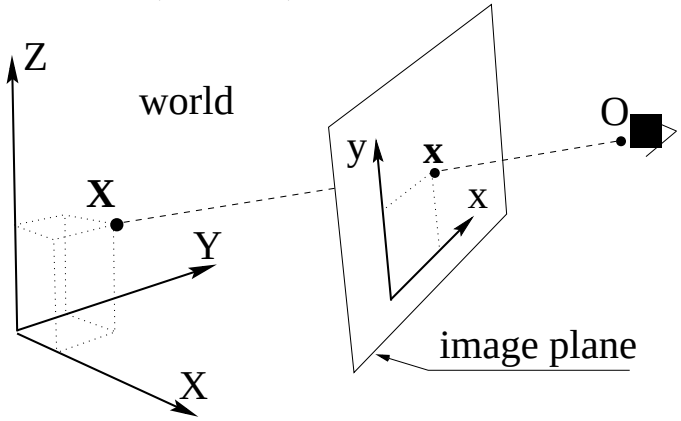

Figure 3.2: **Pinhole camera model:** a point $\mathbf{X}$ in the 3D space is imaged as $\mathbf{x}$. Euclidean coordinates X, Y, Z and x, y are used for the world and image reference systems, respectively. $\mathbf{O}$ is the centre of projection, the viewer.

3.3.2 Planar homography

An interesting specialization of the general central projection described above is a plane-to-plane projection; a 2D-2D projective mapping.

Figure 3.3: **An image of a planar surface induced by a homography:** the homography relates points on the world plane to points on the image and vice-versa.

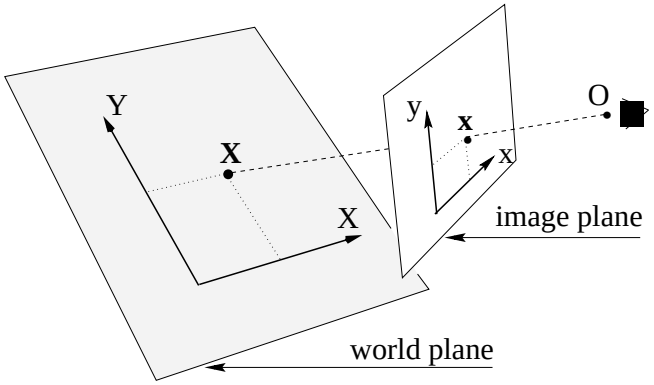

Figure 3.4: **Plane-to-plane camera model:** a point $\mathbf{X}$ on the world plane is imaged as $\mathbf{x}$. Euclidean coordinates X, Y and x, y are used for the world and image planes, respectively. $\mathbf{O}$ is the viewer's position.

Description

The camera model for perspective images of planes, mapping points on a world plane to points on the image plane (and vice-versa) is well known [101]. Points on a plane are mapped to points on another plane by a *plane-to-plane homography*, also known as a plane projective transformation. It is an bijective (thus invertible) mapping induced by the star of rays centred in the camera centre (centre of projection). Planar homographies arise, for instance, when a world planar surface is imaged (see fig. 3.3).

Algebraic parametrization

A homography is described by a 3×3 non-singular matrix. Figure 3.4 shows the imaging process. Under perspective projection corresponding points are related by [85, 101]:

$$\mathbf{x} = \mathtt{H}_i \mathbf{X} \tag{3.2}$$

where $\mathtt{H}_i$ is the 3×3 homogeneous matrix which describes the homography, and "=" is equality up to scale. The world and image points are represented by homogeneous 3-vectors as $\mathbf{X} = (X, Y, W)^\top$ and $\mathbf{x} = (x, y, w)^\top$ respectively. The scale of the matrix does not affect the equation, thus only the eight degrees of freedom corresponding to the ratio of the matrix elements are significant.

Since we are interested in recovering world quantities from images and the homography is an invertible transformation, in the following chapters (3.2) will be written as:

$$\mathbf{X} = \mathtt{H}\mathbf{x} \tag{3.3}$$

with $\mathtt{H} = \mathtt{H}_i^{-1}$ the homography mapping image points into world points.

The camera model is completely specified once the matrix $\mathtt{H}$ is determined. Here too the matrix can be computed from the relative positioning of the two planes and camera centre, and the camera internal parameters; however, it can also be computed directly from image-to-world correspondences. In particular, it can be shown that at least four world-to-image feature (point or line) correspondences (no three points collinear or no three lines concurrent) suffice to define the homography. The relative geometric position of the world features (referred to as "computation points/lines") must be known. This computation is described in section 4.2.

Inter-image homography

A planar surface viewed from two different viewpoints induces a homography between the two images. Points on the world plane can be transferred from one image to the other (fig. 3.5) by

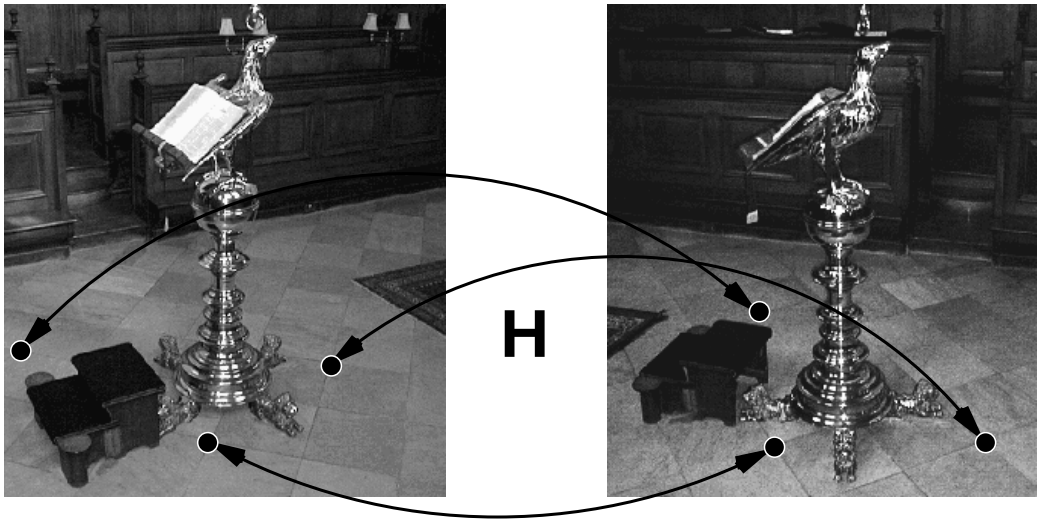

Figure 3.5: **Inter-image homography:** the floor viewed in both images induces a homography. Points can be mapped from one image to the other.

means of a homography mapping. This situation is considered in chapter 6 where the parallax effect of points off the distinguished plane is analysed.

3.3.3 Planar homology

In this section another interesting projective transformation is described, a planar homology. This is used extensively in the following chapters.

Description

A *planar homology* is a plane-to-plane projective transformation and a specialization of the homography. It is characterized by a line of fixed points, called the *axis* and a distinct fixed point not on the axis known as the *vertex* (figure 3.6). Planar homologies arise in several imaging situations, for instance, when different light sources cast shadows of an object onto the same plane.

Algebraic parametrization

Such a transformation is defined by a 3×3 non-singular matrix $\mathtt{H}$ with one distinct eigenvalue whose corresponding eigenvector is the vertex, and two repeated eigenvalues whose corresponding

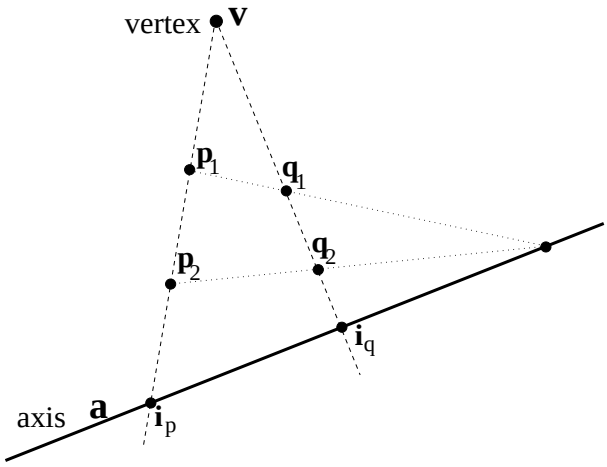

Figure 3.6: **A planar homology is defined by a vertex, an axis and a characteristic ratio:** its characteristic invariant is given by the cross-ratio $< \mathbf{v}, \mathbf{p_1}, \mathbf{p_2}, \mathbf{i}_p >$ where $\mathbf{p_1}$ and $\mathbf{p_2}$ are *any* pair of points mapped by the homology and $\mathbf{i}_p$ is the intersection of the line through $\mathbf{p_1}$ and $\mathbf{p_2}$ and the axis. The point $\mathbf{p_1}$ is projected onto the point $\mathbf{p_2}$ under the homology, and similarly for $\mathbf{q_1}$ and $\mathbf{q_2}$.

eigenvectors span the axis. A planar homology can be interpreted as a particular planar homography.

The projective transformation representing the homology can be parametrized directly in terms of the 3-vector representing the axis $\mathbf{a}$, the 3-vector representing the vertex $\mathbf{v}$, and a scalar factor μ as [123]:

$$\mathtt{H} = \mathtt{I} + \mu \frac{\mathbf{v}\mathbf{a}^\top}{\mathbf{v} \cdot \mathbf{a}} \tag{3.4}$$

The factor μ is the *characteristic* ratio and it can be computed as the cross-ratio of four aligned points as illustrated in figure 3.6. Thus $\mathbf{v}$ and $\mathbf{a}$ specify four degrees of freedom of the homology (the scales of $\mathbf{v}$ and $\mathbf{a}$ have no effect) and μ specifies one more. Then, the $\mathtt{H}$ matrix has only five degrees of freedom (a homography has eight d.o.f.) and thus it can be determined by 2.5 point correspondences.

Examples

Here we show two of the most common situations where planar homologies arise.

Images of planes related by a perspectivity

A perspectivity relating two planes in 3-space is imaged as a homology [122]. A particular

case is when two parallel planes in the world are related by a parallel projection (as in fig. 3.7). The vanishing line of the pencil of parallel planes is the axis and the vanishing point of the direction of projection is the vertex of the homology which relates the images of the two planes in the pencil (fig. 3.7b). Therefore, from (3.4), the homology can be parametrized as

$$\mathtt{H} = \mathtt{I} + \mu \frac{\mathbf{v}\mathbf{l}^\top}{\mathbf{v} \cdot \mathbf{l}} \tag{3.5}$$

where $\mathbf{v}$ is the vanishing point, $\mathbf{l}$ is the plane vanishing line and μ is the characteristic cross-ratio.

The parameter μ in (3.5) is uniquely determined from any pair of image points which correspond between the two planes. Once the matrix $\mathtt{H}$ is computed each point on a plane can be transferred into the corresponding point on the parallel plane. An example of this *homology mapping* is shown in figure 3.7c.

This configuration is extremely useful in chapter 5 to compute affine measurements from single views. Notice that homologies arise in the equivalent case, when a sequence of images of one plane is taken by a purely translating camera; this is described in section 4.5. A homology also relates images of points on a plane in different views taken by a camera purely rotating about the axis orthogonal to the plane.

Desargues configuration

Two triangles on a plane related such that the lines joining their corresponding vertices are concurrent are said to be in a *Desargues configuration.* Desargues' Theorem states that the intersections of their corresponding sides are collinear [101] (see fig. 3.8). Such triangles are related by a planar homology, with the common point of intersection being the vertex of the transformation, and the axis being the line containing the intersections of corresponding sides. Conversely, any triplet of points in correspondence under a homology must be in a Desargues configuration.

This configuration arises in real images, for example, when shadows of objects, originated from several light sources, are cast onto the same plane (see section 5.7). In section 6.3 the link between homologies and the structure and motion is derived in a plane-plus-parallax framework.

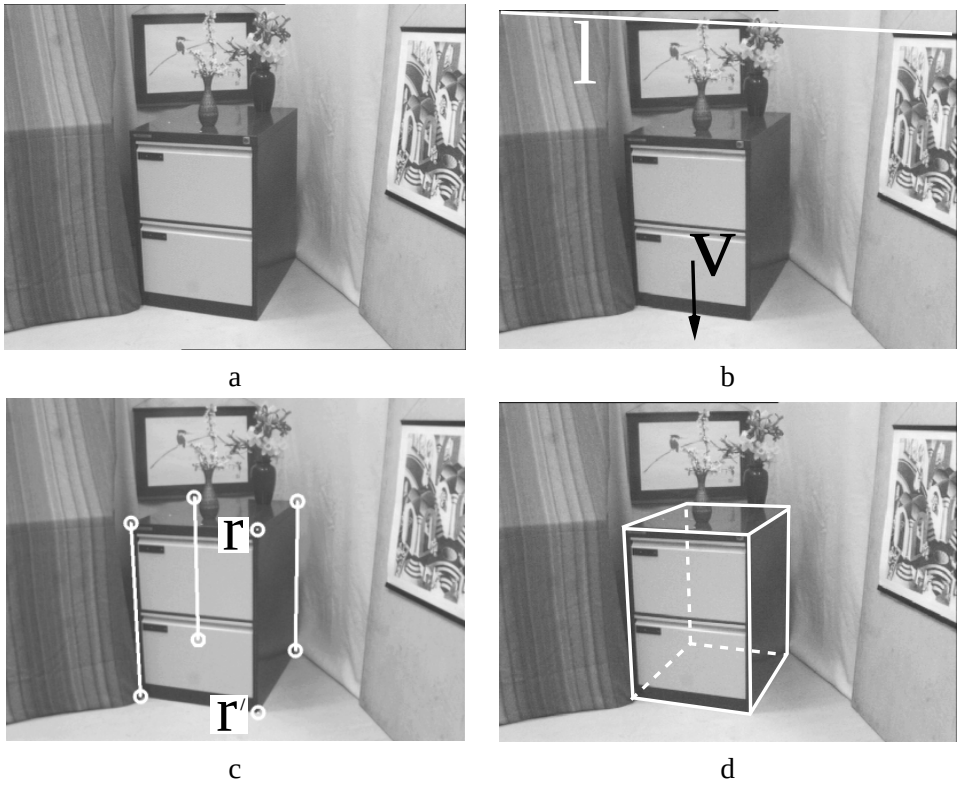

Figure 3.7: **Homology mapping of points from one plane to a parallel one, the two planes are related in the world by a parallel projection**: (a) original image, the floor and the top of the filing cabinet are parallel planes; (b) their common vanishing line (axis of the homology, shown in white) has been computed by intersecting two sets of horizontal edges. The vertical vanishing point (vertex of the homology) has been computed by intersecting vertical edges; (c) two reference corresponding points $\mathbf{r}$ and $\mathbf{r}'$ are selected on the two planes and the characteristic ratio of the homology computed. Three corners of the top plane of the cabinet have been selected and their corresponding points on the floor computed by the homology. Occluded corners have been retrieved too; (d) the wire-frame model shows the structure of the cabinet; occluded sides are dashed.

3.4 Radial distortion correction

A prerequisite of the theory treated in this thesis is that the camera behaves according to the pinhole model.

The problem. This requirement is violated by cheap wide angle lenses, such as those used in security systems. In such cases the grossest distortions from the pinhole model are usually radial. A correction step is, therefore, necessary before any metrology process may be performed.

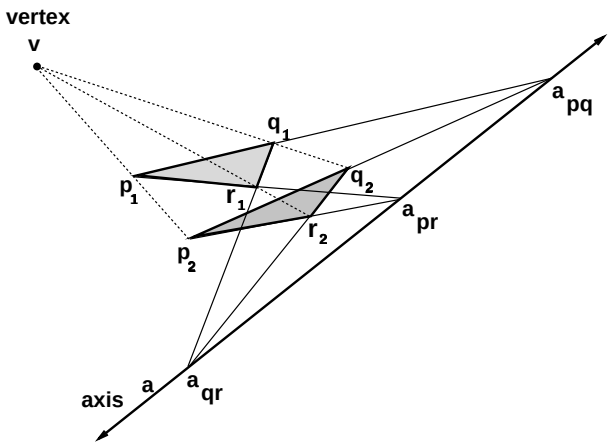

Figure 3.8: **Desargues configuration:** The two triangles $\mathbf{p}_1, \mathbf{q}_1, \mathbf{r}_1$ and $\mathbf{p}_2, \mathbf{q}_2, \mathbf{r}_2$ are in a Desargues configuration: the lines joining their corresponding vertices are concurrent and, as stated by Desargues theorem, the intersections of their corresponding sides are collinear. The two triangles are related by a planar homology where $\mathbf{v}$ is the vertex and $\mathbf{a}$ the axis.

Image correction. Several possible methods have been investigated [62, 113] to correct such a distortion. A simple one has been proposed by Devernay and Faugeras [31] where only one image of the scene is necessary and the radial distortion model is computed from the deformation of images of world straight edges.

Devernay's algorithm has been implemented here employing a slightly more complex radial distortion model to increase the correction accuracy:

$$\mathbf{x}_c = \mathbf{c} + f(r_d) * (\mathbf{x}_d - \mathbf{c}) \tag{3.6}$$

with

$$f(r_d) = 1 + k_1 r_d + k_2 r_d^2 + k_3 r_d^3 + k_4 r_d^4, \quad r_d = d(\mathbf{x}_d, \mathbf{c})$$

where $\mathbf{x}_d$ is a point in the distorted image and $\mathbf{x}_c$ the corresponding point in the corrected image. $\mathbf{c}$ is the centre of distortion. $f(r_d)$ is the correction factor; it depends on the radius r_d ($d(\mathbf{a}, \mathbf{b})$ is distance between the points $\mathbf{a}$ and $\mathbf{b}$) and the correction coefficients k_i.

Account is taken of the fact that the centre of distortion might not coincide with the principal point of the image. Point coordinates are taken with respect to the centre of the image and normal-

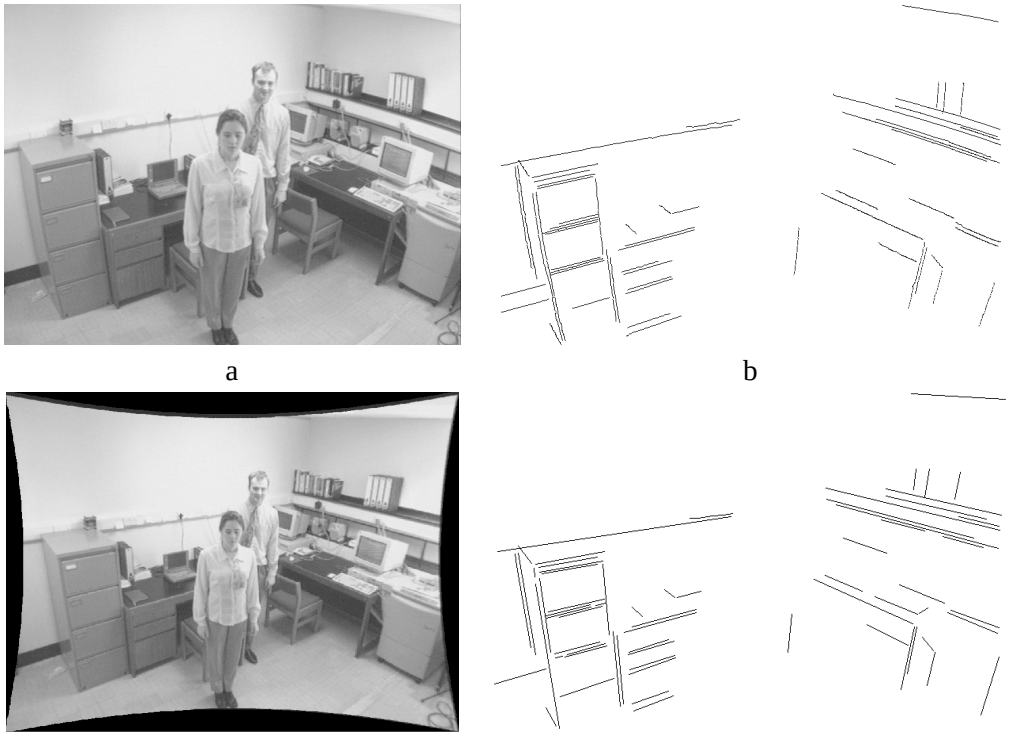

Figure 3.9: **Radial distortion correction:** (a) original image showing radial distortion, note that straight edges in the scene appear curved in the image (e.g. the left edge of the filing cabinet); (b) lines corresponding to straight world edges have been selected in image (a) and used to compute the following distortion parameters: $k_1 = 0.092$, $k2 = -0.007$, $k3 = 0.053$, $k4 = -0.012$ (the centre of distortion has been assumed in this case at the centre of the image); (c) corrected image; (d) edges from corrected image; images of straight scene edges are now straight.

ized. Unit aspect-ratio and square pixels hase also been assumed. The radial correction algorithm simply computes the best distortion parameters ($\mathbf{c}$, $k_i \ \forall i = 1 \cdots 4$) which transform the selected curved edges into straight ones.

An example. Figure 3.9a shows an image captured from a cheap security type camera which exhibited radial distortion (note how straight edges in the scene appear curved in the image).

Edges have been extracted automatically by a Canny edge detector [10]. A set of edges assumed to be straight in the scene has been selected (fig. 3.9b) and from those the distortion parameters computed and the image corrected accordingly (fig. 3.9c). Note that now images of straight

edges in the world are straight (for example, the left edge of the filing cabinet). Such an image is now perspective and metrology algorithms can safely be performed.

3.5 Vanishing points and vanishing lines

Vanishing points and vanishing lines are extremely powerful geometric cues. They convey a lot of information about direction of lines and orientation of planes. These entities can be estimated directly from the images and *no* explicit knowledge of the relative geometry between camera and viewed scene is required [21, 75, 81, 109]. Often they lie outside the physical image (as in fig. 3.7b), but this does not affect the computations.

Objects' straight edges

The first step towards the computation of vanishing points and lines is the accurate detection of straight objects' edges. Straight line segments are detected in an image at sub-pixel accuracy by using a Canny edge detector [10]; edge linking; segmentation of the edgel chain at high curvature points; and finally straight line fitting by orthogonal regression to the resulting chain segments (fig. 3.10b).

Furthermore, lines which are the projection of a physical edge in the world might appear broken in the image because of occlusions. A simple merging algorithm based on orthogonal regression has been implemented to merge several selected edges together. Merging aligned edges to create longer ones increases the accuracy of their location and orientation. An example is shown in figure 3.10c.

Computing vanishing points

Images of parallel world lines intersect each other in the same vanishing point. This is, therefore, defined by at least two such lines. However, if more than two lines are available a *Maximum Likelihood Estimate* (MLE) algorithm is employed to estimate the point [75] (fig 3.11).

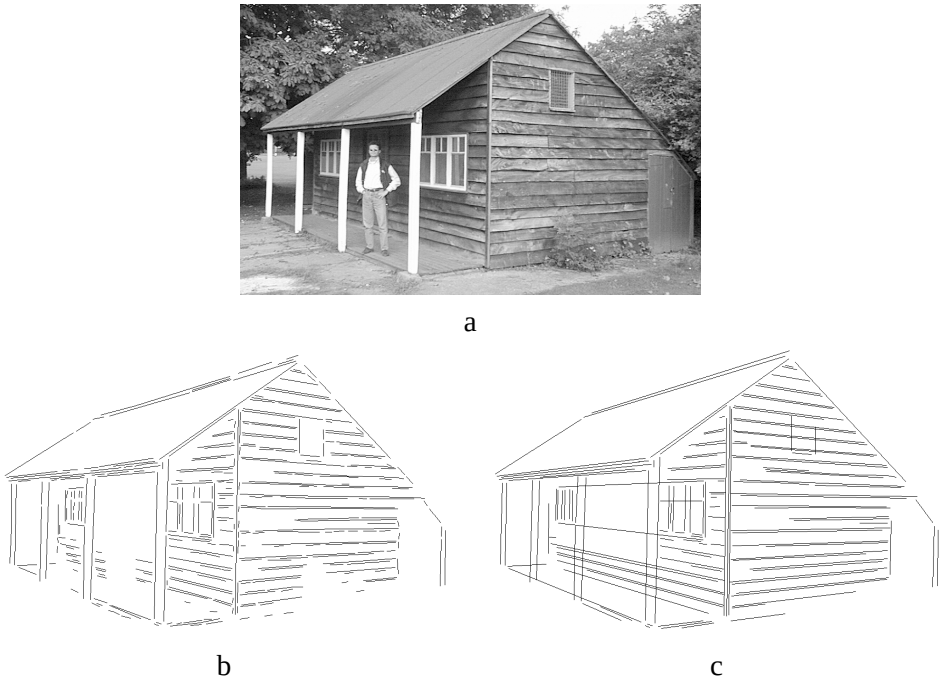

a b c

Figure 3.10: **Computing and merging straight edges:** (a) original image; (b) some of the edges detected by the Canny edge detector. Straight lines have been fitted to them. (c) edges after the merging process. Different segments belonging to the same edge in space are merged together.

Figure 3.11: **Computing the vanishing point of the vertical direction:** images of parallel edges of the tower (Magdalen College, Oxford) intersect in the vanishing point (white circle); only two such lines are sufficient.

Computing vanishing lines

Images of lines parallel to each other and to a plane intersect in points on the plane vanishing line.

Therefore two sets of those lines with different directions are sufficient to define the plane vanishing

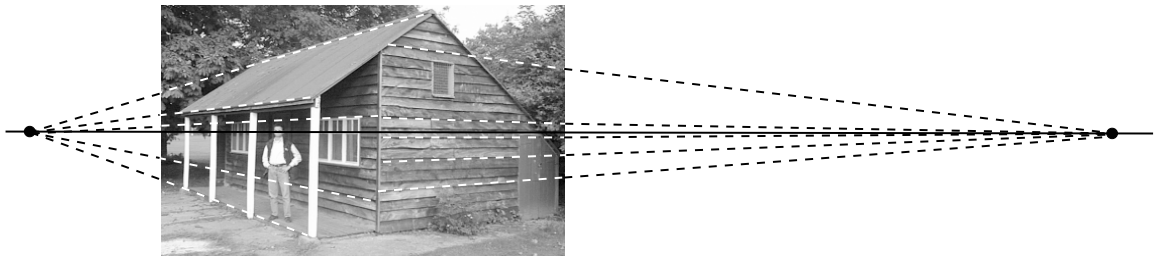

Figure 3.12: **Computing the vanishing line of the ground plane, the horizon:** The vanishing line of the ground is shown in solid black. The planks on both sides of the shed define two sets of lines parallel to the ground (dashed); they intersect in points on the vanishing line. Two such points suffice to define the plane vanishing line.

line (fig 3.12). An MLE algorithm is employed if more than two orientations are available.

3.6 Uncertainty analysis

This section describes the basic ideas underlying the analysis of uncertainties treated in this thesis.

The metrology algorithms described in the following chapters rely on applying non linear transformations to image and world quantities (e.g. points and reference distances) to compute world measurements (e.g. distances between points and ratios of areas). Since the input quantities and the transformations are uncertain, the output measurements are uncertain too (fig. 1.2). In order to determine how the uncertainty propagates from input to output of the computation chain and estimate the measurement accuracy two methods are considered: a statistical one and an analytical one.

Uncertainties are modelled as *Gaussian* noise and described by the associated covariance matrix. For example, the uncertainty in the localisation of a point $\mathbf{X}$ is modelled as a bi-dimensional Gaussian (see fig. 3.13) centred on the point itself. The uncertainty is described by a covariance matrix $\Lambda_{\mathbf{X}}$ and can be visualized also as an ellipse whose axes are given by the principal components of the related covariance matrix. It is not strictly necessary to have such idealised distributions but this has not been found to be a restriction in practice.

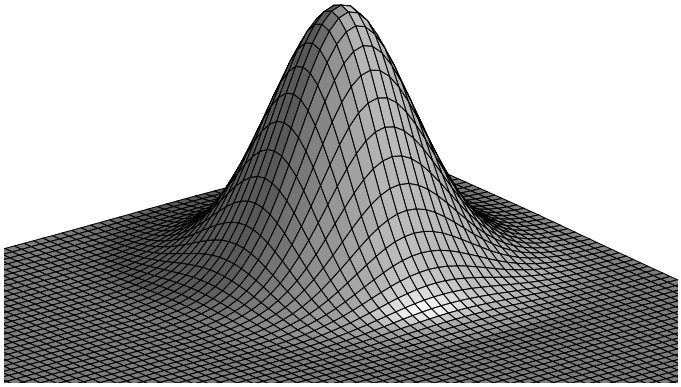

Figure 3.13: **Typical isotropic Gaussian density probability function:** this is used to model the uncertainty in the localisation of points on planes.

Statistical method

This consists of an *iterative* algorithm which makes use of the *Law of Large Numbers*.

By denoting with $\mathbf{x}$ the input data and $\mathbf{f}$ the geometric transformation that maps the input $\mathbf{x}$ into the final measurements $\mathbf{y}$ we can write:

$$\mathbf{y} = \mathbf{f}(\mathbf{x}) \tag{3.7}$$

At each iteration i a random set of input data $\mathbf{x}_i$ is generated (according to its covariance $\Lambda_{\mathbf{x}}$); then a random output measurement, $\mathbf{y}_i$, is obtained from (3.7).

The process is repeated a large number of times N thus obtaining a distribution of measurements around the true mean $\overline{\mathbf{y}}$. If N is large enough then the mean measurement $\overline{\mathbf{y}}$ can be approximated by:

$$\overline{\mathbf{y}} \approx \frac{\sum_{i=1}^{N} \mathbf{y}_i}{N}$$

and its covariance by:

$$\Lambda_{\mathbf{y}} \approx \frac{\sum_{i=1}^{N} \left[(\mathbf{y}_i - \overline{\mathbf{y}})(\mathbf{y}_i - \overline{\mathbf{y}})^{\top} \right]}{N-1} \tag{3.8}$$

This method is very costly in terms of CPU time, and in fact it returns reliable results only for a very large number of iterations. It will be used in the following chapters to validate the analytical method described below.

Analytical method

The analytical method takes account of the fact that the measurement $\mathbf{y}$ is related to the input data $\mathbf{x}$ by an analytical function $\mathbf{f}$ (generally non linear). This relationship is approximated with a linear one by means of a first order *Taylor series expansion.* By assuming noise only on the input data $\mathbf{x}$ and not on the transformation (3.7) becomes [20, 36]:

$$\mathbf{f}(\overline{\mathbf{x}} + \Delta\mathbf{x}) = \mathbf{f}(\overline{\mathbf{x}}) + \boldsymbol{\nabla}\mathbf{f}(\overline{\mathbf{x}})\Delta\mathbf{x} + \mathcal{O}(||\Delta\mathbf{x}||^2)$$

from where, ignoring second order terms, it is easy to compute the mean value of the output measurement:

$$\overline{\mathbf{y}} \approx E\left[\mathbf{f}(\overline{\mathbf{x}}) + \boldsymbol{\nabla}\mathbf{f}(\overline{\mathbf{x}})\Delta\mathbf{x}\right] = E[\mathbf{f}(\overline{\mathbf{x}})] = \mathbf{f}(\overline{\mathbf{x}})$$

consequently the covariance of the measurement $\Lambda_{\mathbf{y}}$ is:

$$\begin{aligned}
\Lambda_{\mathbf{y}} &= E([\mathbf{f}(\overline{\mathbf{x}} + \Delta\mathbf{x}) - \overline{\mathbf{y}}][\mathbf{f}(\overline{\mathbf{x}} + \Delta\mathbf{x}) - \overline{\mathbf{y}}]^\top) \\
&\approx E([\mathbf{f}(\overline{\mathbf{x}} + \Delta\mathbf{x}) - \mathbf{f}(\overline{\mathbf{x}})][\mathbf{f}(\overline{\mathbf{x}} + \Delta\mathbf{x}) - \mathbf{f}(\overline{\mathbf{x}})]^\top) \\
&\approx E(\boldsymbol{\nabla}\mathbf{f}\Delta\mathbf{x}\Delta\mathbf{x}^\top\boldsymbol{\nabla}\mathbf{f}^\top) \\
&= \boldsymbol{\nabla}\mathbf{f}\Lambda_{\mathbf{x}}\boldsymbol{\nabla}\mathbf{f}^\top
\end{aligned}$$

In the case the relationship between input data and final measurement is described by an implicit function then the covariance $\Lambda_{\mathbf{y}}$ is obtained by making use of the *implicit function theorem* [20, 36]. Further analysis must be carried out in both, statistical and analytical methods in the case the transformation $\mathbf{f}$ is uncertain too. When necessary this case will be addressed in the relevant chapters.

The advantage in using such analytical method is that it provides a non iterative and therefore fast algorithm. The main disadvantage is that it introduces an approximation of the non-linear mapping function. Therefore a further analysis to check how much this approximation affects the final results is required.

In the past only the first order theory has been used. This thesis still uses the linear approximation but only after having proved that it is sufficient for the purposes of this work. The check of goodness of the first order analysis is done by comparing the first order results with the second order ones and with a number of Monte Carlo simulations, i.e. the statistical method described above is used as a test of goodness of the analytical approach.

Example

In this example we compute the uncertainty in the localization of a point $\mathbf{x}'$ obtained from a homographic mapping of an uncertain point $\mathbf{x}$ on a different plane. The homography is described by the matrix $\mathtt{H}$ (such that $\mathbf{x}' = \mathtt{H}\mathbf{x}$) and is assumed known and exact. Uncertainty is assumed on the input point $\mathbf{x}$, its covariance being $\Lambda_{\mathbf{x}}$.

Analytical method

From the first order error analysis the uncertainty on the location of the point $\mathbf{x}'$ is:

$$\Lambda_{\mathbf{x}'} = \mathtt{H}\Lambda_{\mathbf{x}}\mathtt{H}^{\top} \tag{3.9}$$

Validation of first order analysis

The statistical Monte Carlo method is now employed to assess the validity of (3.9). The test algorithm is in the following three steps:

- 10000 Gaussian random points centred about a mean value $\mathbf{x}$ with covariance $\Lambda_{\mathbf{x}}$ are generated on the first plane;
- each point is transferred onto the second plane by the homography $\mathtt{H}$, thus creating a distribution of points;
- the covariance of this distribution is computed from (3.8) and compared to the one obtained from (3.9).

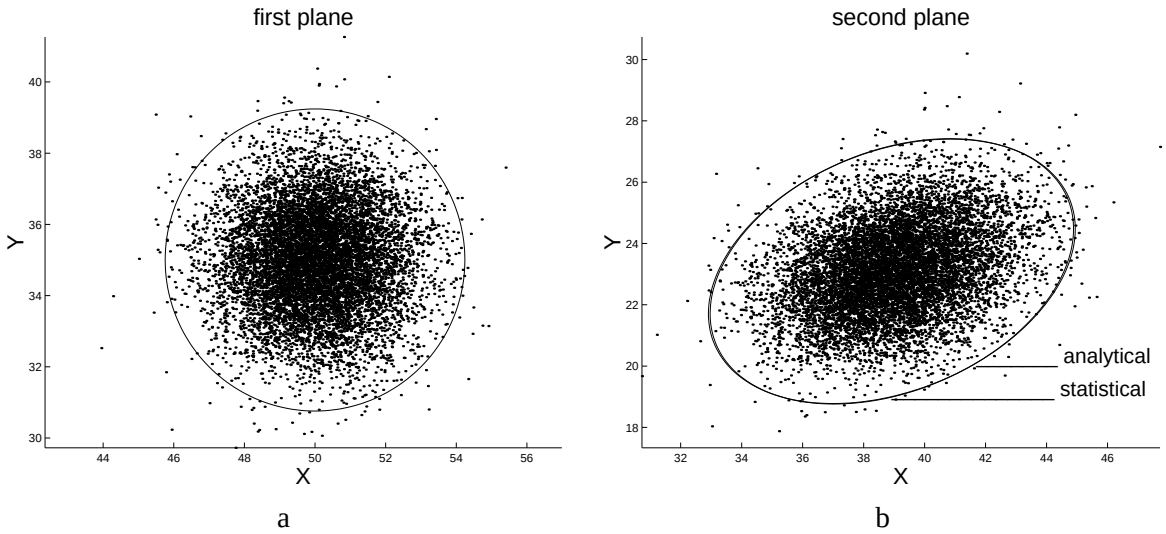

Figure 3.14: **Example of validation of first order error analysis by using a Monte Carlo test:** (a) 10000 Gaussian points have been generated about the mean position $\mathbf{x}$ with covariance $\Lambda_{\mathbf{x}}$ on the first plane. The corresponding 3-standard deviation ellipse is shown. (b) distribution of the output points $\mathbf{x}'$ on the second plane. Both analytical and simulated 3-standard deviation ellipses are drawn. They are almost overlapping, confirming the validity of the analytical prediction.

Figure 3.14 shows the results for synthetic data. Analytical and simulated covariance ellipses are almost overlapping, thus proving the validity of the first order approximation in this case.

Further details and examples on real data are presented in chapter 4.

Chapter 4

Metrology on planes

4.1 Introduction

This chapter develops an algorithm to measure distances on planar surfaces (see also [24]). The position, orientation and internal parameters of the camera are unknown. The imaging process is modelled as in section 3.3.2 as a homographic mapping between the world plane and the image plane.

Once the image-to-world homography matrix is determined the back-projection of an image point to a point on the world plane is straightforward. The distance between two points on the world plane is then simply computed from the Euclidean distance between their back-projected images. The estimation of the homography matrix is described in section 4.2 and then, that is used to obtain a number of world measurements.

Estimating the accuracy (or uncertainty) on planar distance measurement requires a careful treatment of the sources of error, not just the error in selecting the image points but also the error in the homography matrix itself. The latter arises from error in localization of the point correspondences (computation points) from which the matrix is computed.

The uncertainty analysis developed here builds on and extends previous analysis of the uncertainty in relations estimated from homogeneous equations, for example homographies [94, 95] and epipolar geometry [27, 36]. It extends these results because it covers the cases both of where the matrix is exactly *and* is over determined by the world-image correspondences, and it is not adversely affected when the estimation matrix is near singular.

In this chapter first order analysis is proved to be sufficient in typical imaging arrangement. It is also proved to be exact for the affine part of the homography and only an approximation for the non-linear part. An expression for the covariance of the estimated H matrix is derived in section 4.3.2. The correctness of the uncertainty predictions is tested both by Monte Carlo simulation (section 4.3.3) and by numerous experiments on real images (section 4.4). Examples on interior and architectural measurements are shown together with examples on rectification of planes in images of real scenes and paintings from the Italian Renaissance. Finally, in section 4.5 some more properties of the image rectification process are investigated.

4.2 Estimating the homography

As seen in the introduction the main problem is to estimate the homography. From (3.3) each image-to-world point correspondence provides two equations which are linear in the H matrix elements. They are:

$$\begin{aligned} h_{11}x + h_{12}y + h_{13} &= h_{31}xX + h_{32}yX + h_{33}X \\ h_{21}x + h_{22}y + h_{23} &= h_{31}xY + h_{32}yY + h_{33}Y \end{aligned}$$

For n correspondences we obtain a system of $2n$ equations in 8 unknowns. If $n = 4$ (as in fig. 4.1) then an exact solution is obtained. Otherwise, if $n > 4$, the matrix is over determined, and H is estimated by a suitable minimisation scheme.

The covariance of the estimated H matrix depends both on the errors in the position of the points used for its computation *and* the estimation method employed.

There are three standard methods for estimating H:

i. Non-homogeneous linear solution. One of the 9 matrix elements is given a fixed value, usually unity, and the resulting simultaneous equations for the other 8 elements are then solved using a

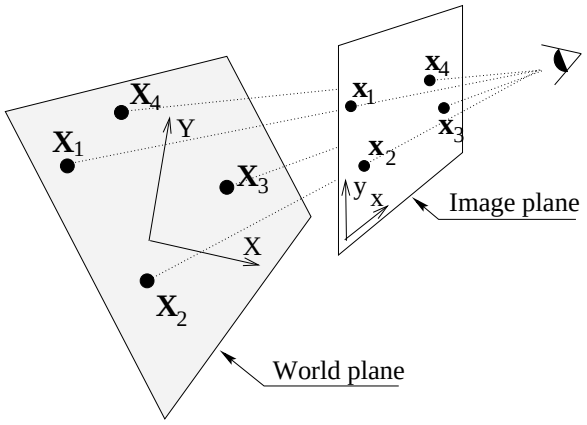

Figure 4.1: **Computing the plane-to-plane homography:** at least four corresponding points (or lines) are necessary to determine the homography between two planes.

pseudo-inverse. This is the most commonly used method. It has the disadvantage that poor estimates are obtained if the chosen element should actually have the value zero[1].

ii. Homogeneous solution. The solution is obtained using SVD. This is the method used here and is explained in more detail below. It does not have the disadvantage of the non-homogeneous method but it minimizes an algebraic error which does not have a geometric meaning.

iii. Non-linear geometric solution. In this case the summed Euclidean distances between the measured and the mapped point is minimised, i.e. minimising the following cost function C:

$$C = \sum_{i=1}^{n} \left\{ \left[\begin{pmatrix} X_i \\ Y_i \end{pmatrix} - \frac{1}{(\mathtt{H}\mathbf{x}_i)_3} \begin{pmatrix} (\mathtt{H}\mathbf{x}_i)_1 \\ (\mathtt{H}\mathbf{x}_i)_2 \end{pmatrix} \right]^2 + \left[\begin{pmatrix} x_i \\ y_i \end{pmatrix} - \frac{1}{(\mathtt{H}^{-1}\mathbf{X}_i)_3} \begin{pmatrix} (\mathtt{H}^{-1}\mathbf{X}_i)_1 \\ (\mathtt{H}^{-1}\mathbf{X}_i)_2 \end{pmatrix} \right]^2 \right\}$$

This returns the Maximum Likelihood Estimation of the $\mathtt{H}$ matrix. This method has the advantage, over the above two algebraic methods, that the quantity minimised is meaningful and corresponds to the error involved in the measurement (similar minimisations are used to estimate the fundamental matrix and trifocal tensor [118, 131]). There is no closed form solution in this case and a numerical minimisation scheme, such as Levenberg-Marquardt [90], is employed. Usually an initial solution is obtained by method (ii), and then "polished" using this method.

[1] This occurs, for instance, if we choose $h_{33} = 1$ and the origin of the image coordinate system lies on the vanishing line of the plane under consideration.

4.2.1 Homogeneous estimation method

Writing the $\mathtt{H}$ matrix as a 9-vector $\mathbf{h} = (h_{11}, h_{12}, h_{13}, h_{21}, h_{22}, h_{23}, h_{31}, h_{32}, h_{33})^\top$ the homogeneous equations (3.3) for n points become $\mathtt{A}\mathbf{h} = \mathbf{0}$, with $\mathtt{A}$ the $2n \times 9$ matrix:

$$\mathtt{A} = \begin{pmatrix} x_1 & y_1 & 1 & 0 & 0 & 0 & -x_1X_1 & -y_1X_1 & -X_1 \\ 0 & 0 & 0 & x_1 & y_1 & 1 & -x_1Y_1 & -y_1Y_1 & -Y_1 \\ x_2 & y_2 & 1 & 0 & 0 & 0 & -x_2X_2 & -y_2X_2 & -X_2 \\ 0 & 0 & 0 & x_2 & y_2 & 1 & -x_2Y_2 & -y_2Y_2 & -Y_2 \\ \vdots & \vdots & \vdots & \vdots & \vdots & \vdots & \vdots & \vdots & \vdots \\ x_n & y_n & 1 & 0 & 0 & 0 & -x_nX_n & -y_nX_n & -X_n \\ 0 & 0 & 0 & x_n & y_n & 1 & -x_nY_n & -y_nY_n & -Y_n \end{pmatrix}$$

The problem of computing the $\mathbf{h}$ vector is reduced to the constrained minimisation of the following cost function:

$$C = \mathbf{h}^\top \mathtt{A}^\top \mathtt{A}\mathbf{h} \tag{4.1}$$

subject to the constraint that $||\mathbf{h}|| = 1$. The corresponding Lagrange function is :

$$\mathcal{L} = \mathbf{h}^\top \mathtt{A}^\top \mathtt{A}\mathbf{h} - \lambda(\mathbf{h}^\top \mathbf{h} - 1) \tag{4.2}$$

Differentiating it with respect to $\mathbf{h}$ and setting these derivatives equal to zero we obtain:

$$\frac{\partial \mathcal{L}}{\partial \mathbf{h}} = 2\mathtt{A}^\top \mathtt{A}\mathbf{h} - 2\lambda\mathbf{h} = 0$$

i.e.

$$\mathtt{A}^\top \mathtt{A}\mathbf{h} = \lambda\mathbf{h}$$

Therefore the solution $\mathbf{h}$ is an unit eigenvector of the matrix $\mathtt{A}^\top\mathtt{A}$ and $\lambda = \mathbf{h}^\top \mathtt{A}^\top \mathtt{A}\mathbf{h}$ is the corresponding eigenvalue.

In order to minimise the C function, only the eigenvector $\tilde{\mathbf{h}}$ corresponding to the minimum eigenvalue $\tilde{\lambda}$ should be considered. This eigenvector can be obtained directly from the SVD of $\mathtt{A}$. In the case of $n = 4$, $\mathbf{h}$ is the null-vector of $\mathtt{A}$ and the residuals are zero.

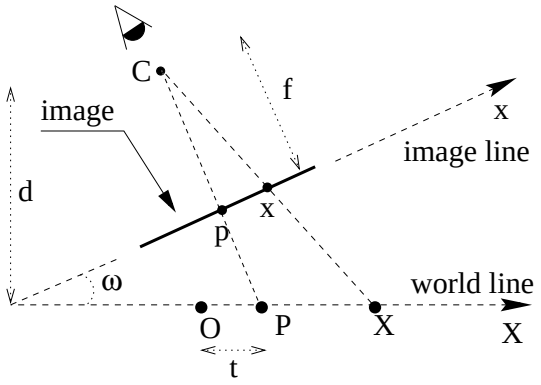

Figure 4.2: **One-dimensional camera model:** the camera centre is at distance f (the focal length) from the image line. The ray at the principal point p is perpendicular to the image line, and intersects the world line at P, with world ordinate t. ω is the angle between the world and image lines.

4.3 Uncertainty analysis

As shown in section 3.3.2 if $\mathbf{x}$ is a point on the image plane its back-projection onto the world plane is given by the (3.3) (in homogeneous coordinates). However the input image point $\mathbf{x}$ is uncertain because of localization errors on the image. Furthermore the homography is uncertain because it is obtained from $n \geq 4$ pairs of uncertain computation points (their location is known but uncertain). These two sources of error affect the localisation of the output point $\mathbf{X}$ on the world plane and consequently the distance between two world points.

The goal here is to model the uncertainty in the localization of a world point and in the distance between two world points once the uncertainty in the localisation of image points and computation pairs is known.

4.3.1 First and second order uncertainty analysis

In order to avoid unnecessarily complicated algebra the comparison between first and second order analysis is developed for a line-to-line homography (see fig. 4.2). The one-dimensional case illustrates all the ideas involved, and the algebraic expressions are easily interpreted. The generalisation to 3×3 matrices is straightforward and does not provide any new insights here.

In the one-dimensional case (3.3) reduces to

$$\begin{pmatrix} X \\ 1 \end{pmatrix} = \mathtt{H}_{2\times 2} \begin{pmatrix} x \\ 1 \end{pmatrix}$$

where $\mathtt{H}_{2\times 2}$ is a 2×2 homography matrix. For the geometry shown in figure 4.2 the matrix is given by

$$\mathtt{H}_{2\times 2} = \begin{pmatrix} \alpha & t \\ \mu & 1 \end{pmatrix}$$

with parameters $\alpha = \frac{d}{fcos^2(\omega)} - \frac{t}{f}tan(\omega)$ and $\mu = -\frac{tan(\omega)}{f}$. Under back-projection an image point x maps as

$$x \to X = \frac{h_{11}x + h_{12}}{h_{21}x + h_{22}} = \frac{\alpha x + t}{\mu x + 1}$$

This non-linear mapping (in inhomogeneous coordinates) can be expanded in a Taylor series. Statistical moments of X, such as the variance, are then computed in terms of the Taylor coefficients and the moments of x [22, 97]. It is assumed here that the homography is exact (no errors) and the measurement of the image test point x is subject to Gaussian noise with standard deviation σ_x. The Taylor series is developed about the point's mean position denoted as $\overline{x}$.

First order

If the Taylor series is truncated to first order in $(x - \overline{x})$ then the mapping is linearised.

$$X \approx \frac{\alpha\overline{x} + t}{\mu\overline{x} + 1} + \frac{\alpha - \mu t}{(\mu\overline{x} + 1)^2}(x - \overline{x})$$

The mean of X is

$$\overline{X} \approx \frac{\alpha\overline{x} + t}{\mu\overline{x} + 1} \tag{4.3}$$

since the mean is a linear operator. The variance of X can be shown to be

$$\sigma_X^2 \approx \frac{(\alpha - \mu t)^2}{(\mu\overline{x} + 1)^4}\sigma_x^2 \tag{4.4}$$

Second order

Usually only the first order approximation is used for error propagation [19, 27, 36, 94, 95]. Here the Taylor expansion is extended to second order so that the approximation involved in truncating to first order can be bounded. It can be shown that to second order in $(x - \overline{x})$

$$X \approx \frac{\alpha\overline{x} + t}{\mu\overline{x} + 1} + \frac{\alpha - \mu t}{(\mu\overline{x} + 1)^2}(x - \overline{x}) - \frac{\mu(\alpha - \mu t)}{(\mu\overline{x} + 1)^3}(x - \overline{x})^2$$

The mean of X is

$$\overline{X} \approx \frac{\alpha\overline{x} + t}{\mu\overline{x} + 1} - \frac{\mu(\alpha - \mu t)}{(\mu\overline{x} + 1)^3}{\sigma^2}_x \tag{4.5}$$

and its variance is

$$\sigma_X^2 \approx \frac{(\alpha - \mu t)^2}{(\mu\overline{x} + 1)^4}\sigma_x^2 \left(1 + \frac{2\mu^2}{(\mu\overline{x} + 1)^2}\sigma_x^2\right) \tag{4.6}$$

Comparison

A comparison between the first order approximation of the perspectivity function and the second order one is now required. We are interested in the error made in the estimation of the mean $\overline{X}$ and of the variance σ_X^2 of the world point X.

Bias on mean

In order to find out whether the first order approximation mean is biased or not a b_X quantity is defined as follow:

$$b_X = \overline{X}^{1^{st}} - \overline{X}^{2^{nd}} = \frac{\mu(\alpha - \mu t)}{(\mu\overline{x} + 1)^3}{\sigma^2}_x$$

Then the bias b_X is just the difference between the mean of X computed from the first order series truncation and that computed from the second order one. The bias has dimensions of length.

The Lagrange remainder of the Taylor series [116] provides an upper bound on the error on the mean if the series is truncated to first order instead of using the complete expansion. Using the first order truncation of the Taylor expansion with the Lagrange remainder we obtain:

$$\overline{X} = \frac{\alpha\overline{x} + t}{\mu\overline{x} + 1} - \frac{\mu(\alpha - \mu t)}{(\mu\xi + 1)^3}{\sigma^2}_x$$

with $\xi \in]x, \overline{x}[$. Therefore the upper bound of the error (absolute value) on the mean of X is

$$Err_{\overline{X}} = \frac{\mu|\alpha - \mu t|}{(\mu\xi + 1)^3}{\sigma^2}_x$$

Thus a measure, M_b, can be defined of the bias in the mean between first and second order approximation using the ratio of Lagrange upper bound of the mean $\overline{X}$ to the mean itself.

$$M_b = \frac{\mu|\alpha - \mu t|(\mu\overline{x} + 1)}{(\alpha\overline{x} + t)(\mu\xi + 1)^3}\sigma_x^2 \tag{4.7}$$

Error in variance

Two new measures are defined here. They are used to assess the error in the standard deviation (or variance) in truncating to first order. The first, M_{v_1}, measures the ratio of the second order variance to first order one. Comparing (4.4) and (4.6) this ratio is

$$M_{v_1} = 2\frac{\mu^2}{(\mu\overline{x} + 1)^2}\sigma_x^2 \tag{4.8}$$

The second measure, M_{v_2}, is obtained from the Lagrange remainder of the Taylor series. This provides an upper bound on the error if the series is truncated to first order instead of using the complete expansion. From Taylor's Theorem the variance σ_X^2 is

$$\sigma_X^2 = \frac{(\alpha - \mu t)^2}{(\mu\overline{x} + 1)^4}\sigma_x^2 + \frac{2\mu^2(\alpha - \mu t)^2}{(\mu\xi + 1)^6}\sigma_x^4$$

This is the sum of the first order term and the Lagrange remainder, which for some ξ such that $|\overline{x} - \xi| < |\overline{x} - x|$ is an exact equation, not an approximation. The measure M_{v_2} is then obtained as the ratio of this truncation error to the first order term.

$$M_{v_2} = 2\frac{\mu^2(\mu\overline{x} + 1)^4}{(\mu\xi + 1)^6}{\sigma^2}_x \tag{4.9}$$

and we compute the worst case of $\xi = \overline{x} - \sigma_x$ for this bound in the range $\overline{x} \pm \sigma_x$.

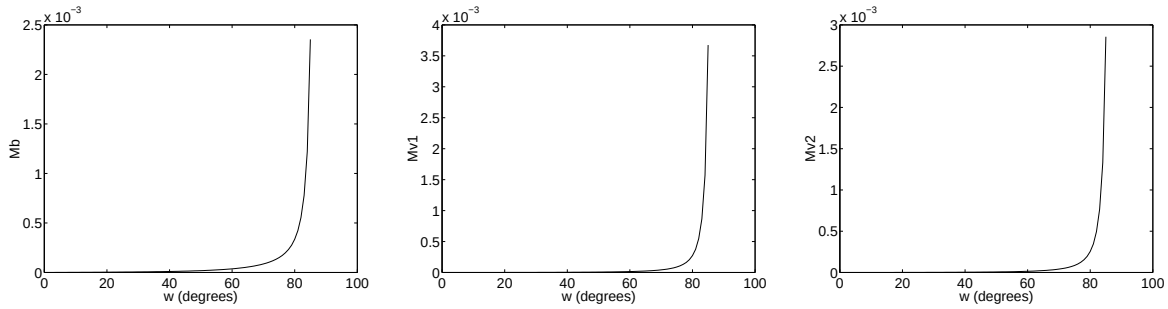

a b c

Figure 4.3: **Comparison of measures of goodness of first order approximation vs. second order:** (a) bias measure M_b; (b) first variance measure M_{v_1}; (c) second variance measure M_{v_2}.

Typical results

The significance of these measures is that they depend only on the elements of the homography matrix. Thus, once a matrix has been estimated the need for a second order approximation can be immediately assessed. All these measures are dimensionless and it makes sense to compare their values to unity.

In figure 4.3 a graph plot of the measures defined is given in order to visualise their behaviour with respect to variations of the angle ω. The three linearity measures are computed for the following values: $f = 8.5mm$, $d = 5m$, $t = 1m$, $x = 50pixels$, $\sigma_x = 1pixel$, and ω varies from 0^o to 85^o (see figure 4.2). For angle values close to $70^o - 80^o$ the non linearity of the projection function suddenly increases and the first error analysis is near the limit of its usefulness.

The same analysis is reported in the table below for discrete values of the angle ω.

ω	30^o	40^o	50^o	60^o	70^o	80^o
M_b	5.9×10^{-6}	1.1×10^{-5}	1.9×10^{-5}	3.9×10^{-5}	9.5×10^{-5}	4.22×10^{-4}
M_{v_1}	1.49×10^{-6}	3.3×10^{-6}	6.9×10^{-6}	1.6×10^{-5}	4.8×10^{-5}	3.7×10^{-4}
M_{v_2}	1.49×10^{-6}	3.3×10^{-6}	6.9×10^{-6}	1.6×10^{-5}	4.6×10^{-5}	3.4×10^{-4}

Note the very small values of the three measures also for large values of the angle ω. That proves that second order terms are not required in typical imaging situations.

When is first order exact?

If $\mu = 0$ in equation (4.6) (for instance when $\omega = 0^o$) then the second order correction is zero and all the three above measures are null. With $\mu = 0$ the homography reduces to an affine transformation, i.e. it is linear. This illustrates the general result that if the homography is affine the first order analysis is exact.

Generally, the H matrix can be decomposed into the product of matrices representing *linear* (affine) and *non linear* (projective) transformations on inhomogeneous coordinates as:

$$\mathtt{H} = \mathtt{AP}$$

where

$$\mathtt{A} = \begin{pmatrix} \alpha_{11} & \alpha_{12} & h_{13} \\ \alpha_{21} & \alpha_{22} & h_{23} \\ 0 & 0 & 1 \end{pmatrix}, \quad \mathtt{P} = \begin{pmatrix} 1 & 0 & 0 \\ 0 & 1 & 0 \\ h_{31} & h_{32} & 1 \end{pmatrix}$$

with $\alpha_{ij} = h_{ij} - h_{3j}h_{i3}$ for $i, j = 1, 2$.

If H is purely an affinity (linear on inhomogeneous coordinates) then P is the identity and the first order theory exact.

In the previous section the first order error propagation theory has been proved good enough for typical values in the case of mono-dimensional camera model. In the following the first order analysis is extended to the bi-dimensional camera model in the case of uncertainty affecting also the projective process. Then, in section 4.3.3 its correctness is proved via Monte Carlo statistical simulations.

4.3.2 Computing uncertainties

There may be errors in the world and image points used to compute the homography, and there may be errors in the image points back-projected to make world measurements. All of these sources of uncertainty must be taken into account in order to compute a cumulative uncertainty for the world measurement.

In this section formulae to compute the uncertainty for planar measurements under various error situations are developed. The first order analysis is assumed sufficient.

All the computation image and world points are assumed to be measured with error modelled as a bi-dimensional Gaussian noise process (see fig. 3.13). $\Lambda_{\mathbf{x}_i}$ and $\Lambda_{\mathbf{X}_i}$ are the covariance matrices of the image computation point $\mathbf{x}_i$ and the world computation point $\mathbf{X}_i$ respectively. The two sources of error (the uncertainty on the homography and the uncertainty in image point localisation) are first considered to operate separately and finally they are merged in order to compute an unique formula embracing both cases.

Uncertainty in the homography $\mathtt{H}$, given uncertain computation points

The covariance of the homography $\mathtt{H}$ estimated from n image-world point correspondences is computed here.

From section 4.2.1 we seek the eigenvector $\mathbf{h}$ with smallest eigenvalue λ of the 3×3 matrix $\mathtt{A}^\top\mathtt{A}$. But if the n computation correspondences are affected by a localisation error also the $\mathtt{A}$ matrix will be uncertain and hence the 9-vector $\mathbf{h}$. This vector is then characterised by a 9×9 covariance matrix $\Lambda_{\mathbf{h}}$ computed as shown in appendix A.

The algorithm in appendix A has a double advantage over other methods such as [19, 36] which require the inverse of $\mathtt{A}^\top\mathtt{A}$ in order to compute $\Lambda_{\mathbf{h}}$. These methods are poorly conditioned if only four correspondences are used, or if $n > 4$ and the correspondences are (almost) noise-free. In both cases the $\mathtt{A}^\top\mathtt{A}$ matrix is singular and thus not invertible. Since the derivation of (A.2) does not involve the inverse, it is well conditioned in both cases.

Uncertainty in point localization

This section lists the formulae used to compute the uncertainty for measurements under various error situations. The first order analysis is assumed sufficient. The uncertainty in the homography is computed as described in the previous section.

Notation

New notation is introduced here to simplify the formulae. Equation (3.3) can be rewritten as

$$\mathbf{X} = \mathtt{B}\mathbf{h}$$

where $\mathtt{B}$ is a 3×9 matrix in the form:

$$\mathtt{B} = \begin{pmatrix} \mathbf{x}^\top & \mathbf{0}^\top & \mathbf{0}^\top \\ \mathbf{0}^\top & \mathbf{x}^\top & \mathbf{0}^\top \\ \mathbf{0}^\top & \mathbf{0}^\top & \mathbf{x}^\top \end{pmatrix} \tag{4.10}$$

In the following we will determine the 3×3 covariance matrix $\Lambda_{\mathbf{X}}$ of the homogeneous world point $\mathbf{X}$. The conversion to a 2×2 covariance matrix $\Lambda_{\mathbf{X}}^{2\times 2}$ for inhomogeneous coordinates is given by: $\Lambda_{\mathbf{X}}^{2\times 2} = \boldsymbol{\nabla} f \Lambda_{\mathbf{X}} \boldsymbol{\nabla} f^\top$ where $\mathbf{X} = (X, Y, W)^\top$ and

$$\boldsymbol{\nabla} f = 1/W^2 \begin{pmatrix} W & 0 & -X \\ 0 & W & -Y \end{pmatrix}$$

f is the function mapping homogeneous to inhomogeneous coordinates. The opposite conversion, from inhomogeneous to homogeneous coordinates, for an image point $\mathbf{x}$ is simply given by:

$$\Lambda_{\mathbf{x}} = \begin{pmatrix} \Lambda_{\mathbf{x}}^{2\times 2} & \mathbf{0} \\ \mathbf{0}^\top & 0 \end{pmatrix}$$

It is easy to prove that, given two homogeneous 3-vectors $\mathbf{x}_1$ and $\mathbf{x}_2$ related by

$$\mathbf{x}_2 = \lambda \mathbf{x}_1 \tag{4.11}$$

with λ a scale factor, and their associated 3×3 covariance matrices $\Lambda_{\mathbf{x}_1}$ and $\Lambda_{\mathbf{x}_2}$, then $\Lambda_{\mathbf{x}_2}^{2\times 2} = \Lambda_{\mathbf{x}_1}^{2\times 2}$ where $\Lambda_{\mathbf{x}_1}^{2\times 2}$ and $\Lambda_{x_2}^{2\times 2}$ are the corresponding inhomogeneous covariance matrices. In fact from (4.11)

$$\Lambda_{\mathbf{x}_2} = \lambda^2 \Lambda_{\mathbf{x}_1} \quad \text{and} \quad \boldsymbol{\nabla} \mathrm{f}_2 = \frac{1}{\lambda} \boldsymbol{\nabla} \mathrm{f}_1$$

Since from first order error analysis $\Lambda_{\mathbf{x}_2}^{2\times 2} = \boldsymbol{\nabla} f_2 \Lambda_{\mathbf{x}_2} \boldsymbol{\nabla} f_2^\top$, by substitution

$$\Lambda_{\mathbf{x}_2}^{2\times 2} = \frac{1}{\lambda} \boldsymbol{\nabla} f_1 \lambda^2 \Lambda_{\mathbf{x}_1} \frac{1}{\lambda} \boldsymbol{\nabla} f_1{}^\top$$

and since $\boldsymbol{\nabla} f_1 \Lambda_{\mathbf{x}_1} \boldsymbol{\nabla} f_1{}^\top = \Lambda_{\mathbf{x}_1}^{2\times 2}$ then $\Lambda_{\mathbf{x}_2}^{2\times 2} = \Lambda_{\mathbf{x}_1}^{2\times 2}$.

Uncertainty in $\mathbf{X}$, given an uncertain $\mathtt{H}$ and exact $\mathbf{x}$

If noise is assumed only on the homography and the input point $\mathbf{x}$ is exact, then the covariance of the corresponding world point $\mathbf{X}$ is:

$$\Lambda_{\mathbf{X}} = \mathtt{B}\Lambda_{\mathbf{h}}\mathtt{B}^{\top} \tag{4.12}$$

Uncertainty in $\mathbf{X}$, given an exact $\mathtt{H}$ and uncertain $\mathbf{x}$

Instead, if noise is assumed only in the input image point and the homography is exact then:

$$\Lambda_{\mathbf{X}} = \mathtt{H}\Lambda_{\mathbf{x}}\mathtt{H}^{\top} \tag{4.13}$$

Uncertainty in $\mathbf{X}$, given an uncertain $\mathtt{H}$ and uncertain $\mathbf{x}$

If noise is assumed in both the homography $\mathtt{H}$ and the input point $\mathbf{x}$ then the covariance $\Lambda_{\mathbf{X}}$ is given by the sum of the previous two equations (4.12, 4.13):

$$\Lambda_{\mathbf{X}} = \begin{pmatrix} \mathtt{B} & \vdots & \mathtt{H} \end{pmatrix} \begin{pmatrix} \Lambda_{\mathbf{h}} & \vdots & \mathtt{0} \\ \cdots & \cdots & \cdots \\ \mathtt{0} & \vdots & \Lambda_{\mathbf{x}} \end{pmatrix} \begin{pmatrix} \mathtt{B}^{\top} \\ \cdots \\ \mathtt{H}^{\top} \end{pmatrix} \tag{4.14}$$

if $\mathtt{H}$ and $\mathbf{x}$ are statistically independent.

Uncertainty in distance measurement

The distance d between two world points $\mathbf{U}_1$ and $\mathbf{U}_2$ also has an associated uncertainty.

Let the two end points of the image of the segment to be measured be $\mathbf{u}_1 = (u_1, v_1)^{\top}$ and $\mathbf{u}_2 = (u_2, v_2)^{\top}$ (in inhomogeneous coordinates). The two corresponding points on the world plane in homogeneus coordinates are:

$\mathbf{X}_1 = (X_1, Y_1, W_1)^{\top}$ and $\mathbf{X}_2 = (X_2, Y_2, W_2)^{\top}$ where $\mathbf{X}_i = \mathtt{H}\,(u_i, v_i, 1)^{\top}$. In inhomogeneus coordinates they are: $\mathbf{U}_i = (U_i, V_i)^{\top}$ with $U_i = X_i/W_i$ and $V_i = Y_i/W_i$. Then the Euclidean distance between the two points $\mathbf{U}_1$ and $\mathbf{U}_2$ on the world plane is

$$d = \sqrt{(U_1 - U_2)^2 + (V_1 - V_2)^2}$$

and its uncertainty is computed below.

Uncertainty on point distance, given an uncertain $\mathtt{H}$ and exact $\mathbf{u}_1, \mathbf{u}_2$

It can be shown that the gradient of the distance d with respect to $\mathbf{h}$ is:

$$\frac{\partial d}{\partial \mathbf{h}} = \frac{1}{d}(\mathbf{U}_1 - \mathbf{U}_2)^\top (\tilde{\mathtt{A}}_1 - \tilde{\mathtt{A}}_2)$$

where the 2×9 matrices $\tilde{\mathtt{A}}_1$ and $\tilde{\mathtt{A}}_2$ are:

$$\tilde{\mathtt{A}}_i = \frac{1}{W_i} \begin{pmatrix} u_i & v_i & 1 & 0 & 0 & 0 & -u_i U_i & -v_i U_i & -U_i \\ 0 & 0 & 0 & u_i & v_i & 1 & -u_i V_i & -v_i V_i & -V_i \end{pmatrix}$$

If noise is assumed only in the homography, then, for the first order analysis, the variance of d is given by:

$$\sigma_d^2 = \frac{\partial d}{\partial \mathbf{h}} \Lambda_{\mathbf{h}} \frac{\partial d}{\partial \mathbf{h}}^\top \tag{4.15}$$

Uncertainty in distance, given exact $\mathtt{H}$ and uncertain $\mathbf{u}_1$ and $\mathbf{u}_2$

The gradient of the distance with respect to the 4-vector $\boldsymbol{\zeta} = (u_1, v_1, u_2, v_2)^\top$ is given by

$$\frac{\partial d}{\partial \boldsymbol{\zeta}} = \frac{1}{d}(\mathbf{U}_1 - \mathbf{U}_2)^\top \begin{pmatrix} \mathtt{B}_1 & \vdots & \mathtt{B}_2 \end{pmatrix}$$

where the matrices $\mathtt{B}_1$ and $\mathtt{B}_2$ are defined as follows:

$$\mathtt{B}_i = \frac{1}{W_i} \begin{pmatrix} h_{11} - h_{31} U_i & h_{12} - h_{32} U_i \\ h_{21} - h_{31} V_i & h_{22} - h_{32} V_i \end{pmatrix}$$

If noise is assumed only in the input points $\mathbf{u}_1, \mathbf{u}_2$, and the two points are independent then the variance σ_d^2 is

$$\sigma_d^2 = \frac{\partial d}{\partial \boldsymbol{\zeta}} \begin{pmatrix} \Lambda_{\mathbf{u}_1} & \vdots & 0 \\ \cdots & \cdots & \cdots \\ 0 & \vdots & \Lambda_{\mathbf{u}_2} \end{pmatrix} \frac{\partial d}{\partial \boldsymbol{\zeta}}^\top \tag{4.16}$$

Uncertainty in distance, given uncertain $\mathtt{H}$ and uncertain $\mathbf{u}_1$ and $\mathbf{u}_2$

Finally, if both the homography $\mathtt{H}$ and the input points $\mathbf{u}_1, \mathbf{u}_2$ are uncertain then the variance σ_d^2 is given by the sum of (4.15) and (4.16):

$$\sigma_d^2 = \begin{pmatrix} \frac{\partial d}{\partial \mathbf{h}} & \vdots & \frac{\partial d}{\partial \boldsymbol{\zeta}} \end{pmatrix} \begin{pmatrix} \Lambda_{\mathbf{h}} & \vdots & 0 & \vdots & 0 \\ \cdots & \cdots & \cdots & \cdots & \cdots \\ 0 & \vdots & \Lambda_{\mathbf{u}_1} & \vdots & 0 \\ \cdots & \cdots & \cdots & \cdots & \cdots \\ 0 & \vdots & 0 & \vdots & \Lambda_{\mathbf{u}_2} \end{pmatrix} \begin{pmatrix} \frac{\partial d}{\partial \mathbf{h}}^\top \\ \cdots \\ \frac{\partial d}{\partial \boldsymbol{\zeta}}^\top \end{pmatrix} \tag{4.17}$$

with $\Lambda_{\mathbf{h}}$ the 9×9 covariance of the homography and $\Lambda_{\mathbf{u}_1}$ and $\Lambda_{\mathbf{u}_2}$ the 2×2 inhomogeneous covariance matrices of the input image points.

4.3.3 Validation of uncertainty analysis

The previous sections have described a complete theory for: (i) computing the ellipse of uncertainty for the localization of a world plane point and (ii) the uncertainty range of the distance between two world points given uncertain homography computation points and uncertain image input points.

This section demonstrates that for typical imaging situations this linear approximation is sufficiently accurate. That has already been proven analytically in the mono-dimensional case. Now the Monte Carlo statistical test is applied to the bi-dimensional camera model theory. In all of the following error is assumed to be in both computation points and measurement points.

Test on uncertainty of point localization

The performed *Monte Carlo* test is described in table 4.1:

- Repeat N times
  - Generate $n \geq 4$ image computation points (Gaussian distributed);
  - Generate $n \geq 4$ world computation points (Gaussian distributed);
  - Compute the homography relating the two sets of points.
  - Generate an image point $\mathbf{x}$ (Gaussian distributed);
  - Back-project the point $\mathbf{x}$ onto the world plane point $\mathbf{X}$.
- Compute the statistical uncertainty ellipse of the distribution of points $\mathbf{X}$ and compare it with the analytical uncertainty.

Table 4.1: **Monte Carlo simulation.**

Figure 4.4a shows a comparison between the covariance ellipse obtained by the first order analysis and the one obtained by a Monte Carlo evaluation of the actual non-linear homography mapping. A number $N = 10000$ iterations is involved in each simulation. Note that the predicted ellipse and the simulated one are almost overlapping. These figures are obtained using parameters related to a real situation.

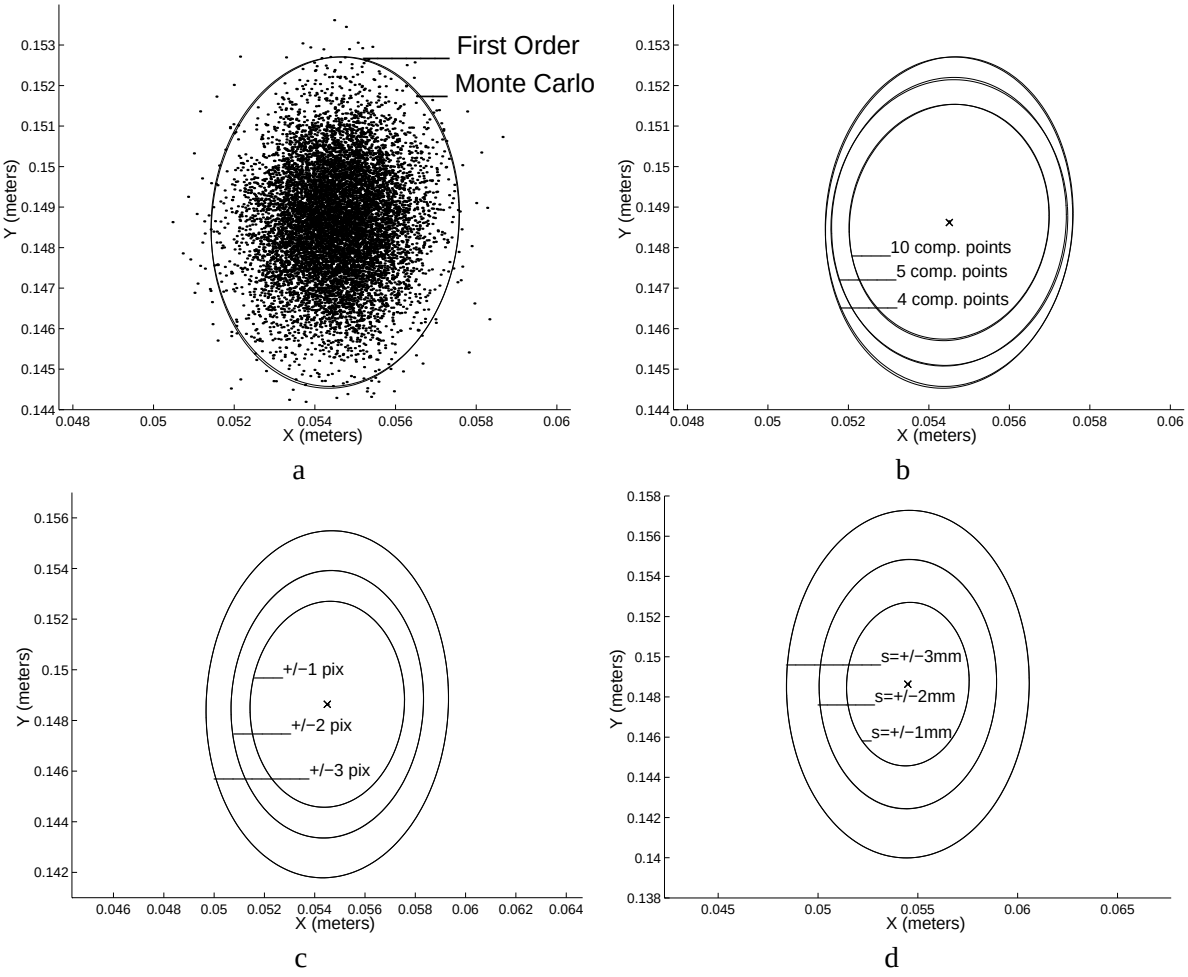

Figure 4.4: **Uncertainty in point localization:** (a) `H` is computed from the theory of sections 4.2.1 and 4.3.2 using only 4 computation points. 10000 image points are randomly generated from a Gaussian distribution centred on an image test point $\overline{x}$ and then back-projected onto the world plane. The statistical covariance ellipse of the world points is computed and plotted together with the predicted one. 3 std. dev. are visualised for each uncertainty ellipse. (b) The first order and simulated uncertainty ellipses areas decrease as the number of computation points increase from 4 to 5 to 10 as expected from the theory. (c) Areas of the predicted ellipses and of the simulated ones increase as the uncertainty of the image computation points increases. (d) Areas of the predicted ellipses and of the simulated ones increase as the uncertainty of the world computation points increases. 3 standard deviations (99.7% of probability level) are visualised in all diagrams.

Similar test has been performed in section 3.6 for a homographic mapping between two generic planes, using synthetic data.

Increasing the number of computation points

Figure 4.4b shows what happens if the number of computation points used to estimate the homography matrix increases. 6 ellipses are drawn, 3 have been predicted by the analytical theory and other 3 obtained from the Monte Carlo test. For each of these three cases it is very hard to distinguish between the simulated and the predicted ellipses.

Furthermore, as expected, increasing the number of computation points increases the accuracy of the `H` matrix and then the accuracy in the final $\mathbf{X}$ point position (smaller ellipses).

Increasing the image computation points standard deviations

Figure 4.4c shows how the area of the uncertainty ellipses increases with the uncertainty of the image computation points. Three predicted ellipses are drawn with the corresponding simulated ones. The standard deviation of the noise in the world points varies from $1pixel$ to $3pixels$.

Increasing the world computation points standard deviations

The increase of the uncertainty ellipses with the uncertainty in the localisation of the world computation points is shown in figure 4.4d. The three predicted ellipses and the corresponding simulated ones are drawn also in this case. The standard deviation of the noise in the world points varies from $1mm$ to $3mm$.

Test on uncertainty of distance measurements

The *Monte Carlo* test performed is described in table 4.2.

Figure 4.5 demonstrates the uncertainty in distance measurements. A comparison between the Gaussian distribution obtained by the first order analysis and, again, the distribution obtained by a Monte Carlo evaluation of the non-linear homography mapping is shown. The predicted curve and the simulated one are again indistinguishable.

Increasing the number of computation points

Figure 4.5b illustrates what happens if the number of computation points used to estimate the

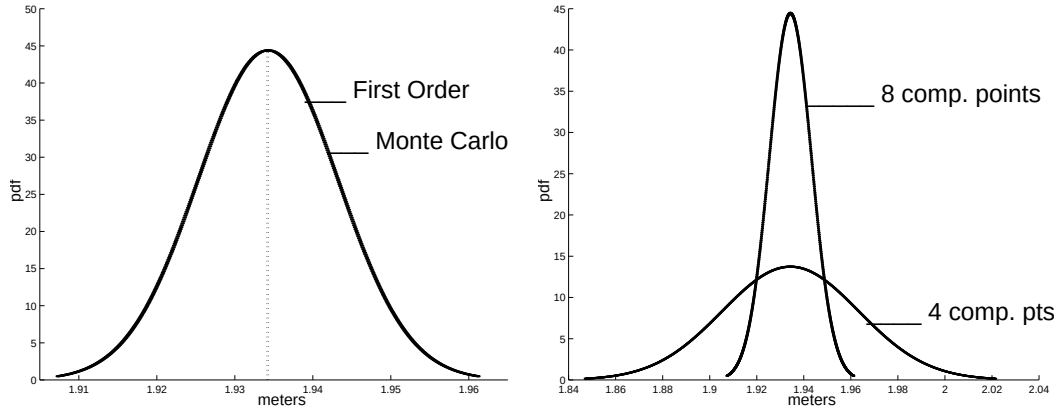

a b

Figure 4.5: **Uncertainty in distance measurement:** (a) H is computed from the theory of sections 4.2.1 and 4.3.2 using only 4 noisy computation points. 10000 image points are randomly generated from a Gaussian distribution centred on an image test point $\overline{x}_1$ and another 10000 points generated from a Gaussian distribution centred on another image test point $\overline{x}_2$. The points are back-projected onto the world plane and the distances between the pairs are computed. The statistical distribution of the distances is computed and plotted together with the predicted one. 3 std. dev. are visualised for each curve; (b) The first order and simulated uncertainties decrease as the number of computation points increases from 4 to 8.

- Repeat N times
  - Generate $n \geq 4$ image computation points (Gaussian distributed);
  - Generate $n \geq 4$ world computation points (Gaussian distributed);
  - Compute the homography relating the two sets of points.
  - Generate an image point $\mathbf{x}_1$ (Gaussian distributed);
  - Back-project the point $\mathbf{x}_1$ onto the world plane point $\mathbf{X}_1$.
  - Generate an image point $\mathbf{x}_2$ (Gaussian distributed);
  - Back-project the point $\mathbf{x}_2$ onto the world plane point $\mathbf{X}_2$.
  - Compute the distance d between $\mathbf{X}_1$ and $\mathbf{X}_2$.
- Compute the statistical variance of the distribution of distances d and compare it with the predicted variance.

Table 4.2: **Monte Carlo simulation.**

homography matrix increases.

Four curves are drawn, two have been predicted by our analytical theory and other two have been obtained from the Monte Carlo test. As expected, increasing the number of computation points

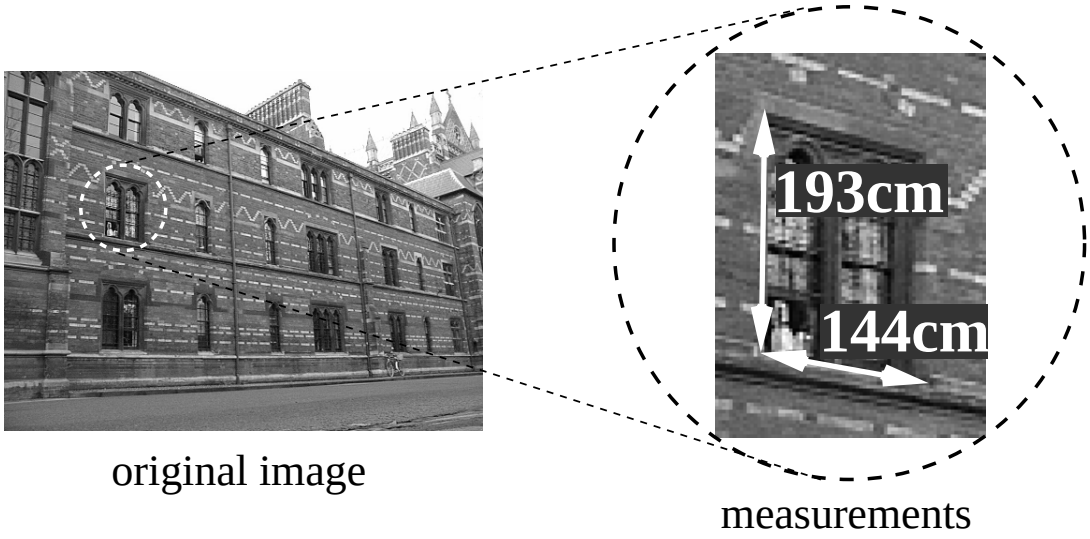

Figure 4.6: **Measuring world distances from images:** the dimensions of the window are measured directly on the image.

increases the accuracy of the distance d (smaller standard deviation).

Figures 4.4 and 4.5 are obtained using data from images of real scenes. In all the previous examples the simulated ellipses are almost exactly overlapping the analytically predicted ones, which justifies the use of the first order theory.

4.4 Application - A plane measuring device

In this section a typical application of the desrcibed plane metrology algorithm and the uncertainty theory is presented.

4.4.1 Description

The device shown here is meant to take distance measurements on real world planes such as floors, walls, doors, just using images acquired with conventional video cameras. (see fig. 4.6). The entire measurement process can be split in two main stages: the calibration stage and the measuring stage.

Calibration stage

First of all, computing the transformation between the viewed plane and the image plane is necessary. This is achieved via the knowledge of a set of world-image point correspondences as already discussed.

Once we have defined how the n chosen world-plane computation points are projected onto the image it is possible to apply the theory of sections 4.2 and 4.3 to compute the `H` matrix and its covariance. The choice of computation points is not completely arbitrary; in fact their number and location with respect to the camera have a significant effect on measurement uncertainties.

In section 4.4.2 some examples are provided to show the variation of the uncertainties according to a variation in the number or location of the computation points.

Measurement stage

Once the homography has been computed two points on the image are selected; they are back-projected onto the world plane and the distance between them computed and shown (see fig. 4.7). The uncertainty in the distance between them is also computed using the formulae presented.

Once the homography is known it is possible to retrieve other useful information such as parallelism of lines lying on a plane (see table below). Therefore the application allows to draw a line, draw the parallel line passing through a chosen point and retrieve the orthogonal distance between the two lines.

The strength of this device is in its easy use; the operator interacts with the system just via a friendly graphic interface both during the calibration stage and the measuring one. The measurement queries are sent to the system via a pointing device like a mouse.

4.4.2 Examples

In this section a number of examples are presented showing possible uses of the described theory, and the correctness of the uncertainty analysis on real images.

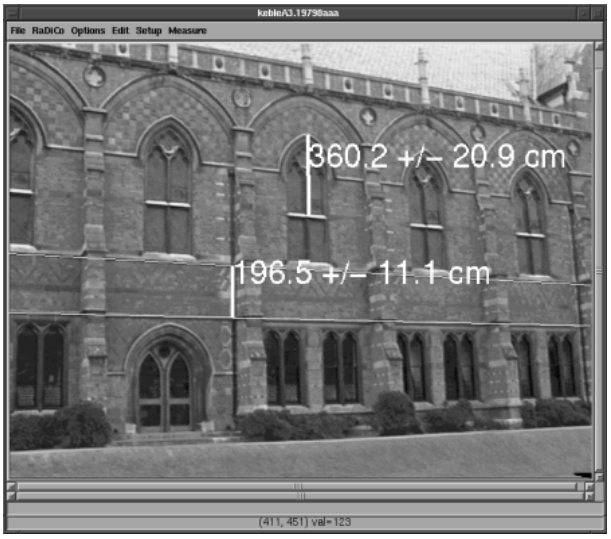

Figure 4.7: **Graphical User Interface:** example of the measurement stage. It involves an easy-to-use graphical interface; the user is only required to select the two end points of the segment to measure.

It is shown that the ground truth measurements always lie within the estimated error bounds. Furthermore, the utility of the analysis is illustrated. The covariance expression *predicts* uncertainty given the number of image-world computation points and their distribution. It is thus possible to decide where correspondences are required in order to achieve a particular desired measurement accuracy.

Creating new views of planar surfaces

Rectification of a planar surface

Once the homography between a world plane and the image has been estimated then it is easy to perform a *fronto-parallel* transformation of the image. From a geometric point of view this operation means the synthesis of a new image, the one seen from a new camera with its acquisition plane parallel to the world plane.

Figure 4.8 shows an image of a college wall which is warped onto a fronto-parallel view. Note that in the warped image angles and ratios of distances are recovered correctly.

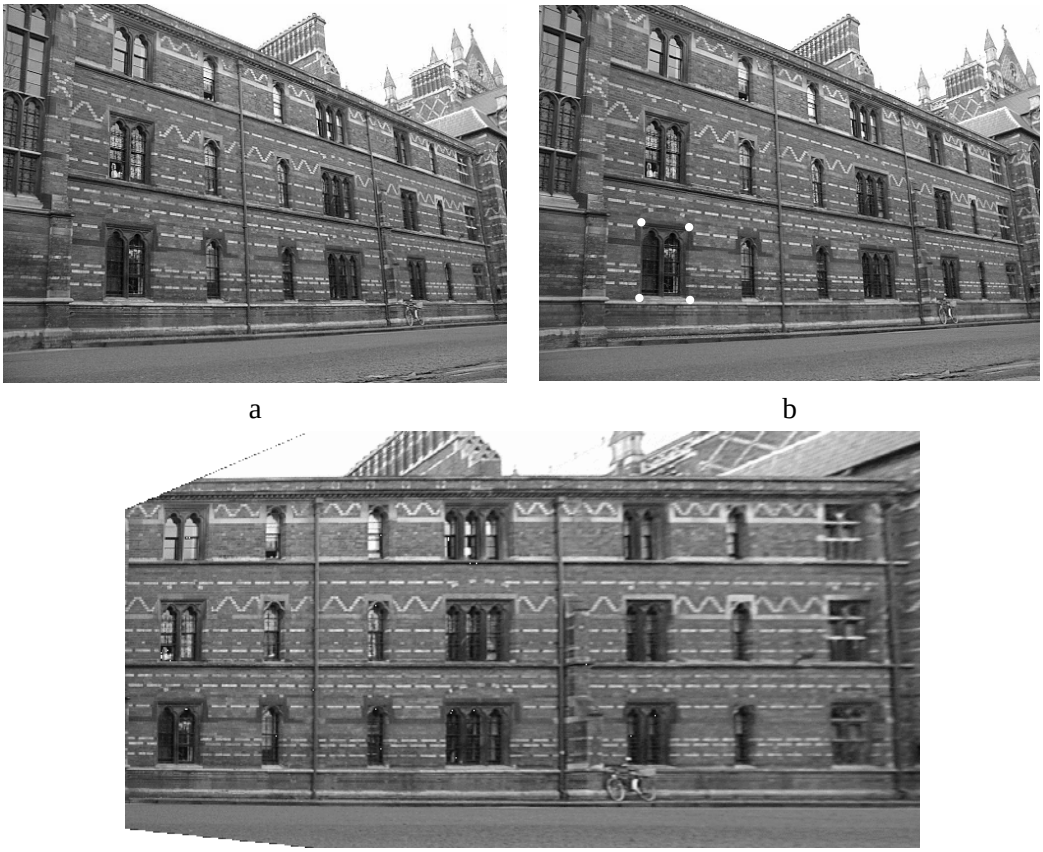

a b

c

Figure 4.8: **Rectification of a planar surface:** (a) original image, Keble College, Oxford; (b) the relative location of the four corners of the marked window have been used as reference to compute the image-to-world plane homography; (b) rectified image; parallel lines in the world are parallel in the rectified image and angles are preserved.

Rectification of a plane in a painting

Figure 4.9 shows another example of plane rectification. Figure 4.9a is a painting by the Italian Renaissance painter Piero della Francesca (1416–1492). The rectification is possible as a result of strict adherence to Renaissance perspective rules by the artist. The painting represents scene geometry almost exactly as it would be captured by a perspective camera, thus the warping technique described is valid.

Figure 4.9c shows the rectified view of the area of the floor hilighted in fig. 4.9b, where Christ is standing. Note that the geometric pattern, barely visible in the original image is clear at

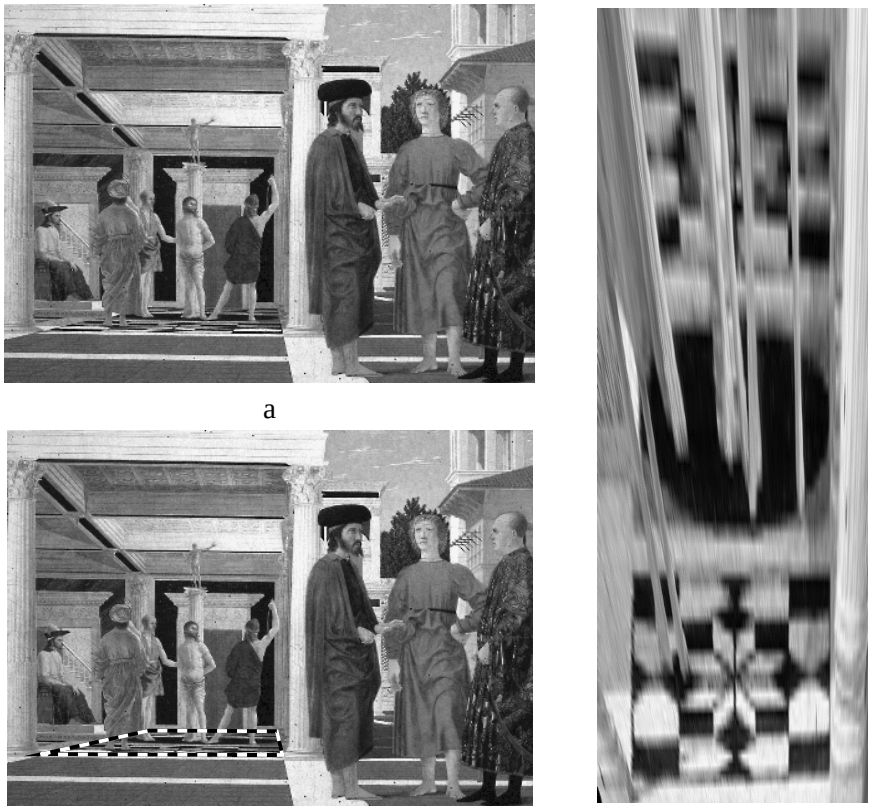

a b c

Figure 4.9: **Rectification of a plane in a painting:** (a) the painting *La Flagellazione di Cristo* by Piero della Francesca (1460, Urbino, Galleria Nazionale delle Marche); (b) original image with part of the floor highlighted; (c) rectified image of the highlighted area. Notice that the beautiful geometrical tile pattern is repeated twice.

the bottom of the rectified one [64]. A second, identical pattern is visible (despite occlusions) on the top of the rectified image.

The image-to-world homography has been computed from the assumption of square floor pattern.

Warping planes between images

If the inter-image homography relating two images is known it is possible to warp one image onto the other.

An example is shown in figure 4.10 where two pictures of the same wall have been taken from two different viewpoints (the camera has undergone a translational and rotational movement). The

a

b

c

Figure 4.10: **Warping planes between images:** (a,b) original images from two different points of view; Crystallography labs, Oxford. (c) first image warped onto the second by the inter-image homography.

inter-image homography has been estimated from corresponding feature points on the wall and the first image warped onto the second one. All the points which do not lie on the facade are mapped into unexpected positions (fig. 4.10c). The parallax effect shown by such points can be used for 3D structural computation (see chapter 6).

Accuracy in point localization

Varying the location of the computations points

Figure 4.11 shows an example of an indoor scene. Figure 4.11a is the original image and in figures 4.11b-d an *uncertainty ellipse map* is superimposed to show how the ellipses change according to a change in the location of the computation points. The `H` matrix is computed using

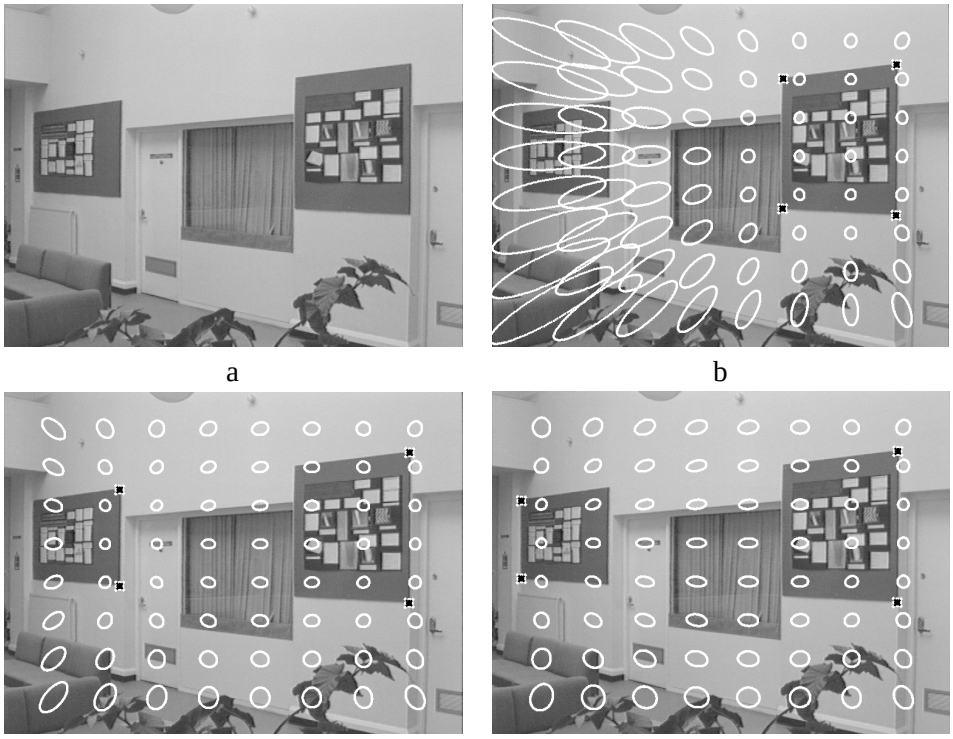

a b

c d

Figure 4.11: **Accuracy in point localization:** (a) original image. (b-d) projectively unskewed back-projection. The computation points used to estimate `H` are marked by black asterisks. The location of the four computations points is different in each image. The uncertainty ellipses shown for test points are at the 9 std. dev. level for clarity.

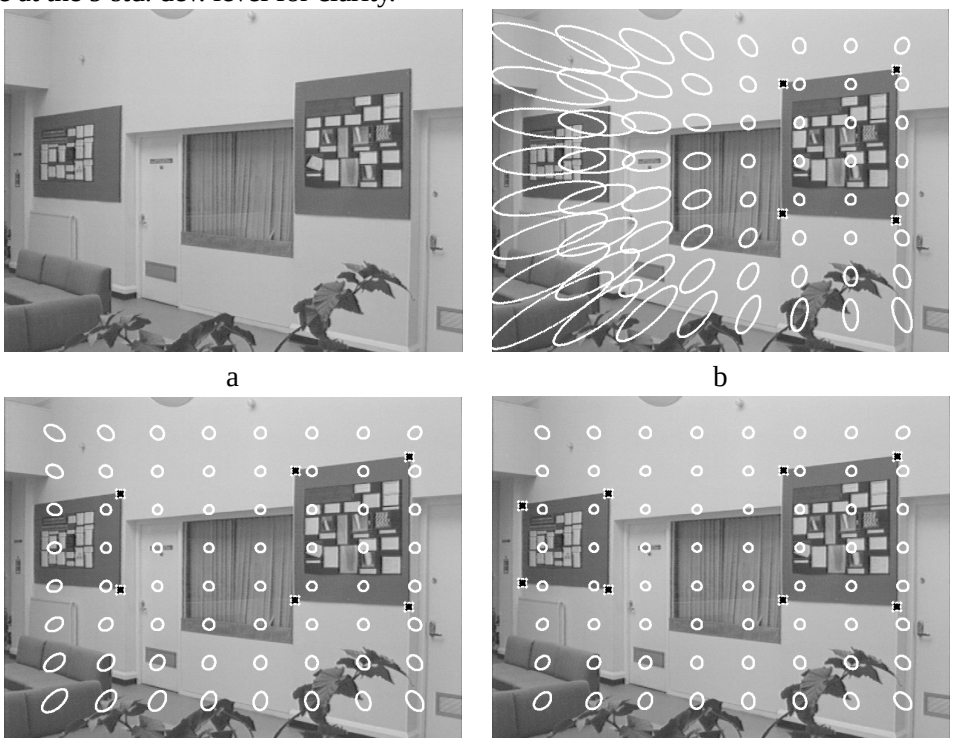

a b

c d

Figure 4.12: **Accuracy in point localization:** (a) original image. (b-d) projectively unskewed back-projection. The computation points used to estimate `H` are marked by black asterisks. The number of computation points varies from 4 to 6 to 8. The uncertainty ellipses shown for test points are at the 9 std. dev. level for clarity.

four computations points in all cases. The covariances used for the computations are:

$$\Lambda_{\mathbf{x}} = \begin{bmatrix} 1 & 0 \\ 0 & 1 \end{bmatrix}$$

(in $pixel^2$) in the image and

$$\Lambda_{\mathbf{X}} = \begin{bmatrix} 0.25 & 0 \\ 0 & 0.25 \end{bmatrix}$$

(in cm^2) in the world.

Several test points are shown with their uncertainty ellipses. Note that as the distance of the test point to computation points increases, the uncertainty increases. More spatially homogeneous uncertainties are achieved by distributing the computation points across the scene.

Varying the number of computation points

Figure 4.12 shows the same scene as before. Figure 4.11a is the original image and figures 4.11b-d show the uncertainty ellipses map.

The `H` matrix is computed using four points in figure 4.11b, six point in figure 4.11c and eight points in figure 4.11d. The covariances used for the computations are as before:

$$\Lambda_{\mathbf{x}} = \begin{bmatrix} 1 & 0 \\ 0 & 1 \end{bmatrix} \quad \Lambda_{\mathbf{X}} = \begin{bmatrix} 0.25 & 0 \\ 0 & 0.25 \end{bmatrix}$$

The same test points are shown with their uncertainty ellipses. Smaller uncertainties are obtained by increasing the number of computation points.

Accuracy of distances

Varying the number of computation points

A similar analysis is now conducted using images of an outside wall, computing distances instead of point locations.

Figure 4.13b-d show length measurements for a homography computed from four, six and eight correspondences. The covariances used for the computations are:

$$\Lambda_{\mathbf{x}} = \begin{bmatrix} 1 & 0 \\ 0 & 1 \end{bmatrix} \quad \Lambda_{\mathbf{X}} = \begin{bmatrix} 1 & 0 \\ 0 & 1 \end{bmatrix}$$

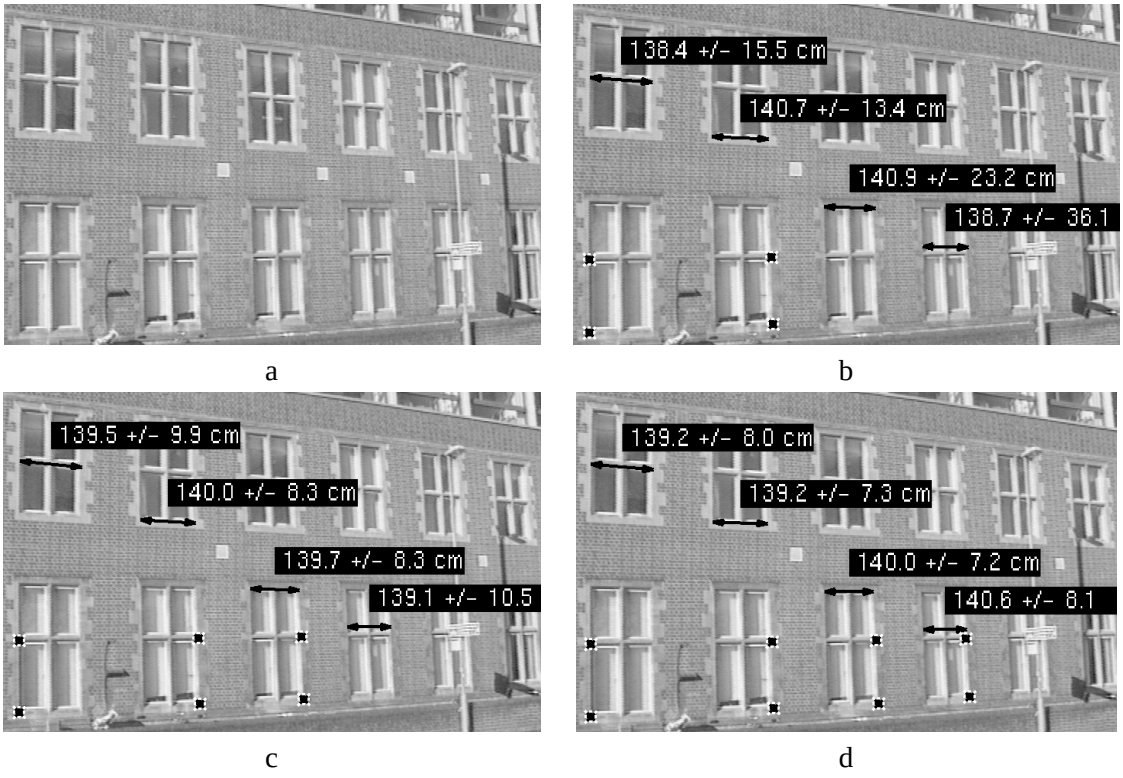

Figure 4.13: **Accuracy of distances:** (a) original image. (b-d) length measurements based on a homography computed from the points marked by black asterisks. The uncertainty bound is ± 3 std. dev. The actual width is $139cm$.

It is worth noticing that measurements farther from the set of computation points present a larger uncertainty. Again, increasing the number of computation points reduces the uncertainties in all the measurements. Note that all the estimated measurement ranges include the actual window width ($139cm$).

Different views, same computation points

Figure 4.14 illustrates that the uncertainties also depend on the observer viewpoint. The computation points for both images are in the same zone of the image frame but the second image is affected by a more severe perspective distortion. In both cases the ground truth lies within the predicted measurement range, but this is larger in the second view.

The figure also illustrates the computation of parallel world lines (see box below). Once a line is selected in the image, the one parameter family of lines parallel to it on the world plane is

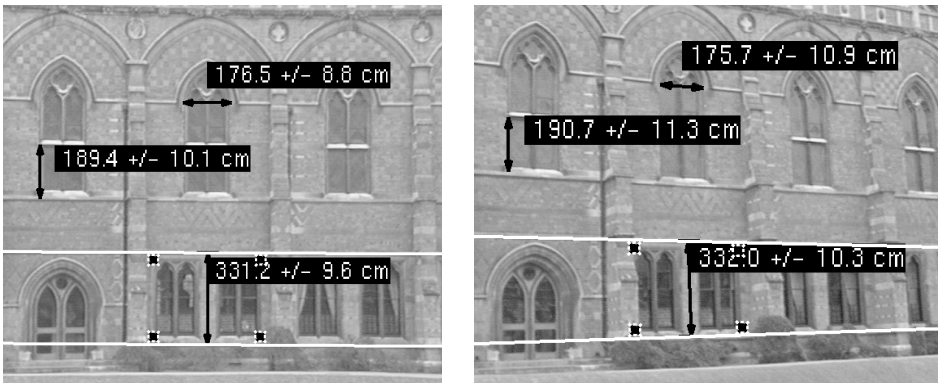

a b

Figure 4.14: **Different views, same computation points:** (a) and (b) two images of Keble College, Oxford. The computation points are the same, but the viewpoint distortion is more severe in (b). This is reflected in the larger (3 std. dev.) uncertainties. The actual width of the upper windows is $176cm$. Note the computed parallel lines.

computed from the estimated $\mathtt{H}$, and when one of them is fixed the distance is computed and shown.

Computing images of parallel lines and measuring their distance. Given the image-to-world homography $\mathtt{H}$ and a line $\mathbf{l}$ on the image the one parameter family of lines parallel to $\mathbf{l}$ in the world is defined.
In fact, given a line $\mathbf{l}$ and a point $\mathbf{x}$ in the image we can find the line $\mathbf{l}'$ through $\mathbf{x}$ whose back-projection $\mathbf{L}'$ is parallel to the back-projection of $\mathbf{l}$ onto the world plane. This is simply $\mathbf{l}' = \mathbf{x} \times \mathbf{v}$ where $\mathbf{v}$ is the vanishing point for that direction; $\mathbf{v}$ is given by $\mathbf{v} = \mathtt{H}^{-1}\mathtt{R}\mathtt{H}^{-\top}\mathbf{l}$ with $\mathtt{R}$ the following filter matrix:

$$\mathtt{R} = \begin{pmatrix} 0 & 1 & 0 \\ -1 & 0 & 0 \\ 0 & 0 & 0 \end{pmatrix}$$

Once a pair of lines $\mathbf{l}, \mathbf{l}'$ is selected their world distance can be easily computed by applying (3.3).

Different views, different computation points

Figure 4.15 shows, again, two different views of a wall. Four different computation points are used in the two images. All the measurements are taken between parallel lines and although the angle between camera and wall plane is large, the parallel lines are correctly computed.

Note that the distance measurements are *invariant* to the choice of computation points, the ground truth is always in the uncertainty range returned by the system (see caption). Notice also in this case the computation of the parallel lines.

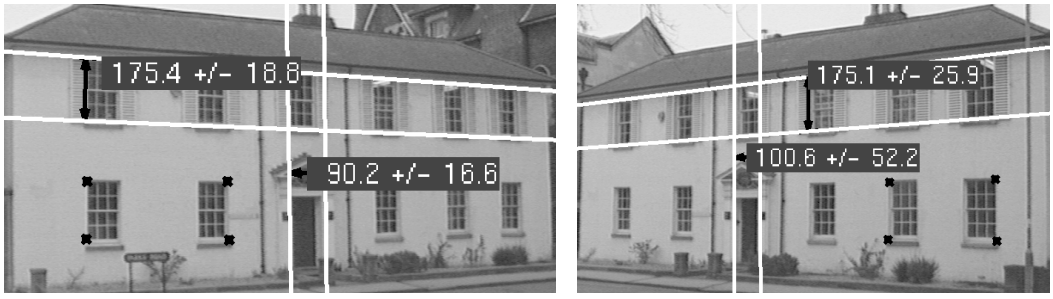

a b

Figure 4.15: **Different views, different computation points:** (a) and (b) two images of the crystallography labs in Oxford. The actual height of all the windows is $174cm$, the door width is $100cm$.

Mosaicing and measuring

If the inter-image homography between two views is known than one image can be warped and stitched to the other thus making a mosaic image. Note, though, that in general only the points lying on the same plane are registered correctly by the homography, while the ones off the plane are warped into unexpected positions [11].

In the case of a purely rotating camera no parallax can be detected and therefore all the points are registered correctly by the homography. An example of a mosaic created from a rotating camera is shown in figure 4.16. Figure 4.16a,b are two different images of an indoor scene taken from the same point of view (no parallax effect). The inter-image homography is computed from the overlapping area between the two images and the second image warped and stitched to the first one to make the mosaic in figure 4.16c. If the homography between the original images and the world plane is known, then, from the mosaicing process the homography between the final image and the world plane can be computed and measurements taken directly on the mosaic image as shown in figure 4.16d.

4.5 Duality and homologies

In the last section of this chapter some interesting properties of the plane rectification process are investigated.

Figure 4.16: **Mosaicing two images:** (a) and (b) original images of The Queen's College MCR in Oxford; the two images are taken from the same viewpoint (no parallax effect); (c) mosaic image; (d) mosaic with measurements superimposed.

In an image of a planar surface in general position the plane appears projectively warped; the image plane, instead, is by definition front-on. By rectifying the image of the world plane via the estimated homography a new image is obtained where the world plane is front-on but the original image plane is now projectively skewed; its boundary rectangle is warped into a projectively skewed quadrilateral (the solid quadrilateral around the image in fig. 4.17c). The relationship between the image plane and the world plane is investigated via an example on a real scene.

Figure 4.17b shows the perspective image of a planar wall (seen already in fig. 4.8a), the image plane is front-on (solid rectangle). Figure 4.17c is the image obtained by rectifying the wall plane. The edges of the image now make a non-rectangular quadrilateral. This is the perspectively

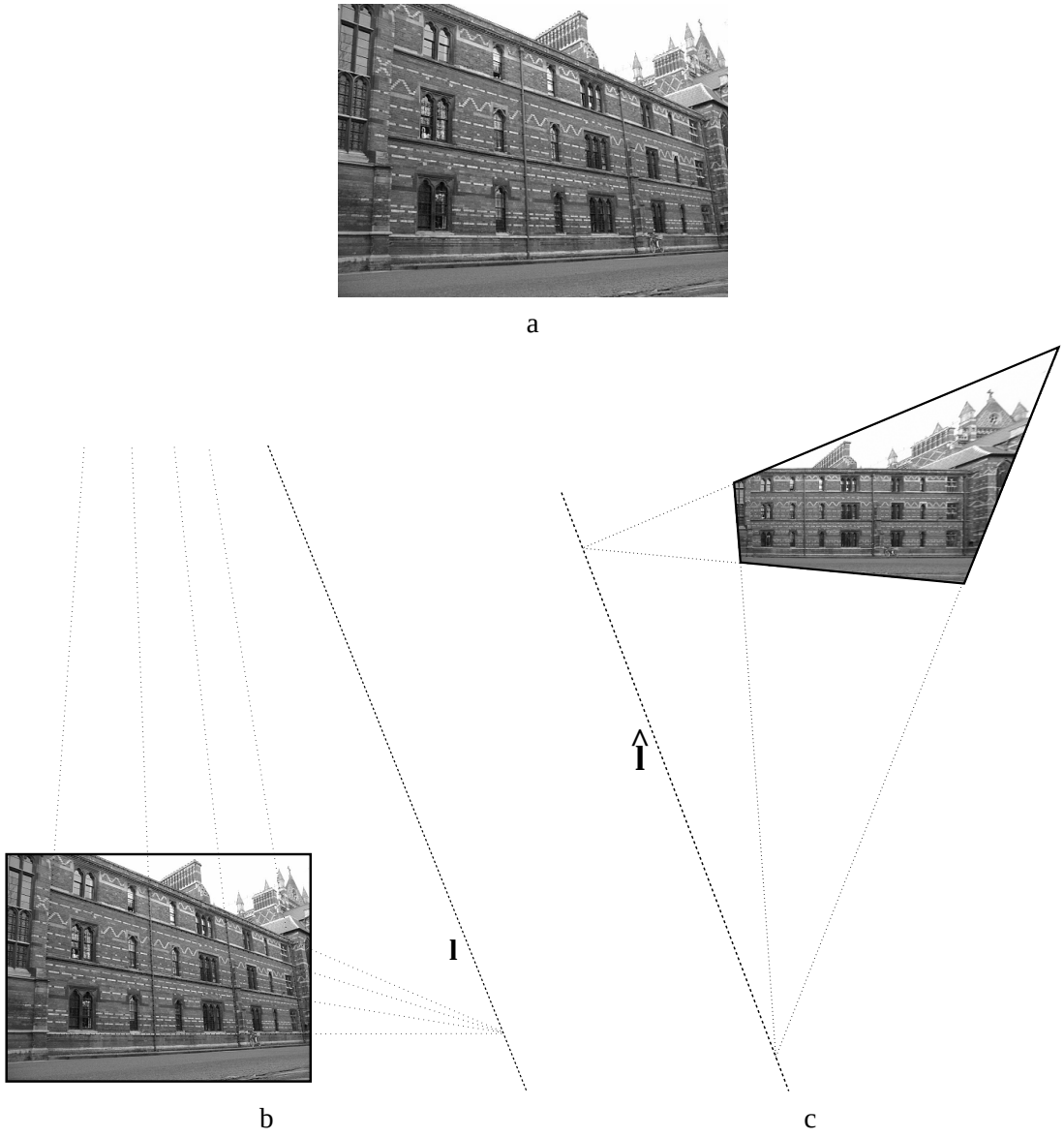

Figure 4.17: **Duality between an image of a plane and its rectification:** (a) original image, Keble College, Oxford; (b) the vanishing line of the plane of the wall has been computed and superimposed; (c) rectified image; this configuration is dual to the one in (a), see text. The boundaries of the image are the intersections of the original visual pyramid with the plane of the wall. Joining the intersections of the opposite sides of this quadrilateral we obtain the line $\hat{\mathbf{l}}$, the dual of the plane vanishing line.

distorted version of the rectangular boundary of the image in fig. 4.17a; it can be interpreted as the intersection of the visual pyramid with the plane of the wall.

In figure 4.17b the vanishing line $\mathbf{l}$ for the wall plane has been computed by joining the

intersections of two sets of parallel world edges lying on the wall. The line $\mathbf{l}$ is the image of the axis of the pencil of planes parallel to the wall and also the intersection of a plane parallel to the wall through the camera centre with the image plane. Algebraically, if $\mathtt{H}$ is the image-to-world plane homography such that $\mathbf{X} = \mathtt{H}\mathbf{x}$ where $\mathbf{x}$ is an image point and $\mathbf{X}$ the corresponding world point then $\mathbf{l}$ is the third row of the matrix $\mathtt{H}$.

On the other hand the line $\hat{\mathbf{l}}$ in figure 4.17c joins the intersections of the opposite sides of the external quadrilateral. $\hat{\mathbf{l}}$ is the intersection of the *focal plane* with the plane of the wall and can be considered as the dual of the plane vanishing line $\mathbf{l}$. Algebraically $\hat{\mathbf{l}}$ is the third row of the matrix $\mathtt{H}^{-1}$.

Furthermore, section 3.3.3 has shown that images of parallel planes related by a parallel projection are related by a planar homology whose axis is the plane vanishing line and vertex is the vanishing point of the direction of projection. Dually we can imagine having a pencil of parallel image planes; that corresponds to having a sequence taken by a purely translating camera. By rectifying all the images in the sequence via the homographies induced by the world plane we obtain the configuration illustrated in figure 4.18b. The corners of the warped image boundaries are related by a planar homology whose axis is the line $\hat{\mathbf{l}}$ and vertex is the rectified epipole. Figures 4.18a,b show an example of a special case where the camera is translating towards the college wall.

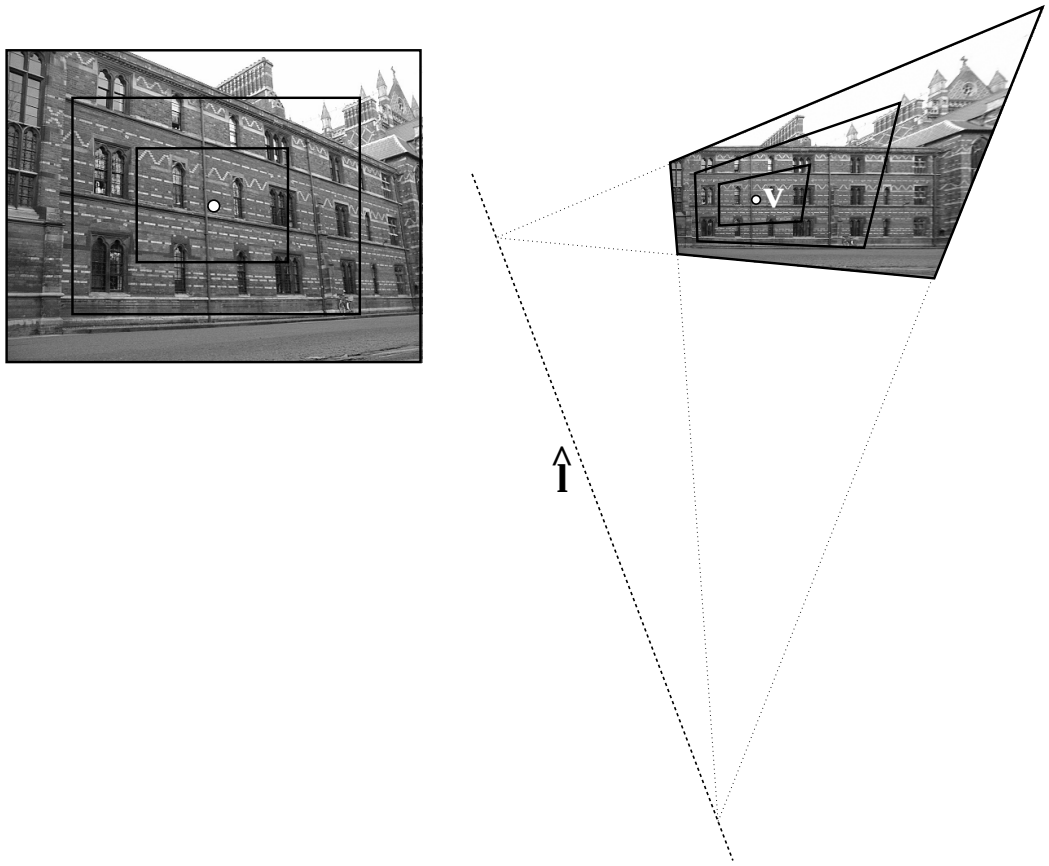

Figure 4.18: (a) original image showing further image planes for a forward translating camera. In this special case the centre of the images is the epipole. (b) the transformed boundary quadrilaterals obtained for a sequence of images from a forward translating camera are related by a homology whose axis is the line $\hat{\mathbf{l}}$ and the vertex is the point $\mathbf{v}$ (warped epipole).

Chapter 5

Single view metrology

5.1 Introduction

The previous chapter has investigated how planar measurements can be taken from uncalibrated images. However, the world is not just one big plane; it is a complex 3D structure. Therefore a more general analysis of the three-dimensional scene is required; this is achieved in this chapter. In particular, this chapter describes how aspects of the affine 3D geometry of a scene may be measured from a single perspective image (see also [25, 26]). The techniques described still concentrate on scenes containing planes and parallel lines, although the methods are not so restricted. The algorithms developed here extend and generalise previous results on single view metrology [56, 65, 91, 95].

In this chapter we assume that the vanishing line of a *reference plane* in the scene may be determined from the image, together with a vanishing point for a *reference direction* (not parallel to the plane). We are then concerned with three canonical types of measurement: (i) measurements of the distance *between* any of the planes which are parallel to the reference plane; (ii) measurements *on* these planes (and comparison of these measurements to those obtained on any parallel plane); and (iii) determining the camera's position in terms of the reference plane and direction.

The measurement methods developed here are independent of the camera internal parameters: focal length, aspect ratio, principal point, skew (uncalibrated camera, unknown internal parameters). We analyse situations where the projection matrix (external calibration) can only be partially determined from scene landmarks. This is an intermediate situation between calibrated reconstruc-

a b

Figure 5.1: **Measuring distances of points from a reference plane (the ground) in a single image:** (a) the four pillars have the same height in the world, although their images clearly are not of the same length due to perspective effects; (b) as shown, however, all pillars are correctly measured to have the same height.

tion (where metric entities like angles between rays can be computed) and completely uncalibrated cameras (where a reconstruction can be obtained only up to a projective transformation).

The ideas in this chapter can be seen as reversing the rules for drawing perspective images given by Leon Battista Alberti [1] in his treatise on perspective (1435). These are the rules followed by the Italian Renaissance painters of the fifteenth century, and indeed the correctness of their mastery of perspective is demonstrated by analysing "La Flagellazione di Cristo" by Piero della Francesca (fig. 4.9a).

Section 5.2 gives simple geometric derivations of how, in principle, three dimensional affine information may be extracted from one image (fig. 5.1). Section 5.3 introduces an algebraic representation of the problem and shows that this representation unifies the three canonical measurement types, leading to simple formulae in each case. Section 5.4 describes how errors in image measurements propagate to errors in the 3D measurements, and hence how to compute confidence intervals on the measurements, i.e. a quantitative assessment of accuracy. A generalization of the algorithm to recovering affine 3D structure is presented in section 5.5. The work has a variety of applications, and three important ones are presented: forensic measurements, virtual modelling and furniture measurements in section 5.6.

5.2 Geometry

The camera model employed here is again central projection (see section 3.3.1). We assume that the vanishing line of a reference plane in the scene may be computed from image measurements, together with a vanishing point for a direction not parallel to the plane (see section 3.5). Effects such as radial distortion which corrupt the central projection model can generally be removed as shown in section 3.4 and are therefore not detrimental to our methods. Although the schematic figures show the camera centre at a finite location, the results derived apply also to the case of a camera centre at infinity, i.e. where the images are obtained by parallel projection.

The basic geometry of the plane's vanishing line and the vanishing point are illustrated in figure 5.2. The vanishing line $\mathbf{l}$ of the reference plane is the projection of the line at infinity of the reference plane into the image. The vanishing point $\mathbf{v}$ is the image of the point at infinity in the reference direction. Note that the reference direction need not be vertical, although for clarity we will often refer to the vanishing point as the "vertical" vanishing point. The vanishing point is then the image of the vertical "footprint" of the camera centre on the reference plane. Likewise, the reference plane will often, but not necessarily, be the ground plane, in which case the vanishing line is more commonly known as the "horizon".

It can be seen (for example, by inspection of figure 5.2) that the vanishing line partitions all points in scene space. Any scene point which projects onto the vanishing line is at the same distance from the plane as the camera centre; if it lies "above" the line it is farther from the plane, and if "below" the vanishing line, then it is closer to the plane than the camera centre.

Two points on separate planes (parallel to the reference plane) *correspond* if the line joining them is parallel to the reference direction; hence the image of each point and the vanishing point are collinear (fig. 5.3b). For example, if the direction is vertical, then the top of an upright person's head and the sole of his/her foot correspond. If the world distance between the two points is known, we term this a *reference distance.*

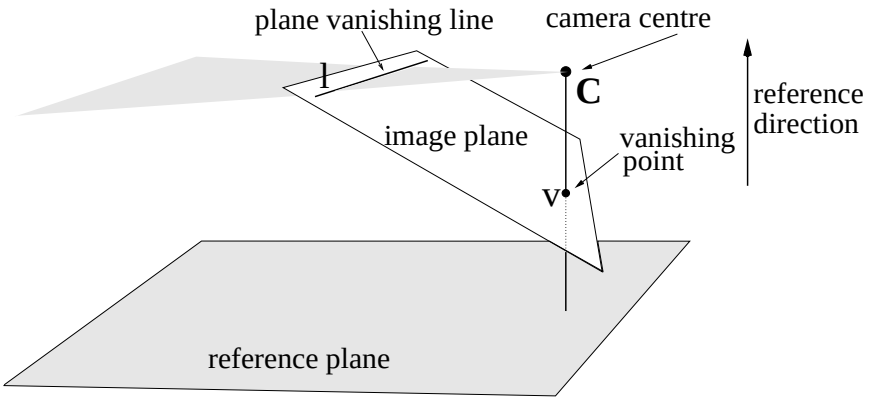

Figure 5.2: **Basic geometry**: the plane's vanishing line $\mathbf{l}$ is the intersection of the image plane with a plane parallel to the reference plane and passing through the camera centre $\mathbf{C}$. The vanishing point $\mathbf{v}$ is the intersection of the image plane with a line parallel to the reference direction through the camera centre.

5.2.1 Measurements between parallel planes

We wish to measure the distance (in the reference direction) between two parallel planes, specified by the image points $\mathbf{x}$ and $\mathbf{x}'$. Figure 5.3 shows the geometry, with points $\mathbf{x}$ and $\mathbf{x}'$ in correspondence. The following theorem holds:

Theorem 1 *Given the vanishing line of a reference plane and the vanishing point for a reference direction, then distances from the reference plane parallel to the reference direction can be computed from their imaged end points up to a common scale factor. The scale factor can be determined from one known reference length.*

Proof

The four points $\mathbf{x}$, $\mathbf{x}'$, $\mathbf{c}$, $\mathbf{v}$ marked on figure 5.3b define a cross-ratio [112]. The vanishing point is the image of a point at infinity in the scene and the point $\mathbf{c}$, since it lies on the vanishing line, is the image of a point at distance Z_c from the plane $\boldsymbol{\pi}$, where Z_c is the distance of the camera centre from $\boldsymbol{\pi}$. In the world the value of the cross-ratio provides an affine length ratio; which determines the distance Z between the planes containing $\mathbf{X}'$ and $\mathbf{X}$ (in fig. 5.3a) relative to the camera's distance Z_c from the plane $\boldsymbol{\pi}$ (or $\boldsymbol{\pi}'$ depending on the ordering of the cross-ratio). Note that the distance Z

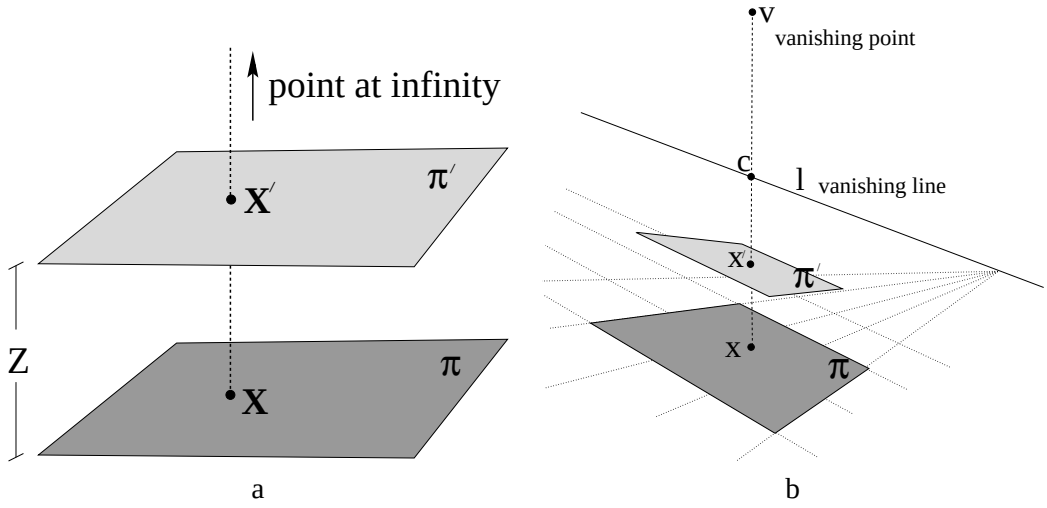

Figure 5.3: **Distance between two planes relative to the distance of the camera centre from one of the two planes**: (a) in the world; (b) in the image. The point $\mathbf{x}$ on the plane $\boldsymbol{\pi}$ corresponds to the point $\mathbf{x}'$ on the plane $\boldsymbol{\pi}'$. The four aligned points $\mathbf{v}$, $\mathbf{x}$, $\mathbf{x}'$ and the intersection $\mathbf{c}$ of the line joining them with the vanishing line define a cross-ratio. The value of the cross-ratio determines a ratio of distances between planes in the world, see text.

can alternatively be computed using a line-to-line homography avoiding the ordering ambiguity of the cross-ratio. For the case in figure 5.3b we obtain

$$\frac{Z}{Z_c} = 1 - \frac{d(\mathbf{x}', \mathbf{c})\, d(\mathbf{x}, \mathbf{v})}{d(\mathbf{x}, \mathbf{c})\, d(\mathbf{x}', \mathbf{v})} \tag{5.1}$$

where $d(\mathbf{x}_1, \mathbf{x}_2)$ is distance between two generic image points $\mathbf{x}_1$ and $\mathbf{x}_2$.

The absolute distance Z can be obtained from the distance ratio (5.1) once the camera's distance Z_c is specified. However it is usually more practical to determine the distance Z via a second measurement in the image, that of a known reference length. In fact, given a known reference distance Z_r, the distance of the camera Z_c can be computed from (5.1) and then the distance Z determined by applying (5.1) to a new pair of end points. □

Theorem 1 can be generalised to the following:

Theorem 2 *Given a set of linked parallel planes, the distance between any pair of planes is sufficient to determine the absolute distance between any other pair. The link being provided by a chain of point correspondences between the set of planes.*

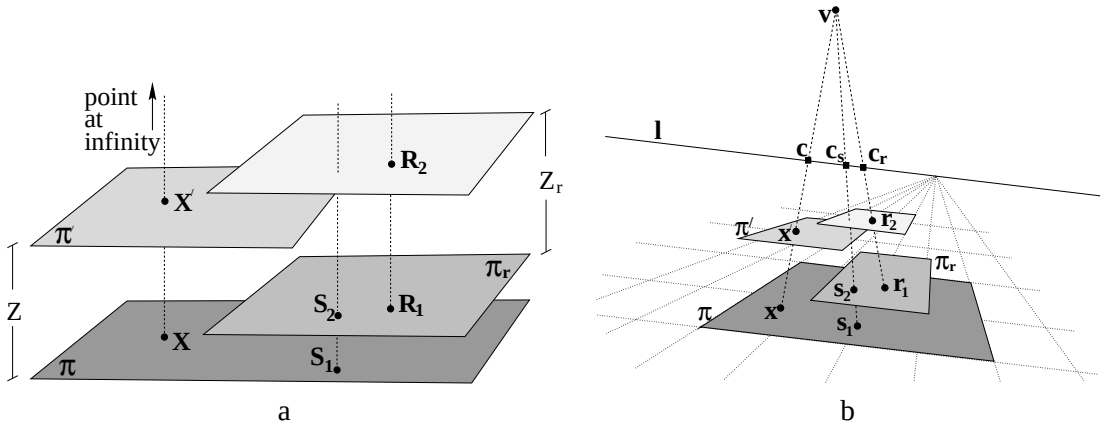

Figure 5.4: **Distance between two planes relative to the distance between two other planes**: (a) in the world; (b) in the image. The point $\mathbf{x}$ on the plane $\boldsymbol{\pi}$ corresponds to the point $\mathbf{x}'$ on the plane $\boldsymbol{\pi}'$. The point $\mathbf{s}_1$ corresponds to the point $\mathbf{s}_2$. The point $\mathbf{r}_1$ corresponds to the point $\mathbf{r}_2$. The distance Z_r in the world between $\mathbf{R}_1$ and $\mathbf{R}_2$ is known and used as reference to compute the distance Z, see text.

Proof

Figure 5.4 shows a diagram where four parallel planes are imaged. They all share the same vanishing line which is the image of the axis of the pencil. The distance Z_r between two of them can be used as reference to compute the distance Z between the other two as follows:

- From the cross-ratio defined by the four aligned points $\mathbf{v}$, $\mathbf{c}_r$, $\mathbf{r}_2$, $\mathbf{r}_1$ and the known distance Z_r between the world points $\mathbf{R}_1$ and $\mathbf{R}_2$ the distance of the camera from the plane $\boldsymbol{\pi}_r$ can be computed.

- That camera distance and the cross-ratio defined by the four aligned points $\mathbf{v}$, $\mathbf{c}_s$, $\mathbf{s}_2$, $\mathbf{s}_1$, determine the distance between the planes $\boldsymbol{\pi}_r$ and $\boldsymbol{\pi}$. The distance Z_c of the camera from the plane $\boldsymbol{\pi}$ is, therefore, determined too.

- The distance Z_c can now be used in (5.1) to compute the distance Z between the two planes $\boldsymbol{\pi}$ and $\boldsymbol{\pi}'$.

□

a b

Figure 5.5: **Measuring the height of a person from single view**: (a) original image; (b) the height of the person is computed from the image as 178.8cm; the true height is 180cm, but note that the person is leaning down a bit on his right foot. The vanishing line is shown in white; the vertical vanishing point is not shown since it lies well below the image. The reference distance is in white (the height of the window frame on the right). Compare the marked points with the ones in fig. 5.4.

Section 5.3.1 presents an algebraic derivation of these results which avoids the need to compute the distance of the camera explicitly and simplifies the measurement procedure.

Example. Figure 5.5 shows that a person's height may be computed from an image given a vertical reference distance elsewhere in the scene. The ground plane is reference. The height of the frame of the window has been measured on site and used as the reference distance (it corresponds to the distance between $\mathbf{R}_1$ and $\mathbf{R}_2$ in the world in fig. 5.4a). This situation corresponds to the one in figure 5.4 where the two points $\mathbf{S}_2$ and $\mathbf{R}_1$ (and therefore $\mathbf{s}_2$ and $\mathbf{r}_1$) coincide. The height of the person is computed from the cross-ratio defined by the points $\mathbf{x}'$, $\mathbf{c}$, $\mathbf{x}$ and the vanishing point (figure 5.4b) as described in the proof above. Since the points $\mathbf{S}_2$ and $\mathbf{R}_1$ coincide the derivation is simpler.

5.2.2 Measurements on parallel planes

If the reference plane π is affine calibrated (its vanishing line is known) then from image measurements we can compute:

1. ratios of lengths of parallel line segments on the plane;

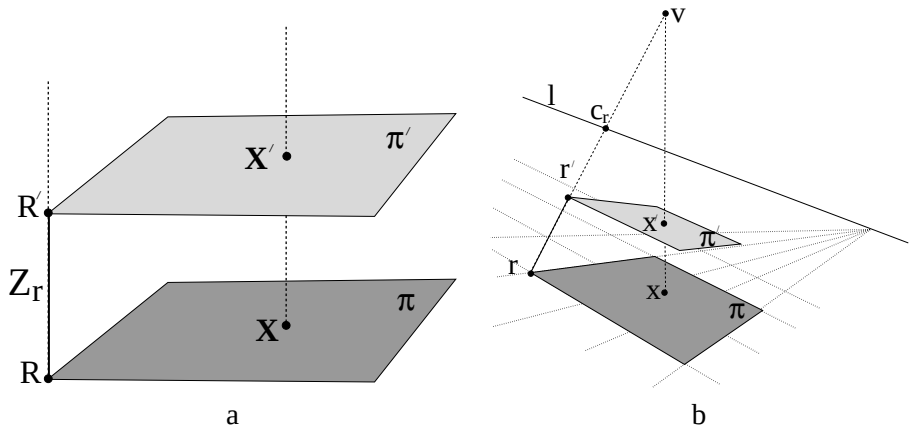

Figure 5.6: **Homology mapping between imaged parallel planes related by parallel projection**: (a) A point $\mathbf{X}$ on the plane $\boldsymbol{\pi}$ is mapped into the point $\mathbf{X}'$ on $\boldsymbol{\pi}'$ by a parallel projection. (b) In the image the mapping between the images of the two planes is a homology, where $\mathbf{v}$ is the *vertex* and $\mathbf{l}$ the *axis*. The correspondence $\mathbf{r} \rightarrow \mathbf{r}'$ fixes the remaining degree of freedom of the homology from the cross-ratio of the four points $\mathbf{v}$, $\mathbf{c}_r$, $\mathbf{r}'$ and $\mathbf{r}$.

2. ratios of areas on the plane.

Moreover the vanishing line is shared by the pencil of planes parallel to the reference plane, hence affine measurements may be obtained for any other plane in the pencil. However, although affine measurements, such as an area ratio, may be made *on* a particular plane, the areas of regions lying on two parallel planes cannot be compared directly. If the region is parallel projected in the scene from one plane onto the other, affine measurements can then be made from the image since both regions are now on the same plane, and parallel projection between parallel planes does not alter affine properties.

A map in the world between parallel planes induces a map in the image between images of points on the two planes. As stated in section 3.3.3 this image map is a *planar homology*. The geometry is illustrated in figure 5.6. In this case the vanishing line of the plane, and the vertical vanishing point, are, respectively, the *axis* and *vertex* of the homology which relates a pair of planes in the pencil.

The homology $\tilde{\mathtt{H}}$ can then be parametrized as in (3.5):

$$\tilde{\mathtt{H}} = \mathtt{I} + \mu \frac{\mathbf{v}\mathbf{l}^\top}{\mathbf{v} \cdot \mathbf{l}} \tag{5.2}$$

where $\mathbf{v}$ is the vanishing point, $\mathbf{l}$ is the plane vanishing line and μ is the characteristic ratio. Thus $\mathbf{v}$ and $\mathbf{l}$ specify four of the five degrees of freedom of the homology. The remaining degree of freedom of the homology, μ, is uniquely determined from any pair of image points which correspond between the planes (points $\mathbf{r}$ and $\mathbf{r}'$ in figure 5.6).

Once the matrix $\tilde{\mathtt{H}}$ is computed each point on a plane can be transferred into the corresponding point on a parallel plane as $\mathbf{x}' = \tilde{\mathtt{H}}\mathbf{x}$. An example of this *homology mapping* is shown in figure 3.7. Consequently measurements made on two separate planes can be compared. In particular we may compute:

1. the ratio between two parallel lengths, one length on each plane;

2. the ratio between two areas, one area on each plane.

In fact all points can be transferred from one plane to the reference plane using the homology. Since the reference plane's vanishing line is known, affine measurements in the plane can be made (e.g. parallel length or area ratios).

Example. Figure 5.7 shows an example. The vanishing line of the two front facing walls and the vanishing point are known as is the point correspondence $\mathbf{r}$, $\mathbf{r}'$ in the reference direction. The ratio of length of parallel line segments is computed by using formulae given in section 5.3.2. Notice that errors in the selection of point positions affect the computations; the veridical values of the ratios in figure 5.7 are exact integers. A proper error analysis is necessary to estimate the uncertainty of these affine measurements.

5.2.3 Determining the camera position

Section 5.2.1 computes distances between planes as a ratio relative to the camera's distance from the reference plane. Conversely, the camera's distance Z_c from a particular plane can be obtained

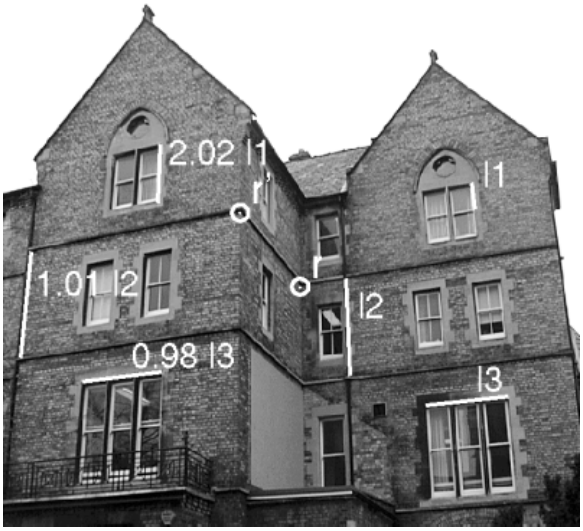

Figure 5.7: **Measuring ratio of lengths of parallel line segments lying on two parallel scene planes**: The points $\mathbf{r}$ and $\mathbf{r}'$ (together with the plane vanishing line and the vanishing point) define the homology between the two planes on the facade of the building.

knowing a single reference distance Z_r.

Furthermore, figure 5.2 shows that the location of the camera relative to the reference plane is the back-projection of the vertical vanishing point onto the reference plane. This back-projection is accomplished by a homography which maps the image to the reference plane (and vice-versa). Although the choice of coordinate frame in the world is somewhat arbitrary, fixing this frame immediately defines the homography uniquely and hence the camera position.

5.3 Algebraic representation

The measurements described in the previous section are computed in terms of cross-ratios. This section develops a uniform algebraic approach to the problem which has a number of advantages over direct geometric construction: first, it avoids potential problems with ordering for the cross-ratio; second, it allows to deal with both minimal or over-constrained configurations uniformly; third, different types of measurement are unified within one representation; and fourth, in section 5.4 this algebraic representation is used to develop an uncertainty analysis for measurements.

To begin, an affine coordinate system XYZ is defined in space [66, 93]. Let the origin of the coordinate frame lie on the reference plane, with the X and Y-axes spanning the plane. The Z-axis is the reference direction, which is thus any direction not parallel to the plane. The image coordinate system is the usual xy affine image frame, and a point $\mathbf{X}$ in space is projected to the image point $\mathbf{x}$ via a 3×4 projection matrix $\mathtt{P}$ as:

$$\mathbf{x} = \mathtt{P}\mathbf{X} = \begin{bmatrix} \mathbf{p}_1 & \mathbf{p}_2 & \mathbf{p}_3 & \mathbf{p}_4 \end{bmatrix} \mathbf{X}$$

where $\mathbf{x}$ and $\mathbf{X}$ are homogeneous vectors in the form: $\mathbf{x} = (x, y, w)^\top$, $\mathbf{X} = (X, Y, Z, W)^\top$, and "$=$" means equality up to scale.

Denoting the vanishing points for the X, Y and Z directions as (respectively) $\mathbf{v}_X$, $\mathbf{v}_Y$ and $\mathbf{v}$, it is clear by inspection [36] that the first three columns of $\mathtt{P}$ are the vanishing points: $\mathbf{v}_X = \mathbf{p}_1$, $\mathbf{v}_Y = \mathbf{p}_2$ and $\mathbf{v} = \mathbf{p}_3$, and that the final column of $\mathtt{P}$ is the projection of the origin of the world coordinate system, $\mathbf{o} = \mathbf{p}_4$. Since our choice of coordinate frame has the X and Y axes in the reference plane $\mathbf{p}_1 = \mathbf{v}_X$ and $\mathbf{p}_2 = \mathbf{v}_Y$ are two distinct points on the vanishing line. Choosing these fixes the X and Y affine coordinate axes. The vanishing line is denoted by $\mathbf{l}$, and to emphasize that the vanishing points $\mathbf{v}_X$ and $\mathbf{v}_Y$ lie on it, we denote them by $\mathbf{l}_1^\perp$, $\mathbf{l}_2^\perp$, with $\mathbf{l}_i^\perp \cdot \mathbf{l} = 0$.

Columns 1, 2 and 4 of the projection matrix are the three columns of the reference plane to image homography. This homography must have rank three, otherwise the reference plane to image map is degenerate. Consequently, the final column (the origin of the coordinate system) must not lie on the vanishing line, since if it does then all three columns are points on the vanishing line, and thus are not linearly independent. Hence we set it to be $\mathbf{o} = \mathbf{p}_4 = \mathbf{l}/||\mathbf{l}|| = \bar{\mathbf{l}}$.

Therefore the final parameterization of the projection matrix $\mathtt{P}$ is:

$$\mathtt{P} = \begin{bmatrix} \mathbf{l}_1^\perp & \mathbf{l}_2^\perp & \alpha\mathbf{v} & \bar{\mathbf{l}} \end{bmatrix} \tag{5.3}$$

where α is a scale factor, which has an important rôle to play in the remainder of the chapter.

Note that the vertical vanishing point $\mathbf{v}$ imposes two constraints on the $\mathtt{P}$ matrix, the vanishing

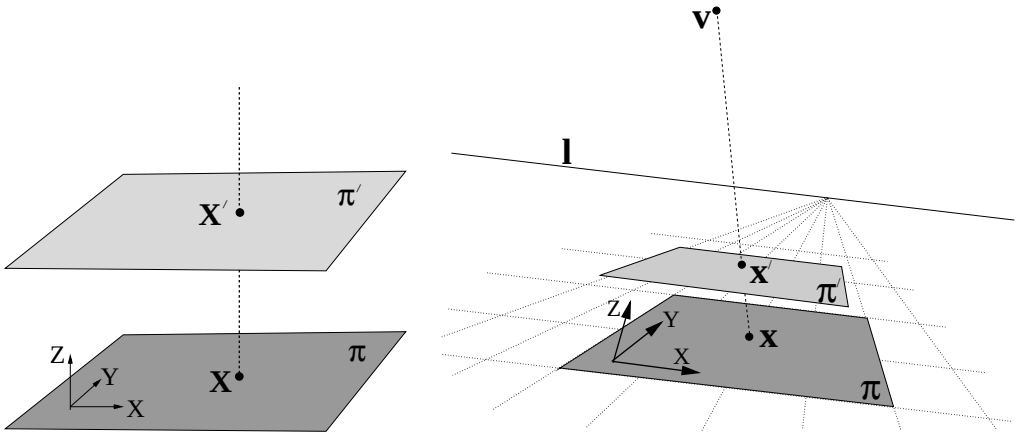

Figure 5.8: Measuring the distance of a plane π' from the parallel reference plane π: (a) in the world; (b) in the image.

line $\mathbf{l}$ two and the α parameter only one for a total of five independent constraints. In general however the $\mathtt{P}$ matrix has eleven degrees of freedom, which can be regarded as comprising eight for the world-to-image homography induced by the reference plane, two for the vanishing point and one for the affine parameter α. In our case the vanishing line determines two of the eight d.o.f. of the homography.

The following sections show how to compute various measurements from this projection matrix. Measurements of distances between planes are independent of the first two (in general under-determined) columns of $\mathtt{P}$. If $\mathbf{v}$ and $\mathbf{l}$ are specified the only unknown quantity for these measurements is α. Coordinate measurements within the planes depend on the first two and the fourth columns of $\mathtt{P}$. They define an affine coordinate frame within the plane. Affine measurements (e.g. area ratios), though, are independent of the actual coordinate frame and depend only on the fourth column of $\mathtt{P}$. If any metric information on the plane is known, that can be used to impose constraints on the choice of the frame.

5.3.1 Measurements between parallel planes

Distance of a plane from the reference plane π

We wish to measure the distance between scene planes specified by a point $\mathbf{X}$ and a point $\mathbf{X}'$ in the scene (see fig. 5.3a). These points may be chosen as respectively $\mathbf{X} = (X, Y, 0)^\top$ and $\mathbf{X}' = (X, Y, Z)^\top$, and their images are $\mathbf{x}$ and $\mathbf{x}'$ (fig. 5.8). If $\mathtt{P}$ is the projection matrix then the image coordinates are

$$\mathbf{x} = \mathtt{P}\begin{pmatrix} X \\ Y \\ 0 \\ 1 \end{pmatrix}, \qquad \mathbf{x}' = \mathtt{P}\begin{pmatrix} X \\ Y \\ Z \\ 1 \end{pmatrix}$$

The equations above can be rewritten as

$$\mathbf{x} = \rho(X\mathbf{p}_1 + Y\mathbf{p}_2 + \mathbf{p}_4) \tag{5.4}$$

$$\mathbf{x}' = \rho'(X\mathbf{p}_1 + Y\mathbf{p}_2 + Z\mathbf{p}_3 + \mathbf{p}_4) \tag{5.5}$$

where ρ and ρ' are unknown scale factors, and $\mathbf{p}_i$ is the i^{th} column of the $\mathtt{P}$ matrix.

Since $\mathbf{p}_1 \cdot \bar{\mathbf{l}} = \mathbf{p}_2 \cdot \bar{\mathbf{l}} = 0$ and $\mathbf{p}_4 \cdot \bar{\mathbf{l}} = 1$, taking the scalar product of (5.4) with $\bar{\mathbf{l}}$ yields $\rho = \bar{\mathbf{l}} \cdot \mathbf{x}$, and combining this with the third column of (5.3) and (5.5) we obtain

$$\alpha Z = -\frac{||\mathbf{x} \times \mathbf{x}'||}{(\bar{\mathbf{l}} \cdot \mathbf{x})||\mathbf{v} \times \mathbf{x}'||} \tag{5.6}$$

Since αZ scales linearly with α we have obtained affine structure. If α is known, then we immediately obtain a metric value for Z as:

$$Z = -\frac{||\mathbf{x} \times \mathbf{x}'||}{(\mathbf{p}_4 \cdot \mathbf{x})||\mathbf{p}_3 \times \mathbf{x}'||} \tag{5.7}$$

Conversely, if Z is known (i.e. it is a reference distance) then (5.6) provides a means of computing α, and hence removing the affine ambiguity.

Metric calibration from multiple references.

If more than one reference distance is known then an estimate of α can be derived from an error minimization algorithm. Here a special case is considered where all distances are measured from

the same reference plane and an algebraic error is minimized. An optimal minimization algorithm will be described in section 5.4.2.

For the i^{th} reference distance Z_i with end points $\mathbf{r}_i$ and $\mathbf{r}'_i$ we define: $\beta_i = ||\mathbf{r}_i \times \mathbf{r}'_i||$, $\rho_i = \bar{\mathbf{l}} \cdot \mathbf{r}_i$, $\gamma_i = ||\mathbf{v} \times \mathbf{r}'_i||$. Therefore, from (5.6):

$$\alpha Z \rho_i \gamma_i = -\beta_i \tag{5.8}$$

Note that all the points $\mathbf{r}_i$ are images of world points $\mathbf{R}_i$ on the reference plane $\boldsymbol{\pi}$. By reorganising (5.8) the following matrix $\mathtt{A}$ is defined:

$$\mathtt{A} = \begin{pmatrix} Z_1\rho_1\gamma_1 & \beta_1 \\ \vdots & \vdots \\ Z_i\rho_i\gamma_i & \beta_i \\ \vdots & \vdots \\ Z_n\rho_n\gamma_n & \beta_n \end{pmatrix}$$

where n is the number of reference distances.

If the references are not affected by measurement error or $n = 1$ then $\mathtt{A}\mathbf{s} = \mathbf{0}$ where $\mathbf{s} = \begin{pmatrix} s_1 & s_2 \end{pmatrix}^\top$ is a homogeneous 2-vector and

$$\alpha = \frac{s_1}{s_2} \tag{5.9}$$

In general $n > 1$ and uncertainty is present in the reference distances. In this case we find the solution $\mathbf{s}$ which minimizes $||\mathtt{A}\mathbf{s}||$. That is the eigenvector of the 2×2 matrix $\mathtt{M} = \mathtt{A}^\top \mathtt{A}$ corresponding to its minimum eigenvalue. The parameter α is finally computed from (5.9). With more reference distances Z_i, α is estimated more accurately (see section 5.4), but no more constraints are added on the $\mathtt{P}$ matrix.

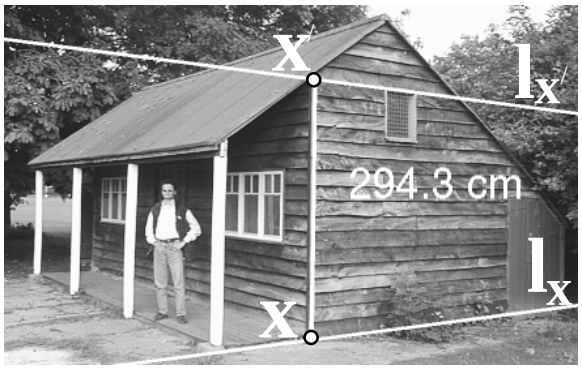

Figure 5.9: **Measuring heights using parallel lines:** The vertical vanishing point and the vanishing line for the ground plane have been computed. The distance of the top of the window on the left wall from the ground is known and used as reference. The distance of the top of the window on the right wall from the ground is computed from the distance between the two horizontal lines whose images are $\mathbf{l}_{x'}$ and $\mathbf{l}_x$. The top line $\mathbf{l}_{x'}$ is defined by the top edge of the window, and the line $\mathbf{l}_x$ is the corresponding one on the ground plane. The distance between them is computed to be 294.3cm.

– worked example –

Objective: in figure 5.9 the distance of a horizontal line from the ground is measured.

- The vertical vanishing point $\mathbf{v}$ is computed by intersecting vertical (scene) edges;

All images of lines parallel to the ground plane intersect in points on the horizon, therefore:

- a vanishing point $\mathbf{v}_1$ on the horizon is computed by intersecting the edges of the planks on the right side of the shed;
- a second vanishing point $\mathbf{v}_2$ is computed by intersecting the edges of the planks on the left side of the shed and the parallel edges on the roof;
- the plane vanishing line $\mathbf{l}$ is computed by joining those two points: $\mathbf{l} = \mathbf{v}_1 \times \mathbf{v}_2$;
- the distance of the top of the frame of the window on the left from the ground has been measured on site and used as reference to compute α as in (5.6).
- the line $\mathbf{l}_{x'}$, the image of a horizontal line, is selected in the image by choosing any two points on it;
- the associated vanishing point $\mathbf{v}_h$ is computed as $\mathbf{v}_h = \mathbf{l}_{x'} \times \mathbf{l}$;
- the line $\mathbf{l}_x$, which is the image of a line parallel to $\mathbf{l}_{x'}$ in the scene is constrained to pass through $\mathbf{v}_h$, therefore $\mathbf{l}_x$ is specified by choosing one additional point on it;
- a point $\mathbf{x}'$ is selected along the line $\mathbf{l}_{x'}$ and its corresponding point $\mathbf{x}$ on the line $\mathbf{l}_x$ computed as $\mathbf{x} = (\mathbf{x}' \times \mathbf{v}) \times \mathbf{l}_x$;
- equation (5.7) is now applied to the pair of points $\mathbf{x}$, $\mathbf{x}'$ to compute the distance $Z = 294.3$cm.

Distance between any two parallel planes

The projection matrix $\mathtt{P}$ from the world to the image is defined in (5.3) with respect to a coordinate frame on the reference plane (fig. 5.8). In this section we determine the projection matrix $\mathtt{P}'$ referred to the parallel plane $\boldsymbol{\pi}'$ and we show how distances from the plane $\boldsymbol{\pi}'$ can be computed.

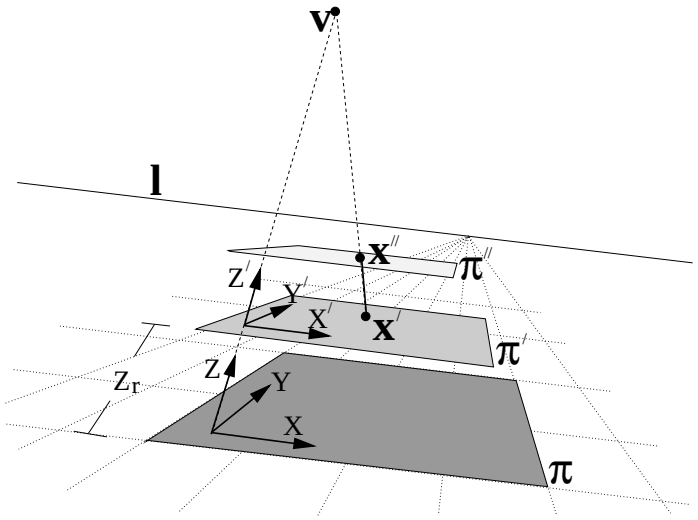

Figure 5.10: Measuring the distance between any two planes $\boldsymbol{\pi}'$ and $\boldsymbol{\pi}''$ parallel to the reference plane $\boldsymbol{\pi}$; the geometry.

Suppose the world coordinate system is translated by Z_r from the plane $\boldsymbol{\pi}$ onto the plane $\boldsymbol{\pi}'$ along the reference direction (fig. 5.10), then the new projection matrix $\mathtt{P}'$ can be parametrized as:

$$\mathtt{P}' = \begin{bmatrix} \mathbf{p}_1 & \mathbf{p}_2 & \mathbf{p}_3 & Z_r\mathbf{p}_3 + \mathbf{p}_4 \end{bmatrix} \tag{5.10}$$

Note that if $Z_r = 0$ then $\mathtt{P}' = \mathtt{P}$ as expected.

The distance Z' of the plane $\boldsymbol{\pi}''$ from the plane $\boldsymbol{\pi}'$ in space can be computed as (*cf.* (5.7)).

$$Z' = -\frac{||\mathbf{x}' \times \mathbf{x}''||}{\rho'||\mathbf{p}_3 \times \mathbf{x}''||} \quad \text{with} \quad \rho' = \frac{\mathbf{p}_4 \cdot \mathbf{x}'}{1 + \mathrm{Z_r}\mathbf{p}_3 \cdot \mathbf{p}_4} \tag{5.11}$$

– worked example –

Objective: in figure 5.11 the height of a file on a desk is computed from the height of the desk itself

- The ground is the reference plane $\boldsymbol{\pi}$ and the top of the desk is the plane denoted as $\boldsymbol{\pi}'$ in figure 5.10;
- the plane vanishing line and vertical vanishing point are computed as usual by intersecting parallel edges;
- the distance Z_r between the points $\mathbf{r}$ and $\mathbf{r}'$ is known (the height of the desk has been measured on site) and used to compute the α parameter from (5.6);
- equation (5.11) is now applied to the end points of the marked segment to compute the height Z' = 32.0cm.

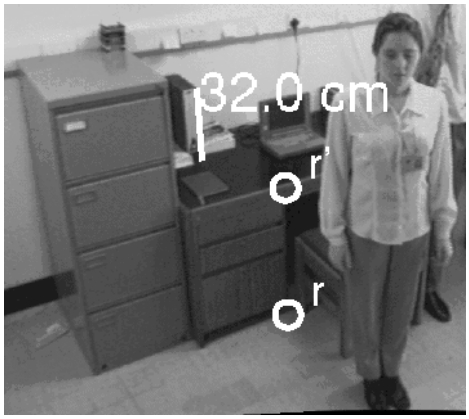

Figure 5.11: **Measuring heights of objects on separate planes**: the height of the desk is known and the height of the file on the desk is computed.

5.3.2 Measurements on parallel planes

As described in section 5.2.2, given the homology between two planes $\boldsymbol{\pi}$ and $\boldsymbol{\pi}'$ in the pencil we can transfer all points from one plane to the other and make affine measurements in either plane.

The homology between the planes can be derived directly from the two projection matrices (5.3) and (5.10). The plane-to-image homographies may be extracted from the projection matrices ignoring the third column, to give:

$$\mathtt{H} = \begin{bmatrix} \mathbf{p}_1 & \mathbf{p}_2 & \mathbf{p}_4 \end{bmatrix}, \quad \mathtt{H}' = \begin{bmatrix} \mathbf{p}_1 & \mathbf{p}_2 & Z_r\mathbf{p}_3 + \mathbf{p}_4 \end{bmatrix}$$

Then $\tilde{\mathtt{H}} = \mathtt{H}'\mathtt{H}^{-1}$ maps image points on the plane $\boldsymbol{\pi}$ onto points on the plane $\boldsymbol{\pi}'$ and so defines the homology. By inspection, since $\mathbf{p}_1 \cdot \mathbf{p}_4 = 0$ and $\mathbf{p}_2 \cdot \mathbf{p}_4 = 0$ then $(\mathtt{I} + Z_r\mathbf{p}_3\mathbf{p}_4^\top)\mathtt{H} = \mathtt{H}'$, hence the homology matrix $\tilde{\mathtt{H}}$ is:

$$\tilde{\mathtt{H}} = \mathtt{I} + Z_r\mathbf{p}_3\mathbf{p}_4^\top \tag{5.12}$$

Alternatively from (5.3) the homology matrix can be written as:

$$\tilde{\mathtt{H}} = \mathtt{I} + \psi\mathbf{v}\bar{\mathbf{l}}^\top \tag{5.13}$$

with $\psi = \alpha Z_r$.

If the distance Z_r and the last two columns of the matrix $\mathtt{P}$ are known then the homology between the two planes $\boldsymbol{\pi}$ and $\boldsymbol{\pi}'$ is computed as in (5.12). Otherwise, if only $\mathbf{v}$ and $\mathbf{l}$ are known and two corresponding points $\mathbf{r}$ and $\mathbf{r}'$ are viewed, then the homology parameter ψ in (5.13) can be computed from (5.6) (in fact $\alpha Z_r = \psi$) without knowing either the distance Z_r between the two planes or the α parameter.

Examples of homology transfer and affine measurements are shown in figures 5.7 and 5.12.

– worked example –

Objective: in figure 5.12 the ratio between the areas of two windows $\frac{A_1}{A_2}$ in the world is computed.

- The orthogonal vanishing point $\mathbf{v}$ is computed by intersecting the edges of the small windows linking the two front planes;
- the plane vanishing line $\mathbf{l}$ (common to both front planes) is computed by intersecting two sets of parallel edges on the two planes;
- the only remaining parameter ψ of the homology $\tilde{\mathtt{H}}$ in (5.13) is computed from (5.6) as

$$\psi = -\frac{||\mathbf{r} \times \mathbf{r}'||}{(\bar{\mathbf{l}} \cdot \mathbf{r})||\mathbf{v} \times \mathbf{r}'||}$$

- each of the four corners of the window on the left is transferred by the homology $\tilde{\mathtt{H}}$ onto the corresponding points on the plane of the other window (fig. 5.12b);

Now we have two quadrilaterals on the same plane

- the image is affine-warped pulling the plane vanishing line to infinity [75];
- the ratio between the two areas in the world is computed as the ratio between the areas in the affine-warped image. We obtain $\frac{A_1}{A_2} = 1.45$.

5.3.3 Determining the camera position

Suppose the camera centre is $\mathbf{C} = (X_c, Y_c, Z_c, W_c)^\top$ in affine coordinates (see figure 5.2). Then since $\mathtt{P}\mathbf{C} = \mathbf{0}$ we have

$$\mathtt{P}\mathbf{C} = \mathbf{p}_1 X_c + \mathbf{p}_2 Y_c + \mathbf{p}_3 Z_c + \mathbf{p}_4 W_c = \mathbf{0} \tag{5.14}$$

The solution to this set of equations is given (using Cramer's rule) by

$$X_c = -\det\begin{bmatrix} \mathbf{p}_2 & \mathbf{p}_3 & \mathbf{p}_4 \end{bmatrix}, \quad Y_c = \det\begin{bmatrix} \mathbf{p}_1 & \mathbf{p}_3 & \mathbf{p}_4 \end{bmatrix},$$

$$Z_c = -\det\begin{bmatrix} \mathbf{p}_1 & \mathbf{p}_2 & \mathbf{p}_4 \end{bmatrix}, \quad W_c = \det\begin{bmatrix} \mathbf{p}_1 & \mathbf{p}_2 & \mathbf{p}_3 \end{bmatrix} \tag{5.15}$$

a b

Figure 5.12: **Measuring ratios of areas on separate planes:** (a) original image with two windows hilighted; (b) the left window is transferred onto the plane identified by $\mathbf{r}'$ by the homology mapping (5.13). The two areas now lie on the same plane and can, therefore, be compared. The ratio between the areas of the two windows is then computed as: $\frac{A_1}{A_2} = 1.45$.

if P is entirely known the location of the camera centre is metric defined. If α is unknown we can write:

$$X_c = -\det\begin{bmatrix} \mathbf{p}_2 & \mathbf{v} & \mathbf{p}_4 \end{bmatrix}, \quad Y_c = \det\begin{bmatrix} \mathbf{p}_1 & \mathbf{v} & \mathbf{p}_4 \end{bmatrix},$$

$$\alpha Z_c = -\det\begin{bmatrix} \mathbf{p}_1 & \mathbf{p}_2 & \mathbf{p}_4 \end{bmatrix}, \quad W_c = \det\begin{bmatrix} \mathbf{p}_1 & \mathbf{p}_2 & \mathbf{v} \end{bmatrix} \tag{5.16}$$

and obtain the distance Z_c of the camera centre from the plane up to the affine scale factor α. As before, the distance Z_c can be upgraded to metric with knowledge of α, or use knowledge of the camera height to compute α and upgrade the affine structure.

Note that affine viewing conditions (where the camera centre is at infinity) present no problem in expressions (5.15) and (5.16), since in this case we have $\bar{\mathbf{l}} = \begin{bmatrix} 0 & 0 & * \end{bmatrix}^\top$ and $\mathbf{v} = \begin{bmatrix} * & * & 0 \end{bmatrix}^\top$. Hence $W_c = 0$ thus a camera centre on the plane at infinity is obtained, as expected. This point on $\boldsymbol{\pi}_\infty$ represents the viewing direction for the parallel projection.

If the viewpoint is finite (i.e. not affine viewing conditions) then the formula for αZ_c may be developed further by taking the scalar product of both sides of (5.14) with the vanishing line $\bar{\mathbf{l}}$. The

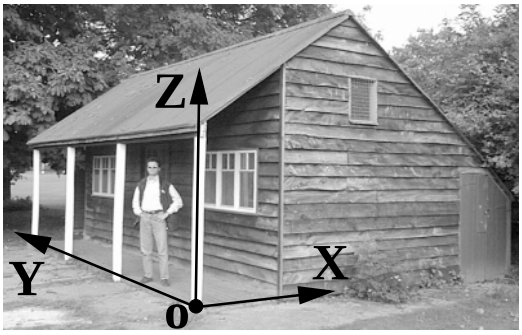

Figure 5.13: **Computing the location of the camera**: equations (5.15) are used to obtain: X_c = -381.0cm, Y_c = -653.7cm, Z_c = 162.8cm.

result is

$$\alpha Z_c = -(\bar{\mathbf{l}} \cdot \mathbf{v})^{-1} \tag{5.17}$$

– worked example –

Objective: in figure 5.13 the position of the camera centre with respect to the chosen Cartesian coordinate system is determined. Note that in this case we have chosen $\mathbf{p}_4$ to be the point $\mathbf{o}$ in the figure instead of $\bar{\mathbf{l}}$.

- The ground plane (X, Y plane) is the reference;
- the vertical vanishing point is computed by intersecting vertical edges;
- the two sides of the rectangular base of the porch have been measured thus providing the position of four points on the reference plane. The world-to-image homography is computed from those points [24];
- the distance of the top of the frame of the window on the left from the ground has been measured on site and used as reference to compute α as in (5.6).
- the 3D position of the camera centre is then computed simply by applying equations (5.15). We obtain

$$X_c = -381.0cm \;\; Y_c = -653.7cm \;\; Z_c = 162.8cm$$

In figure 5.23c, the camera has been superimposed into a virtual view of the reconstructed scene.

5.4 Uncertainty analysis

Feature detection and extraction, whether manual or automatic (e.g. using an edge detector), can only be achieved to a finite accuracy. Any features extracted from an image, therefore, are subject to measurements errors. In this section we consider how these errors propagate through the measurement formulae in order to quantify the uncertainty on the final measurements [36]. This is achieved by using a first order error analysis (see section 3.6).

The uncertainty on the projection matrix is analysed first and then the uncertainty on distance measurements.

5.4.1 Uncertainty on the P matrix

The uncertainty in P depends on the location of the vanishing line, the location of the vanishing point, and on α, the affine scale factor. Since only the final two columns contribute, the uncertainty in P is modelled as a 6×6 homogeneous covariance matrix, $\Lambda_{\mathtt{P}}$. Since the two columns have only five degrees of freedom (two for $\mathbf{v}$, two for $\mathbf{l}$ and one for α), the covariance matrix is singular, with rank five.

Assuming statistical independence between the two column vectors $\mathbf{p}_3$ and $\mathbf{p}_4$ the 6×6 rank five covariance matrix $\Lambda_{\mathtt{P}}$ can be written as:

$$\Lambda_{\mathtt{P}} = \begin{pmatrix} \Lambda_{\mathbf{p}_3} & 0 \\ 0 & \Lambda_{\mathbf{p}_4} \end{pmatrix} \tag{5.18}$$

Furthermore, assuming statistical independence between α and $\mathbf{v}$, since $\mathbf{p}_3 = \alpha\mathbf{v}$:

$$\Lambda_{\mathbf{p}_3} = \alpha^2 \Lambda_{\mathbf{v}} + \sigma_\alpha^2 \mathbf{v}\mathbf{v}^\top \tag{5.19}$$

with $\Lambda_{\mathbf{v}}$ the homogeneous 3×3 covariance of the vanishing point $\mathbf{v}$, and the variance σ_α^2 computed as in appendix D.

Since $\mathbf{p}_4 = \bar{\mathbf{l}} = \frac{\mathbf{l}}{||\mathbf{l}||}$ its covariance is:

$$\Lambda_{\mathbf{p}_4} = \frac{\partial \mathbf{p}_4}{\partial \mathbf{l}} \Lambda_{\mathbf{l}} \frac{\partial \mathbf{p}_4}{\partial \mathbf{l}}^\top \tag{5.20}$$

where the 3×3 Jacobian $\frac{\partial \mathbf{p}_4}{\partial \mathbf{l}}$ is

$$\frac{\partial \mathbf{p}_4}{\partial \mathbf{l}} = \frac{\mathbf{l} \cdot \mathbf{l}\mathtt{I} - \mathbf{l}\mathbf{l}^\top}{(\mathbf{l} \cdot \mathbf{l})^{\frac{3}{2}}}$$

5.4.2 Uncertainty on measurements between planes

When making measurements between planes (5.7), uncertainty arises from the uncertain image locations of the points $\mathbf{x}$ and $\mathbf{x}'$ and from the uncertainty in P.

The uncertainty in the end points $\mathbf{x}$, $\mathbf{x}'$ of the length to be measured (resulting largely from the finite accuracy with which these features may be located in the image) is modeled by covariance matrices $\Lambda_{\mathbf{x}}$ and $\Lambda_{\mathbf{x}'}$.

Maximum likelihood estimation of the end points and uncertainties.

In this section the P matrix is assumed noise-free; this assumption is removed below (5.23).

Since in the error-free case, $\mathbf{x}$ and $\mathbf{x}'$ must be aligned with the vertical vanishing point $\mathbf{v}$ the Maximum Likelihood estimates ($\hat{\mathbf{x}}$ and $\hat{\mathbf{x}}'$) of their true locations can be determined by minimizing the sum of the Mahalanobis distances between the input points $\mathbf{x}$ and $\mathbf{x}'$ and their MLE estimates $\hat{\mathbf{x}}$ and $\hat{\mathbf{x}}'$

$$\min_{\hat{\mathbf{x}}_2, \hat{\mathbf{x}}'_2,} \left[(\mathbf{x}_2 - \hat{\mathbf{x}}_2)^\top \Lambda_{\mathbf{x}_2}^{-1} (\mathbf{x}_2 - \hat{\mathbf{x}}_2) + (\mathbf{x}'_2 - \hat{\mathbf{x}}'_2)^\top \Lambda_{\mathbf{x}'_2}^{-1} (\mathbf{x}'_2 - \hat{\mathbf{x}}'_2) \right] \tag{5.21}$$

subject to the *alignment constraint*

$$\mathbf{v} \cdot (\hat{\mathbf{x}} \times \hat{\mathbf{x}}') = 0 \tag{5.22}$$

(the subscript 2 indicates inhomogeneous 2-vectors).

This is a constrained minimization problem. A closed form solution can be found (by the Lagrange multiplier method) in the special case that

$$\Lambda_{\mathbf{x}'_2} = \gamma^2 \Lambda_{\mathbf{x}_2}$$

with γ a scalar, but, unfortunately, in the general case there is no closed form solution to the problem. Nevertheless, in the general case, an initial solution can be computed by using the approximation given in appendix B and then refining it by running a numerical algorithm such as Levenberg-Marquardt.

Once the MLE end points have been estimated, standard techniques [20, 36] are employed to obtain a first order approximation to the 4×4, rank-three covariance of the MLE 4-vector $\hat{\boldsymbol{\zeta}}^\top = (\hat{\mathbf{x}}_2'^\top \quad \hat{\mathbf{x}}_2^\top)$. Figure 5.14 illustrates the idea (see appendix C for details).

a b c

Figure 5.14: **Maximum Likelihood estimation of the end points:** (a) Original image (closeup of fig. 5.15). (b) The uncertainty ellipses of the end points, $\Lambda_{\mathbf{x}}$ and $\Lambda_{\mathbf{x}'}$, are shown. These ellipses are defined manually; they indicate a 3-standard deviation confidence region for localizing the points. (c) MLE end points $\hat{\mathbf{x}}$ and $\hat{\mathbf{x}}'$ are aligned with the vertical vanishing point (outside the image).

Uncertainty on distance measurements.

Assuming noise in both end points and projection matrix and statistical independence between $\hat{\boldsymbol{\zeta}}$ and $\mathtt{P}$ we obtain a first order approximation for the variance of the distance Z of a point from a plane:

$$\sigma_Z^2 = \boldsymbol{\nabla}_Z \begin{pmatrix} \Lambda_{\hat{\boldsymbol{\zeta}}} & 0 \\ 0 & \Lambda_{\mathtt{P}} \end{pmatrix} \boldsymbol{\nabla}_Z{}^\top \tag{5.23}$$

where $\boldsymbol{\nabla}_Z$ is the 1×10 ($\Lambda_{\hat{\boldsymbol{\zeta}}}$ is 4×4 and $\Lambda_{\mathtt{P}}$ is 6×6) Jacobian matrix of the function (5.7) which maps the projection matrix and the end points $\mathbf{x}$, $\mathbf{x}'$ to their world distance Z. The computation of $\boldsymbol{\nabla}_Z$ is explained in detail in appendix C.

5.4.3 Uncertainty on camera position

The distance of the camera centre from the reference plane is computed according to (5.17) which can be rewritten as:

$$Z_c = -(\mathbf{p}_4 \cdot \mathbf{p}_3)^{-1} \tag{5.24}$$

If an exact $\mathtt{P}$ matrix is assumed, then the camera distance is exact too, in fact it depends only on the matrix elements of $\mathtt{P}$. Similarly, the accuracy of Z_c depends only on the accuracy of the $\mathtt{P}$

matrix.

Equation (5.24) maps $\mathcal{R}^6$ into $\mathcal{R}$, and the associated 1×6 Jacobian matrix ∇Z_c is readily derived to be

$$\nabla Z_c = Z_c^2 \begin{pmatrix} \mathbf{p}_4^\top & \mathbf{p}_3^\top \end{pmatrix}$$

and, from a first order analysis the variance of Z_c is

$$\sigma_{Z_c}^2 = \nabla Z_c \Lambda_{\mathtt{P}} \nabla Z_c{}^\top \tag{5.25}$$

where $\Lambda_{\mathtt{P}}$ is computed in section 5.4.1.

The variances $\sigma_{X_c}^2$ and $\sigma_{Y_c}^2$ of the X, Y location of the camera can be computed in a similar way [24].

5.4.4 Example - uncertainty on measuring heights of people

In this section we show the effects of the number of reference distances and image localization error on the predicted uncertainty in measurements.

An image obtained from a poor quality security camera is shown in figure 5.15a. It has been corrected for radial distortion using the method described in section 3.4, and the floor taken as the reference plane. Vertical and horizontal lines are used to compute the P matrix of the scene. The vanishing line for the ground plane is shown in white at the top of each image.

The scene is calibrated by identifying two points $\mathbf{v}_1, \mathbf{v}_2$ on the reference plane's vanishing line (shown in white at the top of each image) and the vertical vanishing point $\mathbf{v}$. These points are computed by intersecting sets of parallel lines. The uncertainty on each point is assumed to be Gaussian and isotropic with standard deviation $0.1 pixels$. The uncertainty of the vanishing line is derived from a first order propagation through the vector product operation $\mathbf{l} = \mathbf{v}_1 \times \mathbf{v}_2$. The projection matrix P is therefore uncertain with its covariance given by (5.18).

In addition the end points of the height to be measured are assumed to be uncertain and their covariances estimated as in section 5.4.2. The uncertainties in the height measurements shown are

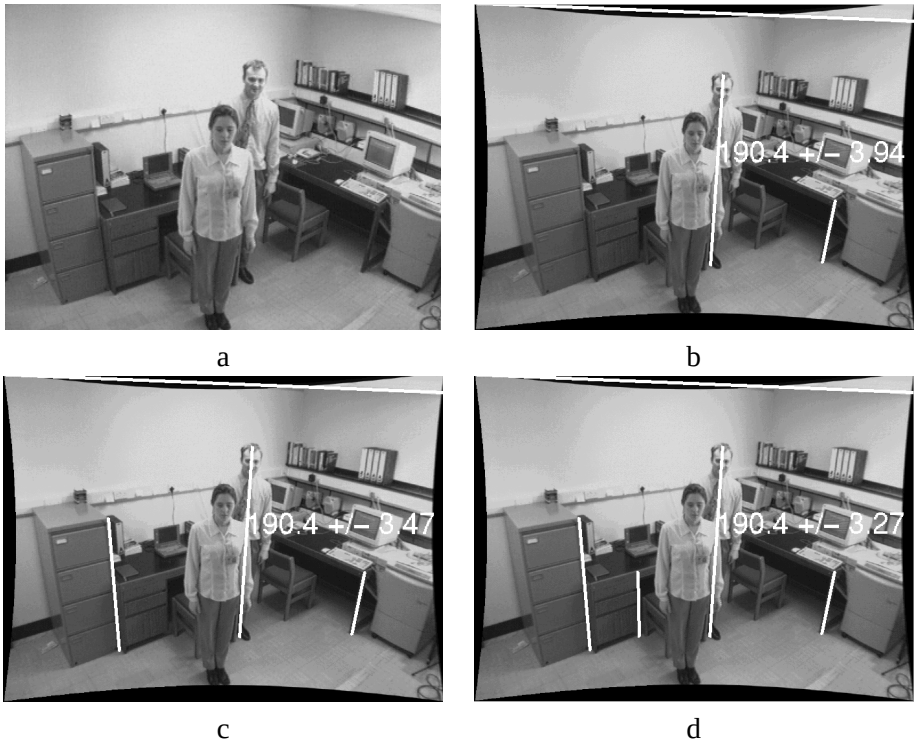

Figure 5.15: **Measuring heights and estimating their uncertainty:** (a) original image; (b) image corrected for radial distortion and measurements superimposed. With only *one* supplied reference height the man's height has been measured to be Z = 190.4 $\pm$ 3.94cm, (*cf.* ground truth value 190cm). The uncertainty has been estimated by using (5.23) (the uncertainty bound is at $\pm$ 3 std.dev.); (c) with *two* reference heights Z = 190.4 $\pm$ 3.47cm; (d) with *three* reference heights Z = 190.4 $\pm$ 3.27cm. In the limit $\Lambda_{\mathtt{P}} = \mathtt{0}$ (error-free P matrix) the height uncertainty reduces to 2.16cm for all (b,c,d); the residual error, in this case, is due only to the error on the two end points.

Figure 5.16: **Measuring heights and estimating their uncertainty, second point of view:** (a) original image; (b) the image has been corrected for radial distortion and height measurements computed and superimposed. With *one* supplied reference height Z = 190.2 $\pm$ 5.01cm (*cf.* ground truth value 190cm); (c) with *two* reference heights Z = 190.4 $\pm$ 3.34cm. See figure 5.15 for details.

computed as 3-standard deviation intervals.

In figure 5.15b one reference height is used to compute the affine scale factor α from (5.6) (i.e. the minimum number of references). Uncertainty has been assumed in the reference heights, vertical vanishing point and plane vanishing line. Once α is computed other measurements in the same direction are metric. The height of the man has been computed and shown in the figure. It differs by $4mm$ from the known true value.

The uncertainty associated with the height of the man is computed from (5.23) and displayed in figure 5.15b. Note that the true height value falls always within the computed 3-standard deviation range as expected.

As the number of reference distances is increased (see figures 5.15c,d), the uncertainty on $\mathtt{P}$ (in fact just on α) decreases, resulting in a decrease in uncertainty of the measured height, as theoretically expected (see appendix C for details). Equation (5.9) has been employed, here, to metric calibrate the distance from the floor.

Figure 5.16 shows images of the same scene with the same people, but acquired from a different point of view. As before the uncertainty on the measurements decreases as the number of references increases (fig. 5.16b,c). The measurement is the same as in the previous view (fig. 5.15) thus demonstrating invariance to camera location.

Figure 5.17 shows an example, where the height of the woman and the related uncertainty are computed for two different orientations of the uncertainty ellipses of the end points. In figure 5.17b the two input ellipses of figure 5.17a have been rotated by an angle of approximately 40^o, maintaining the size and position of the centres. The angle between the direction defined by the major axes (direction of maximum uncertainty) of each ellipse and the measuring direction is smaller than in fig. 5.17a and the uncertainty in the measurements greater as expected.

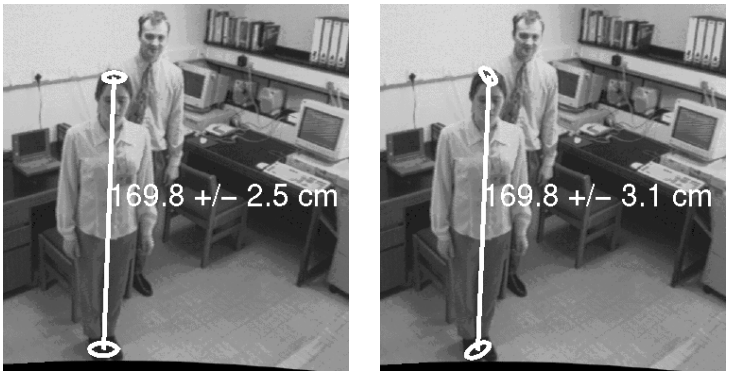

a b

Figure 5.17: **Estimating the uncertainty in height measurements for different orientations of the input 3-standard deviation uncertainty ellipses**: (a) cropped version of image 5.15b with measurements superimposed: Z = 169.8 $\pm$ 2.5cm (at 3-standard deviations). The ground truth is Z = 170cm, it lies within the computed range; (b) the input ellipses have been rotated keeping their size and position fixed: Z = 169.8 $\pm$ 3.1cm (at 3-standard deviations). The height measurement is less accurate.

5.4.5 Validation of uncertainty analysis

In this section the first order error analysis previously described is validated by computing the uncertainty of the height of the man in fig. 5.15e using Monte Carlo simulations as described in table 5.1 and comparing it to first order analytical result. Specifically, the statistical standard deviation of the man's height from a reference plane is computed and compared with the standard deviation obtained from the first order error analysis.

Uncertainty is modeled as Gaussian noise and described by covariance matrices (see section 3.6). Noise is assumed on the end points of the three reference distances and also on the vertical vanishing point, the plane vanishing line and on the end points of the height to be measured.

Figure 5.18 shows the results of the test. The base point is randomly distributed according to a 2D non-isotropic Gaussian about the mean location $\mathbf{x}$ (on the feet of the man in figure 5.15) with covariance matrix $\Lambda_{\mathbf{x}}$ (figure 5.18a). Similarly the top point is randomly distributed according to a 2D non-isotropic Gaussian about the mean location $\mathbf{x}'$ (on the head of the man in figure 5.15), with covariance $\Lambda_{\mathbf{x}'}$ (figure 5.18b).

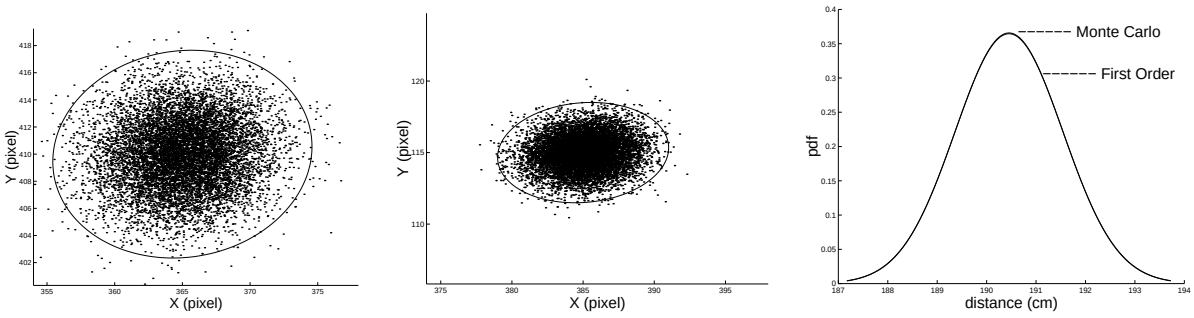

a b c

Figure 5.18: **Monte Carlo simulation of the example in fig. 5.15d:** (a) distribution of the input base point $\mathbf{x}$ and the corresponding 3-standard deviation ellipse; (b) distribution of the input top point $\mathbf{x}'$ and the corresponding 3-standard deviation ellipse. Figures (a) and (b) are drawn at the same scale; (c) the analytical and simulated distributions of the computed distance Z. The two curves are almost perfectly overlapping.

- for j=1 to N (with N = number of samples)
  - For each reference: given the measured reference end points $\mathbf{r}$ (on the reference plane) and $\mathbf{r}'$, generate a random base point $\mathbf{r}_j$, a random top point $\mathbf{r}'_j$ and a random reference distance $\mathbf{Z}_{r_j}$ according to the associated covariances.
  - Generate a random vanishing point according to its covariance $\Lambda_{\mathbf{v}}$.
  - Generate a random plane vanishing line according to its covariance $\Lambda_{\mathbf{l}}$.
  - Compute the α parameter by applying (5.9) to the references, and the current P matrix (5.3).
  - Generate a random base point $\mathbf{x}_j$ and a random top point $\mathbf{x}'_j$ for the distance to be computed according to their respective covariances $\Lambda_{\mathbf{x}}$ and $\Lambda_{\mathbf{x}'}$.
  - Project the points $\mathbf{x}_j$ and $\mathbf{x}'_j$ onto the best fitting line through the vanishing point (see sect. 5.4.2).
  - Compute the current distance Z_j by applying (5.7).
- The statistical standard deviation of the population of simulated Z_j values is computed as

$$\sigma'^2_Z = \frac{\sum_{j=1}^{N}(Z_j - \overline{Z})^2}{N-1}$$

and compared to the analytical one (5.23).

Table 5.1: **Monte Carlo simulation.**

The two covariance matrices are respectively:

$$\Lambda_{\mathbf{x}} = \begin{pmatrix} 10.18 & 0.59 \\ 0.59 & 6.52 \end{pmatrix} \quad \Lambda_{\mathbf{x}'} = \begin{pmatrix} 4.01 & 0.22 \\ 0.22 & 1.36 \end{pmatrix}$$

Suitable values for the covariances of the three references, the vanishing point and the vanishing line have been used. The simulation has been run with $N = 10000$ samples.

Analytical and simulated distributions of Z are plotted in figure 5.18c; the two curves are al-

most overlapping. Any slight difference is due to the assumptions of statistical independence (5.18, 5.19, 5.23) and first order truncation introduced by the error analysis.

A comparison between statistical and analytical standard deviations is reported in the table below with the corresponding relative error:

First Order σ_Z	Monte Carlo σ'_Z	relative error $\frac{\lvert\sigma_Z - \sigma'_Z\rvert}{\sigma'_Z}$
1.091 cm	1.087 cm	0.37 %

Note that $Z = 190.45$cm and the associated first order uncertainty $3 * \sigma_Z = 3.27$cm is shown in fig. 5.15d.

In the limit $\Lambda_{\mathtt{P}} = \mathtt{0}$ (error-free P matrix) the simulated and analytical results are even closer.

This result shows the validity of the first order approximation in this case and numerous other examples have followed the same pattern. However some care must be exercised since as the input uncertainty increases, not only does the output uncertainty increase, but the relative error between statistical and analytical output standard deviations also increases. For large covariances, the assumption of linearity is poorly founded; therefore the first order analysis no longer holds.

This is illustrated in the table below where the relative error is shown for various increasing values of the input uncertainties. The uncertainties of references distances and end points are multiplied by the increasing factor γ; for instance, if $\Lambda_{\mathbf{x}}$ is the covariance of the image point $\mathbf{x}$ then $\Lambda_{\mathbf{x}}(\gamma) = \gamma^2 \Lambda_{\mathbf{x}}$.

γ	1	5	10	20	30
$\frac{\lvert\sigma_Z - \sigma'_Z\rvert}{\sigma'_Z}(\%)$	0.37	1.68	3.15	8.71	16.95

In the *affine case* (when the vertical vanishing point and the plane vanishing line are at infinity) the first order error propagation is exact (no longer just an approximation as in the general projective case), the analytic and Monte Carlo simulation results coincide.

5.5 Three-dimensional metrology from a single view

This section describes a very simple but effective generalization of the theory described above.

The single view techniques for measuring distances between two planes in a pencil are extended to making full 3D measurements in the observed scene. The key idea is a new description of the 3D space as a collection of three pencils of parallel planes in three different directions [7]. That leads to a complete 3D reconstruction from single images.

5.5.1 The 3D space as a collection of pencils of parallel planes

If $\mathbf{v}_x$, $\mathbf{v}_y$ and $\mathbf{v}_z$ are the three vanishing points (with unit third coordinate) for three directions in space (not necessarily orthogonal to each other) and $\mathbf{o}$ is the origin of the image coordinate system, then the $\mathbf{P}$ matrix can be written as [36]:

$$\mathtt{P} = \left[\begin{array}{cccc} \alpha_x \mathbf{v}_x & \alpha_y \mathbf{v}_y & \alpha_z \mathbf{v}_z & \mathbf{o} \end{array} \right] \tag{5.26}$$

with $\alpha_x, \alpha_y, \alpha_z$ three unknown scale factors.

Equation (5.26) generalises (5.3) and allows us to extend the theory discussed in section 5.3 to parametrizing the space as *three* pencils of planes rather than only one. Measurements can now be computed in three directions thus specifying complete 3D affine position of world points.

As explained in section 5.3 attention must be paid to the fact that the image point $\mathbf{o}$ can be chosen arbitrarily but, in order to avoid degeneracies in the parametrization, it must not lie on any of the three vanishing lines identified by the three vanishing points $\mathbf{v}_x$, $\mathbf{v}_y$, $\mathbf{v}_z$, i.e.

$$\mathbf{o} \cdot (\mathbf{v}_i \times \mathbf{v}_j) \neq 0 \qquad \forall i, j = x, y, z$$

A possible choice of the point $\mathbf{o}$ may then be the average (centre of mass) of the three vanishing points in homogeneous coordinates:

$$\mathbf{o} = \frac{\sum_{i=x,y,z} \mathbf{v}_i}{3}$$

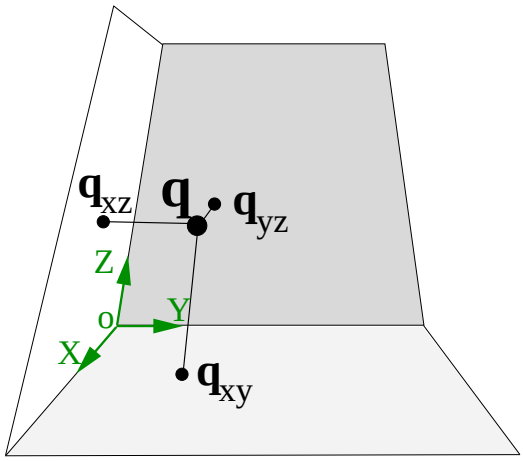

Figure 5.19: **Complete affine 3D reconstruction from single images:** The 3D space is parametrized as three pencils of parallel planes (only one plane for each pencil is shown, the three pencils do not need to be orthogonal to each other). The location of a world point $\mathbf{Q}$ can be computed by applying (5.27) (see also (5.6)).

5.5.2 3D location of points

Generalizing (5.6) the X, Y, Z location of a 3D point $\mathbf{Q}$ may be computed from single images applying the following formulae (see fig. 5.19):

$$\begin{aligned} \alpha_x X &= -\frac{\mathbf{o}\cdot\mathbf{l}_{yz}}{\mathbf{q}_{yz}\cdot\mathbf{l}_{yz}}\frac{||\mathbf{q}_{yz}\times\mathbf{q}||}{||\mathbf{v}_x\times\mathbf{q}||} \\ \alpha_y Y &= -\frac{\mathbf{o}\cdot\mathbf{l}_{xz}}{\mathbf{q}_{xz}\cdot\mathbf{l}_{xz}}\frac{||\mathbf{q}_{xz}\times\mathbf{q}||}{||\mathbf{v}_y\times\mathbf{q}||} \\ \alpha_z Z &= -\frac{\mathbf{o}\cdot\mathbf{l}_{xy}}{\mathbf{q}_{xy}\cdot\mathbf{l}_{xy}}\frac{||\mathbf{q}_{xy}\times\mathbf{q}||}{||\mathbf{v}_z\times\mathbf{q}||} \end{aligned} \tag{5.27}$$

Where $\mathbf{q}$ is the image of the world point $\mathbf{Q}$, $\mathbf{l}_{ij} = \mathbf{v}_i \times \mathbf{v}_j$ and $\mathbf{q}_{ij}$ is the intersection of the plane spanned by the axis i and j with the line through $\mathbf{Q}$ parallel to the direction k ($\forall i, j, k = x, y, z$). If the α_i parameters are known then metric structure can be computed for the point $\mathbf{Q}$; otherwise only affine structure can be obtained.

Only one of the points $\mathbf{q}_{xy}$, $\mathbf{q}_{yz}$ and $\mathbf{q}_{xz}$ is necessary

In images of real scenes it is quite rare to find a situation in which the three base points $\mathbf{q}_{xy}$, $\mathbf{q}_{yz}$ and $\mathbf{q}_{xz}$ are all visible. We now show that only one of those points needs to be known and that

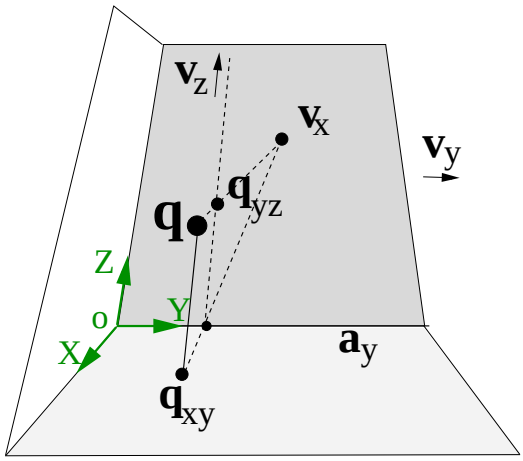

Figure 5.20: **Geometric construction of the point $\mathbf{q}_{yz}$:** the points $\mathbf{q}$, $\mathbf{q}_{xy}$, $\mathbf{v}_x$, $\mathbf{v}_z$ and the line $\mathbf{a}_y$ are known and the point $\mathbf{q}_{yz}$ is constructed by lines intersections. Similar construction applies for the point $\mathbf{q}_{xz}$.

the other two can be computed.

For instance, it is easy to prove that if $\mathbf{q}_{xy}$ is known and $\mathbf{a}_x$ and $\mathbf{a}_y$ are the images of the chosen world coordinates axes X and Y respectively then:

$$\mathbf{q}_{yz} = (\mathbf{q} \times \mathbf{v}_x) \times (\mathbf{v}_z \times (\mathbf{a}_y \times (\mathbf{q}_{xy} \times \mathbf{v}_x))) \tag{5.28}$$

$$\mathbf{q}_{xz} = (\mathbf{q} \times \mathbf{v}_y) \times (\mathbf{v}_z \times (\mathbf{a}_x \times (\mathbf{q}_{xy} \times \mathbf{v}_y))) \tag{5.29}$$

The image points $\mathbf{q}_{yz}$ and $\mathbf{q}_{xz}$ can also be constructed geometrically as illustrated in figure 5.20. These operations correspond, in the world, to parallel projections of the 3D point $\mathbf{Q}$ into the plane YZ along the X-direction in (5.28); into the plane XZ along the Y-direction in (5.29). Symmetrical formulae can be derived in the cases $\mathbf{q}_{yz}$ or $\mathbf{q}_{xz}$ are known.

Equations (5.28), (5.29) (or the symmetrical ones) may be substituted in (5.27) to obtain formulae which depend on one base point only.

5.5.3 3D location of the camera

Equations (5.15) to compute the camera location still hold. But they can be rewritten at the light of this new parametrization, in the case of unknown α parameters as:

$$\alpha_x X_c = -\det\begin{bmatrix} \mathbf{v}_y & \mathbf{v}_z & \mathbf{p}_4 \end{bmatrix}, \quad \alpha_y Y_c = \det\begin{bmatrix} \mathbf{v}_x & \mathbf{v}_z & \mathbf{p}_4 \end{bmatrix},$$

$$\alpha_z Z_c = -\det\begin{bmatrix} \mathbf{v}_x & \mathbf{v}_y & \mathbf{p}_4 \end{bmatrix}, \; W_c = \det\begin{bmatrix} \mathbf{v}_x & \mathbf{v}_y & \mathbf{v}_z \end{bmatrix} \tag{5.30}$$

and thus the affine location of the camera centre is computed. As before, metric structure is obtained if the α parameters are known.

5.5.4 Camera calibration

Given a world coordinate system XYZ with origin in **O** and an image coordinate system xy. If we know the three vanishing points for the X, Y and Z directions and at least one world distance measurement along each direction, by applying (5.27) the three calibration parameters α_i can be computed (see section 5.3.1). We can choose the origin **o** to be the image of **O** and from (5.26) the full world-to-image projection matrix `P` is determined and the scene calibrated. In fact the origin **o** and each vanishing point provide 2 d.o.f. The three scalars α_i provide 3 more d.o.f for a total of 11 independent degrees of freedom. Full external camera calibration is, therefore, obtained from a single image.

Once the scene has been calibrated metric structure of points and cameras can be recovered from (5.27) and (5.30) respectively. Moreover the three image-to-world homographies for each of the planes can be extracted directly from (5.26).

If the homography between a world plane (e.g. the plane x, y) and the image is known, then only the α parameter for the direction not on that plane (e.g. α_z) must be known to compute a complete metric 3D reconstruction, since computing the two remaining calibration parameters (α_x and α_y) from the known homography is straightforward.

Partial calibration. There may be situations where only some of the calibration parameters α are known. In that case we obtain an intermediate, *partially affine* and *partially metric* structure. Partial calibration leads to a partial reconstruction of the scene. For instance, the situation analysed in section 5.3.2 is characterized by affine calibration on the plane and metric off the plane (if α is known). That has been sufficient to compute metric distances from the reference plane (and only affine measurements on the plane).

The theory developed in section 5.3.1 concerning the use of homologies to transfer measurements and points from one plane to a parallel one, and in section 5.4 concerning the uncertainty analysis on distances between planes still apply with the necessary attention to which pencil of planes is currently under investigation.

5.6 Applications

The validity of the metrology algorithm presented is demonstrated in this section with a number of practical applications.

5.6.1 Forensic science

A common requirement in surveillance images is to obtain measurements from the scene, such as the height of a suspect. Although, the suspect has usually departed the scene, reference lengths can be measured from fixtures such as tables and windows.

Figure 5.21 illustrates the computation of the height of the person standing next to a phone box. The ground is the reference plane and the vertical is the reference direction. The edges of the paving stones are used to compute the plane vanishing line, the edges of the phone box to compute the vertical vanishing point and the height of the phone box provides the metric calibration in the vertical direction (figure 5.21b). Only one reference height (minimal set) has been used in this example. The height of the person is then computed using (5.7) and shown in figure 5.21c. The

a b c

Figure 5.21: **The height of a person standing by a phonebox is computed**: (a) original image; (b) the ground plane is the reference plane, and its vanishing line is computed from the paving stones on the floor. The vertical vanishing point is computed from the edges of the phonebox, whose height is known and used as reference. Vanishing line and reference height are shown; (c) the computed height of the person and the estimated uncertainty are shown. The veridical height is 187cm, note that the person is leaning slightly on his right foot.

ground truth is 187cm, notice that the person is leaning slightly down on his right foot.

The associated uncertainty has also been estimated; two uncertainty ellipses have been defined manually, one on the head of the person and one on the feet and then propagated across the chain of computations as described in section 5.4 to give the 2.2cm 3-standard deviation uncertainty range shown in figure 5.21c.

5.6.2 Furniture measurements

In this section another application is described. Heights of furniture like shelves, tables or windows in an indoor environment are measured.

Figure 5.22a shows a desk in The Queen's College upper library in Oxford. The floor is the reference plane and its vanishing line has been computed by intersecting edges of the floorboards. The vertical vanishing point has been computed by intersecting the vertical edges of the bookshelf. The vanishing line is shown in figure 5.22b with the reference height used.

The computed heights and associated uncertainties are shown in figure 5.22c. The uncertainty

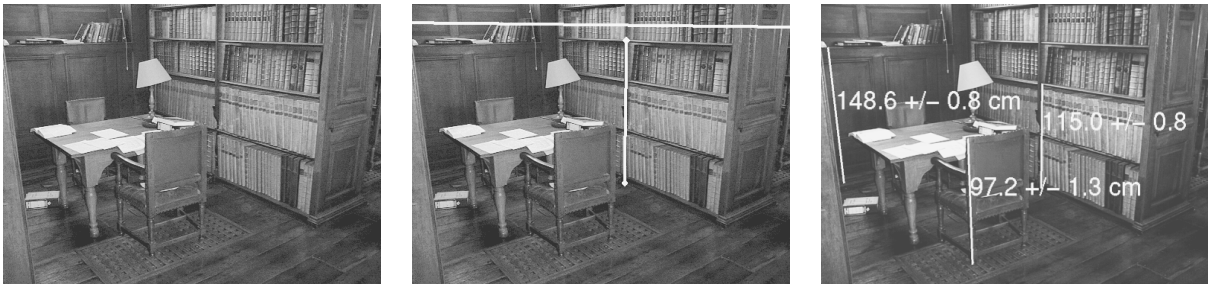

a b c

Figure 5.22: **Measuring height of furniture in The Queen's College Upper Library, Oxford**: (a) original image; (b) the plane vanishing line (white horizontal line) and reference height (white vertical line) are superimposed on the original image; the marked shelf is 156cm high; (c) computed heights and related uncertainties; the uncertainty bound is at $\pm 3 std.dev$. The ground truth is: 115cm for the right hand shelf, 97cm for the chair and 149cm for the shelf on the left. Observe that the ground truth always falls within the computed uncertainty range.

bound is ± 3 standard deviations. Note that the ground truth always falls within the computed uncertainty range. The height of the camera is computed as $1.71m$ from the floor.

5.6.3 Virtual modelling

Figure 5.23 shows an example of complete 3D reconstruction of a real scene from single image. Two sets of horizontal edges are used to compute the vanishing line for the ground plane, and vertical edges used to compute the vertical vanishing point.

The height of the window frame, and the height of one of the pillars are used as reference heights. Furthermore the two sides of the base of the porch have been measured thus defining the metric calibration of the ground plane.

Figure 5.23b shows a view of the reconstructed model. The person is represented as a flat silhouette since it is not possible to recover volume from one image only. The position of the camera centre is also estimated and superimposed on a different view of the 3D model in figure 5.23c.

5.6.4 Modelling paintings

Figure 5.24 shows a masterpiece of Italian Renaissance painting, *La Flagellazione di Cristo* by Piero della Francesca (1416 - 1492). The painting, thanks to the artist's famous mathematical skills [30],

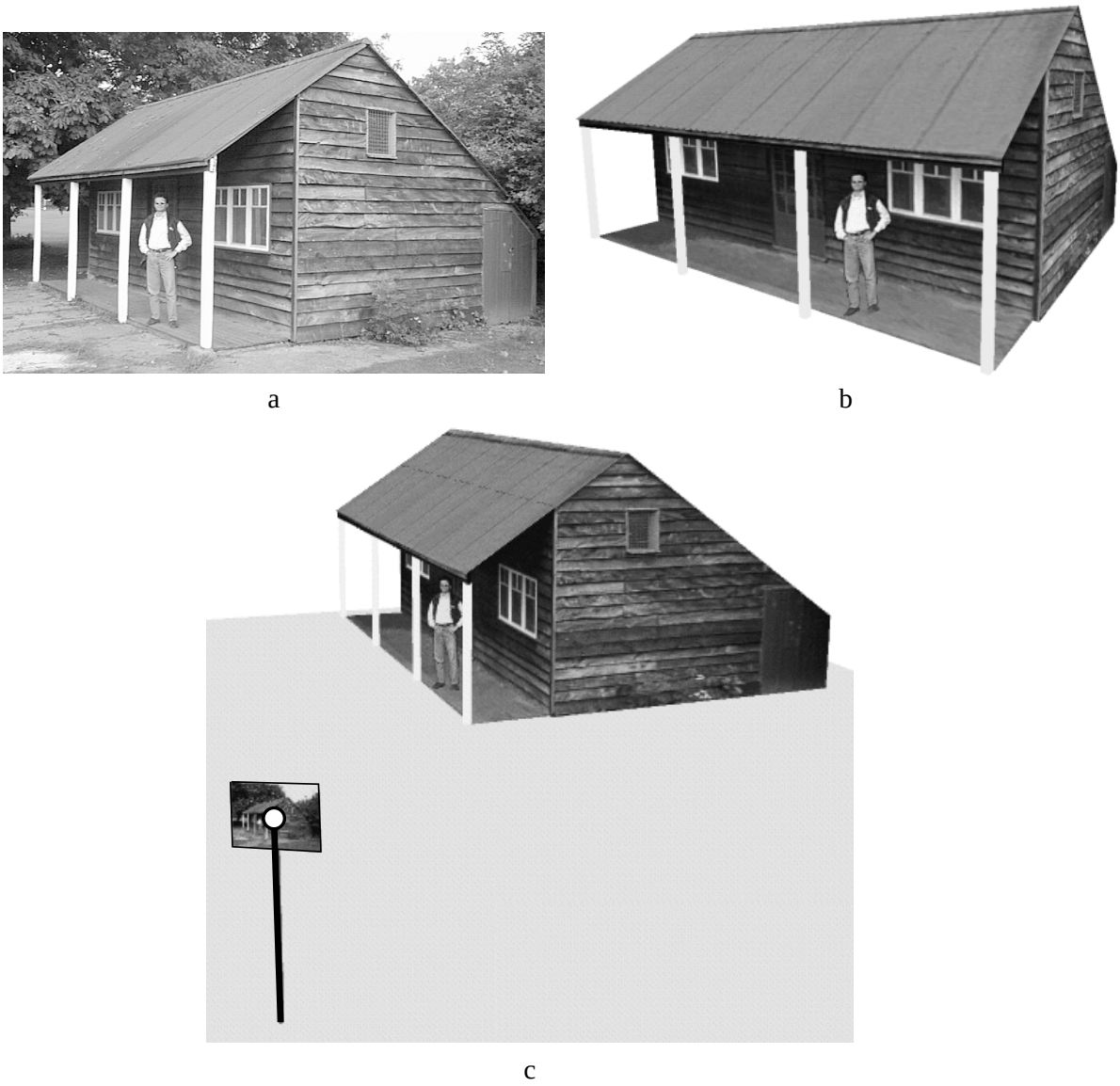

a b c

Figure 5.23: **Complete 3D reconstruction of a real scene**: (a) original image; (b) a view of the reconstructed 3D model; (c) a view of the reconstructed 3D model which shows the camera position and height with respect to the scene.

faithfully follows the geometric rules of linear perspective, and therefore the techniques described can be applied to compute the structure of the scene.

Unlike other techniques [56] whose main aim is to create convincing new views of the painting regardless of the correctness of the 3D geometry, here a geometrically correct 3D model of the

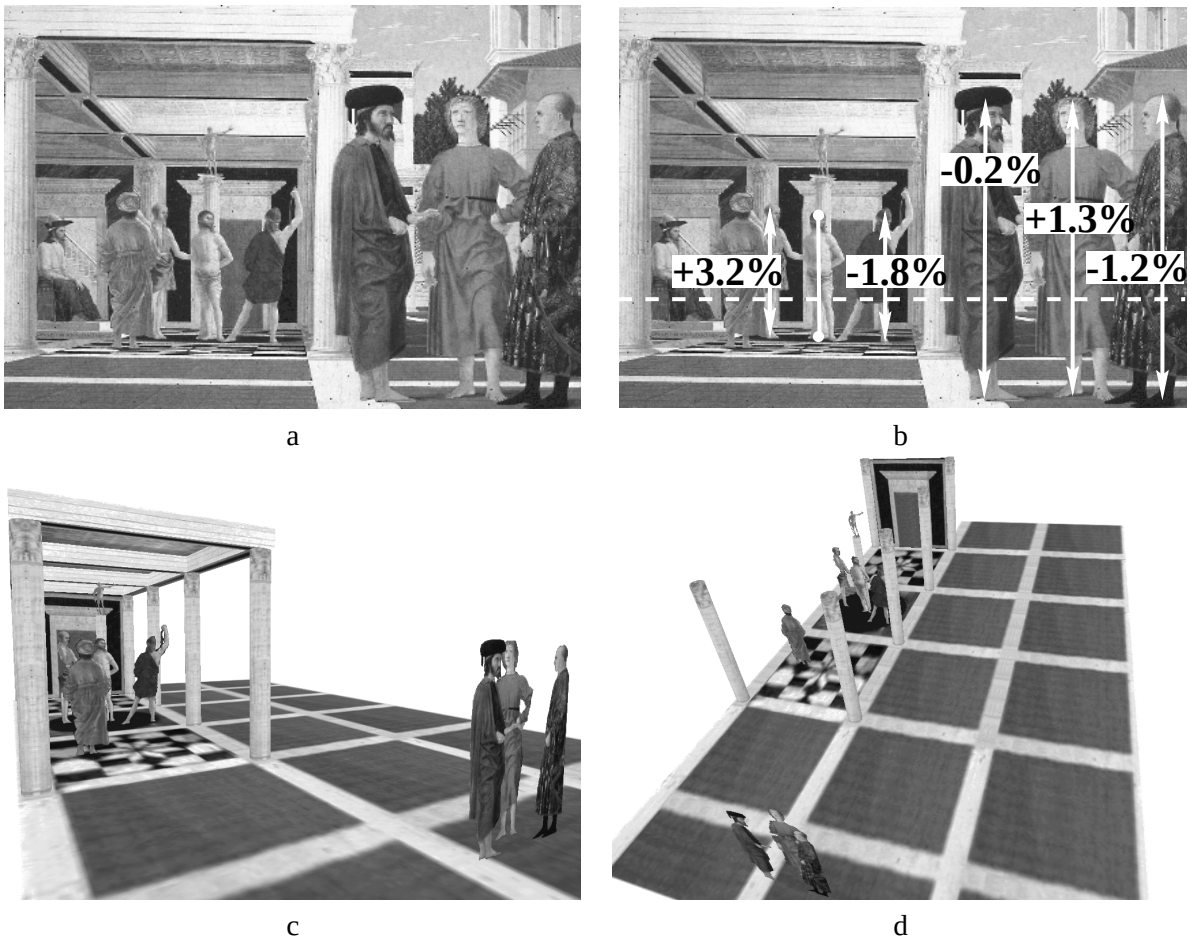

Figure 5.24: **Complete 3D reconstruction of a Renaissance painting**: (a) *La Flagellazione di Cristo*, (1460, Urbino, Galleria Nazionale delle Marche); (b) height measurements are superimposed on the original image. Christ's height is taken as reference and the heights of all the other people are expressed as percent differences. The vanishing line is dashed; (c) a view of the reconstructed 3D model. The patterned floor has been reconstructed in areas where it is occluded by taking advantage of the symmetry of its pattern; (d) another view of the model with the roof removed to show the relative positions of people and architectural elements in the scene. Note the repeated geometric pattern on the floor in the area delimited by the columns (barely visible in the painting). Note that the people are represented simply as flat silhouettes since it is not possible to recover their volume from one image, they have been cut out manually from the original image. The columns have been approximated with cylinders.

viewed scene is reconstructed (see fig. 5.24c,d).

In the painting analysed here, the ground plane is chosen as reference and its vanishing line computed from the several parallel lines on it. The vertical vanishing point follows from the vertical lines and consequently the relative heights of people and columns is defined. Figure 5.24b shows the painting with height measurements superimposed. Christ's height is taken as reference and the heights of the other people are expressed as relative percentage differences. Notice the consistency between the height of the people in the foreground with the height of the people in the background.

By assuming a square floor pattern the ground plane is rectified and the position of each object estimated [24, 74]. The scale of the floor relative to heights is set from the ratio between height and base of the frontoparallel archway. The measurements, up to an overall scale factor are used to compute a three dimensional model of the scene (scaled Euclidean structure).

Figure 5.24c shows a view of the reconstructed model. The people are represented, again, as flat silhouettes. The columns have been approximated with cylinders. The partially seen ceiling has been reconstructed correctly. Figure 5.24d shows a different view of the reconstructed model, where the roof has been removed to show the relative position of the people in the scene.

5.7 Missing base point

A restriction of the single-view measurement algorithm presented in this chapter is the need to identify corresponding points between planes.

The problem. One case where the method does not apply, therefore, is that of measuring the distance of a general 3D point to a reference plane where the corresponding point on the floor in undefined (see fig. 5.25). Here the homology is under-determined, and the line joining the image of this point with the vertical reference vanishing direction gives the locus of points which may correspond (therefore an uncertainty range for the height may still be computed).

a b

Figure 5.25: **Single view metrology cannot be applied when the base point is not defined:** (a) original image: the lectern in The Queen's College chapel; (b) we want to measure the distance of the beak of the eagle from the floor, but the intersection of the ground plane with the vertical through the tip of the beak is not defined and therefore the single view metrology cannot be applied.

Possible solutions. A second view provides another locus, and the intersection of these loci in either view (transferred by the inter-image homography induced by the reference plane) uniquely defines the corresponding point on the reference plane. This construction was used in [95] to determine the vertical projection of a football onto the ground plane (see also [98] for a similar construction). The distance may then be computed as described in the main body of this chapter, or by using more direct formulae developed in the next chapter (see also [59]).

Here one intermediate case of interest is explored; when only one view is provided and a light-source casts shadows onto the reference plane. The light-source provides restrictions analogous to a second viewpoint [122], thus the projection (in the reference direction) of the 3D point onto the reference plane may be determined as the intersection of a pair of one-dimensional loci (fig. 5.26). In [96] this method was used to compute the trajectory of a football.

5.7.1 Using shadows

We wish to compute the distance of a 3D point $\mathbf{X}$ from a reference plane π but the intersection of the vertical line through $\mathbf{X}$ with the plane (base point $\mathbf{X}'$) is not defined. (figure 5.26a shows a schematic of the described situation as it appears on an image). Therefore the single view metrology

algorithm is no use unless the image base point $\mathbf{x}'$ can be computed.

A reference height needs to be considered where top and base points can be identified (figure 5.26a). The light source $\mathbf{s}$ casts a shadow $\mathbf{x}_s$ on the reference plane for the point $\mathbf{x}$ and similarly it casts a shadow $\mathbf{r}_s$ for the reference point $\mathbf{r}$. The point $\mathbf{r}'$ corresponds to $\mathbf{r}$ along the reference direction.

By representing points as homogeneous 3-vectors the intersection of the line $< \mathbf{XR} >$ in space with the plane $\boldsymbol{\pi}$ can be computed in the image as $\mathbf{p} = (\mathbf{x} \times \mathbf{r}) \times (\mathbf{x}_s \times \mathbf{r}_s)$ (referred to as the *piercing point*, see fig. 5.26b). If we assume light source at infinity then the two shadow lines $< \mathbf{R}'\mathbf{R}_s >$ and $< \mathbf{X}'\mathbf{X}_s >$ are parallel to each other in space and the point $\mathbf{v}_h$ is the vanishing point of their direction. The point $\mathbf{v}_h$ can be computed by intersecting the reference shadow line and the vanishing line: $\mathbf{v}_h = (\mathbf{r}_s \times \mathbf{r}') \times \mathbf{l}$. Therefore the image point $\mathbf{x}'$ on the plane $\boldsymbol{\pi}$ can be computed as $\mathbf{x}' = (\mathbf{x}_s \times \mathbf{v}_h) \times (\mathbf{p} \times \mathbf{r}')$. The algorithm described in section 5.3.1 may, now, be applied to compute the world distance between $\mathbf{x}$ and $\mathbf{x}'$. Furthermore, the vanishing point $\mathbf{v}$ for the reference direction may be computed as $\mathbf{v} = (\mathbf{r} \times \mathbf{r}') \times (\mathbf{x} \times \mathbf{x}')$.

The described configuration is analogous to the case of having one perspective and one affine camera described by Zhang *et al.* in [130].

Planar homology. It is interesting to notice that the two triangles $\mathbf{r}, \mathbf{r}', \mathbf{r}_s$ and $\mathbf{x}, \mathbf{x}', \mathbf{x}_s$ are in a Desargues configuration and therefore they are related by a planar homology whose vertex is the piercing point and the axis is the line $< \mathbf{sv}_h >$ (figure 5.26c). Therefore, an alternative, algebraic way to compute the point $\mathbf{x}'$ is:

- estimating the homology $\mathtt{H}$ from its vertex (the point $\mathbf{p}$), axis (the line $< \mathbf{sv}_h >$) and a pair of corresponding points (e.g. $\mathbf{r}, \mathbf{x}$ or $\mathbf{r}_s, \mathbf{x}_s$) by applying (3.4);

- computing the base point $\mathbf{x}'$ from the homology projection:

$$\mathbf{x}' = \mathtt{H}\mathbf{r}' \tag{5.31}$$

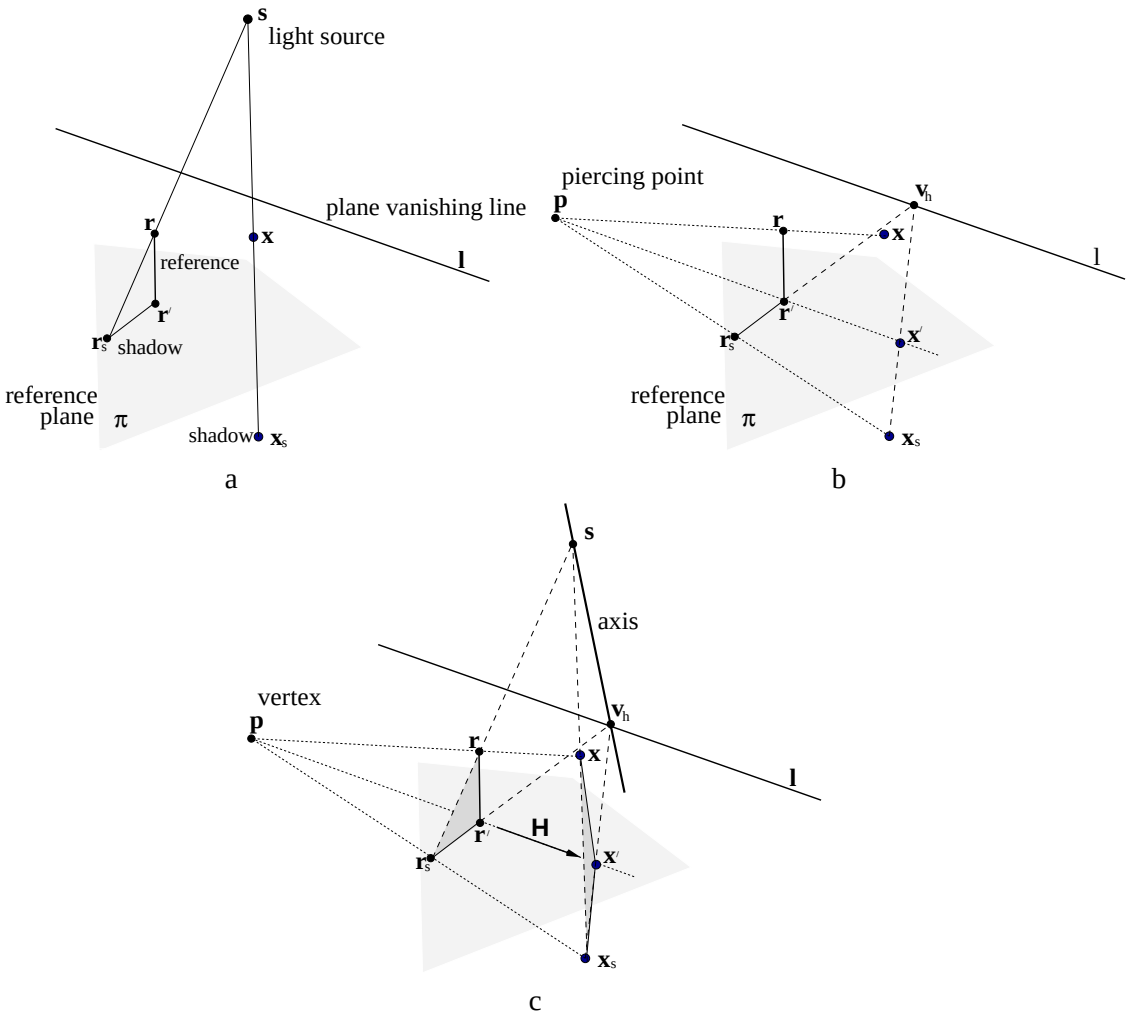

Figure 5.26: **Using shadows to compute distances in single views:** (a) we wish to compute the distance of the point $\mathbf{x}$ from the plane $\boldsymbol{\pi}$ but the base point is not defined. The reference point $\mathbf{r}$ (off the plane) and its base $\mathbf{r}'$ (on the plane) correspond along the reference direction. The light source $\mathbf{s}$ (at infinity) casts the shadow points $\mathbf{r}_s$ and $\mathbf{x}_s$ onto the reference plane; (b) the position of the base point $\mathbf{x}'$ is computed by making use of the shadows on the plane $\boldsymbol{\pi}$ (see text); (c) the two triangles $\mathbf{r}, \mathbf{r}', \mathbf{r}_s$ and $\mathbf{x}, \mathbf{x}', \mathbf{x}_s$ are related by a planar homology $\mathbf{H}$. The piercing point $\mathbf{p}$ (image of the intersection of the line $< \mathbf{XR} >$ with the plane $\boldsymbol{\pi}$) is its vertex and the line joining the points $\mathbf{s}$ and $\mathbf{v}_h$ its axis.

From Desargues theorem the vanishing point $\mathbf{v}$ for the reference direction lies on the axis of the homology, too: $\mathbf{v} \cdot (\mathbf{s} \times \mathbf{v}_h) = 0$. Often both $\mathbf{v}$ and $\mathbf{s}$ are known. In this case the position of the point $\mathbf{x}'$ is over-determined and it can be computed employing a MLE algorithm.

The case of finite light source. In the case where the light source is finite then the two shadow lines $< \mathbf{R}'\mathbf{R}_s >$ and $< \mathbf{X}'\mathbf{X}_s >$ are no longer parallel to each other and therefore the vanishing point $\mathbf{v}_h$ cannot be computed.

Nevertheless if the vertical vanishing point $\mathbf{v}$ for the reference direction is known then the axis of the homology is still defined: $\mathbf{a} = \mathbf{v} \times \mathbf{s}$; and the homology $\mathtt{H}$ can be computed. Hence the point $\mathbf{x}'$ can be computed from (5.31). Computing the world distance of $\mathbf{x}'$ from the reference plane is now straightforward.

Chapter 6

Metrology from planar parallax

6.1 Introduction

This chapter explores the geometry of two and three views in a *plane-plus-parallax* framework. Algorithms for structure and camera computation are developed and the results compared with the single view metrology described in the previous chapter (see also [23]; similar, independent work can be found in [59]).

In particular, we address the problem of computing distances of points from planes when the intersection of the plane with the line through the point parallel to the reference direction is not defined (see fig. 5.25). In such a case the single view metrology approach is not sufficient. In section 5.7 we have shown how to overcome the problem when a light source casts a shadow onto a plane. In the case where no shadows can be detected then one more view provides the solution.

The plane-plus-points configuration has received significant attention in the past, not least because it arises frequently in everyday scenes. A useful and popular approach to the problem decomposes the image motion into a planar homographic transfer plus a residual image parallax vector [58, 59, 69, 100]. This decomposition has the advantage that it partially factors out dependence on the camera relative rotation and internal parameters.

In recent work Carlsson and Weinshall *et al.* [13, 14, 125, 127] have demonstrated the fundamental duality of the 3D reconstruction problem. They show that for points and cameras in *general position,* the problem of computing camera locations from n points in m views is mathematically equivalent to the problem of reconstructing $m + 4$ points in $n - 4$ views. This chapter analyzes, in

m views	n pts	general position	coplanar
2	7	$3n+7 = 28 d.o.f.$ $2mn = 28 constraints$ F determined up to a 3-fold ambiguity no further constraints	$3n-1+7 = 27 d.o.f.$ $2mn = 28 constraints$ F determined uniquely motion constraint (one) in addition $\exists$ *homology*: maps between views, *vertex* is epipole, i.e. intersection of plane and camera baseline, *axis* is intersection of plane with plane containing remaining three points.
3	6	$3n+18 = 36 d.o.f.$ $2mn = 36 constraints$ T determined up to a 3-fold ambiguity no further constraints	$3n-1+18 = 35 d.o.f.$ $2mn = 36 constraints$ T determined uniquely structure constraint (one) in addition $\exists$ *homology*: maps between points, *vertex* is intersection of plane and line joining the remaining two points, *axis* is intersection of plane and plane containing the camera centres.

Table 6.1: **Camera/point duality results** for (i) points in general position and (ii) four points lying on a distinguished plane. The fundamental matrix F has 7 degrees of freedom and the trifocal tensor T has 18 d.o.f.

particular, the geometry of two views of seven points, four of which are coplanar, and the geometry of three views of six points, four of which are coplanar. We also prove that the two configurations are dual, and that the fundamental geometric constraints in each case are encapsulated by a planar homology [101, 121]. A summary of the duality results contrasted with the general position cases is shown in table 6.1.

The work here unifies a number of previously diverse results related to planar parallax [58, 69, 100], duality [13, 14, 125, 127] and planar homologies [121].

Formulae for computing the distance of the cameras from a distinguished world plane and formulae for structure computations, and associated uncertainty are presented in the second part of

this chapter where also the trifocal tensor [53, 106, 111] is derived in the plane-plus-points case, showing that it is obtained uniquely. Structure and camera computations are obtained directly from image measurements, i.e. the parallax vectors, *without* needing to compute the epipolar geometry.

The remainder of the chapter is organised as follows. We begin with a discussion of background material, notation and parallax geometry. Then the geometry of two views, seven points, four of which are coplanar is described. We show that there exists a homology on the plane relating the two views and derive necessary conditions for the homology directly in terms of the parallax measurements. Section 6.3.2 shows the duality of the geometry of three views, six points to the two view, seven point case, and hence obtain analogous necessary conditions. We also derive the trifocal tensor and show that it is over-constrained. Section 6.4 derives expressions for the distance of the cameras from the distinguished plane and the structure of points in terms of affine invariants and we show how the plane-plus-parallax geometry can be employed to compute the line of intersection between two planes. An uncertainty analysis on those measurements is performed in section 6.5 to estimate the confidence interval around each distance measurement. This analysis is validated, once more, by comparing the results to Monte Carlo statistical tests. Several examples on real images are presented.

6.2 Background

6.2.1 Notation

The area of a triangle with general vertices $\mathbf{a}$, $\mathbf{b}$, and $\mathbf{c}$ is denoted $A_{\mathbf{abc}}$, and can be determined via the formula $A_{\mathbf{abc}} = \frac{1}{2}|\mathbf{abc}|$ where the points $\mathbf{a}$, $\mathbf{b}$, and $\mathbf{c}$ are represented as homogeneous 3-vectors with last component equal to one.

Numbered subscripts are used to distinguish different views, with the first camera centre given by $\mathbf{O}_1$, the second by $\mathbf{O}_2$ and the third by $\mathbf{O}_3$. The projection of an image point onto the distinguished world plane from the ith view is denoted $\mathbf{p}_i$.

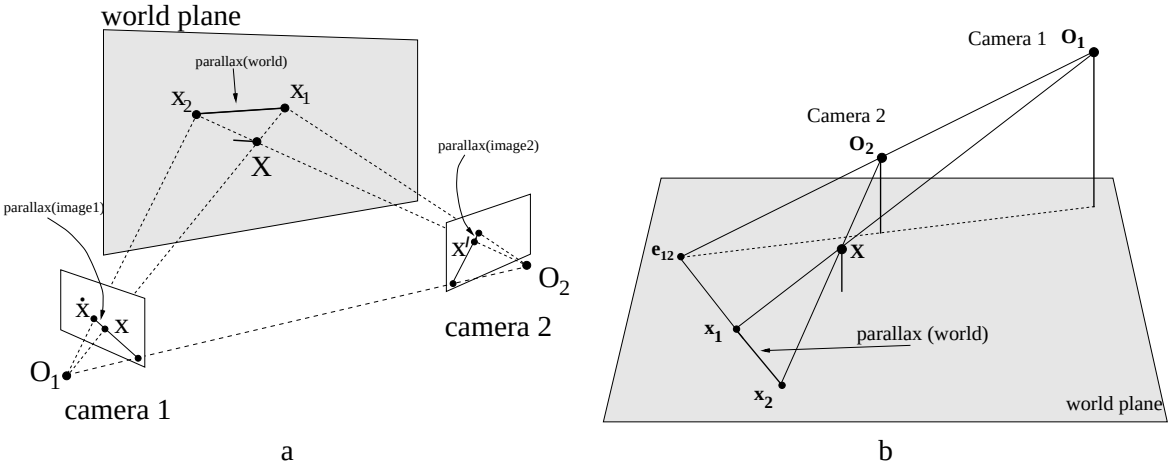

Figure 6.1: **Parallax geometry:** (a) general configuration; (b) viewed on the distinguished plane. The parallax vector $< \mathbf{x}_1\mathbf{x}_2 >$ passes through the epipole $\mathbf{e}_{12}$.

Superscripts identify projections of a 3D point onto different views, thus the 3D point $\mathbf{X}$ is imaged as $\mathbf{x}$ in the first image, $\mathbf{x}'$ in the second and $\mathbf{x}''$ in the third. The symbols ‘ ˙ ’ and ‘ ¨ ’ indicate the homographic projection of a point from the second or third image into the first one, respectively; thus $\dot{\mathbf{x}} = \mathtt{H}_{21}\mathbf{x}'$ and $\ddot{\mathbf{x}} = \mathtt{H}_{31}\mathbf{x}''$ where $\mathtt{H}_{21}$ is the homography that maps points from the second image onto the first one and $\mathtt{H}_{31}$ is the homography that maps points from the third image onto the first one.

6.2.2 Planar parallax

The underlying parallax geometry is shown in figure 6.1; two views and a reference world plane are shown. The distinguished world plane induces a homography between the two views meaning that the images of points on the plane can be transferred via the inter-image homography between views 1 and 2 (see sec. 3.3.2). The homography can be determined as usual from a minimum of four correspondences in the two views of points (or lines) on the distinguished plane.

The parallax vector in the first view is the vector joining the image $\mathbf{x}$ of a world point $\mathbf{X}$ with the transferred location $\dot{\mathbf{x}}$ of $\mathbf{X}$’s image in the other view (the point $\mathbf{x}'$). Furthermore, since the three planes (distinguished world plane and two image planes) are equivalent up to a plane projectivity,

we can also measure parallax in the second view, or, if the image-to-world plane homographies are known, on the distinguished world plane. In fact it is particularly clear to work with the world plane. In this case all dependence on the rotational and internal parameters of the cameras is removed (aggregated into the image-to-world plane homographies) leaving only a dependence on the camera centres.

Since the clarity of the underlying geometry is greatly increased, we depict all relevant points and vectors on the world plane in all of the figures. However, the computations do *not* require the image-to-world homographies to be known and they can be carried out from images directly.

The parallax vector is directed towards (or away from) the epipole (see fig. 6.1b), thus two such vectors are sufficient to compute its position, and the full epipolar geometry follows [6, 77, 82]. The magnitude of the parallax vector is related to the distance of the world point and cameras from the world plane. Although others have described this function in detail [58, 69, 100] we re-derive the relationship in section 6.4.

6.3 Geometry and duality

6.3.1 Geometry of two views

Let us consider the case of imaging seven points, four of which are coplanar from two distinct viewpoints. Each of the non-coplanar three points $\mathbf{P}$, $\mathbf{Q}$ and $\mathbf{X}$ not on the plane gives rise to a parallax vector, which is depicted on the world plane in figure 6.2.

The plane $\mathbf{PQX}$ (referred to as the *tripoint plane*), intersects the world plane in a line (referred to as the *tripoint line*), and the camera baseline intersects the world plane in a point, the epipole. It can be seen by inspection of figures 6.2 and 6.3 that the geometry under consideration (seven points, two views) leads directly to a Desargues configuration (see section 3.3.3) in which the epipole is the vertex of the homology and the tripoint line is the axis of the homology. The two triangles in the Desargues configuration are the two "shadows" of the space triangle $\mathbf{PQX}$. This key observation

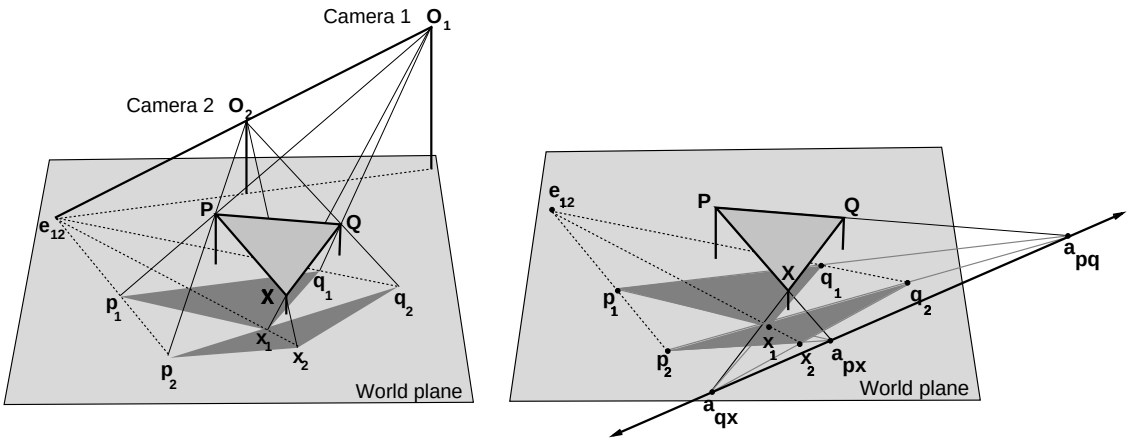

Figure 6.2: **The geometry of three points in two views:** (a) the triangle $\mathbf{p}_i\mathbf{q}_i\mathbf{x}_i$ is the "shadow" of $\mathbf{PQX}$ under the camera $\mathbf{O}_i$; (b) the axis of the homology is given by the intersection of the plane $\mathbf{PQX}$ with the world plane, and the vertex (epipole $\mathbf{e}_{12}$) by the intersection of the baseline with the world plane.

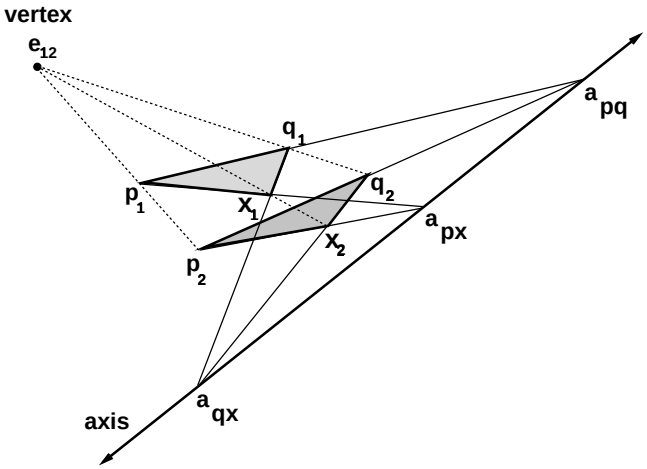

Figure 6.3: **Desargues configuration in the two view - three point (off the plane) case:** three points in two views relative to a known plane leads directly to a Desargues configuration on the plane.

underpins the results which follow.

As stated in section 3.3.3, a homology has five degrees of freedom, and therefore three point correspondences over-determine it. The extra constraint available can be used as a test for the rigidity of the scene and is equivalent to the epipolar constraint.

Clearly the constraint can be tested geometrically by using point correspondences either to

construct the intersections of corresponding sides and testing their collinearity, or testing the concurrence of the parallax vectors. Alternatively an algebraic test could, for example, compute the epipole using two point correspondences, use the epipole plus the three point correspondences to solve for a general homography, then test the homography to determine if it is a homology (two identical eigenvalues).

The geometric test has the disadvantage of requiring the construction of features which may be far removed from the measured image features themselves, while the algebraic test gives little insight into the underlying geometry.

Below we derive novel bilinear and trilinear constraints which are necessary conditions on the homology. We refer to these as *motion constraints* and they are equivalent to the epipolar constraint, but have the advantage that the computations involve only those features which can be measured directly, namely the parallax vectors.

Motion constraints

Six points (four of which are coplanar) in two views uniquely define the epipolar geometry. Therefore the two images of one more point off the plane are constrained to lie on each other's epipolar lines.

Here we give necessary conditions for the homology (which are therefore necessary for scene rigidity in two views) in the form of an identity involving only areas of triangles defined by three vertices, computable from the parallax vectors. Two such conditions and their symmetric forms can be determined. The first is derived from the collinearity of the epipole $\mathbf{e}_{12}$ and corresponding points and is bilinear in the areas. The second is derived from the collinearity of the points $\mathbf{a}_{qx}$, $\mathbf{a}_{px}$ and $\mathbf{a}_{pq}$ (fig. 6.2b) and leads to a constraint which is trilinear in the areas.

Details about the derivations can be found in appendix E. The results are summarised in table 6.2 which shows formulae for both the distinguished *plane form* (6.1 – 6.5) and the *image form* (6.6 – 6.10). In the plane form areas of triangles are computed on the distinguished plane and

MOTION CONSTRAINTS		
Distinguished plane form		
B_1	$A_{\mathbf{p}_1\mathbf{p}_2\mathbf{x}_2}A_{\mathbf{q}_1\mathbf{q}_2\mathbf{x}_1} = A_{\mathbf{p}_1\mathbf{p}_2\mathbf{x}_1}A_{\mathbf{q}_1\mathbf{q}_2\mathbf{x}_2}$	(6.1)
B_2	$A_{\mathbf{x}_1\mathbf{x}_2\mathbf{p}_2}A_{\mathbf{q}_1\mathbf{q}_2\mathbf{p}_1} = A_{\mathbf{x}_1\mathbf{x}_2\mathbf{p}_1}A_{\mathbf{q}_1\mathbf{q}_2\mathbf{p}_2}$	(6.2)
B_3	$A_{\mathbf{p}_1\mathbf{p}_2\mathbf{q}_2}A_{\mathbf{x}_1\mathbf{x}_2\mathbf{q}_1} = A_{\mathbf{p}_1\mathbf{p}_2\mathbf{q}_1}A_{\mathbf{x}_1\mathbf{x}_2\mathbf{q}_2}$	(6.3)
T_1	$A_{\mathbf{p}_1\mathbf{p}_2\mathbf{x}_1}A_{\mathbf{q}_1\mathbf{q}_2\mathbf{p}_1}A_{\mathbf{x}_1\mathbf{x}_2\mathbf{q}_1} = A_{\mathbf{p}_1\mathbf{p}_2\mathbf{q}_1}A_{\mathbf{q}_1\mathbf{q}_2\mathbf{x}_1}A_{\mathbf{x}_1\mathbf{x}_2\mathbf{p}_1}$	(6.4)
T_2	$A_{\mathbf{p}_1\mathbf{p}_2\mathbf{x}_2}A_{\mathbf{q}_1\mathbf{q}_2\mathbf{p}_2}A_{\mathbf{x}_1\mathbf{x}_2\mathbf{q}_2} = A_{\mathbf{p}_1\mathbf{p}_2\mathbf{q}_2}A_{\mathbf{q}_1\mathbf{q}_2\mathbf{x}_2}A_{\mathbf{x}_1\mathbf{x}_2\mathbf{p}_2}$	(6.5)
Image form		
B_1	$A_{\mathbf{p}\dot{\mathbf{p}}\dot{\mathbf{x}}}A_{\mathbf{q}\dot{\mathbf{q}}\mathbf{x}} = A_{\mathbf{p}\dot{\mathbf{p}}\mathbf{x}}A_{\mathbf{q}\dot{\mathbf{q}}\dot{\mathbf{x}}}$	(6.6)
B_2	$A_{\mathbf{x}\dot{\mathbf{x}}\dot{\mathbf{p}}}A_{\mathbf{q}\dot{\mathbf{q}}\mathbf{p}} = A_{\mathbf{x}\dot{\mathbf{x}}\mathbf{p}}A_{\mathbf{q}\dot{\mathbf{q}}\dot{\mathbf{p}}}$	(6.7)
B_3	$A_{\mathbf{p}\dot{\mathbf{p}}\dot{\mathbf{q}}}A_{\mathbf{x}\dot{\mathbf{x}}\mathbf{q}} = A_{\mathbf{p}\dot{\mathbf{p}}\mathbf{q}}A_{\mathbf{x}\dot{\mathbf{x}}\dot{\mathbf{q}}}$	(6.8)
T_1	$A_{\mathbf{p}\dot{\mathbf{p}}\mathbf{x}}A_{\mathbf{q}\dot{\mathbf{q}}\mathbf{p}}A_{\mathbf{x}\dot{\mathbf{x}}\mathbf{q}} = A_{\mathbf{p}\dot{\mathbf{p}}\mathbf{q}}A_{\mathbf{q}\dot{\mathbf{q}}\mathbf{x}}A_{\mathbf{x}\dot{\mathbf{x}}\mathbf{p}}$	(6.9)
T_2	$A_{\mathbf{p}\dot{\mathbf{p}}\dot{\mathbf{x}}}A_{\mathbf{q}\dot{\mathbf{q}}\dot{\mathbf{p}}}A_{\mathbf{x}\dot{\mathbf{x}}\dot{\mathbf{q}}} = A_{\mathbf{p}\dot{\mathbf{p}}\dot{\mathbf{q}}}A_{\mathbf{q}\dot{\mathbf{q}}\dot{\mathbf{x}}}A_{\mathbf{x}\dot{\mathbf{x}}\dot{\mathbf{p}}}$	(6.10)

Table 6.2: **Motion constraints**: two view bilinear (B_i) and trilinear (T_i) motion constraints equivalent to the epipolar constraint; computed on the plane and on the image. Bilinear and trilinear constraints are projective invariant.

therefore the knowledge of each world-to-image homography is required; while in the image form areas of triangles are computed directly in the first image (but either image can be used) and only the knowledge of the inter-image homography is necessary.

Violation of any of (6.1 – 6.10) is a clear indication that there has been non-rigid motion between the views. However if any (or all) of the points $\mathbf{P}$, $\mathbf{Q}$ and $\mathbf{X}$ moves in its own epipolar plane then the equations are still satisfied and non-rigidity is not detected.

Example. An example of motion detection is shown in figure 6.4. Here we demonstrate two view independent motion detection using the described alternative forms of the epipolar constraint. In this example the homography between the views induced by the world plane (the wall) has been computed using four image correspondences on each view. Two points not on the wall have then been selected and used as reference.

Figure 6.4: **Consistency with the epipolar geometry:** (a) and (b) left and right view of an indoor scene in which the person has changed his position. Four pairs of corresponding points on the wall (white circles) have been used to compute the inter-image homography. Two pairs of corresponding points not on the wall plane (white boxes) have been used to compute the parallax geometry (points $\mathbf{p}$, $\mathbf{p}'$, $\mathbf{q}$ and $\mathbf{q}'$ in text). (c) and (d) some points have been selected on the left image (white crosses, point $\mathbf{x}$ in text) and the corresponding epipolar lines shown on the right image. The corresponding points ($\mathbf{x}'$ in text) have been selected on the right image. The points which conform to the motion of the camera (they satisfy (6.6)) are marked with white crosses, the ones which undergo an independent motion (they do not satisfy (6.6)), are marked with black crosses.

The motion constraint (6.6) is applied to each pair of corresponding points selected in figures 6.4c,d. The independent motion of the person has been detected correctly (black marks). The epipolar lines have been shown for clarity in figure 6.4 but no explicit computation of the epipolar geometry is necessary in our formulation of the motion constraint.

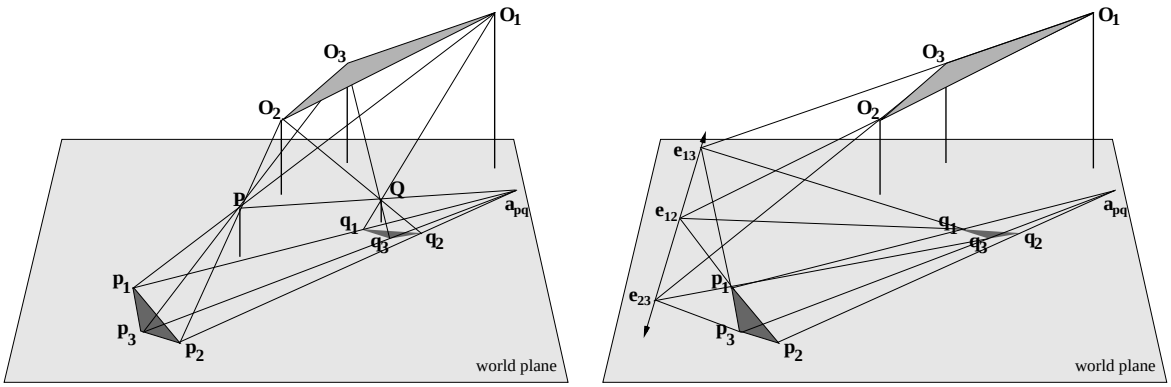

Figure 6.5: **The geometry of three views with two points off the plane:** (a) the triangles $\mathbf{p}_1\mathbf{p}_2\mathbf{p}_3$ and $\mathbf{q}_1\mathbf{q}_2\mathbf{q}_3$ are "shadows" of $\mathbf{O}_1\mathbf{O}_2\mathbf{O}_3$ under the points $\mathbf{P}$ and $\mathbf{Q}$ respectively; (b) the three epipoles are collinear, lying on the trifocal line which is the intersection of the plane $\mathbf{O}_1\mathbf{O}_2\mathbf{O}_3$ with the world plane. The piercing point $\mathbf{a}_{pq}$ is the intersection of the line $< \mathbf{PQ} >$ with the world plane.

6.3.2 Geometry of three views

We now consider the geometry of six points, four of which are coplanar, in three views. This is the situation addressed by Irani and Anandan in [58]. The geometry is shown in figure 6.5.

We begin by demonstrating the duality of this case to the two view case described in section 6.3.1, and obtain a *structural constraint* directly from the measured image features. Then the trifocal tensor is derived for the three view, six point (four coplanar) case. Since the trifocal tensor is over-constrained by six points, four of which are coplanar, another form of the structure constraint is also obtained.

Duality

It is clear by inspection of figure 6.5 that the three view geometry is dual to that of figure 6.2 in which points off the plane have been exchanged for camera positions. The vertex of the homology is given by the intersection of the line $< \mathbf{PQ} >$ with the world plane (referred to as the *piercing point*, $\mathbf{a}_{pq}$), and the axis by the intersection of the trifocal plane containing the three camera centres $\mathbf{O}_1$, $\mathbf{O}_2$, $\mathbf{O}_3$ with the world plane (referred to as the *trifocal line*). (see also figure 6.6).

Having established the duality of the two situations, we are now in a position to invoke duality

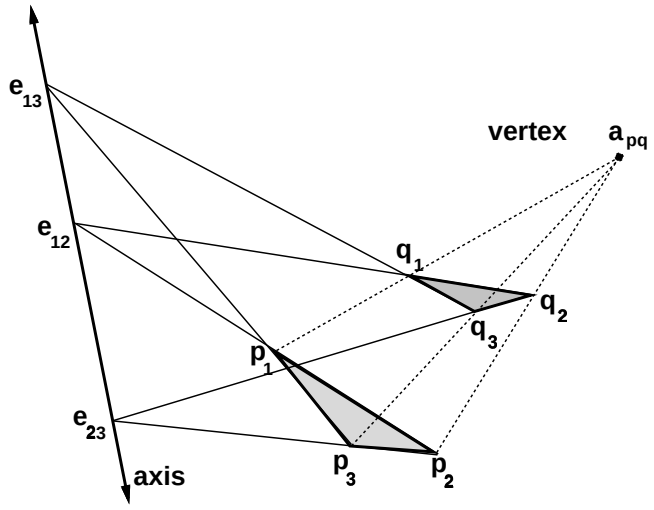

Figure 6.6: **Desargues configuration in the three view - two point case:** the planar geometry in the three view two point case is also clearly a Desargues configuration and point correspondences $\mathbf{p}_1 \leftrightarrow \mathbf{q}_1$, $\mathbf{p}_2 \leftrightarrow \mathbf{q}_2$ and $\mathbf{p}_3 \leftrightarrow \mathbf{q}_3$ are related by a homology. This situation is clearly dual to that in figure 6.3.

in order to prove further results. We make the substitutions reported in table 6.3 into the equations in table 6.2 and the dual trilinear and bilinear constraints given in table 6.4 follow. Note that the bilinear constraints (6.11) – (6.13) are exactly the constraints given by Irani and Anandan [58]. All the other constraints are new.

Geometrically the structure constraint simply means that it is not possible to *arbitrarily* select the images of two points off a plane from three views. The images of the two points are in fact constrained. For example, on the distinguished plane (see fig. 6.5) once the projections $\mathbf{p}_1$, $\mathbf{p}_2$ and $\mathbf{p}_3$ for the point $\mathbf{P}$ and the projections $\mathbf{q}_1$ and $\mathbf{q}_2$ of the point $\mathbf{Q}$ are known, then the point $\mathbf{q}_3$ is constrained to lie on the line $< \mathbf{p}_3 \mathbf{a}_{pq} >$ (*dual of the epipolar line*).

The trifocal tensor

This section demonstrates that the trifocal tensor is uniquely determined from three views of six points, four of which are coplanar. We begin with a familiar form of the trifocal tensor (after [51]) in which we consider the image projection matrices and image point locations. We then show how the form of the tensor is simplified when we consider all geometric objects (lines, points, etc.)

DUALITY SUBSTITUTIONS						
Distinguished plane form						
2 views	$\mathbf{p}_1$	$\mathbf{p}_2$	$\mathbf{x}_1$	$\mathbf{x}_2$	$\mathbf{q}_1$	$\mathbf{q}_2$
3 views	$\mathbf{p}_1$	$\mathbf{q}_1$	$\mathbf{p}_2$	$\mathbf{q}_2$	$\mathbf{p}_3$	$\mathbf{q}_3$
Image form						
2 views	$\mathbf{p}$	$\dot{\mathbf{p}}$	$\mathbf{x}$	$\dot{\mathbf{x}}$	$\mathbf{q}$	$\dot{\mathbf{q}}$
3 views	$\mathbf{p}$	$\mathbf{q}$	$\dot{\mathbf{p}}$	$\dot{\mathbf{q}}$	$\ddot{\mathbf{p}}$	$\ddot{\mathbf{q}}$

Table 6.3: **Duality substitution of symbols** for both the distinguished plane form and the image form. The epipole $\mathbf{e}_{12}$ in the two-view case is dual to the piercing point $\mathbf{a}_{pq}$ in the three-view case.

STRUCTURE CONSTRAINTS		
Distinguished plane form		
B_1	$A_{\mathbf{q}_1\mathbf{q}_2\mathbf{p}_1}A_{\mathbf{p}_2\mathbf{p}_3\mathbf{q}_3} = A_{\mathbf{p}_1\mathbf{p}_2\mathbf{q}_1}A_{\mathbf{q}_2\mathbf{q}_3\mathbf{p}_3}$	(6.11)
B_2	$A_{\mathbf{q}_1\mathbf{q}_2\mathbf{p}_2}A_{\mathbf{p}_1\mathbf{p}_3\mathbf{q}_3} = A_{\mathbf{p}_1\mathbf{p}_2\mathbf{q}_2}A_{\mathbf{q}_1\mathbf{q}_3\mathbf{p}_3}$	(6.12)
B_3	$A_{\mathbf{q}_1\mathbf{q}_3\mathbf{p}_1}A_{\mathbf{p}_2\mathbf{p}_3\mathbf{q}_2} = A_{\mathbf{p}_1\mathbf{p}_3\mathbf{q}_1}A_{\mathbf{q}_2\mathbf{q}_3\mathbf{p}_2}$	(6.13)
T_1	$A_{\mathbf{p}_1\mathbf{p}_2\mathbf{q}_1}A_{\mathbf{p}_1\mathbf{p}_3\mathbf{q}_3}A_{\mathbf{p}_2\mathbf{p}_3\mathbf{q}_2} = A_{\mathbf{p}_1\mathbf{p}_3\mathbf{q}_1}A_{\mathbf{p}_2\mathbf{p}_3\mathbf{q}_3}A_{\mathbf{p}_1\mathbf{p}_2\mathbf{q}_2}$	(6.14)
T_2	$A_{\mathbf{q}_1\mathbf{q}_2\mathbf{p}_1}A_{\mathbf{q}_1\mathbf{q}_3\mathbf{p}_3}A_{\mathbf{q}_2\mathbf{q}_3\mathbf{p}_2} = A_{\mathbf{q}_1\mathbf{q}_3\mathbf{p}_1}A_{\mathbf{q}_2\mathbf{q}_3\mathbf{p}_3}A_{\mathbf{q}_1\mathbf{q}_2\mathbf{p}_2}$	(6.15)
Image form		
B_1	$A_{\mathbf{q}\dot{\mathbf{q}}\mathbf{p}}A_{\dot{\mathbf{p}}\ddot{\mathbf{p}}\ddot{\mathbf{q}}} = A_{\mathbf{p}\dot{\mathbf{p}}\mathbf{q}}A_{\dot{\mathbf{q}}\ddot{\mathbf{q}}\ddot{\mathbf{p}}}$	(6.16)
B_2	$A_{\mathbf{q}\dot{\mathbf{q}}\dot{\mathbf{p}}}A_{\mathbf{p}\ddot{\mathbf{p}}\ddot{\mathbf{q}}} = A_{\mathbf{p}\dot{\mathbf{p}}\dot{\mathbf{q}}}A_{\mathbf{q}\ddot{\mathbf{q}}\ddot{\mathbf{p}}}$	(6.17)
B_3	$A_{\mathbf{q}\ddot{\mathbf{q}}\mathbf{p}}A_{\dot{\mathbf{p}}\ddot{\mathbf{p}}\dot{\mathbf{q}}} = A_{\mathbf{p}\ddot{\mathbf{p}}\mathbf{q}}A_{\dot{\mathbf{q}}\ddot{\mathbf{q}}\dot{\mathbf{p}}}$	(6.18)
T_1	$A_{\mathbf{p}\dot{\mathbf{p}}\mathbf{q}}A_{\mathbf{p}\ddot{\mathbf{p}}\ddot{\mathbf{q}}}A_{\dot{\mathbf{p}}\ddot{\mathbf{p}}\dot{\mathbf{q}}} = A_{\mathbf{p}\ddot{\mathbf{p}}\mathbf{q}}A_{\dot{\mathbf{p}}\ddot{\mathbf{p}}\ddot{\mathbf{q}}}A_{\mathbf{p}\dot{\mathbf{p}}\dot{\mathbf{q}}}$	(6.19)
T_2	$A_{\mathbf{q}\dot{\mathbf{q}}\mathbf{p}}A_{\mathbf{q}\ddot{\mathbf{q}}\ddot{\mathbf{p}}}A_{\dot{\mathbf{q}}\ddot{\mathbf{q}}\dot{\mathbf{p}}} = A_{\mathbf{q}\ddot{\mathbf{q}}\mathbf{p}}A_{\dot{\mathbf{q}}\ddot{\mathbf{q}}\ddot{\mathbf{p}}}A_{\mathbf{q}\dot{\mathbf{q}}\dot{\mathbf{p}}}$	(6.20)

Table 6.4: **Structure constraints**: three view bilinear (B_i) and trilinear (T_i) structure constraints; computed on the plane and on the image. Bilinear and trilinear constraints are projective invariant.

projected onto the distinguished plane.

Image form

Suppose the homographies induced by the plane of the points are $\mathtt{H}_{12}$ and $\mathtt{H}_{13}$, such that $\mathbf{x}' = \mathtt{H}_{12}\mathbf{x}$ and $\mathbf{x}'' = \mathtt{H}_{13}\mathbf{x}$ for images of points on the plane. These homographies are computed from the images of the four coplanar points.

The images of the first camera centre in the second and third images, denoted $\mathbf{e}'$ and $\mathbf{e}''$ respectively, are the epipoles. They are determined by intersecting parallax vectors, as described in section 6.3.1, so that $\mathtt{F}_{12} = [\mathbf{e}']_\times \mathtt{H}_{12}$, and $\mathtt{F}_{13} = [\mathbf{e}'']_\times \mathtt{H}_{13}$. It is straightforward to show that the three camera projection matrices can be chosen as

$$\mathtt{P} = [\mathtt{I} \mid \mathbf{0}], \quad \mathtt{P}' = [\mathtt{H}_{12} \mid \mathbf{e}'], \quad \mathtt{P}'' = [\mathtt{H}_{13} \mid \lambda \mathbf{e}''] \tag{6.21}$$

up to a homography of 3-space, where λ is an unknown scalar. This unknown scalar is determined by line transfer.

The line through the (non-coplanar) points $\mathbf{P}$, $\mathbf{Q}$, is imaged as $\mathtt{l} = \mathbf{p} \times \mathbf{q}$, $\mathtt{l}' = \mathbf{p}' \times \mathbf{q}'$, $\mathtt{l}'' = \mathbf{p}'' \times \mathbf{q}''$ in the first, second and third views respectively. It is then straightforward to show that lines transfer as follows (alternatively point transfer may be considered):

$$\mathtt{l} = \lambda(\mathbf{e}'' \cdot \mathtt{l}'')\mathtt{H}_{12}{}^\top \mathtt{l}' - (\mathbf{e}' \cdot \mathtt{l}')\mathtt{H}_{13}{}^\top \mathtt{l}'' \tag{6.22}$$

The scalar λ is the only unknown in this equation. It is determined by taking the vector product with $\mathtt{l}$.

$$\lambda(\mathbf{e}'' \cdot \mathtt{l}'')\mathtt{l} \times (\mathtt{H}_{12}{}^\top \mathtt{l}') = (\mathbf{e}' \cdot \mathtt{l}')\mathtt{l} \times (\mathtt{H}_{13}{}^\top \mathtt{l}'') \tag{6.23}$$

This provides two equations in the one unknown λ and so we can solve uniquely for the trifocal tensor and obtain one further constraint, namely the rigidity condition that the imaged intersection of the line through $\mathbf{P}, \mathbf{Q}$ is the same when computed from views one and two ($\mathtt{l} \times (\mathtt{H}_{12}{}^\top \mathtt{l}')$) as from views one and three ($\mathtt{l} \times (\mathtt{H}_{13}{}^\top \mathtt{l}'')$). This is yet another form of the constraints (6.11 – 6.20). The scale factor λ is obtained by normalising both sides of (6.23):

$$\lambda = \frac{||(\mathbf{e}' \cdot \mathtt{l}')\mathtt{l} \times (\mathtt{H}_{13}{}^\top \mathtt{l}'')||}{||(\mathbf{e}'' \cdot \mathtt{l}'')\mathtt{l} \times (\mathtt{H}_{12}{}^\top \mathtt{l}')||} \tag{6.24}$$

Distinguished plane form

On the distinguished plane $\mathtt{H}_{12} = \mathtt{H}_{13} = \mathtt{I}$, so the equivalent of (6.22) for point transfer is

$$\mathbf{x}_3 = \lambda \mathbf{e}_{13}(\mathtt{l}_2 \cdot \mathbf{x}_1) - (\mathbf{e}_{12} \cdot \mathtt{l}_2)\mathbf{x}_1 \tag{6.25}$$

where $\mathbf{x}_1$, $\mathbf{x}_2$, $\mathbf{x}_3$ are the distinguished plane images of a general 3D point $\mathbf{X}$, and $\mathbf{l}_2$ is any line through $\mathbf{x}_2$. This equation depends only on the positions of the epipoles on the distinguished plane, with all dependence on camera internals and relative rotations having been factored out into the image-to-plane homographies.

Additionally the projection matrices have the very simple form

$$\mathtt{P}_1 = [\mathtt{I} \mid \mathbf{0}], \quad \mathtt{P}_2 = [\mathtt{I} \mid \mathbf{e}_{12}], \quad \mathtt{P}_3 = [\mathtt{I} \mid \lambda \mathbf{e}_{13}] \tag{6.26}$$

Hence, representing a general 3D point as $\mathbf{X} = \begin{pmatrix} x_1 \\ \rho \end{pmatrix}$, we determine the distinguished plane images to be:

$$\mathbf{x}_1 = \mathtt{P}_1\mathbf{X}, \quad \mathbf{x}_2 = \mathtt{P}_2\mathbf{X} = \mathbf{x}_1 + \rho\mathbf{e}_{12}, \quad \mathbf{x}_3 = \mathtt{P}_3\mathbf{X} = \mathbf{x}_1 + \rho\lambda\mathbf{e}_{13} \tag{6.27}$$

We now give an interpretation of ρ and λ on the distinguished plane (see figure 6.7).

The ratio λ depends only on the camera centres, not on the points, and can be determined as $\lambda = d(\mathbf{e}_{12}, \mathbf{e}_{23})/d(\mathbf{e}_{13}, \mathbf{e}_{23})$ where $d()$ is the distance between the points on the distinguished plane. The parameter ρ is the relative affine invariant of Shashua [105], and is related to the point depth. On the distinguished plane it is obtained as $\rho = d(\mathbf{x}_2, \mathbf{x}_1)/d(\mathbf{x}_2, \mathbf{e}_{12})$.

So point transfer using the trifocal tensor simply involves computing the ratio ρ from $\mathbf{x}_1$, $\mathbf{x}_2$ and $\mathbf{e}_{12}$ and employing λ to define the transferred point $\mathbf{x}_3$ on the line between $\mathbf{e}_{13}$ and $\mathbf{x}_1$ as $\mathbf{x}_3 = \mathbf{x}_1 + \rho\lambda\mathbf{e}_{13}$ in (6.27). This is identical to the point transfer of (6.25), as can be seen by considering similar triangles in figure 6.7.

Trifocal transfer in the case of collinear camera centres is not degenerate

In the case that the three camera centres are collinear then the three epipoles $\mathbf{e}_{13}$, $\mathbf{e}_{23}$ and $\mathbf{e}_{12}$ coincide and the epipolar transfer would fail. The trifocal transfer, instead, does not present such a degeneracy. It is still well defined in the case of three concurrent (or almost concurrent) epipoles. In fact, the ratio λ is defined and can be obtained using the distinguished plane equivalent of (6.24).

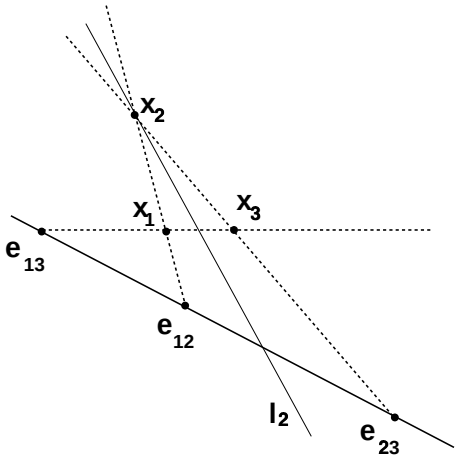

Figure 6.7: **Point transfer:** the ratios of the distances between $\mathbf{x}_1$, $\mathbf{x}_2$ and $\mathbf{e}_{12}$ and the three epipoles define the transfer of the point $\mathbf{x}_1$ to $\mathbf{x}_3$. The scalars λ and ρ (see text) can be measured as ratios of point distances as: $\lambda = d(\mathbf{e}_{12}, \mathbf{e}_{23})/d(\mathbf{e}_{13}, \mathbf{e}_{23})$ and $\rho = d(\mathbf{x}_2, \mathbf{x}_1)/d(\mathbf{x}_2, \mathbf{e}_{12})$.

6.4 Scene reconstruction

In this section we discuss a number of useful structural computations which can be achieved using ratios of areas. This requires *affine* measurements on the world plane, which can be obtained either from four world plane points known up to an affinity (and hence the image-to-world plane homographies, this is *distinguished plane form case*), or from the inter-image homography between two views and the vanishing line of the world plane in either image (this is *image form case*). In either case we obtain results for the scene structure without resorting first to compute the epipolar geometry.

A significant novel aspect of the formulae given in sections 6.4.1 and 6.4.2 is that measurements can be computed without knowing the vanishing point for the reference direction and without seeing the base point in the image unlike in the single view metrology approach described in chapter 5.

We begin by re-deriving the basic parallax relationship for the cases where the parallax is measured on the distinguished world plane (6.30) and on the image (6.31).

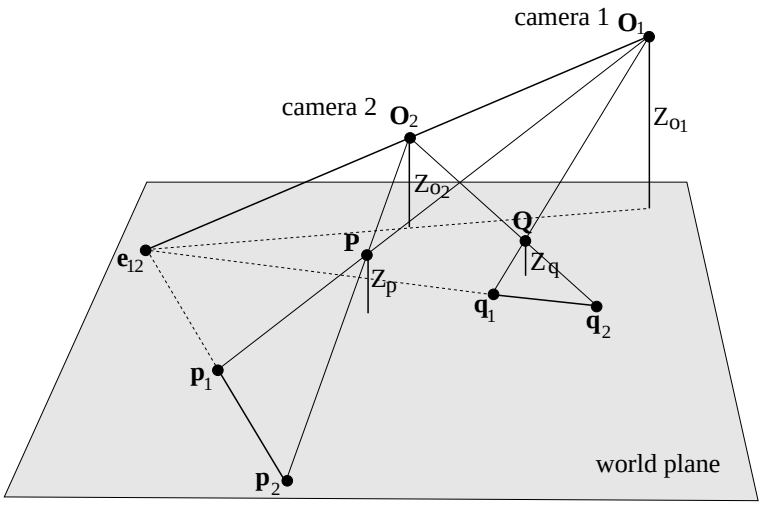

Figure 6.8: **Parallax geometry of two points off the plane.**

Distinguished plane form. Considering figure 6.8 and writing $\mathbf{p}_1 = \mathbf{O}_1 + \frac{Z_{O_1}}{Z_{O_1}-Z_p}(\mathbf{P}-\mathbf{O}_1)$, $\mathbf{p}_2 = \mathbf{O}_2 + \frac{Z_{O_2}}{Z_{O_2}-Z_p}(\mathbf{P}-\mathbf{O}_2)$ and $\mathbf{e}_{12} = \mathbf{O}_2 + \frac{Z_{O_2}}{Z_{O_2}-Z_p}(\mathbf{O}_1-\mathbf{O}_2)$. Then eliminating $\mathbf{O}_1$ and $\mathbf{O}_2$ yields

$$\boldsymbol{\mu}_p = \frac{Z_p}{Z_{O_2}-Z_p}\frac{\Delta_{Z_O}}{Z_{O_1}}(\mathbf{p}_1-\mathbf{e}_{12}) \tag{6.28}$$

where $\boldsymbol{\mu}_p = \mathbf{p}_2 - \mathbf{p}_1$ is the planar parallax vector and $\Delta_{Z_O} = Z_{O_1} - Z_{O_2}$ is the component of camera translation towards the plane.

Let γ be the ratio of the distance of a point to the plane and the point to the first camera (measured in the same direction), i.e. $\gamma_p = \frac{Z_p}{Z_{O_1}-Z_p}$ and $\gamma_q = \frac{Z_q}{Z_{O_1}-Z_q}$ then combining the basic parallax equation (6.28) for two points $\mathbf{P}$ and $\mathbf{Q}$ gives

$$\gamma_q\boldsymbol{\mu}_p - \gamma_p\boldsymbol{\mu}_q = \gamma_p\gamma_q\frac{\Delta_{Z_O}}{Z_{O_2}}(\mathbf{p}_2-\mathbf{q}_2) \tag{6.29}$$

Finally, taking the cross product of both sides of the equation with $\mathbf{p_2}-\mathbf{q}_2$ and taking magnitudes yields an expression for $\frac{\gamma_q}{\gamma_p}$ as a ratio of areas (see figure 6.9) of the form

$$\frac{\gamma_q}{\gamma_p} = \frac{|\boldsymbol{\mu}_q\times(\mathbf{p}_2-\mathbf{q}_2)|}{|\boldsymbol{\mu}_p\times(\mathbf{p}_2-\mathbf{q}_2)|} = \frac{A_{\mathbf{q_1q_2p_2}}}{A_{\mathbf{p_1p_2q_2}}} \tag{6.30}$$

This ratio is computable solely from the parallax measurements, and, being a ratio of areas, is clearly affine invariant.

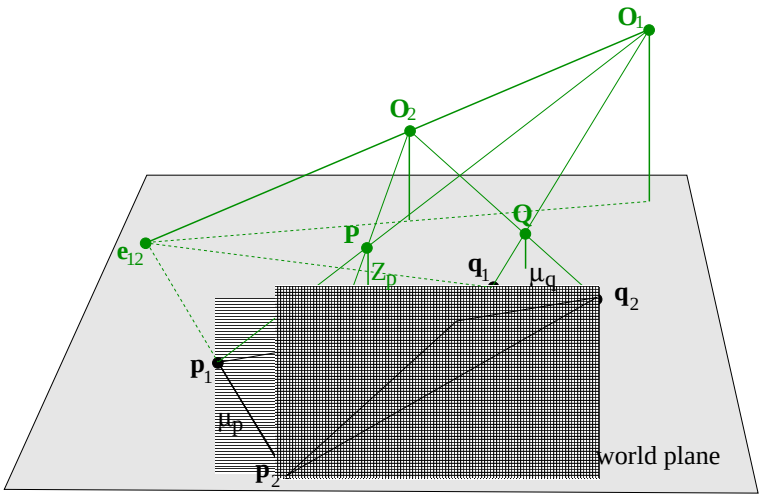

Figure 6.9: The relative structure $\frac{\gamma_q}{\gamma_p}$ can be expressed as a ratio of areas on the world plane as in (6.30).

Image form. In the case the image-to-world homographies are unknown, since $\dot{\mathbf{p}} = \mathtt{H}_{21}\mathbf{p}'$ and $\dot{\mathbf{q}} = \mathtt{H}_{21}\mathbf{q}'$ equation (6.30) becomes (see section E.2 in appendix E for details):

$$\frac{\gamma_q}{\gamma_p} = \frac{A_{\mathbf{q}\dot{\mathbf{q}}\dot{\mathbf{p}}}(\mathbf{l}\cdot\mathbf{p})}{A_{\mathbf{p}\dot{\mathbf{p}}\dot{\mathbf{q}}}(\mathbf{l}\cdot\mathbf{q})} \tag{6.31}$$

with $\mathbf{l}$ the vanishing line of the reference plane in the first image. A similar formula can be obtained with reference to the second image instead of the first one.

This derivation is equivalent to Irani and Anandan's construction [58], but note that in our formulation only affine constructs have been used (no orthogonality has been assumed and the formulae are homogeneous). Furthermore, thanks to the affine invariance of ratios of areas if the vanishing line $\mathbf{l}$ of the reference plane is known in either image then the ratio (6.30) can be computed from image measurements only, thus obtaining (6.31).

These results are derived for the two view, seven point case. However because of the fundamental duality proved in section 6.3.2, they are equally valid (with appropriate symbol substitutions, see table 6.3) in the three view, six point case. For example (6.38) can be used to compute the height of a third point given two other known heights in the two view, seven point case; dually, in the three

view, six point case, it can be used to obtain the height of a third camera given the other two camera heights.

6.4.1 Determining the position of the cameras

This section presents formulae to compute the position of the cameras, from a pair of images, with respect to the reference plane.

Ordinal distances

To begin, we show that, the position of the epipoles $\mathbf{e}$ and $\mathbf{e}'$ and the plane vanishing lines $\mathbf{l}$ and $\mathbf{l}'$ in the two images provide useful information about the relative location of the two cameras. Given the vanishing line $\mathbf{l}$ of the reference plane on the first image, its corresponding vanishing line $\mathbf{l}'$ in the second image is computed as: $\mathbf{l}' = \mathtt{H}_{12}^{-\top}\mathbf{l}$ (where $\mathbf{x}' = \mathtt{H}_{12}\mathbf{x}$ for images of points on the reference plane).

As noted in section 5.2 the vanishing line of a plane partitions the scene points into the ones which are closer to the plane than the camera centre and the ones which are farther. This simple consideration, generalized in the two view case, leads to the following result:

- $\mathbf{e} \cdot \mathbf{l} = 0 \iff \mathbf{e}' \cdot \mathbf{l}' = 0$ and in this case the two cameras have the same distance from the distinguished plane $\boldsymbol{\pi}$, $Z_{O_2} = Z_{O_1}$;
- if $\mathbf{e} \cdot \mathbf{l} \neq 0$ one camera is higher than the other; for instance, if $\mathbf{e}$ lies above the vanishing line then $\mathbf{e}'$ lies below and $Z_{O_2} > Z_{O_1}$. The vice-versa is also true.

Therefore we obtain ordering for the distances of the cameras from the plane $\boldsymbol{\pi}$.

Affine distances

If two reference points are seen in both images then affine distances of the cameras can be computed. The vanishing point of the measuring direction is not required. The following theorem holds:

Theorem 3 *Given the planar parallax vectors of two reference world points* $\mathbf{P}$ *and* $\mathbf{Q}$*, the ratio of distances of these points from the world plane* $\frac{Z_p}{Z_q}$ *(measured in the same but arbitrary direction, with* $Z_p \neq Z_q$*), and affine measurements on the world plane; then the affine distance of either camera to the world plane (measured in the same direction as* Z_p *and* Z_q*) can be computed.*

Distinguished plane form. Rearranging (6.30) provides the following expressions for the distance of the cameras from the plane:

$$\begin{aligned} \frac{Z_{O_1}}{Z_p} &= \frac{A_{\mathbf{p_1 p_2 q_2}} - A_{\mathbf{q_1 q_2 p_2}}}{A_{\mathbf{p_1 p_2 q_2}} - \frac{Z_p}{Z_q} A_{\mathbf{q_1 q_2 p_2}}} \\ \frac{Z_{O_2}}{Z_p} &= \frac{A_{\mathbf{p_1 p_2 q_1}} - A_{\mathbf{q_1 q_2 p_1}}}{A_{\mathbf{p_1 p_2 q_1}} - \frac{Z_p}{Z_q} A_{\mathbf{q_1 q_2 p_1}}} \end{aligned} \tag{6.32}$$

Image form. Taking into account (6.31) the previous equations can be computed directly in the image as:

$$\begin{aligned} \frac{Z_{O_1}}{Z_p} &= \frac{(\mathbf{l}\cdot\mathbf{q})A_{\mathbf{p\dot{p}\dot{q}}} - (\mathbf{l}\cdot\mathbf{p})A_{\mathbf{q\dot{q}\dot{p}}}}{(\mathbf{l}\cdot\mathbf{q})A_{\mathbf{p\dot{p}\dot{q}}} - \frac{Z_p}{Z_q}(\mathbf{l}\cdot\mathbf{p})A_{\mathbf{q\dot{q}\dot{p}}}} \\ \frac{Z_{O_2}}{Z_p} &= \frac{(\mathbf{l}'\cdot\mathbf{q}')A_{\mathbf{p\dot{p}q}} - (\mathbf{l}'\cdot\mathbf{p}')A_{\mathbf{q\dot{q}p}}}{(\mathbf{l}'\cdot\mathbf{q}')A_{\mathbf{p\dot{p}q}} - \frac{Z_p}{Z_q}(\mathbf{l}'\cdot\mathbf{p}')A_{\mathbf{q\dot{q}p}}} \end{aligned} \tag{6.33}$$

Since $\frac{Z_{O_1}}{Z_p}$ and $\frac{Z_{O_2}}{Z_p}$ scale linearly with Z_p (unknown) we have obtained affine structure.

□

Euclidean distances

An immediate corollary follows from the previous theorem. In fact, if the values of the reference distances Z_p and Z_q are known then the above measurements can be upgraded to Euclidean.

Distinguished plane form. From (6.32) we obtain:

$$\begin{aligned} Z_{O_1} &= \frac{Z_p Z_q (A_{\mathbf{p_1 p_2 q_2}} - A_{\mathbf{q_1 q_2 p_2}})}{Z_q A_{\mathbf{p_1 p_2 q_2}} - Z_p A_{\mathbf{q_1 q_2 p_2}}} \\ Z_{O_2} &= \frac{Z_p Z_q (A_{\mathbf{p_1 p_2 q_1}} - A_{\mathbf{q_1 q_2 p_1}})}{Z_q A_{\mathbf{p_1 p_2 q_1}} - Z_p A_{\mathbf{q_1 q_2 p_1}}} \end{aligned} \tag{6.34}$$

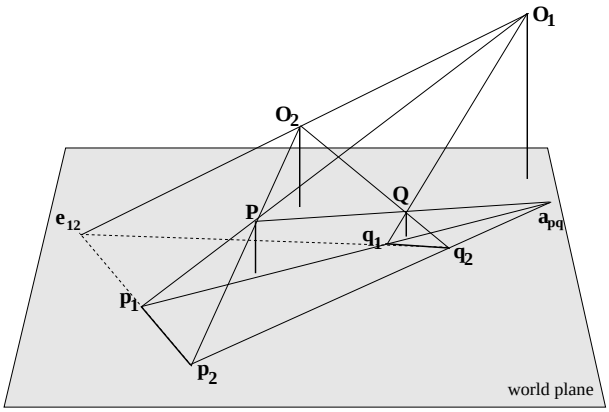

Figure 6.10: **Computing ordinal heights of points from parallax vectors and piercing point:** if $d(\mathbf{p}_1\mathbf{a}_{pq}) > d(\mathbf{q}_1\mathbf{a}_{pq})$ then $Z_p > Z_q$ and vice-versa.

Image form. And from (6.33):

$$\begin{aligned} Z_{O_1} &= \frac{Z_p Z_q \left[(\mathbf{l}\cdot\mathbf{q})A_{\mathbf{p}\dot{\mathbf{p}}\dot{\mathbf{q}}} - (\mathbf{l}\cdot\mathbf{p})A_{\mathbf{q}\dot{\mathbf{q}}\dot{\mathbf{p}}}\right]}{Z_q(\mathbf{l}\cdot\mathbf{q})A_{\mathbf{p}\dot{\mathbf{p}}\dot{\mathbf{q}}} - Z_p(\mathbf{l}\cdot\mathbf{p})A_{\mathbf{q}\dot{\mathbf{q}}\dot{\mathbf{p}}}} \\ Z_{O_2} &= \frac{Z_p Z_q \left[(\mathbf{l}'\cdot\mathbf{q}')A_{\mathbf{p}\dot{\mathbf{p}}\mathbf{q}} - (\mathbf{l}'\cdot\mathbf{p}')A_{\mathbf{q}\dot{\mathbf{q}}\mathbf{p}}\right]}{Z_q(\mathbf{l}'\cdot\mathbf{q}')A_{\mathbf{p}\dot{\mathbf{p}}\mathbf{q}} - Z_p(\mathbf{l}'\cdot\mathbf{p}')A_{\mathbf{q}\dot{\mathbf{q}}\mathbf{p}}} \end{aligned} \tag{6.35}$$

Example

In the example in figure 6.14 we have used (6.34) to compute the heights of the camera above the floor as 566cm and 586cm (left and right views respectively).

6.4.2 Distances of points from planes

Ordinal distances

If two points off the distinguished plane $\mathbf{P}$ and $\mathbf{Q}$ are viewed in two images, then it is possible to obtain ordering for their distances from the plane. This is obtained from comparing the locations of the projections of the points onto the plane and the piercing point. By inspection of figure 6.10 if $d(\mathbf{p}_1, \mathbf{a}_{pq}) > d(\mathbf{q}_1, \mathbf{a}_{pq})$ then $Z_p > Z_q$ and vice-versa. Similar computation can be performed directly on the images.

Affine distances

This section demonstrates that affine height of points can be computed from two references. As before, the vanishing point for the reference direction is not required. The following theorem holds:

Theorem 4 *Given the parallax vectors of three world points* $\mathbf{P}$, $\mathbf{Q}$ *and* $\mathbf{X}$, *the ratio of distances of two of these points* $\frac{Z_p}{Z_q}$ *from the world plane (measured in the same but arbitrary direction, with* $Z_p \neq Z_q$*), and affine measurements on the world plane; then the affine distance of the third point* $\mathbf{X}$ *from the plane (measured in the same direction as* Z_p *and* Z_q*) can be computed.*

Distinguished plane form. From (6.30) we have that $\frac{\gamma_x}{\gamma_p} = \frac{A_{\mathbf{x_1 x_2 p_1}}}{A_{\mathbf{p_1 p_2 x_1}}}$ and $\frac{\gamma_x}{\gamma_q} = \frac{A_{\mathbf{x_1 x_2 q_1}}}{A_{\mathbf{q_1 q_2 x_1}}}$. After eliminating the camera distance between these equations we obtain an expression for the ratio Z_x/Z_p where Z_x is the distance of the point $\mathbf{X}$ from the plane:

$$\frac{Z_x}{Z_p} = \frac{|\mathtt{M}_1|}{|\mathtt{M}_2|} \tag{6.36}$$

where

$$\mathtt{M}_1 = \begin{bmatrix} A_{\mathbf{x_1 x_2 q_1}} & A_{\mathbf{q_1 q_2 x_1}} \\ A_{\mathbf{x_1 x_2 p_1}} & A_{\mathbf{p_1 p_2 x_1}} \end{bmatrix}, \quad \mathtt{M}_2 = \begin{bmatrix} A_{\mathbf{x_1 x_2 q_1}} & A_{\mathbf{q_1 q_2 x_1}} & A_{\mathbf{q_1 q_2 x_1}} \\ Z_p/Z_q & 0 & -1 \\ A_{\mathbf{p_1 p_2 x_1}} & A_{\mathbf{p_1 p_2 x_1}} & A_{\mathbf{x_1 x_2 p_1}} \end{bmatrix}$$

Image form. The ratio $\frac{Z_x}{Z_p}$ in (6.36) can be computed directly in the image as:

$$\frac{Z_x}{Z_p} = \frac{|\tilde{\mathtt{M}}_1|}{|\tilde{\mathtt{M}}_2|} \tag{6.37}$$

where

$$\tilde{\mathtt{M}}_1 = \begin{bmatrix} (\mathbf{l}\cdot\mathbf{q})A_{\mathbf{x\dot{x}\dot{q}}} & A_{\mathbf{q\dot{q}\dot{x}}} \\ (\mathbf{l}\cdot\mathbf{p})A_{\mathbf{x\dot{x}\dot{p}}} & A_{\mathbf{p\dot{p}\dot{x}}} \end{bmatrix}, \quad \tilde{\mathtt{M}}_2 = \begin{bmatrix} (\mathbf{l}\cdot\mathbf{q})A_{\mathbf{x\dot{x}\dot{q}}} & A_{\mathbf{q\dot{q}\dot{x}}} & (\mathbf{l}\cdot\mathbf{x})A_{\mathbf{q\dot{q}\dot{x}}} \\ Z_p/Z_q & 0 & -1 \\ (\mathbf{l}\cdot\mathbf{x})A_{\mathbf{p\dot{p}\dot{x}}} & A_{\mathbf{p\dot{p}\dot{x}}} & (\mathbf{l}\cdot\mathbf{p})A_{\mathbf{x\dot{x}\dot{p}}} \end{bmatrix}$$

thus affine structure is recovered.

□

Euclidean distances

As for the camera, also in this case the formulae above can be upgraded to Euclidean if the absolute distances of the two reference points Z_p and Z_q are known.

Distinguished plane form. From (6.36) we obtain:

$$Z_x = \frac{|\mathtt{M}_1|}{|\mathtt{M}_2|} \tag{6.38}$$

where

$$\mathtt{M}_1 = Z_p Z_q \begin{bmatrix} A_{\mathbf{x}_1\mathbf{x}_2\mathbf{q}_1} & A_{\mathbf{q}_1\mathbf{q}_2\mathbf{x}_1} \\ A_{\mathbf{x}_1\mathbf{x}_2\mathbf{p}_1} & A_{\mathbf{p}_1\mathbf{p}_2\mathbf{x}_1} \end{bmatrix}, \quad \mathtt{M}_2 = \begin{bmatrix} A_{\mathbf{x}_1\mathbf{x}_2\mathbf{q}_1} & A_{\mathbf{q}_1\mathbf{q}_2\mathbf{x}_1} & A_{\mathbf{q}_1\mathbf{q}_2\mathbf{x}_1} \\ Z_p & 0 & -Z_q \\ A_{\mathbf{p}_1\mathbf{p}_2\mathbf{x}_1} & A_{\mathbf{p}_1\mathbf{p}_2\mathbf{x}_1} & A_{\mathbf{x}_1\mathbf{x}_2\mathbf{p}_1} \end{bmatrix}$$

Image form. And from (6.37):

$$Z_x = \frac{|\tilde{\mathtt{M}}_1|}{|\tilde{\mathtt{M}}_2|} \tag{6.39}$$

where

$$\tilde{\mathtt{M}}_1 = Z_p Z_q \begin{bmatrix} (\mathbf{l}\cdot\mathbf{q})A_{\mathbf{x}\dot{\mathbf{x}}\dot{\mathbf{q}}} & A_{\mathbf{q}\dot{\mathbf{q}}\dot{\mathbf{x}}} \\ (\mathbf{l}\cdot\mathbf{p})A_{\mathbf{x}\dot{\mathbf{x}}\dot{\mathbf{p}}} & A_{\mathbf{p}\dot{\mathbf{p}}\dot{\mathbf{x}}} \end{bmatrix}, \quad \tilde{\mathtt{M}}_2 = \begin{bmatrix} (\mathbf{l}\cdot\mathbf{q})A_{\mathbf{x}\dot{\mathbf{x}}\dot{\mathbf{q}}} & A_{\mathbf{q}\dot{\mathbf{q}}\dot{\mathbf{x}}} & (\mathbf{l}\cdot\mathbf{x})A_{\mathbf{q}\dot{\mathbf{q}}\dot{\mathbf{x}}} \\ Z_p & 0 & -Z_q \\ (\mathbf{l}\cdot\mathbf{x})A_{\mathbf{p}\dot{\mathbf{p}}\dot{\mathbf{x}}} & A_{\mathbf{p}\dot{\mathbf{p}}\dot{\mathbf{x}}} & (\mathbf{l}\cdot\mathbf{p})A_{\mathbf{x}\dot{\mathbf{x}}\dot{\mathbf{p}}} \end{bmatrix}$$

Derivations of these formulae are shown in appendix E.

Ambiguity in structure computation

As mentioned the distance Z_x is computed along the direction of the two reference distances Z_p and Z_q (parallel to each other in any fixed direction not on the reference plane, fig 6.11). But the reference direction is not known (its vanishing point is not needed in (6.39), (6.38)) and the position of the projection of the point $\mathbf{X}$ on the plane (its X and Y coordinates) cannot be completely determined. In can be proven, though, that the X, Y position of the point $\mathbf{X}$ can be retrieved up to a one-parameter family.

In order to retrieve the complete 3D reconstruction of a point $\mathbf{X}$ the X, Y coordinates of at least one of the two reference points ($\mathbf{P}$ or $\mathbf{Q}$) is necessary. Similar analysis applies to camera computation.

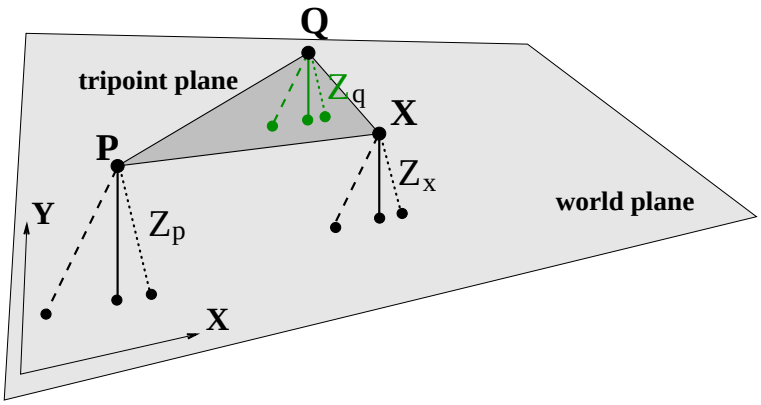

Figure 6.11: **Ambiguity in the reconstruction using a plane-plus-parallax approach:** the distance Z_x of the point $\mathbf{X}$ from the plane $\boldsymbol{\pi}$ is computed using (6.38) or (6.39) but its X, Y coordinates are not defined since the reference direction (off the plane) is not defined.

Degeneracy

Note that in the case $Z_p = Z_q$ the matrices above are singular and (6.32 – 6.39) are degenerate. However this situation can be avoided in practice. The degeneracy is understood in terms of the geometry as follows. In general we obtain projective structure (since F is determined uniquely). If in addition $Z_p \neq Z_q$ (fig. 6.12a), the line $< \mathbf{PQ} >$ intersects $\boldsymbol{\pi}_\infty$ in the point $\mathbf{v}_{pq}$ which can be identified in both images since the four aligned points $\mathbf{p}$, $\mathbf{q}$, $\mathbf{a}_{pq}$ and $\mathbf{v}_{pq}$ define a cross-ratio and the ratio $\frac{Z_p}{Z_q}$ is known (fig. 6.13). The point $\mathbf{v}_{pq}$ and the vanishing line of the world plane, $\mathbf{l}$, determine $\boldsymbol{\pi}_\infty$, hence we can obtain affine structure. When $Z_p = Z_q$ (fig. 6.12b) then the line $< \mathbf{PQ} >$ intersects $\boldsymbol{\pi}_\infty$ on $\mathbf{l}$ and so no additional information about $\boldsymbol{\pi}_\infty$ is obtained; it is determined only up to a one parameter family (the pencil of planes with $\mathbf{l}$ as its axis).

Examples

Figure 6.14 shows an example in which point distances from the floor have been estimated. The floor tiling and the perpendicular heights of two other points were measured by hand with a tape measure and used as reference. Correspondences on the patterned floor tiling have been used to compute the inter-image homography and the vanishing line of the floor in the left image. The distances of several points have been computed with the method described above and shown in the

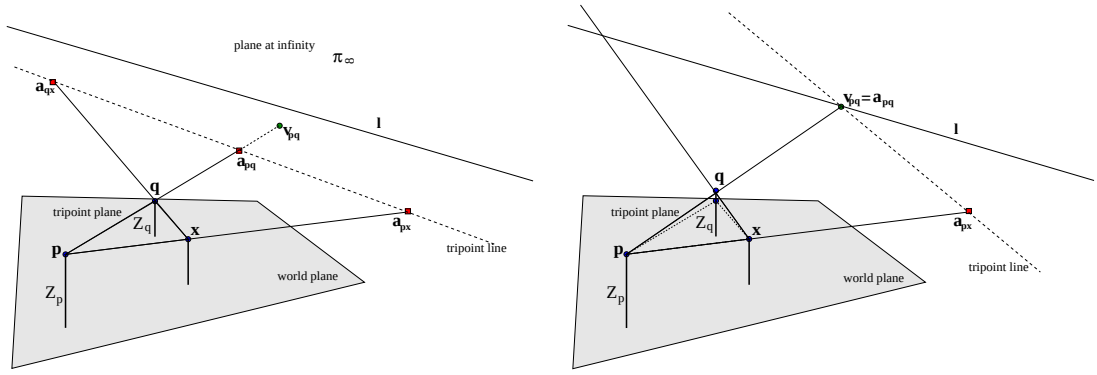

Figure 6.12: **The plane-plus-parallax approach is degenerate if the two reference distances coincide:** (a) if $Z_p \neq Z_q$ the point $\mathbf{v}_{pq}$ does not lie on the plane vanishing line $\mathbf{l}$, then the plane at infinity is defined. (b) if $Z_p = Z_q$ the point $\mathbf{v}_{pq}$ lies on the plane vanishing line $\mathbf{l}$ and the plane at infinity is not defined.

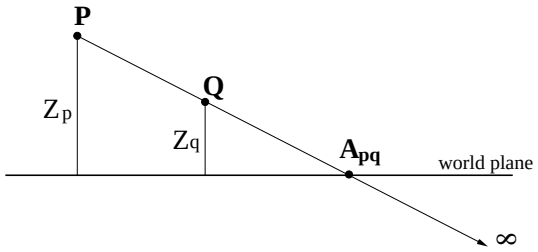

Figure 6.13: **Computing the vanishing point $\mathbf{v}_{pq}$.** The position of the vanishing point $\mathbf{v}_{pq}$ in figure 6.12a can be computed from the cross-ratio: $\frac{d(\mathbf{p},\mathbf{a}_{pq})}{d(\mathbf{q},\mathbf{a}_{pq})}\frac{d(\mathbf{p},\mathbf{v}_{pq})}{d(\mathbf{q},\mathbf{v}_{pq})} = \frac{d(\mathbf{P},\mathbf{A}_{pq})}{d(\mathbf{Q},\mathbf{A}_{pq})} = \frac{Z_p}{Z_q}$.

figure. A second example is shown in figure 6.17.

6.4.3 Intersection between two planar surfaces

This section shows another application of the plane-plus-parallax geometry: computing the line of intersection between two planar surfaces from two views.

Using two inter-image homographies. Given two views of two planar surfaces $\boldsymbol{\pi}_1$ and $\boldsymbol{\pi}_2$ and the related inter-image homographies between the two images, the line of intersection $\mathbf{l}$ between the two planes can be computed in both images.

Let $\mathtt{H}_1$ be the homography which maps points on $\boldsymbol{\pi}_1$ on the first image into the corresponding plane in the second image and $\mathtt{H}_2$ the homography which maps points on $\boldsymbol{\pi}_2$ in the first image into

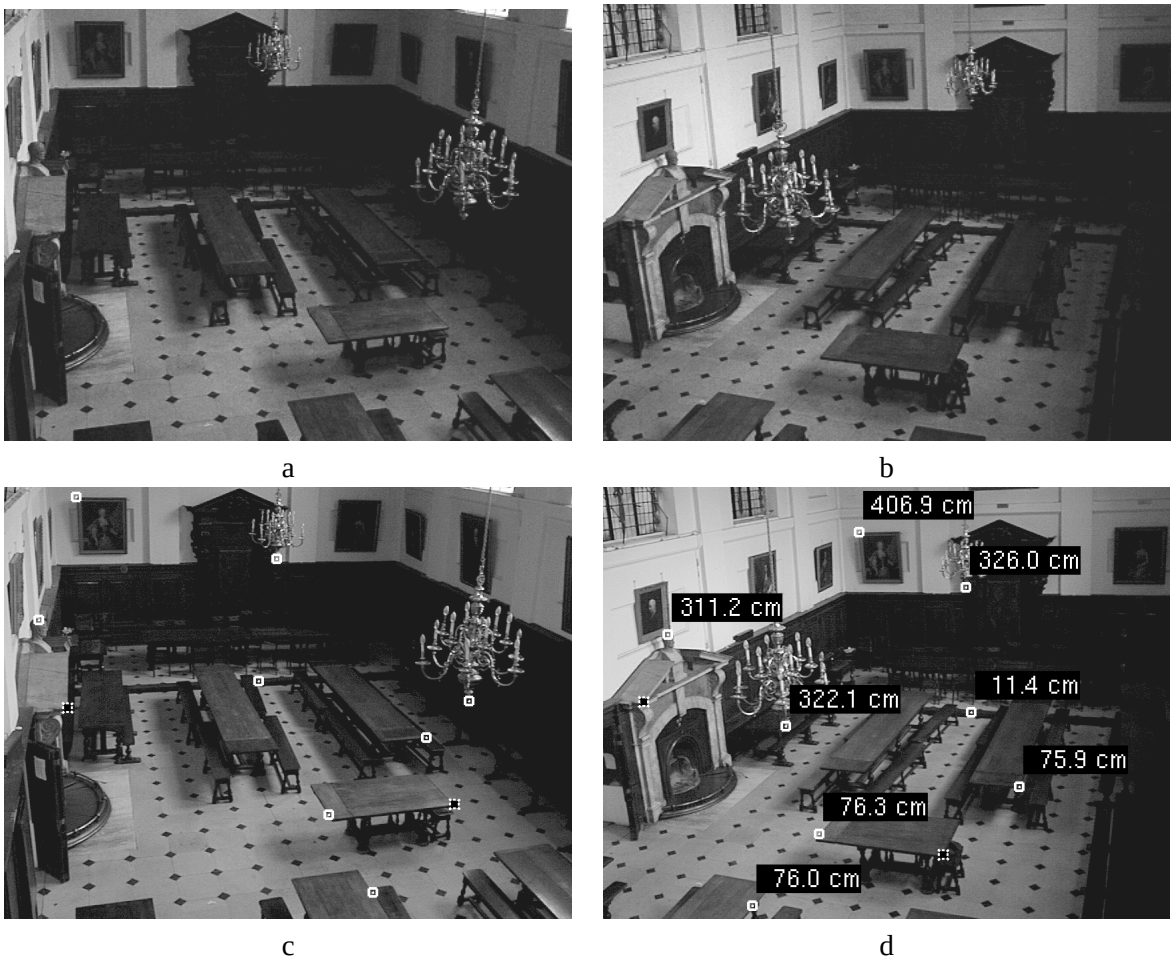

Figure 6.14: **Estimating the heights of points from two views of The Queen's College dining hall:** (a) and (b) original left and right images; (c) and (d) the heights of the two reference points, shown black on white, were measured by hand to be 76cm (table top), and 230cm (fireplace). Note, for instance, that the step was computed to be 11.4cm high and measured by hand as 11.0cm.

the corresponding ones on the second image (see fig 6.15). Furthermore, let $\mathbf{l}$ be the intersection line in the first image and $\mathbf{l}'$ the corresponding line on the second image, then

$$\mathbf{l}' = \mathtt{H}_1^{-\top}\mathbf{l}, \quad \mathbf{l}' = \mathtt{H}_2^{-\top}\mathbf{l} \tag{6.40}$$

from which [110]

$$\tilde{\mathtt{H}}\mathbf{l} = \lambda \mathtt{I}\mathbf{l} \tag{6.41}$$

with $\tilde{\mathtt{H}} = \mathtt{H}_2^{\top}\mathtt{H}_1^{-\top}$. The 3×3 matrix $\tilde{\mathtt{H}}$ represents a homology, since it has a repeated eigenvalue (see section 3.3.3). The line $\mathbf{l}$ on the first image is the unique eigenvector corresponding to the different

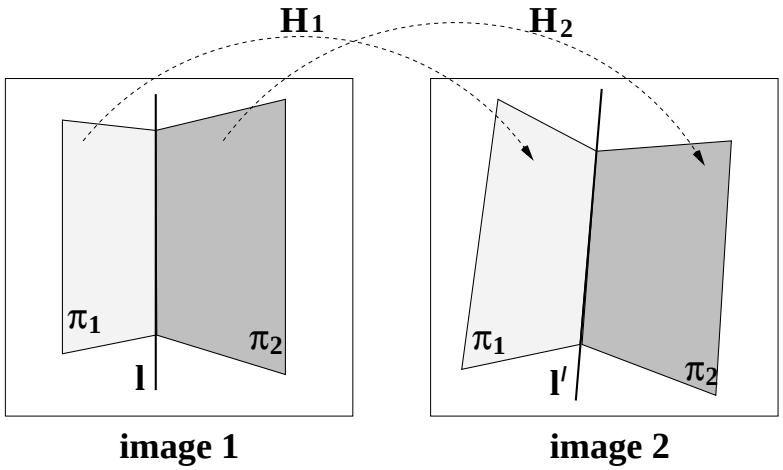

Figure 6.15: **Computing the line of intersection between two planar surfaces** using planar homographies and two views.

eigenvalue of the matrix $\tilde{\mathtt{H}}$. The intersection line $\mathtt{l}'$ on the second image is computed simply by applying (6.40).

Using plane-plus-parallax. In the previous approach the inter-image homographies for both planes are required. Employing the plane-plus-parallax approach the problem of computing the line of intersection between two planes reduces to:

- choosing one plane as reference and computing the inter-image homography induced by that plane between the two images (as usual from at least four correspondences);
- defining three pairs of corresponding points on the second plane (they define the images of the tripoint plane);
- projecting those points into the other image via the homography, thus defining the other two shadow triangles;
- the intersection lines $\mathtt{l}$ and $\mathtt{l}'$ are the images of the tripoint line and are computed by fitting a line through the points of intersection of corresponding sides of the two shadow triangles in each image.

This approach has the advantage that the inter-image homography induced by the second plane does not need to be known, with only three point correspondences sufficient (affine mapping). Likewise it is straightforward to prove that also two line correspondences on the second plane are sufficient.

Figure 6.16 shows an example. Figures 6.16a and 6.16b show two images of an indoor scene, taken from two different points of view. Figures 6.16c and 6.16d show the same images where we have marked the four points used (corners of the poster) to compute the inter-image homography induced by the left wall, and the two triangles and the computed intersection lines.

Since the two shadow triangles in each image are in a Desargues configuration the lines through corresponding vertices intersect in the epipole. Therefore the triangles are related in each image by a homology whose vertex is the epipole and the axis is the tripoint line.

An alternative derivation of the intersection line is as follows: from 6 points (4 coplanar) the F matrix and the inter-image homography for one of the two planes are determined. From one more point off the plane the inter-image homography induced by the second plane is defined and therefore the first method can be applied.

6.5 Uncertainty analysis

As in section 5.4 here we analyze how input errors propagate through the computations in order to estimate the uncertainty on the final distance measurements. This is achieved by employing, once more, first order error analysis. The validity of the approximation is assessed in section 6.5.4 by Monte Carlo statistical tests.

The uncertainty analysis has been developed here for the case of distances computed directly from the images. However it can be easily extended to the distinguished plane case.

6.5.1 Uncertainty on camera distances

When computing distances of cameras from planes (6.35) uncertainty arises from the uncertain locations of the reference pairs $\mathbf{p}$, $\mathbf{p}'$, $\mathbf{q}$, $\mathbf{q}'$, the uncertainty location of their 3D counterparts, the

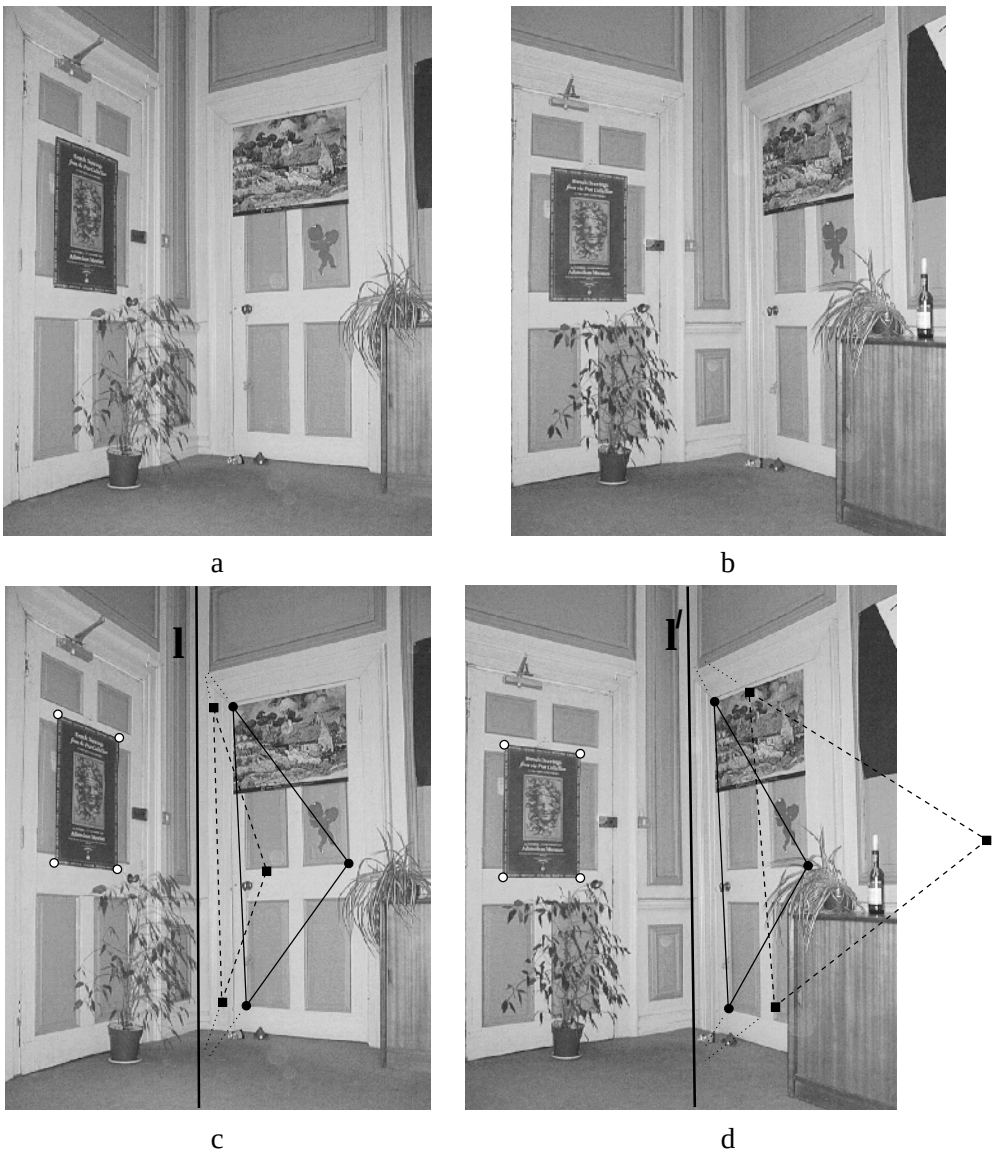

Figure 6.16: **Computing the line of intersection between two planar surfaces:** (a) and (b) original left and right views of a corner of a room; (c) and (d) the four vertices of the poster on the left wall (marked with white circles) have been used to compute the inter-image homography induced by the left wall; the three corresponding points on the right wall (black circles) define the tripoint triangle; these points have been projected via the homography into the other view (black squares); the two shadow triangles are shown (dashed); the lines of intersection between the two walls have been computed by intersecting the corresponding sides of the two shadow triangles in each view.

uncertainty in the inter-image homography and the uncertainty in the plane vanishing line $\mathbf{l}$. Uncertainties in image reference points and plane vanishing line are modelled by 3×3 homogeneous covariance matrices. The uncertainty of the inter-image homography $\mathtt{H}$ is defined by a 9×9 homogeneous covariance matrix and can be computed as in sec. 4.3.2.

By using a first order propagation the variance of the distance Z_{O_1} of the first camera from the reference plane is given by

$$\sigma^2_{Z_{O_1}} = \boldsymbol{\nabla}_{Z_{O_1}} \Lambda \boldsymbol{\nabla}^\top_{Z_{O_1}} \tag{6.42}$$

where the 26×26 covariance matrix Λ is

$$\Lambda = \mathrm{diag}\left(\Lambda_{\mathbf{l}}, \Lambda_{\mathbf{h}}, \sigma^2_{Z_\mathrm{p}}, \Lambda_{\mathbf{p}}, \Lambda_{\mathbf{p}'}, \sigma^2_{Z_\mathrm{q}}, \Lambda_{\mathbf{q}}, \Lambda_{\mathbf{q}'},\right)$$

with all the covariance matrices homogeneous and the 1×26 Jacobian $\boldsymbol{\nabla}_{Z_{O_1}}$

$$\boldsymbol{\nabla}_{Z_{O_1}} = \begin{pmatrix} \frac{\partial Z_{O_1}}{\partial \mathbf{l}} & \frac{\partial Z_{O_1}}{\partial \mathbf{h}} & \frac{\partial Z_{O_1}}{\partial Z_p} & \frac{\partial Z_{O_1}}{\partial \mathbf{p}} & \frac{\partial Z_{O_1}}{\partial \mathbf{p}'} & \frac{\partial Z_{O_1}}{\partial Z_q} & \frac{\partial Z_{O_1}}{\partial \mathbf{q}} & \frac{\partial Z_{O_1}}{\partial \mathbf{q}'} \end{pmatrix}$$

The computation of $\boldsymbol{\nabla}_{Z_{O_1}}$ is described in appendix F. Similar analysis applies for the estimation of $\sigma^2_{Z_{O_2}}$.

6.5.2 Uncertainty on distance of points

When computing distances of points from planes (6.39), uncertainty arises from the sources analyzed in the previous section and from the uncertain image locations of the points $\mathbf{x}$ and $\mathbf{x}'$. The uncertainty in each of the points $\mathbf{x}$, $\mathbf{x}'$ (resulting largely from the finite accuracy with which these features may be located in the image) is modelled by 3×3 homogeneous covariance matrices $\Lambda_{\mathbf{x}}$ and $\Lambda_{\mathbf{x}'}$.

Maximum Likelihood Estimation of the input points. Note that here, as in chapter 5, a constraint on the location of the two input points $\mathbf{x}$ and $\mathbf{x}'$ exists. In this case the epipolar geometry constrains the two points to lie on each other's epipolar line. Therefore, as in section 5.4.2 a Maximum Likelihood Estimate of the true points $\hat{\mathbf{x}}$ and $\hat{\mathbf{x}}'$ can be performed [54].

Not considering this intermediate step introduces a further approximation into the uncertainty propagation procedure. Nevertheless, the degradation of the results due to neglecting the ML estimation has proven smaller than the approximation introduced by the first order truncation in the case that the two points $\mathbf{x}$ and $\mathbf{x}'$ are sufficiently close to the relative epipolar lines.

In order to keep the uncertainty analysis simple, then, the ML estimation of the true position of the input points has not been performed. The validity of the analysis is, as usual, assessed by Monte Carlo statistical tests.

Variance of distance. By using a first order uncertainty propagation and assuming statistical independence in all the different sources of error the variance of Z_x is given by

$$\sigma_{Z_x}^2 = \boldsymbol{\nabla}_{Z_x} \Lambda \boldsymbol{\nabla}_{Z_x}^\top \tag{6.43}$$

where the 32×32 covariance matrix Λ is

$$\Lambda = \operatorname{diag}\left(\Lambda_{\mathbf{l}}, \Lambda_{\mathbf{h}}, \sigma_{Z_\mathrm{p}}^2, \Lambda_{\mathbf{p}}, \Lambda_{\mathbf{p}'}, \sigma_{Z_\mathrm{q}}^2, \Lambda_{\mathbf{q}}, \Lambda_{\mathbf{q}'}, \Lambda_{\mathbf{x}}, \Lambda_{\mathbf{x}'}\right)$$

with all the covariance matrices homogeneous and the 1×32 Jacobian $\boldsymbol{\nabla}_{Z_x}$

$$\boldsymbol{\nabla}_{Z_x} = \begin{pmatrix} \frac{\partial Z_x}{\partial \mathbf{l}} & \frac{\partial Z_x}{\partial \mathbf{h}} & \frac{\partial Z_x}{\partial Z_p} & \frac{\partial Z_x}{\partial \mathbf{p}} & \frac{\partial Z_x}{\partial \mathbf{p}'} & \frac{\partial Z_x}{\partial Z_q} & \frac{\partial Z_x}{\partial \mathbf{q}} & \frac{\partial Z_x}{\partial \mathbf{q}'} & \frac{\partial Z_x}{\partial \mathbf{x}} & \frac{\partial Z_x}{\partial \mathbf{x}'} \end{pmatrix} \tag{6.44}$$

Detailed description of the computation of $\boldsymbol{\nabla}_{Z_x}$ is given in appendix F.

6.5.3 Example

Figure 6.17 shows an example where heights of points and the associated uncertainties are computed for an indoor scene. Figure 6.17a and 6.17b are, respectively, left and right views of the interior of a chapel. We wish to measure perpendicular distances of points of the lectern from the floor.

Two perpendicular heights have been measured by hand as reference (marked as white boxes). The inter-image homography between the two images has been estimated from four corresponding points on the floor tiling. Distances of several lectern points (marked as white circles) from the floor

have been computed by using the described parallax method. A 3-standard deviation uncertainty ellipse has also been defined for each point and then the 3-standard deviation uncertainty associated with the final measurement has been estimated and displayed. Notice in fig. 6.17c that the ground truth always falls within the computed uncertainty range.

6.5.4 Validation of uncertainty analysis

This section validates the first order error analysis described above by estimating the uncertainty in height of the beak of the eagle in the lectern in fig. 6.17. It compares the results from the first order analytical method to the uncertainty derived from Monte Carlo simulation as described in table 6.5. The diagrams in figure 6.18 illustrate the results.

In the simulations Gaussian noise is assumed on the image points of the two reference distances and on their world height. Uncertainty is assumed also on the plane vanishing line, on the inter-image homography and on the image points of the height to be measured.

The input point $\mathbf{x}$ on the left image is randomly distributed according to a 2D non-isotropic Gaussian about the mean location, with covariance matrix $\Lambda_{\mathbf{x}}$ (figure 6.18a). Similarly the corresponding point on the right image is randomly distributed according to a 2D non-isotropic Gaussian about the mean location $\mathbf{x}'$, with covariance $\Lambda_{\mathbf{x}'}$ (figure 6.18b).

The two covariance matrices for the pair of input points are respectively (values in $pixel^2$):

$$\Lambda_{\mathbf{x}} = \begin{pmatrix} 0.255081 & -0.0237127 \\ -0.0237127 & 0.265752 \end{pmatrix} \quad \Lambda_{\mathbf{x}'} = \begin{pmatrix} 0.484301 & -0.14857 \\ -0.14857 & 0.56621 \end{pmatrix}$$

Suitable values for the covariances of the two references, and the vanishing line have been used. The covariance of the inter-image homography has been computed as in section 4.3.2. The simulation has been run with $N = 10000$ samples.

Analytical and simulated distributions of Z_x are plotted in figure 6.18c; the two curves are almost overlapping. Any slight difference is due to the assumptions of statistical independence and first order truncation introduced by the error analysis.

a b

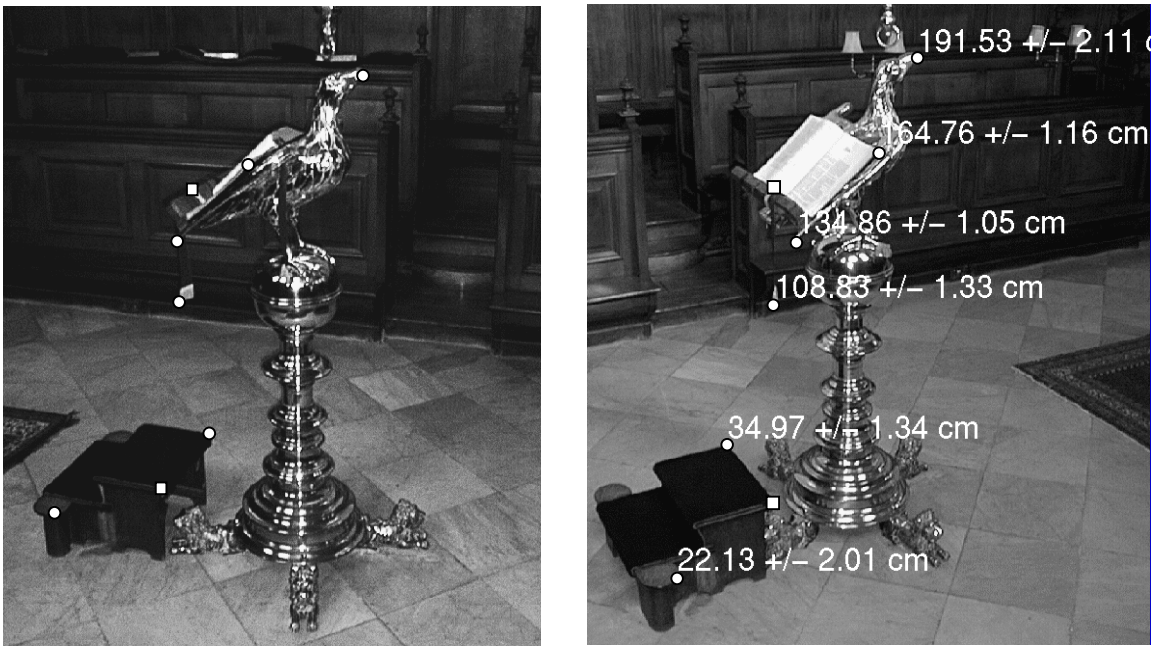

c d

Measured	191.5	165.0	135.0	109.1	35.0	22.9
Computed	191.5 ± 2.1	164.7 ± 1.2	134.8 ± 1.0	108.8 ± 1.3	34.9 ± 1.3	22.1 ± 2.0

e

Figure 6.17: **Estimating heights and associated uncertainties from two views of the lectern in The Queen's College chapel:** (a) and (b) original left and right images; (c) and (d) the heights of the reference points (white squares) were measured by hand (± 0.5cm) to be 150cm (top edge of lectern), and 35cm (height of foot stool). In (e), all height measurements are given in centimetres. The error between the heights computed using the image parallax and the ones measured manually is always less than one centimetre. The 3-standard deviation uncertainties of the computed heights are shown too. Note that the ground truth falls always within the computed uncertainty range.

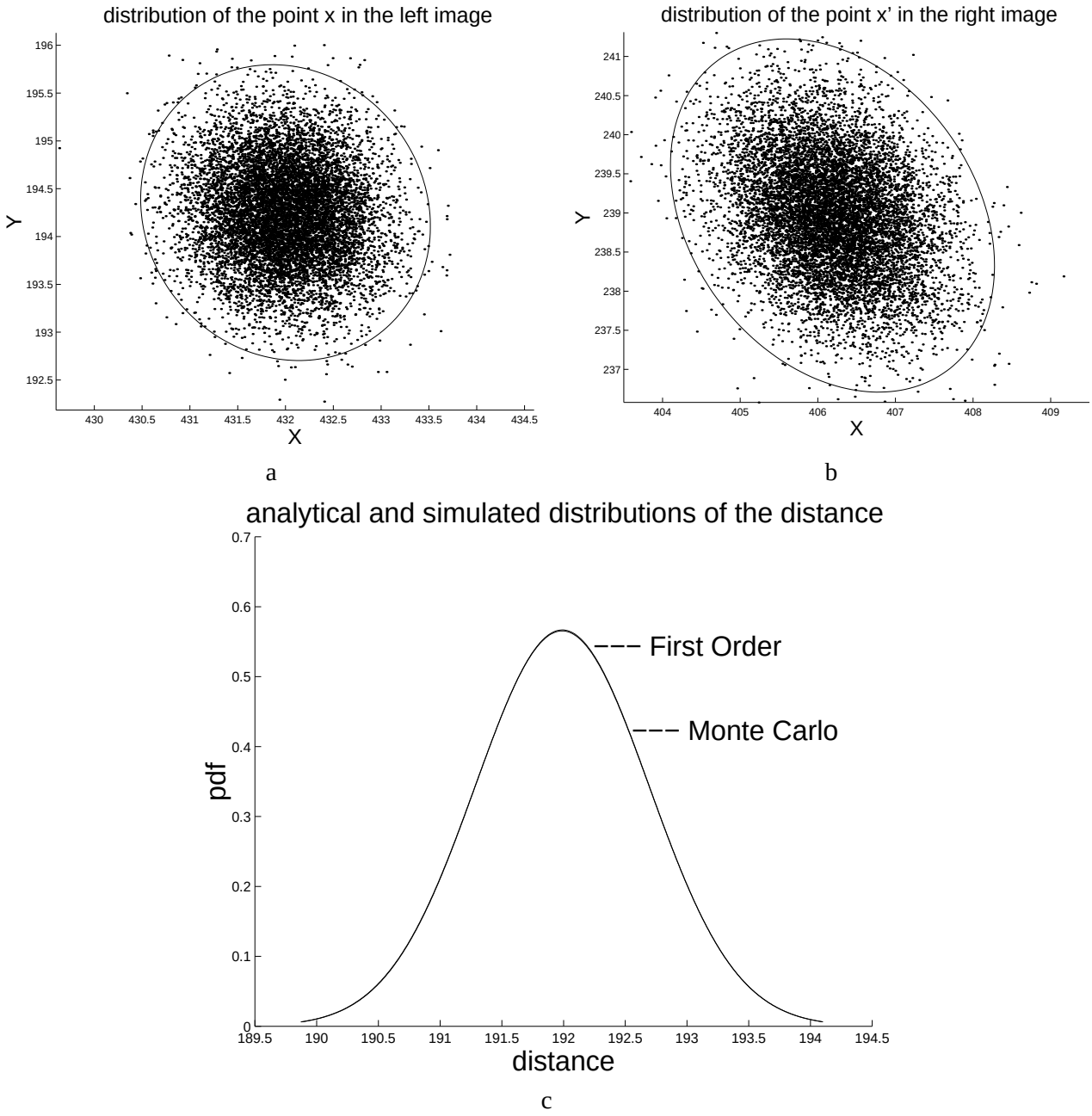

Figure 6.18: **Monte Carlo simulation of the example in fig. 6.17:** (a) distribution of the input point $\mathbf{x}$ on the left image and the corresponding 3-standard deviation ellipse. (b) distribution of the input point $\mathbf{x}'$ on the right image and the corresponding 3-standard deviation ellipse. Figures (a) and (b) are drawn at the same scale; (c) the analytical and simulated distributions of the computed distance Z. The two curves are almost perfectly overlapping.

- for j=1 to N (with N = number of samples)
  - For each of the two references: given the measured reference points on left and right image, generate a random point on the left image, a random point on the right image and random reference distance according to the associated covariances.
  - Generate a random plane vanishing line according to its covariance $\Lambda_{\mathbf{l}}$.
  - Generate random values for the inter-image homography $\tilde{\mathbf{H}}$ according to the computed 9×9 covariance matrix $\Lambda_{\mathbf{h}}$.
  - Generate a random point $\mathbf{x}_j$ on the left image and a random point $\mathbf{x}'_j$ on the right image according to their respective covariances $\Lambda_{\mathbf{x}}$ and $\Lambda_{\mathbf{x}'}$.
  - Compute the current distance Z_{x_j} by applying (6.35).
- The statistical standard deviation of the population of simulated Z_{x_j} values is computed as

$$\sigma'^2_Z = \frac{\sum_{j=1}^{N}(Z_j - \overline{Z})^2}{N-1}$$

and compared to the analytical one (6.43).

Table 6.5: **Monte Carlo simulation.**

A comparison between statistical and analytical standard deviations is reported in the table below with the corresponding relative error:

First Order σ_{Z_x}	Monte Carlo σ'_{Z_x}	relative error $\frac{\lvert\sigma_{Z_x} - \sigma'_{Z_x}\rvert}{\sigma'_{Z_x}}$
0.7039 cm	0.70561 cm	0.24 %

The measurement $Z = 191.8cm$ and the associated first order uncertainty $3 * \sigma_{Z_x} = 2.11cm$ is shown in fig. 6.17d.

Similar tests on several other examples consistently yield the same results. This shows that also in the plane-plus-parallax approach, for typical imaging situations, the first order approximation is a valid one.

As usual, some care must be exercised since the relative error between statistical and analytical output standard deviations increases with the input uncertainty. For large covariances, the assumption of linearity becomes less well founded.

Chapter 7

Gallery of examples

7.1 Introduction

This chapter shows examples of reconstructions obtained employing the techniques described in chapters 4 and 5. The techniques have been applied to both real scenes and perspectively correct paintings. Convincing animations and fly-throughs have also been created[1].

7.2 Reconstruction from photographs

Colour images of the three dimensional model of a garden shed reconstructed from a single photograph appear in figure 7.1. The reconstruction algorithm employed is described in section 5.6.

The height and position of the person is computed correctly but, since it is not possible to recover volume from one image alone, the person is represented as a flat silhouette. The outline of the silhouette was extracted by fitting a spline curve to the contour of the image.

7.3 Reconstruction from paintings

Linear Perspective can be described mathematically by Projective Geometry. If a painting conforms to the rules of Linear Perspective (see section 1.4.3) then it behaves geometrically as a perspective image and it can be treated as a photograph. The metrology techniques previously described can thus be applied to compute the structure of the scene. Since no Euclidean scene measurements are known (usually the scenes depicted do not exist), the models are obtained up to a similarity

[1] The reconstructed 3D environments can be "virtually explored" in the VR-CUBE at KTH, Stockholm. VRML three-dimensional models, and MPEG animations can also be viewed at the following web page:
`http://www.robots.ox.ac.uk/~vgg/projects/SingleView/`

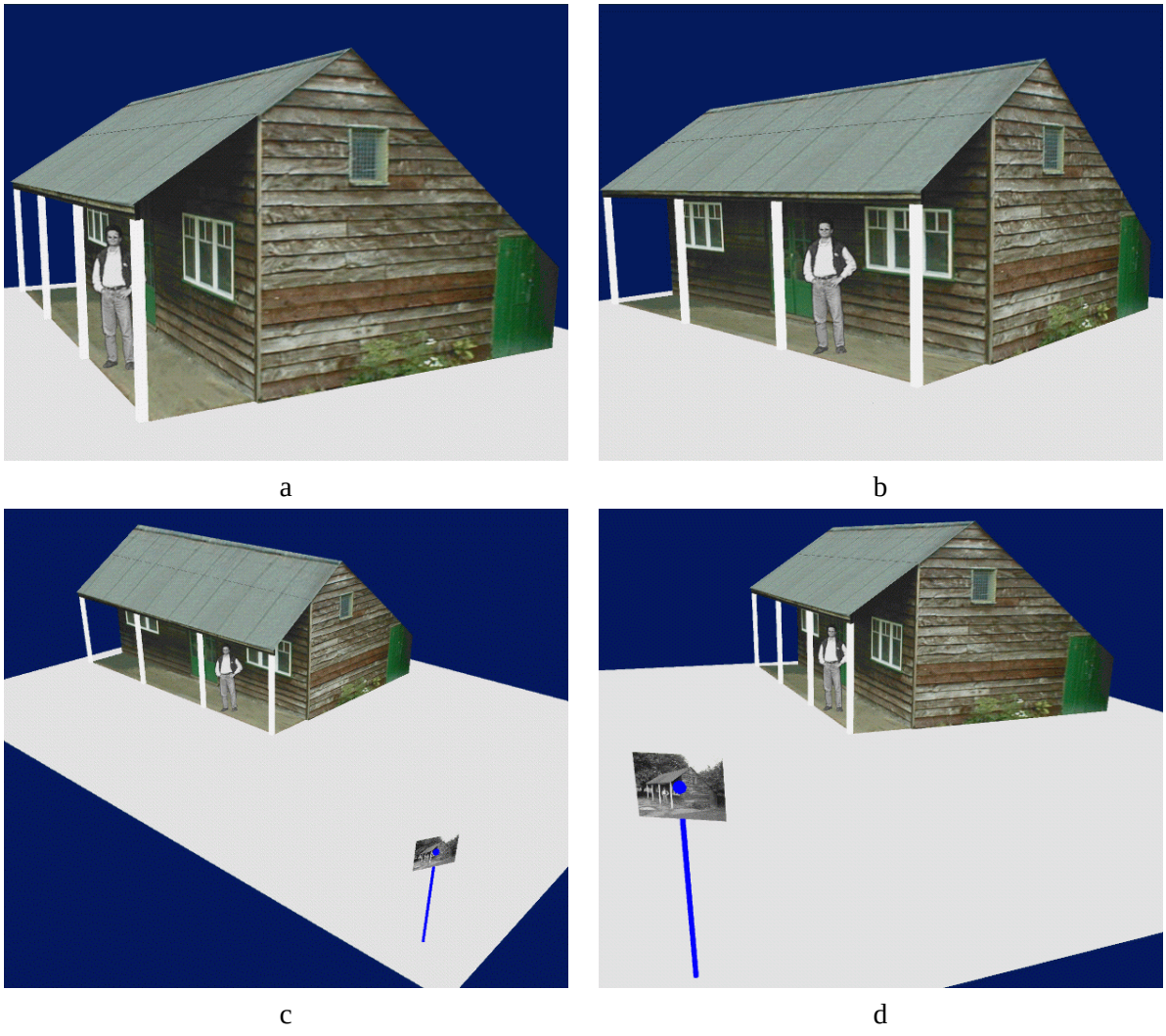

Figure 7.1: **3D reconstruction of a garden shed:** (a) and (b) two views of the reconstructed three-dimensional model of the shed in figure 5.23a. The person is represented as a flat silhouettes since it is not possible to recover its volume from one image. The silhouette has been cut out manually from the original image and positioned in the correct place; (c) and (d) two more views of the 3D model showing the computed camera position.

transformation. This level of reconstruction is precisely that required for a graphical 3D model where the absolute pose and scale are not necessary for visualization.

The correctness of the perspective in the paintings considered has been assessed by computing the location of vanishing points and vanishing lines. Perspective distortion in repeated patterns (e.g. the rate of diminution of the coffers on the curved vault in fig. 7.2a or the tiles on the floor in

fig. 7.4a) has been checked using cross-ratios.

7.3.1 La Trinità

La Trinità (in fig. 7.2a) is a fresco. It is, arguably, the first perspective image in history; the first example of the application of Filippo Brunelleschi's rules of perspective.

A three-dimensional model of the chapel represented in the top half of the fresco has been computed here by applying the algorithm described in chapter 5. Different views of the model are shown in figure 7.2b-e. Notice the hemi-cylindrical vault. The parts of the vault which are occluded by the capitals and by the head of God have been left blank. Their texture can be filled in by making use of the regularity of the pattern.

Ambiguity in recovering depth. Since one image alone is used and no scene metric information is known (the chapel is not real), an ambiguity arises in the reconstruction. It is not possible to recover the depth of the chapel without making some assumptions about the geometry of the scene. Two equally valid assumptions can be made: either the coffers on the vault of the chapel are square (this is the assumption used in the model in fig. 7.2) or the floor is square.

Both models have been computed (the two reconstructions are mathematically related by an affine transformation, a scaling in one direction). Images of the floor of the chapel and of the pattern on the cylindrical vault are shown in figure 7.3 from both cases.

This shows that the two assumptions cannot coexist in the same reconstruction even though the ambiguity is not apparent to the naive observer. Speculations about which of the two configurations is the one that most likely the artist wanted to represent are left to the reader.

7.3.2 La Flagellazione di Cristo

La Flagellazione di Cristo (in fig. 7.4a) is one of the most studied paintings from the Italian Renaissance period; mostly because of the "obsessive" correctness of its perspective [64]. In the past the

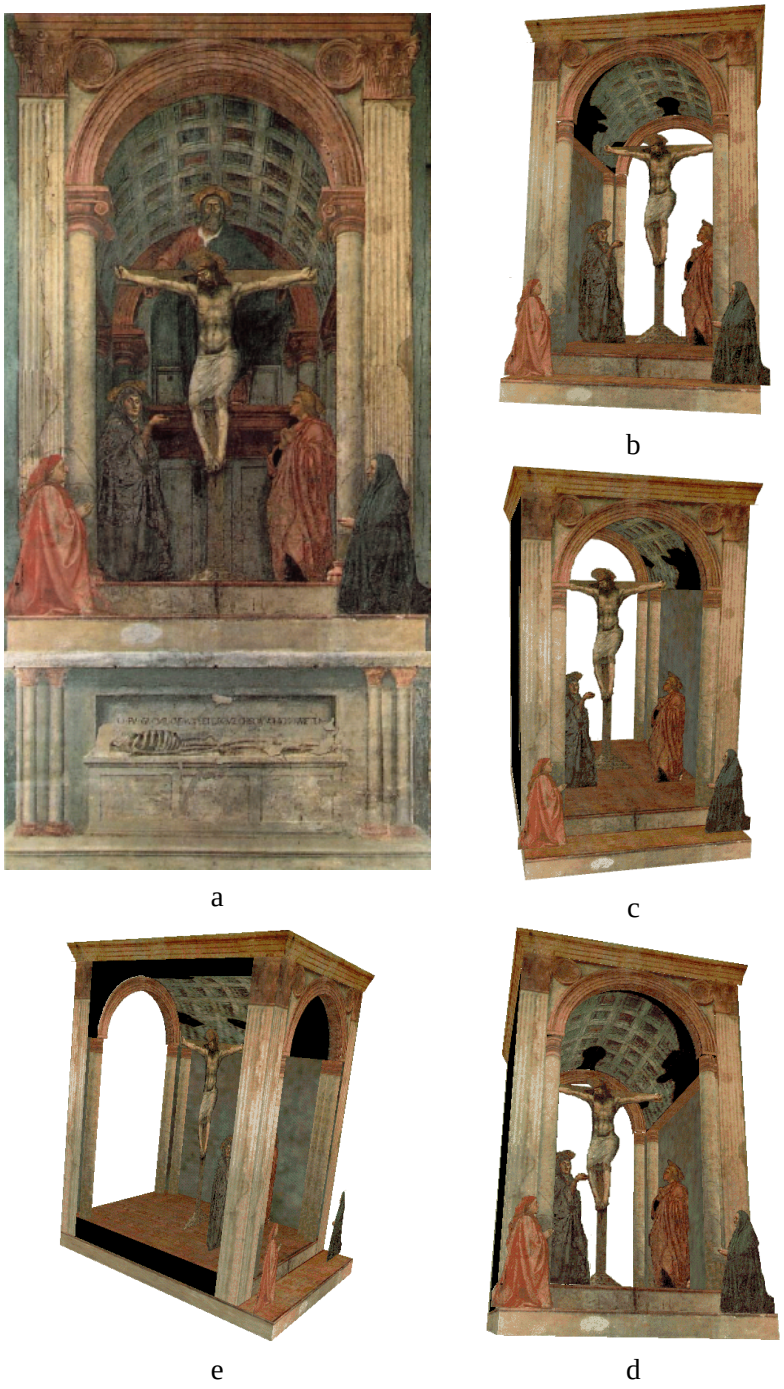

Figure 7.2: **3D reconstruction of "La Trinità":** (a) *La Trinità* (1426, Florence, Santa Maria Novella); fresco by Masaccio (1401-1428); (b) view of the reconstructed 3D model of the chapel from the right. Notice the hemi-cylindrical vault; (c) view of the model from the left; (d) view of the model from below; (e) a more extreme view from the left side. The left wall has been removed to show the inside structure of the chapel.

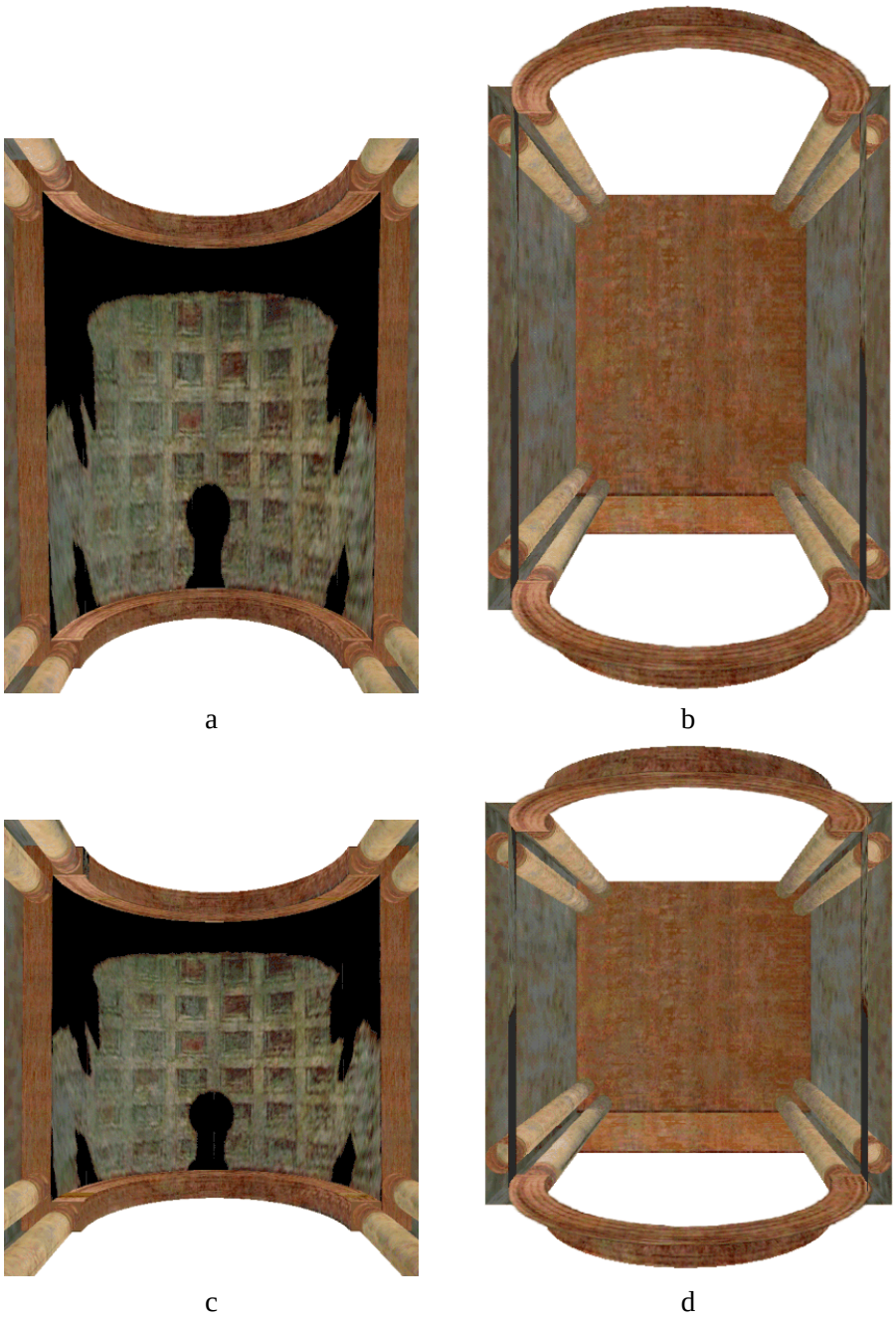

Figure 7.3: **Comparing two possible reconstructions of "La Trinità":** (a) and (b) view of the vault and view of the floor assuming *square coffers*. The base plane is rectangular; (c) and (d) view of the vault and view of the floor assuming *square floor*. The coffers are rectangular. A simple affine mapping relates the two reconstructions.

painting has attracted the interest of several artists and art historians who, in different ways, have been studying its carefully represented geometry.

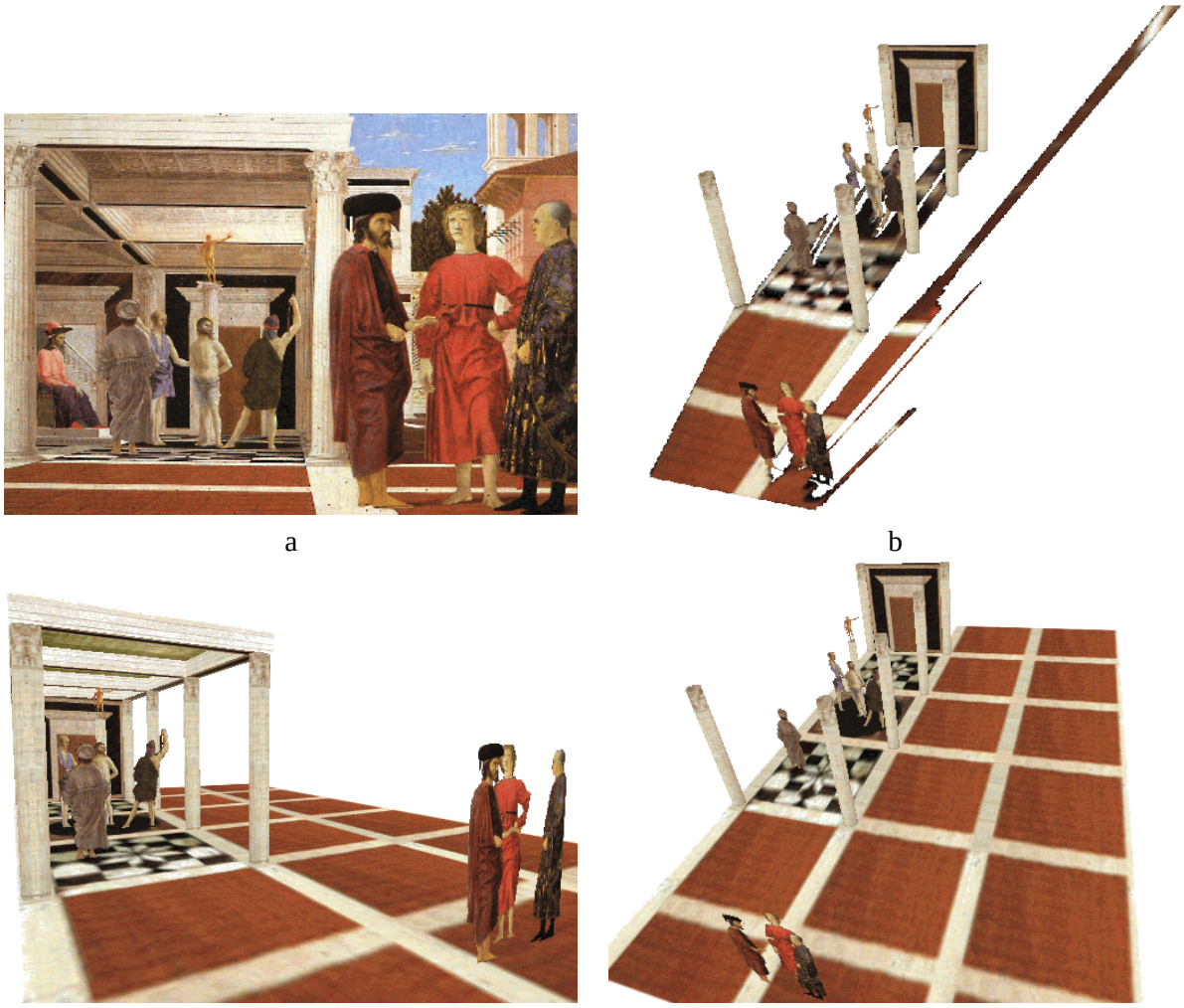

Figure 7.4: **3D reconstruction of "La Flagellazione di Cristo":** (a) *La Flagellazione di Cristo* (1460, Urbino, Galleria Nazionale delle Marche); by Piero della Francesca (1416-1492); (b) a view of the reconstructed 3D model with the roof removed to show the relative positions of people and architectural elements in the scene. The occlusions on the floor have been left blank and the people are represented as flat silhouettes. The columns have been approximated by cylinders; (c) another view of the reconstructed 3D model where the patterned floor has been reconstructed in areas where it is occluded by taking advantage of the symmetry of its pattern. Note the repeated geometric pattern on the floor in the area delimited by the columns (barely visible in the original painting) (d) another view of the model with the roof. The partially seen ceiling has also been reconstructed.

Since this painting conforms faithfully to the rules of Linear Perspective the depicted scene can correctly be reconstructed in three dimensions. Images of the computed model, taken from different viewpoints are shown in figure 7.4b-d.

7.3.3 St Jerome in his Study

St Jerome in his Study (in fig. 7.5a) is an oil painting by the Dutch artist H. Steinwick (1580-1649). It is particularly interesting for two reasons: the correctness of the perspective (when this masterpiece was realized Linear Perspective was a well established theory) and the amazing management of light and shading. The sunlight streaming through the window gives the painting a beautiful photo-realistic touch.

Numerous parallel lines and planar surfaces have been detected and employed to produce the reconstruction results illustrated in figure 7.5b-f.

Detecting inconsistencies in the perspective rendering. Figure 7.6a shows a fronto-parallel view of the big window on the left wall of the scene. This image has been obtained, as usual, by rectifying the original texture in the painting by inferring affine and metric information (parallel lines and right angles) on the wall plane.

Notice that while parallelism and angles have been recovered correctly (look at the window pattern) a strange, asymmetric curvature of the top arch can be detected. That is due to the fact that the artist has painted a fairly complicated curve on a very slanted view of the window (compare with the original painting in fig. 7.5a). Large uncertainty characterizes the localization of points in such a situation (*cf.* examples in section 4.4.2). The error is less evident in views taken from locations closer to the original viewpoint (figure 7.6b).

7.4 Discussion

At this point I would like to invite the reader to reflect on a particular aspect of the relationship between science and art.

Some Computer Vision researchers describe their field as a combination of **maths**, **science** and **engineering** [79]. But is that all ? Is there any space left for **art**? Can art help us understand

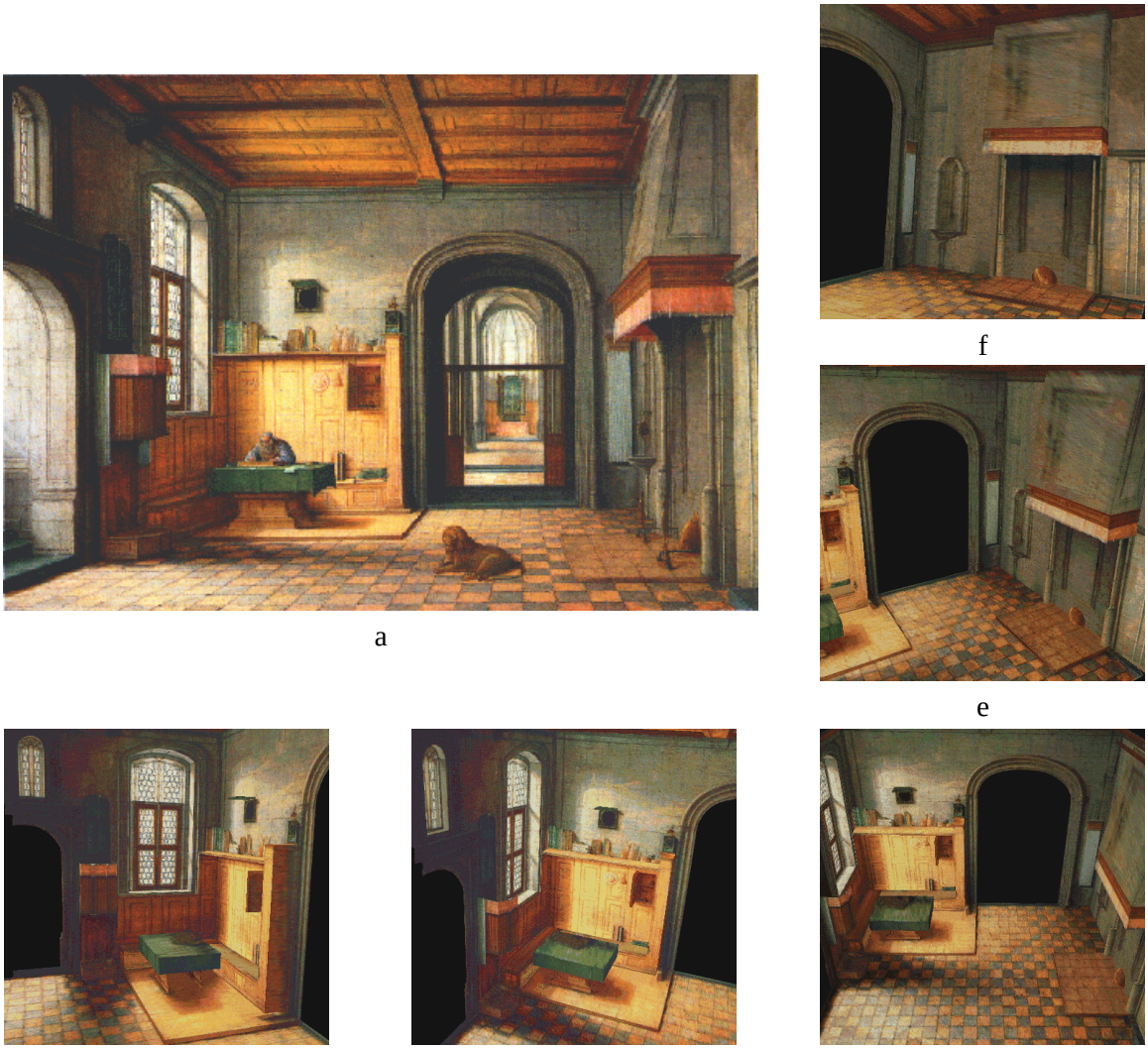

Figure 7.5: **3D reconstruction of "St Jerome in his Study":** (a) *St Jerome in his Study* (1630, Joseph R.Ritman Collection) by Henry V Steinwick (1580-1649); (b-f) different views of the reconstructed 3D model; (b) the left wall; the texture of the partially seen windows has been reconstructed by making use of the symmetrical pattern in their texture; (c) the corner where St Jerome is working; (d) view of the whole study from above; (e) view of the fireplace from above; (f) another view of the fireplace.

vision or vice-versa?

For instance, when looking at photographs of a scene visual cues such as converging straight lines, shading effects, texture, shadows, and specularities are processed by our brain to retrieve consistent information about the surrounding 3D world.

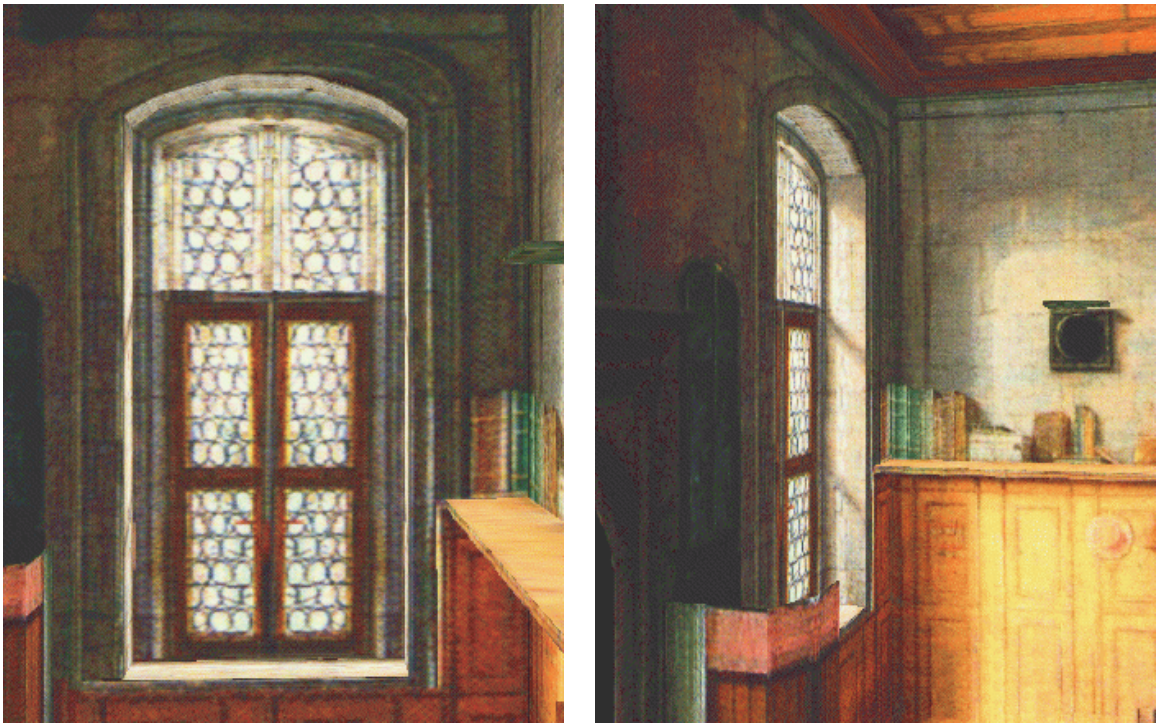

a b

Figure 7.6: **Comparing two views of a window in a reconstruction of "St Jerome in his Study":** (a) a fronto-parallel view of the window on the left wall of the reconstructed model of "St Jerome in his Study". The right part of the arch is not correct; (b) it is harder to notice the error in the arch curvature from a point of view closer to the original one.

The same cues are employed by artists in their paintings. However, since these works of art are not created by an automatic imaging process (such as a camera) but by the skilled hands of a painter, they are prone to personal interpretation and inaccuracies. These visual signals might therefore not be consistent with each other (e.g. images of parallel lines may not intersect in the same point). However, they might still convey the desired three-dimensional illusion (*cf.* fig. 7.7a).

A number of questions arise: which perceptual cues are more important to the 3D illusion? To what extent do humans forgive wrong cues? Since paintings and single photographs are capable of conveying an illusion of the 3D space, how necessary is stereo vision? These points may also lead the way to further physiological speculations.

On the other hand Projective Geometry can provide artists and art historians with fast and

powerful mathematical tools (e.g. planar projections, cross-ratio) to answer questions like: how do I construct the geometry of the painting such that the perspective looks correct when viewed from such a viewpoint? How correct is the perspective (e.g. vanishing points, perspective distortion) in Luca Signorelli's *La Circoncisione* (fig. 7.7b)? What does the pattern on the floor in Domenico Veneziano's *Pala di Santa Lucia* (fig. 7.7c) look like? Is the height of the foreground figures consistent with the height of the background figures in Raffaello's *Il Matrimonio della Vergine* (fig. 7.7d)?

In my opinion Computer Vision, Art and Art History are well distinguished fields, each with its own aims and motivations. Nevertheless, each might learn from and be enriched by the others. Furthermore, the tools developed in one area may be useful in another.

a

b

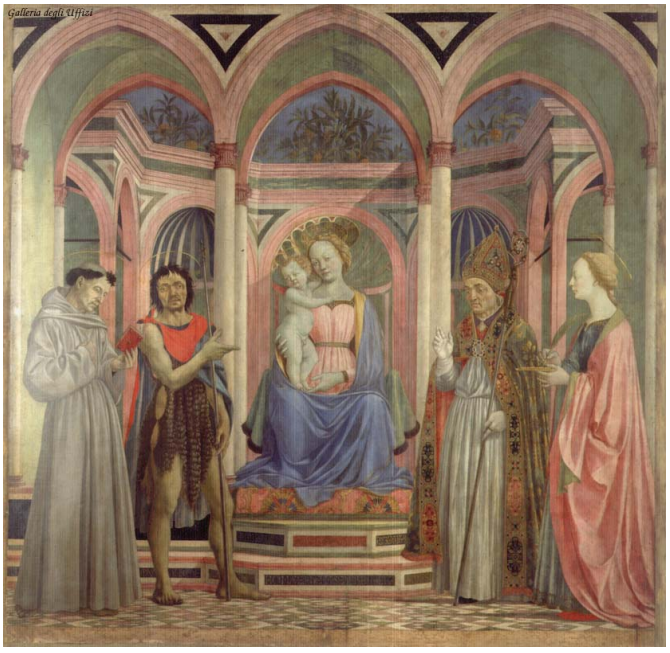

c

d

Figure 7.7: (a) *The Arnolfini Marriage* (1434, London, National Gallery) by Jan van Eyck (active from 1422–1441). (b) *La Circoncisione* (London, National Gallery) by Luca Signorelli (1445–1523). (c) *Pala di Santa Lucia* (1444, Firenze, Uffizi) by Domenico Veneziano (1400–1461). (d) *Il Matrimonio della Vergine* (1504, Milano, Brera) by Raffaello (Raffello Sanzio) (1483–1520).

Chapter 8

Conclusion

8.1 Summary

This thesis has developed new, flexible and accurate algorithms for the use of a camera as a 3D measuring device.

A solid theoretical framework employing techniques drawn from Projective Geometry has been developed to compute measurements from single and multiple uncalibrated views.

The process of measuring has been treated as a true engineering task, therefore particular attention has been paid to predicting the uncertainty on the final measurements due to the uncertainty on the input data.

The theory in this thesis has been developed in steps: from simpler metrology on planar surfaces to more complicated three-dimensional measurements and from single to multiple images.

Metrology on planes. At the beginning of the thesis we have shown how to compute measurements on planar surfaces (chapter 4). Distances between points and parallel lines, image rectification and image mosaicing have been demonstrated.

The effectiveness of such techniques has been demonstrated with an application capable of computing measurements from single images of indoor and outdoor scenes as well as rectifying projectively distorted views and mosaicing together several images of a planar structure.

Planar projective mappings such as homographies and homologies have proven extremely useful, simple and powerful mathematical tools and they have been employed throughout the thesis.

Single view metrology. We have also explored how three-dimensional affine measurements can be retrieved from single views (chapter 5). The key has been the novel parametrization of the 3D space as a collection of pencils of parallel planes. 3D geometry has been successfully described in terms of the relationships between homographies, homologies and 3D-2D projective mappings.

This approach has made possible the reconstruction of the 3D space in a stratified fashion. The available scene information may be used to upgrade the computed structure from affine to Euclidean.

This work has been applied successfully to a number of different areas: scientific, artistic and commercial. Applications employing some of the presented algorithms have been developed and they are currently used by forensic companies.

Metrology from planar parallax. The use of a multi-view approach in cases where single view techniques are not sufficient has been addressed.

We have investigated the use of a plane-plus-parallax approach to make optimal use of the redundancies between different views of a scene. This has led to the discovery of elegant duality relationships between configurations of points and cameras as described in chapter 6.

Furthermore, we have demonstrated that the fundamental geometric constraints (epipolar geometry and trifocal tensor) are captured by a planar homology relating the images of points across views. Consequently, a number of previously diverse results related to planar parallax, duality and planar homologies have been unified.

Formulae for determining distances of cameras and points from a world plane have been presented, with the proper uncertainty analysis, and have been tested on real images.

8.2 Discussion

Advantages and disadvantages of the proposed metrology algorithms are discussed in this section.

An accurate and reliable measuring device. Camera internal parameters are quite unstable and sensitive to variation in temperature or mechanical shock. Metrology algorithms which rely on the camera calibration are therefore strongly affected by such instability.

The proposed algorithms do not make use of internal calibration, thus leading to greater robustness and reliability. Since no knowledge about the cameras is needed the algortihms can be applied to existing images.

The accuracy of the measuring device described in this thesis has been modelled mathematically, thus providing a tool to assess the precision of the output measurements given uncertain input data and transformations. Moreover, the uncertainty analysis provides a powerful tool to increase the accuracy on the measurements. In fact, by observing the behaviour of the predicted accuracy, the ideal location of camera and references can be chosen such that the output uncertainty is minimized. This makes the device particularly effective in typical engineering or architectural applications such as modelling buildings and interior design (see sec. 4.4).

As expected, the quality of the results increases with the resolution of the images. Nevertheless, a 1024×768 resolution has proven sufficient for the applications considered.

Robustness for noisy images. The images the metrology device is required to deal with may contain a large amount of random noise. This happens quite often in forensic data, where the images are recorded on old tapes.

Nevertheless, useful geometric cues (like edges) can still be detected even for large amount of noise. The precautions during the process of detecting lines and vanishing points (Canny edge detection, straight line fitting, edge merging and ML estimates of intersection points, *cf.* sec. 3.5)

provide the proposed metrology algorithms with an increased robustness and insensitivity to noise.

Flexibility. Since no internal camera calibration is required at any time this device can be applied to a wide range of input images: old footage, archived photographs, postcards and even paintings. Effectively the algorithms can deal with any perspective image, no matter how that is obtained or where it comes from.

This is demonstrated, in particular, by the interest shown by researchers in fields like Art History towards the capabilities offered by such techniques. Artists and art historians are becoming increasingly aware of the potential of modern technology. Some of the most fascinating applications such as taking measurements on a painted scene (real or not), reconstructing it as a Virtual Reality model and creating animations and fly-throughs have been presented in this thesis.

As mentioned above, these strongly geometrical techniques can only be applied to projective images. Therefore they are particularly useful when applied to paintings from the Italian Renaissance whose masters invented Linear Perspective [1]. Numerous perspective paintings are also found amongst the Dutch masterpieces of the seventeenth century and in some contemporary works of art.

Apart from the obvious applications in Art History and Computer Graphics, analyzing paintings can be a useful aid to the understanding of vision and the perception of the world around us.

Radial distortion correction. When a camera becomes part of a measuring device the accuracy and sensitivity of the camera itself has to be investigated. In particular, high quality lenses and high resolution CCD arrays may be required in order to get the most precise information from the viewed scene.

Quite often images taken with wide angle lenses cameras (often pictures of indoor scenes) are corrupted by lens-generated distortions like radial distortion. These images, therefore, are not perspective. A blind application of calibrated or uncalibrated metrology techniques would yield wrong

results. This problem has been overcome, in this thesis, by employing a simple and robust preprocessing stage where a radial correction algorithm (section 3.4) warps the image into a perspective one.

This correction algorithm, though, is no use when the camera lenses show more complicated aberrations. Most of the modern digital still or video cameras do not suffer this problem, and therefore the correction step is unnecessary.

Automation. The proposed metrology algorithms must be supervised. In fact, image interest features (e.g. edges and corners) are detected automatically and localized with great accuracy, but interactivity is necessary to make the right inference from the images: selecting a set of parallel lines or a set of planar points (orthogonality is not necessary); identifying reference distances and selecting the end points of the length to be measured.

While complete automation is desirable in the long term, and indeed some of the stages which are currently supervised could be automated (e.g. detecting concurrent lines and vanishing points [92]), this was not a central issue in this thesis.

8.3 Future work

The described measurement and structure recovery algorithms work particularly well for man-made environments. It is more complicated to apply those techniques to images of scenes where fewer regular structures and well defined geometric cues (e.g. parallel lines and planes) are present. In such cases different sources of geometric information must be used.

Use of shadows, reflections, symmetries and repetitions in single views. As mentioned in section 5.7 shadows, reflections, symmetries and repetitions constitute an important source of pure geometric information (see fig. 8.1). These cues provide restrictions analogous to a second viewpoint. It has been proven that projective or affine structure can be computed from single images

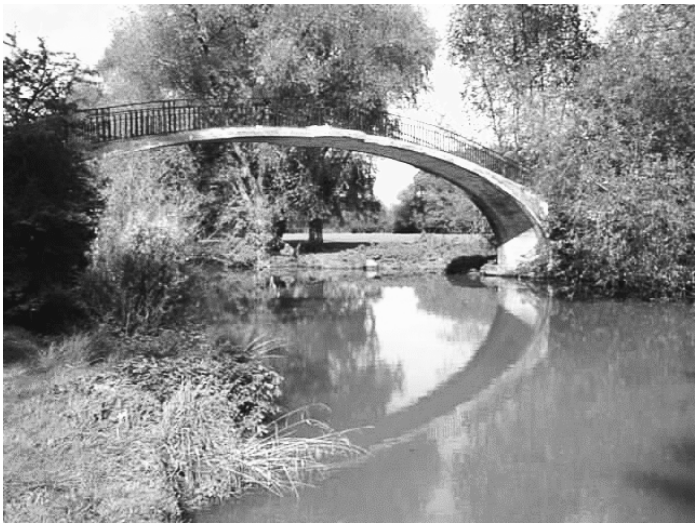

Figure 8.1: **Reconstructing curved surfaces from single views using reflections:** a view of the bridge in the University Parks in Oxford. The reflection of the bridge on the water of the river provides information about the geometry of the bridge itself.

with a plane of symmetry (e.g. a mirror, a lake) [57, 99]. Curved surfaces and non planar objects can be reconstructed from single views by making good use of those geometric cues.

Shadows, reflections, symmetries of planes and repetitions can be described by homologies. One of the future goals of this work is then to build a systematic interpretation of the single view approach which makes further use of the generality of the homology mapping.

A possible application is the reconstruction of complicated vault structures in churches from postcards, drawings and paintings. For instance, in figure 8.2 the symmetry and repetition of the 3D pattern in the vaults carry useful information about their shape and geometry[1].

Being able to recover the shape of non-planar and generally curved objects may lead to an increase in the amount of detail present in reconstructed scenes.

Analyzing natural scenes. Currently we are trying to address the problem of dealing with "natural" scenes, where no "strong" geometric cues or straightforward geometric relationships (e.g.

[1] Note that the arches in fig. 7.2 and fig. 7.5 have been easily reconstructed because they lie on fronto-parallel planes. In figure 7.2 the arch is simply a semicircle.

a b

Figure 8.2: **Reconstructing curved surfaces from single views using symmetry:** (a) a postcard showing the interior of the Bodleian Library in Oxford; (b) *Interior of St.Bavo's church at Harlem*(1648), The National Galleries of Scotland, an oil painting by Pieter Jansz. Saenradam (1597-1665); Reconstructing the beautiful and fairly complicated vaults from single image is a challenge.

homologies) can be identified. This will probably require a statistical interpretation of texture and shading of surfaces.

Less strictly geometry-based approaches may be applied in interpreting images of countryscapes and paintings. These images do not present many reliable geometric fixtures, but other less well defined "cues" may convey the perception of depth, distance and shape of surfaces. Shape can be perceived, for instance, from the texture of surfaces [46, 63] (see fig. 8.3) and depth and distance from the variation of the intensity and saturation of the light [2]. This "atmospheric cue" might prove useful not only to measure relative distances between objects (like buildings [87]) but, if reference distances are known, to measure the humidity or pollution of the air itself.

[2] "*There is another kind of perspective which I call aerial, because by the difference in the atmosphere one is able to distinguish the various distances of different buildings, which appear based on a single line.*" *Leonardo da Vinci (1452-1519).* (*cf.* Leonardo's painting *The Virgin of the Rocks*, 1508, National Gallery, London.)

a b

Figure 8.3: **Recovering surface orientation from texture:** (a) a photograph of the pond in the University Parks in Oxford; (b) *Water lilies* (1906), The Art Institute of Chicago, an oil painting by Claude Monet (1840-1926). The distribution and shape of the water lilies provide geometric clues to identify the orientation of the surface of the lake.

Uncertainty analysis with bootstrap methods. On the error analysis front we are investigating alternative methods for predicting the uncertainty on the final measurements which avoid the some times tedious computation of Jacobian matrices required by first order error propagation techniques.

One possibility is employing numerical algorithms. *Bootstrap* methods [80] are currently under investigation. These techniques are very similar to the Monte Carlo approach, with the main difference that no knowledge about the statistical distribution of the input data is required (in this thesis Gaussian noise has been assumed in the input data). Bootstrap algorithms, however, like the Monte Carlo ones, are based on an iterative refinement of the solution and therefore can be very slow.

"Questa conclusione, benché trovata da povera gente, c'è parsa cosí giusta, che abbiam pensato di metterla qui, come il sugo di tutta la storia.
La quale, se non v'è dispiaciuta affatto, vogliatene bene a chi l'ha scritta, e anche un pochino a chi l'ha raccomodata. Ma se in vece fossimo riusciti ad annoiarvi, credete che non s'è fatto apposta."

da *I Promessi Sposi* (1826) di A.Manzoni (1785-1873)

"This conclusion, though written by simple people, seems so apt that we have thought of putting it here, as the sauce for the whole story.
Which, if you did not dislike it, then show some sympathy to those who wrote it, and also a little to those who mended it. If, instead, you found it tiresome, believe that we did not do it on purpose."

from *The Betrothal* (1826) by A.Manzoni (1785-1873)

Bibliography

[1] Leon Battista Alberti. *De Pictura*. 1435. Reproduced by Laterza (1980).

[2] M. Armstrong. Euclidean structure and camera calibration from image sequences. First year report, Dept. of Engineering Science, University of Oxford, 1994.

[3] M. Armstrong, A. Zisserman, and R. Hartley. Self-calibration from image triplets. In *Proc. European Conference on Computer Vision*, LNCS 1064/5, pages 3–16. Springer-Verlag, 1996.

[4] S. Avidan and A. Shashua. Novel view synthesis in tensor space. In *Proceedings of the Conference on Computer Vision and Pattern Recognition*, page Poster session 6, 1997.

[5] P. Beardsley, P. Torr, and A. Zisserman. 3D model acquisition from extended image sequences. In *Proc. European Conference on Computer Vision*, LNCS 1064/1065, pages 683–695. Springer-Verlag, 1996.

[6] P. A. Beardsley, D. Sinclair, and A. Zisserman. Ego-motion from six points. Insight meeting, Catholic University Leuven, Feb 1992.

[7] M. Berger. *Geometry II*. Springer-Verlag, 1987.

[8] F. Callari and F. Ferrie. Active recognition: Using uncertainty to reduce ambiguity. Technical Report 11, Centre for Intelligent Machine, McGill University, Montreal, Quebec, Canada, September 1995.

[9] J. F. Canny. Finding edges and lines in images. Master's thesis, MIT, 1983.

[10] J. F. Canny. A computational approach to edge detection. *IEEE Transactions on Pattern Analysis and Machine Intelligence*, 8(6):679–698, 1986.

[11] D. Capel and A. Zisserman. Automated mosaicing with super-resolution zoom. In *Proceedings of the Conference on Computer Vision and Pattern Recognition, Santa Barbara*, pages 885–891, June 1998.

[12] B. Caprile and V. Torre. Using vanishing points for camera calibration. *International Journal of Computer Vision*, pages 127–140, 1990.

[13] S. Carlsson. Duality of reconstruction and positioning from projective views. In *IEEE Workshop on Representation of Visual Scenes, Boston*, 1995.

[14] S. Carlsson and D. Weinshall. Dual computation of projective shape and camera positions from multiple images. *International Journal of Computer Vision*, 1998. in Press.

[15] R. Cipolla. *Active visual inference of surface shape.* PhD thesis, Dept. of Engineering Science, University of Oxford, 1991.

[16] R. Cipolla, T. Drummond, and D. Robertson. Camera calibration from vanishing points in images of architectural scenes. In *Proc. British Machine Vision Conference*, September 1999.

[17] R. Cipolla and P. Giblin. *Visual Motion of Curves and Surfaces.* Number ISBN 0-521-63251-X. Cambridge University Press, 2000.

[18] R. Cipolla, Y. Okamoto, and Y. Kuno. Robust structure from motion using motion parallax. In *Proc. 4th International Conference on Computer Vision, Berlin*, pages 374–382, Los Alamitos, CA, 1993. IEEE Computer Society Press.

[19] J. C. Clarke. First order error propagation: A primer. *Image and Vision Computing*, 1996.

[20] J. C. Clarke. Modelling uncertainty: A primer. Technical Report 2161/98, University of Oxford, Dept. Engineering Science, 1998.

[21] R. T. Collins and R. S. Weiss. Vanishing point calculation as a statistical inference on the unit sphere. In *Proc. 3rd International Conference on Computer Vision, Osaka*, pages 400–403, December 1990.

[22] H. Cramer. *Mathematical Methods of Statistics.* Princeton Univ. Press., 1946.

[23] A. Criminisi, I. Reid, and A. Zisserman. Duality, rigidity and planar parallax. In *Proc. European Conference on Computer Vision*, pages 846–861. Springer-Verlag, June 1998.

[24] A Criminisi, I. Reid, and A Zisserman. A plane measuring device. *Image and Vision Computing*, 17(8):625–634, 1999.

[25] A. Criminisi, I. Reid, and A. Zisserman. Single view metrology. In *Proc. 7th International Conference on Computer Vision, Kerkyra, Greece*, pages 434–442, September 1999.

[26] A. Criminisi, A. Zisserman, L. Van Gool, Bramble S., and D. Compton. A new approach to obtain height measurements from video. In *Proc. of SPIE, Boston, Massachussets, USA*, volume 3576, 1-6 November 1998.

[27] G. Csurka, C. Zeller, Z. Zhang, and O. D. Faugeras. Characterizing the uncertainty of the fundamental matrix. Technical Report 2560, I.N.R.I.A., France, 1995.

[28] M. De Mey. Perspektief in 3-D. *Gent Universiteit*, 8ste jaargang(3):14–17, December 1993.

[29] P. E. Debevec, C. J. Taylor, and J. Malik. Modeling and rendering architecture from photographs: A hybrid geometry- and image- based approach. In *Proceedings, ACM SIGGRAPH*, pages 11–20, 1996.

[30] Piero della Francesca. *De Prospectiva Pingendi*. Firenze, Italy, 1474. Reproduced by ed. Sansoni (1942), Edizione Critica.

[31] F. Devernay and O. D. Faugeras. Automatic calibration and removal of distortion from scenes of structured environments. In *SPIE*, volume 2567, San Diego, CA, July 1995.

[32] F. Devernay and O. D. Faugeras. From projective to euclidean reconstruction. In *Proceedings of the Conference on Computer Vision and Pattern Recognition*, pages 264–269, 1996.

[33] S. Dubin, J. Nissanov, S. Zietz, B. Schrope, R. Morano, and R. Hananiah. Bioengineering approach to non-invasive measurement of body composition. In *Rocky Mountain Bioengineering Symposium*, pages 21–23, April 1994.

[34] Euclid. *Optica.* ca. 300 B.C. See also H. E. Burton, "The optics of Euclid" J.Opt.Soc.Am. 35, 357-372 (1945).

[35] O. Faugeras. What can be seen in three dimensions with an uncalibrated stereo rig? In *Proc. European Conference on Computer Vision*, LNCS 588, pages 563–578. Springer-Verlag, 1992.

[36] O. D. Faugeras. *Three-Dimensional Computer Vision: a Geometric Viewpoint.* MIT Press, 1993.

[37] O. D. Faugeras. Stratification of three-dimensional vision: projective, affine, and metric representation. *Journal of the Optical Society of America*, A12:465–484, 1995.

[38] O. D. Faugeras, S. Laveau, L. Robert, G. Csurka, and C. Zeller. 3-D reconstruction of urban scenes from sequences of images. Tech. report, INRIA, 1995.

[39] O. D. Faugeras, Q. Luong, and S. Maybank. Camera self-calibration: Theory and experiments. In *Proc. European Conference on Computer Vision*, LNCS 588, pages 321–334. Springer-Verlag, 1992.

[40] O. D. Faugeras and L. Robert. What can two images tell us about a third one. In J. O. Eckland, editor, *Proc. 3rd European Conference on Computer Vision, Stockholm*, pages 485–492. Springer-Verlag, 1994.

[41] O. D. Faugeras and G. Toscani. The calibration problem for stereo. In *Proceedings of the Conference on Computer Vision and Pattern Recognition*, pages 15–20, 1986.

[42] J. V. Field. Alberti, the Abacus and Piero della Francesca's proof of perspective. *Renaissance Studies*, 11(2), 1997.

[43] J. V. Field. *The Invention of Infinity, mathematics and arts in the Renaissance.* Oxford University Press, 1997.

[44] J. V. Field, R. Lunardi, and T. B. Settle. *The Perspective Scheme of Masaccio's Trinity Fresco.* Leo S. Olschki Editore, Firenze, 1989.

[45] F. Figueroa and A. Mahajan. A robust method to determine the coordinates of a wave source for 3-D position sensing. *ASME Journal of Dynamic Systems, Measurements and Control*, 116:505–511, September 1994.

[46] J. J. Gibson. *The Perception of the Visual World.* Houghton Mifflin, Boston, 1950.

[47] G. H. Golub and C.F. Van Loan. *Matrix Computations.* The John Hopkins University Press, Baltimore, MD, second edition, 1989.

[48] G. Gracie. Analytical photogrammetry applied to single terrestrial photograph mensuration. In *XIth International Conference of Photogrammetry, Lausanne, Switzerland*, July 1968.

[49] C. J. Harris and M. Stephens. A combined corner and edge detector. In *Proc. 4th Alvey Vision Conference, Manchester*, pages 147–151, 1988.

[50] R. I. Hartley. Estimation of relative camera positions for uncalibrated cameras. In *Proc. European Conference on Computer Vision*, LNCS 588, pages 579–587. Springer-Verlag, 1992.

[51] R. I. Hartley. Lines and points in three views – a unified approach. In *ARPA Image Understanding Workshop, Monterrey*, 1994.

[52] R. I. Hartley. Self-calibration from multiple views with a rotating camera. In *Proc. European Conference on Computer Vision*, LNCS 800/801, pages 471–478. Springer-Verlag, 1994.

[53] R. I. Hartley. A linear method for reconstruction from lines and points. In *Proc. International Conference on Computer Vision*, pages 882–887, 1995.

[54] R. I. Hartley and P. Sturm. Triangulation. In *Proc. Conference Computer Analysis of Images and Patterns*, Prague, Czech Republic, 1995.

[55] R. I. Hartley and A. Zisserman. *Multiple View Geometry in Computer Vision.* Cambridge University Press, 1999. (to appear).

[56] Y. Horry, K. Anjyo, and K. Arai. Tour into the picture: Using a spidery mesh interface to make animation from a single image. In *Proceedings of the ACM SIGGRAPH Conference on Computer Graphics*, pages 225–232, 1997.

[57] D. Huynh. Affine reconstruction from monocular vision in the presence of a symmetry plane. In *Proc. 7th International Conference on Computer Vision, Kerkyra, Greece*, September 1999.

[58] M. Irani and P. Anandan. Parallax geometry of pairs of points for 3D scene analysis. In B. Buxton and R. Cipolla, editors, *Proc. 4th European Conference on Computer Vision, LNCS 1064, Cambridge*, pages 17–30. Springer, 1996.

[59] M. Irani, P. Anandan, and D. Weinshall. From reference frames to reference planes: Multi-view parallax geometry and applications. In *Proc. European Conference on Computer Vision*, 1998.

[60] A. R. Jarvis. A perspective on range finding techniques for computer vision. *IEEE Trans. on Pattern Analysis and Machine Intelligence*, 5(2):122–139, 1983.

[61] K. Kanatani. Statistical optimization for geometric computation: theory and practice. Technical report, AI Lab, Dept of Computer Science, Gunma University, 1995.

[62] S. B. Kang. Semiautomatic mathods for recovering radial distortion parameters from a single image. Technical Report CRL 97/3, Digital CRL, 1997.

[63] M. Kass and A. Witkin. Analyzing oriented patterns. In *Proc. International Joint Conference on Artificial Intelligence*, Los Angeles CA, 1985.

[64] M. Kemp. *The Science of Art.* Yale University Press, New Haven and London, 1989.

[65] T. Kim, Y. Seo, and K. Hong. Physics-based 3D position analysis of a soccer ball from monocular image sequences. *Proc. International Conference on Computer Vision*, pages 721 – 726, 1998.

[66] J. J. Koenderink and A. J. van Doorn. Affine structure from motion. *J. Opt. Soc. Am. A*, 8(2):377–385, 1991.

[67] E. Kruppa. Zur ermittlung eines objektes aus zwei perspektiven mit innerer orientierung. *Sitz.-Ber. Akad. Wiss., Wien, Math. Naturw. Abt. IIa*, 122:1939–1948, 1913.

[68] R. Kumar, P. Anandan, and K. Hanna. Shape recovery from multiple views: a parallax based approach. In *ARPA Image Understanding Workshop, Monterey, CA,*, 2929 Campus Drive, Suite 260, San Mateo, California 94403o, November 1994. ARPA, Image Understanding, Morgan Kauffmann Publishers.

[69] R. Kumar, P. Anandan, M. Irani, J. Bergen, and K. Hanna. Representation of scenes from collections of images. In *ICCV Workshop on the Representation of Visual Scenes*, 1995.

[70] R. Kumar and A. R. Hanson. Robust methods for estimating pose and a sensitivity analysis. *Computer Vision, Graphics and Image Processing*, vol. 60(3):313–342, 1994.

[71] J. M. Lawn and R. Cipolla. Epipole estimation using affine motion-parallax. In *Proc. 4th British Machine Vision Conference, Guildford*, 1993.

[72] J. M. Lawn and R. Cipolla. Robust egomotion estimation from affine motion parallax. In *Proc. 3rd European Conference on Computer Vision, Stockholm*, pages 205–210. Springer-Verlag, 1994.

[73] M. Levoy. The digital Michelangelo project. In *Proc. EuroGraphics*, volume 18, September 1999.

[74] D. Liebowitz, A. Criminisi, and A. Zisserman. Creating architectural models from images. In *Proc. EuroGraphics*, volume 18, pages 39–50, September 1999.

[75] D. Liebowitz and A. Zisserman. Metric rectification for perspective images of planes. In *Proceedings of the Conference on Computer Vision and Pattern Recognition*, pages 482–488, June 1998.

[76] H. C. Longuet-Higgins. A computer algorithm for reconstructing a scene from two projections. *Nature*, 293:133–135, 1981.

[77] Q.-T. Luong and T. Viéville. Canonic representations for the geometries of multiple projective views. In *Proc. 3rd European Conference on Computer Vision, Stockholm*, pages 589–599, May 1994.

[78] H.-G. Maas. Robust automatic surface reconstruction with structured light. In *International Archives of Photogrammetry and Remote Sensing*, volume XXIX of *Part B5*, pages 102–107. 1992.

[79] J. Malik. Vision Algorithms, Theory and Practice, Kerkyra, Greece, September 1999. personal communication.

[80] B. Matei and P. Meer. Bootstraping a heteroscedastic regression model with application to 3D rigid motion evaluation. In *Vision Algorithms, Theory and Practice*, Kerkyra, Greece, September 1999. Springer.

[81] G. F. McLean and D. Kotturi. Vanishing point detection by line clustering. *IEEE Transactions on Pattern Analysis and Machine Intelligence*, 17(11):1090–1095, 1995.

[82] R. Mohr. Projective geometry and computer vision. In C.H. Chen, L.F. Pau, and P.S.P. Wang, editors, *Handbook of Pattern Recognition and Computer Vision*. World Scientific, 1992.

[83] R. Mohr, B. Boufama, and P. Brand. Accurate projective reconstruction. In *Applications of Invariance in Computer Vision*, pages 257–276,, Aores, Portugal, October 1993.

[84] T. Moons, L. Van Gool, M. Van Diest, and A. Oosterlinck. Affine structure from perspective image pairs obtained by a translating camera. In J. L. Mundy, A. Zisserman, and D. Forsyth, editors, *Applications of invariance in computer vision*, pages 297–316. Springer-Verlag, 1994.

[85] J. Mundy and A. Zisserman. *Geometric Invariance in Computer Vision*. MIT Press, 1992.

[86] J. Mundy, A. Zisserman, and D. Forsyth. *Applications of Invariance in Computer Vision*. LNCS 825. Springer-Verlag, 1994.

[87] S. Nayar and S. Narasimhan. Vision in bad weather. In *Proc. 7th International Conference on Computer Vision, Kerkyra, Greece*, pages 820–827, September 1999.

[88] S. B. Pollard. *Identifying Correspondences in Binocular Stereo.* PhD thesis, University of Sheffield, 1985.

[89] M. Pollefeys, R. Koch, and L. Van Gool. Self calibration and metric reconstruction in spite of varying and unknown internal camera parameters. In *Proc. 6th International Conference on Computer Vision, Bombay, India,* pages 90–96, 1998.

[90] W. Press, B. Flannery, S. Teukolsky, and W. Vetterling. *Numerical Recipes in C.* Cambridge University Press, 1988.

[91] M. Proesmans, T. Tuytelaars, and L. J. Van Gool. Monocular image measurements. Technical Report Improofs-M12T21/1/P, K.U.Leuven, 1998.

[92] M. Proesmans, L. J. Van Gool, and F. Defoort. Reading between the lines – a method for extracting dynamic 3D with texture. In *Proc. 6th International Conference on Computer Vision, Bombay, India,* pages 1081–1086, 1998.

[93] L. Quan and R. Mohr. Affine shape representation from motion through reference points. *Journal of Mathematical Imaging and Vision,* 1:145–151, 1992.

[94] I. Reid and A. Zisserman. Accurate metrology in uncalibrated video sequences. Technical report, Oxford University, Dept. of Engineering Science, 1996.

[95] I. Reid and A. Zisserman. Goal-directed video metrology. In R. Cipolla and B. Buxton, editors, *Proc. 4th European Conference on Computer Vision, LNCS 1065, Cambridge*, volume II, pages 647–658. Springer, April 1996.

[96] I. D. Reid and A. North. 3D trajectories from a single viewpoint using shadows. *Proc. British Machine Vision Conference,* 1998.

[97] J. A. Rice. *Mathematical Statistics and Data Analysis.* Wadsworth and Brooks, California, 1988.

[98] L. Robert and O. D. Faugeras. Relative 3D positioning and 3D convex hull computation from a weakly calibrated stereo pair. In *Proc. 4th International Conference on Computer Vision, Berlin*, pages 540–544, 1993.

[99] C. Rothwell, D. Forsyth, A. Zisserman, and J. Mundy. Extracting projective structure from single perspective views of 3D point sets. In *Proc. International Conference on Computer Vision*, pages 573–582, 1993.

[100] H. S. Sawhney. Simplifying motion and structure analysis using planar parallax and image warping. In *Proceedings of the Conference on Computer Vision and Pattern Recognition*, 1994.

[101] J. Semple and G. Kneebone. *Algebraic Projective Geometry*. Oxford University Press, 1979.

[102] L. S. Shapiro and J. M. Brady. Rejecting outliers and estimating errors in an orthogonal regression framework. Technical report 1974/93, Department of Engineering Science, University of Oxford, 1993.

[103] L. S. Shapiro and J. M. Brady. Rejecting outliers and estimating errors in an orthogonal regression framework. *Philosophical Transactions of the Royal Society of London, SERIES A*, 350:407–439, 1995.

[104] L. S. Shapiro, A. Zisserman, and M. Brady. 3D motion recovery via affine epipolar geometry. *International Journal of Computer Vision*, 16(2):147–182, 1995.

[105] A. Shashua. On geometric and algebraic aspects of 3D affine and projective structures from perspective 2D views. In J. Mundy, A. Zisserman, and D. Forsyth, editors, *Applications of Invariance in Computer Vision LNCS 825*, pages 127–143. Springer-Verlag, 1994.

[106] A. Shashua. Trilinearity in visual recognition by alignment. In *Proc. 3rd European Conference on Computer Vision, Stockholm*, volume 1, pages 479–484, May 1994.

[107] A. Shashua. Multiple-view geometry and photometry. In Springer Verlag, editor, *ACCV*, Singapore, December 1995.

[108] A. Shashua. On photometric issues in 3D visual recognition from a single 2D image. *International Journal of Computer Vision — in press, 1995*, Hebrew University, 1995.

[109] J. A. Shufelt. Performance and analysis of vanishing point detection techniques. *IEEE Transactions on Pattern Analysis and Machine Intelligence*, 21(3):282–288, March 1999.

[110] D. A. Sinclair. *Experiments in Motion and Correspondence.* PhD thesis, University of Oxford, 1992.

[111] M. E. Spetsakis and J. Aloimonos. Structure from motion using line correspondences. *International Journal of Computer Vision*, 4(3):171–183, 1990.

[112] C. E. Springer. *Geometry and Analysis of Projective Spaces.* Freeman, 1964.

[113] G. P. Stein. *Geometric and Photometric Constraints: Motion and Structure from three Views*. PhD thesis, MIT, 1997.

[114] G. Stern and A. Schindler. Three-dimensional visualization of bone surfaces from ultrasound scanning. Technical report, A.I.DuPont Institute, 1994.

[115] G. W. Stewart and J. Sun. *Matrix Perturbation Theory.* Academic Press Inc., USA, 1990.

[116] K. A. Stroud. *Engineering Mathematics.* MacMillan Education, 3rd edition, 1987.

[117] B. Taylor. *Linear Perspective.* London, 1715.

[118] P. H. S. Torr and A. Zisserman. Robust parametrization and computation of the trifocal tensor. In *Proc. 7th British Machine Vision Conference, Edinburgh*, 1996.

[119] Y. R. Tsai. An efficient and accurate camera calibration technique for 3D machine vision. In *Proceedings of the Conference on Computer Vision and Pattern Recognition*, 1986.

[120] Y. R. Tsai. A versatile camera calibration technique for high-accuracy 3D machine vision metrology using off-the-shelf tv cameras and lenses. *IEEE Journal of Robotics and Automation*, RA-3(4):323–344, August 1987.

[121] L. Van Gool, M. Proesmans, and A. Zisserman. Grouping and invariants using planar homologies. In *Workshop on Geometrical Modeling and Invariants for Computer Vision*. Xidian University Press, 1995.

[122] L. Van Gool, M. Proesmans, and A. Zisserman. Planar homologies as a basis for grouping and recognition. *Image and Vision Computing*, 16:21–26, January 1998.

[123] T. Viéville and D. Lingrand. Using singular displacements for uncalibrated monocular vision systems. Technical Report 2678, I.N.R.I.A., 1995.

[124] D. Weinshall, P. Anandan, and M. Irani. From ordinal to euclidean reconstruction with partial scene calibration. In R. Koch and L. van Gool, editors, *Proc. of SMILE98, 3D Structure from Multiple Images of Large-Scale Environments*, pages 208–223. Springer, 1998.

[125] D. Weinshall, M. Werman, and A. Shashua. Duality of multi-point and multi-frame geometry: Fundamental shape matrices and tensors. In B. Buxton and R. Cipolla, editors, *Proc. 4th European Conference on Computer Vision, LNCS 1065, Cambridge*, pages 217–227. Springer–Verlag, 1996.

[126] J. Weng, T. S. Huang, and N. Ahuja. Motion and structure from two perspective views: algorithms, error analysis and error estimation. *IEEE Transactions on Pattern Analysis and Machine Intelligence*, 11(5):451–476, 1989.

[127] M. Werman, D. Weinshall, and A. Shashua. Shape tensors for efficient and learnable indexing. In *IEEE Workshop on Representation of Visual Scenes, Boston*, 1995.

[128] J. H. Wilkinson. *The Algebraic Eigenvalue Problem*. Clarendon Press, Oxford, 1965.

[129] Z. Zhang. Determining the epipolar geometry and its uncertainty: A review. *To appear in the International Journal of Computer Vision*, 1997.

[130] Z. Zhang, P. Anandan, and H. Y. Shum. What can be determined from a full and a weak perspective image? In *Proc. 7th International Conference on Computer Vision, Kerkyra, Greece*, September 1999.

[131] Z. Zhang, R. Deriche, O. D. Faugeras, and Q. Luong. A robust technique for matching two uncalibrated images through the recovery of the unknown epipolar geometry. *Artificial Intelligence*, 78:87–119, 1995.

[132] Z. Zhang and A. R. Hanson. 3D reconstruction based on homography mapping. In *ARPA Image Understanding workshop*, Palm Springs, CA, 1996.

[133] Z. Zhang, Q. T. Luong, and O. D. Faugeras. Motion of an uncalibrated stereo rig: Self-calibration and metric reconstruction. *IEEE Trans. Robotics and Automation*, 12(1):103–113, Feb. 1996.

[134] A. Zisserman, P. Beardsley, and I. Reid. Metric calibration of a stereo rig. In *IEEE Workshop on Representation of Visual Scenes, Boston*, pages 93–100, 1995.

Appendix A

Metrology on planes, computing homography uncertainty

In section 4.2.1, in order to compute the planar homography $\mathtt{H}$, we seek the eigenvector $\mathbf{h}$ with smallest eigenvalue λ of the matrix $\mathtt{A}^\top\mathtt{A}$. If the measured points are noise-free, or $n = 4$, then $\mathbf{h} = \mathrm{Null}(\mathtt{A})$, and in general it can be assumed that for $\mathbf{h}$ the residual error $\mathbf{h}^\top\mathtt{A}^\top\mathtt{A}\mathbf{h} = \lambda \approx 0$.

We now use matrix perturbation theory [47, 115, 128] to compute the covariance $\Lambda_{\mathbf{h}}$ of $\mathbf{h}$ based on this zero approximation. Let us define

$$\mathbf{z} = \begin{pmatrix} x_1 & y_1 & x_2 & y_2 & x_3 & y_3 & \cdots & x_n & y_n \end{pmatrix}^\top$$

the vector of the $2n$ components of the n noisy image computation points, referred to an image coordinate system. Because of the noise we have:

$$\begin{aligned} \mathbf{z} = \quad \tilde{\mathbf{z}} + \delta\mathbf{z} = \quad & \begin{pmatrix} \tilde{x}_1 & \tilde{y}_1 & \tilde{x}_2 & \tilde{y}_2 & \tilde{x}_3 & \tilde{y}_3 & \cdots & \tilde{x}_n & \tilde{y}_n \end{pmatrix}^\top + \\ & \begin{pmatrix} \delta x_1 & \delta y_1 & \delta x_2 & \delta y_2 & \delta x_3 & \delta y_3 & \cdots & \delta x_n & \delta y_n \end{pmatrix}^\top \end{aligned}$$

where the $\tilde{}$ indicates noiseless quantities. Similarly for the world plane computation points we define

$$\mathbf{Z} = \begin{pmatrix} X_1 & Y_1 & X_2 & Y_2 & X_3 & Y_3 & \cdots & X_n & Y_n \end{pmatrix}^\top$$

the vector of the $2n$ components of the n noisy world plane computation points referred to a world coordinates system and

$$\begin{aligned} \mathbf{Z} = \quad \tilde{\mathbf{Z}} + \delta\mathbf{Z} = \quad & \begin{pmatrix} \tilde{X}_1 & \tilde{Y}_1 & \tilde{X}_2 & \tilde{Y}_2 & \tilde{X}_3 & \tilde{Y}_3 & \cdots & \tilde{X}_n & \tilde{Y}_n \end{pmatrix}^\top + \\ & \begin{pmatrix} \delta X_1 & \delta Y_1 & \delta X_2 & \delta Y_2 & \delta X_3 & \delta Y_3 & \cdots & \delta X_n & \delta Y_n \end{pmatrix}^\top \end{aligned}$$

We assume that the noise is Gaussian with null mean and that there is no correlation between the noise of different computation points. That means: $\mathrm{E}(\delta \mathrm{z_i} \delta \mathrm{z_j}) = \delta_{\mathrm{ij}} \sigma_{\mathrm{i}}^2$ and $\mathrm{E}(\delta \mathrm{Z_i} \delta \mathrm{Z_j}) = \delta_{\mathrm{ij}} \Sigma_{\mathrm{i}}^2$ where δ_{ij} is the Kronecker delta

$$\delta_{ij} = \begin{cases} 0 & i \neq j \\ 1 & i = j \end{cases} , i, j = 1 \cdots 2n$$

The generic odd row 1×9 vector of the $\mathtt{A}$ matrix is

$$\mathbf{a}_{2i-1} = \begin{pmatrix} x_i & y_i & 1 & 0 & 0 & 0 & -x_i X_i & -y_i X_i & -X_i \end{pmatrix}$$

and the even row 1×9 vector is

$$\mathbf{a}_{2i} = \begin{pmatrix} 0 & 0 & 0 & x_i & y_i & 1 & -x_i Y_i & -y_i Y_i & -Y_i \end{pmatrix}$$

with $i = 1 \cdots n$.

But $\mathbf{a}_{2i-1} = \tilde{\mathbf{a}}_{2i-1} + \delta \mathbf{a}_{2i-1}$ and $\mathbf{a}_{2i} = \tilde{\mathbf{a}}_{2i} + \delta \mathbf{a}_{2i}$ and therefore

$$\delta \mathbf{a}_{2i-1} = \begin{pmatrix} \delta x_i & \delta y_i & 0 & 0 & 0 & 0 & -(\delta x_i X_i + x_i \delta X_i) & -(\delta y_i X_i + y_i \delta X_i) & -\delta X_i \end{pmatrix}$$

and

$$\delta \mathbf{a}_{2i} = \begin{pmatrix} 0 & 0 & 0 & \delta x_i & \delta y_i & 0 & -(\delta x_i Y_i + x_i \delta Y_i) & -(\delta y_i Y_i + y_i \delta Y_i) & -\delta Y_i \end{pmatrix}$$

It's easy to prove that

$$\left.\begin{array}{rcl} \mathrm{E}(\delta \mathbf{a}_{2\mathrm{i}-1}^\top \delta \mathbf{a}_{2\mathrm{j}-1}) & = & \delta_{ij} \mathtt{S}_i^o \\ \mathrm{E}(\delta \mathbf{a}_{2\mathrm{i}}^\top \delta \mathbf{a}_{2\mathrm{j}}) & = & \delta_{ij} \mathtt{S}_i^e \\ \mathrm{E}(\delta \mathbf{a}_{2\mathrm{i}-1}^\top \delta \mathbf{a}_{2\mathrm{j}}) & = & \delta_{ij} \mathtt{S}_i^{oe} \\ \mathrm{E}(\delta \mathbf{a}_{2\mathrm{i}}^\top \delta \mathbf{a}_{2\mathrm{j}-1}) & = & \delta_{ij} \mathtt{S}_i^{eo} \end{array}\right\} \quad \forall i, j = 1 \cdots n$$

where

$$\mathtt{S}_i^o = \begin{bmatrix} \mathtt{\Lambda}_{\mathbf{x}_i} & \mathtt{0} & -X_i \mathtt{\Lambda}_{\mathbf{x}_i} \\ \mathtt{0} & \mathtt{0} & \mathtt{0} \\ -X_i \mathtt{\Lambda}_{\mathbf{x}_i} & \mathtt{0} & X_i^2 \mathtt{\Lambda}_{\mathbf{x}_i} + \Sigma_{X_i}^2 \mathbf{x}_i \mathbf{x}_i^\top \end{bmatrix}, \quad \mathtt{S}_i^e = \begin{bmatrix} \mathtt{0} & \mathtt{0} & \mathtt{0} \\ \mathtt{0} & \mathtt{\Lambda}_{\mathbf{x}_i} & -Y_i \mathtt{\Lambda}_{\mathbf{x}_i} \\ \mathtt{0} & -Y_i \mathtt{\Lambda}_{\mathbf{x}_i} & Y_i^2 \mathtt{\Lambda}_{\mathbf{x}_i} + \Sigma_{Y_i}^2 \mathbf{x}_i \mathbf{x}_i^\top \end{bmatrix}$$

$$\mathtt{S}_i^{oe} = \begin{bmatrix} \mathtt{0} & \mathtt{\Lambda}_{\mathbf{x}_i} & -Y_i \mathtt{\Lambda}_{\mathbf{x}_i} \\ \mathtt{0} & \mathtt{0} & \mathtt{0} \\ \mathtt{0} & -X_i \mathtt{\Lambda}_{\mathbf{x}_i} & X_i Y_i \mathtt{\Lambda}_{\mathbf{x}_i} + \Sigma_{XY_i} \mathbf{x}_i \mathbf{x}_i^\top \end{bmatrix}, \quad \mathtt{S}_i^{eo} = \mathtt{S}_i^{oe\top}$$

with $\Lambda_{\mathbf{x}_i}$ the homogeneous covariance matrix of the image point $\mathbf{x}_i = (x_i, y_i, 1)^\top$ and $\Lambda_{\mathbf{X}_i}$ the homogeneous covariance matrix of the world point $\mathbf{X}_i$ in the form:

$$\Lambda_{\mathbf{x}_i} = \begin{bmatrix} \sigma_{x_i}^2 & \sigma_{xy_i} & 0 \\ \sigma_{xy_i} & \sigma_{y_i}^2 & 0 \\ 0 & 0 & 0 \end{bmatrix}, \quad \Lambda_{\mathbf{X}_i} = \begin{bmatrix} \Sigma_{X_i}^2 & \Sigma_{XY_i} & 0 \\ \Sigma_{XY_i} & \Sigma_{Y_i}^2 & 0 \\ 0 & 0 & 0 \end{bmatrix}$$

In the case of homogeneous and isotropic noise the above equations simplify.

Furthermore if we define the matrix $\mathtt{M} = \mathtt{A}^\top \mathtt{A}$ then

$$\mathtt{M} = (\tilde{\mathtt{A}} + \delta\mathtt{A})^\top (\tilde{\mathtt{A}} + \delta\mathtt{A}) = \tilde{\mathtt{A}}^\top \tilde{\mathtt{A}} + \delta\mathtt{A}^\top \tilde{\mathtt{A}} + \tilde{\mathtt{A}}^\top \delta\mathtt{A} + \delta\mathtt{A}^\top \delta\mathtt{A}$$

Thus $\mathtt{M} = \tilde{\mathtt{M}} + \delta\mathtt{M}$ and for the first order approximation $\delta\mathtt{M} = \delta\mathtt{A}^\top \tilde{\mathtt{A}} + \tilde{\mathtt{A}}^\top \delta\mathtt{A}$.

Now let us define $\mathbf{u}_1$ as the eigenvector corresponding to the null eigenvalue of the matrix $\tilde{\mathtt{M}}$ (the solution vector $\mathbf{h}$). The other eigensolutions are: $\tilde{\mathtt{M}}\tilde{\mathbf{u}}_j = \tilde{\lambda}_j \tilde{\mathbf{u}}_j$ with $j = 2 \cdots 9$. It has been proven [47, 102] that the variation of the solution is related to the noise of the matrix as in the following formula:

$$\delta\mathbf{u}_1 = -\sum_{k=2}^{9} \frac{\tilde{\mathbf{u}}_k \tilde{\mathbf{u}}_k^\top}{\tilde{\lambda}_k} \delta\mathtt{M} \tilde{\mathbf{u}}_1$$

but $\delta\mathtt{M}\tilde{\mathbf{u}}_1 = \delta\mathtt{A}^\top \tilde{\mathtt{A}} \tilde{\mathbf{u}}_1 + \tilde{\mathtt{A}}^\top \delta\mathtt{A} \tilde{\mathbf{u}}_1$ and we know that $\tilde{\mathtt{A}}\tilde{\mathbf{u}}_1 = 0$ thus

$$\delta\mathtt{M}\tilde{\mathbf{u}}_1 = \tilde{\mathtt{A}}^\top \delta\mathtt{A} \tilde{\mathbf{u}}_1$$

from where $\delta\mathbf{u}_1 = \tilde{\mathtt{J}} \tilde{\mathtt{A}}^\top \delta\mathtt{A} \tilde{\mathbf{u}}_1$ with $\tilde{\mathtt{J}} = -\sum_{k=2}^{9} \frac{\tilde{\mathbf{u}}_k \tilde{\mathbf{u}}_k^\top}{\tilde{\lambda}_k}$.

Therefore:

$$\begin{aligned} \Lambda_{\mathbf{h}} = \Lambda_{\mathbf{u}_1} = \mathrm{E}\left(\delta\mathbf{u}_1 \delta\mathbf{u}_1^\top\right) = \tilde{\mathtt{J}}\mathrm{E}\left(\tilde{\mathtt{A}}^\top \delta\mathtt{A} \tilde{\mathbf{u}}_1 \tilde{\mathbf{u}}_1^\top \delta\mathtt{A}^\top \tilde{\mathtt{A}}\right) \tilde{\mathtt{J}}^\top = \\ \tilde{\mathtt{J}}\mathrm{E}\left(\sum_{\mathrm{i}=1}^{2\mathrm{n}} \tilde{\mathbf{a}}_\mathrm{i}^\top (\delta\tilde{\mathbf{a}}_\mathrm{i} \cdot \tilde{\mathbf{u}}_1)(\sum_{\mathrm{j}=1}^{2\mathrm{n}} \tilde{\mathbf{a}}_\mathrm{j} (\delta\tilde{\mathbf{a}}_\mathrm{j} \cdot \tilde{\mathbf{u}}_1)\right) \tilde{\mathtt{J}}^\top = \\ \tilde{\mathtt{J}}\mathrm{E}\left(\sum_{\mathrm{i}=1}^{2\mathrm{n}} \tilde{\mathbf{a}}_\mathrm{i}^\top (\sum_{\mathrm{j}=1}^{2\mathrm{n}} \tilde{\mathbf{a}}_\mathrm{j} \tilde{\mathbf{u}}_1^\top (\delta\tilde{\mathbf{a}}_\mathrm{i}^\top \delta\tilde{\mathbf{a}}_\mathrm{j}) \tilde{\mathbf{u}}_1)\right) \tilde{\mathtt{J}}^\top = \\ \tilde{\mathtt{J}}\left(\sum_{i=1}^{2n} \tilde{\mathbf{a}}_i^\top (\sum_{j=1}^{2n} \tilde{\mathbf{a}}_j \tilde{\mathbf{u}}_1^\top \mathrm{E}(\delta\tilde{\mathbf{a}}_\mathrm{i}^\top \delta\tilde{\mathbf{a}}_\mathrm{j}) \tilde{\mathbf{u}}_1)\right) \tilde{\mathtt{J}}^\top \end{aligned} \tag{A.1}$$

having used that $(\delta\tilde{\mathbf{a}}_i \cdot \tilde{\mathbf{u}}_1)(\delta\tilde{\mathbf{a}}_j \cdot \tilde{\mathbf{u}}_1) = \tilde{\mathbf{u}}_1^\top(\delta\tilde{\mathbf{a}}_i^\top \delta\tilde{\mathbf{a}}_j)\tilde{\mathbf{u}}_1$.

Now considering that $\tilde{\mathtt{J}}$ is a symmetric matrix ($\tilde{\mathtt{J}}^\top = \tilde{\mathtt{J}}$) equation (A.1) can be written as

$$\Lambda_{\mathbf{h}} = \tilde{\mathtt{J}}\mathtt{S}\tilde{\mathtt{J}}$$

where $\mathtt{S}$ is a 9×9 matrix obtained as follows:

$$\begin{aligned}\mathtt{S} = \sum_{i=1}^{n} (&\tilde{\mathbf{a}}_{2i-1}^\top \tilde{\mathbf{a}}_{2i-1} \tilde{\mathbf{u}}_1^\top \mathrm{E}(\delta\tilde{\mathbf{a}}_{2\mathrm{i}-1}^\top \delta\tilde{\mathbf{a}}_{2\mathrm{i}-1})\tilde{\mathbf{u}}_1 + \tilde{\mathbf{a}}_{2\mathrm{i}}^\top \tilde{\mathbf{a}}_{2\mathrm{i}} \tilde{\mathbf{u}}_1^\top \mathrm{E}(\delta\tilde{\mathbf{a}}_{2\mathrm{i}}^\top \delta\tilde{\mathbf{a}}_{2\mathrm{i}})\tilde{\mathbf{u}}_1 + \\ &\tilde{\mathbf{a}}_{2i-1}^\top \tilde{\mathbf{a}}_{2i} \tilde{\mathbf{u}}_1^\top \mathrm{E}(\delta\tilde{\mathbf{a}}_{2\mathrm{i}-1}^\top \delta\tilde{\mathbf{a}}_{2\mathrm{i}})\tilde{\mathbf{u}}_1 + \tilde{\mathbf{a}}_{2\mathrm{i}}^\top \tilde{\mathbf{a}}_{2\mathrm{i}-1} \tilde{\mathbf{u}}_1^\top \mathrm{E}(\delta\tilde{\mathbf{a}}_{2\mathrm{i}}^\top \delta\tilde{\mathbf{a}}_{2\mathrm{i}-1})\tilde{\mathbf{u}}_1)\end{aligned}$$

yielding

$$\mathtt{S} = \sum_{i=1}^{n} \left(\tilde{\mathbf{a}}_{2i-1}^\top \tilde{\mathbf{a}}_{2i-1} \tilde{\mathbf{u}}_1^\top \mathtt{S}_i^o \tilde{\mathbf{u}}_1 + \tilde{\mathbf{a}}_{2i}^\top \tilde{\mathbf{a}}_{2i} \tilde{\mathbf{u}}_1^\top \mathtt{S}_i^e \tilde{\mathbf{u}}_1 + \tilde{\mathbf{a}}_{2i-1}^\top \tilde{\mathbf{a}}_{2i} \tilde{\mathbf{u}}_1^\top \mathtt{S}_i^{oe} \tilde{\mathbf{u}}_1 + \tilde{\mathbf{a}}_{2i}^\top \tilde{\mathbf{a}}_{2i-1} \tilde{\mathbf{u}}_1^\top \mathtt{S}_i^{eo} \tilde{\mathbf{u}}_1 \right)$$

Note that many of the above equations require the true noise-free quantities, which in general are not available. Weng et al. [126] pointed out that if one writes, for instance, $\tilde{\mathtt{A}} = \mathtt{A} - \delta\mathtt{A}$ and substitutes this in the relevant equations, the term in $\delta\mathtt{A}$ disappears in the first order expression, allowing $\tilde{\mathtt{A}}$ to be simply interchanged with $\mathtt{A}$, and so on.

Finally the 9×9 covariance matrix $\Lambda_{\mathbf{h}}$ is

$$\Lambda_{\mathbf{h}} = \mathtt{J}\mathtt{S}\mathtt{J} \tag{A.2}$$

where $\mathtt{J} = -\sum_{k=2}^{9} \frac{\mathbf{u}_k \mathbf{u}_k{}^\top}{\lambda_k}$, with $\mathbf{u}_k$ the k^{th} eigenvector of the $\mathtt{A}^\top\mathtt{A}$ matrix and λ_k the corresponding eigenvalue. The 9×9 matrix $\mathtt{S}$ is:

$$\mathtt{S} = \sum_{i=1}^{n} \left(\mathbf{a}_{2i-1}^\top \mathbf{a}_{2i-1} \mathbf{h}^\top \mathtt{S}_i^o \mathbf{h} + \mathbf{a}_{2i}^\top \mathbf{a}_{2i} \mathbf{h}^\top \mathtt{S}_i^o \mathbf{h} + \mathbf{a}_{2i-1}^\top \mathbf{a}_{2i} \mathbf{h}^\top \mathtt{S}_i^{oe} \mathbf{h} + \mathbf{a}_{2i}^\top \mathbf{a}_{2i-1} \mathbf{h}^\top \mathtt{S}_i^{eo} \mathbf{h} \right) \tag{A.3}$$

with $\mathbf{a}_i$ i^{th} row vector of the $\mathtt{A}$ matrix; n is the number of computation points.

Appendix B

Maximum likelihood estimation of end points for isotropic uncertainties

Given two image points $\mathbf{x}$ and $\mathbf{x}'$ with distributions $\Lambda_{\mathbf{x}}$ and $\Lambda_{\mathbf{x}'}$ isotropic but not necessarily equal (fig. B.1), we estimate the points $\hat{\mathbf{x}}$ and $\hat{\mathbf{x}}'$ such that the cost function (5.21) is minimized and the alignment constraint (5.22) satisfied. It is a constrained minimization problem; a closed form solution exists in this case.

The 2×2 covariance matrices $\Lambda_{\mathbf{x}}$ and $\Lambda_{\mathbf{x}'}$ for the two inhomogeneous end points $\mathbf{x}$ and $\mathbf{x}'$ define two circles with radius $r = \sigma_x = \sigma_y$ and $r' = \sigma_{x'} = \sigma_{y'}$ respectively. The line $\mathbf{l}$ through the vanishing point $\mathbf{v}$ that best fits the points $\mathbf{x}$ and $\mathbf{x}'$ can be computed as (in homogeneous form):

$$\mathbf{l} = \begin{pmatrix} 1 + \sqrt{1+\xi^2} \\ \xi \\ -(1+\sqrt{1+\xi^2})v_x - \xi v_y \end{pmatrix}, \quad \xi = 2\frac{r' d_x d_y + r d'_x d'_y}{r'(d_x^2 - d_y^2) + r(d_x'^2 - d_y'^2)}$$

where

$$\mathbf{d} = \mathbf{x} - \mathbf{v}, \quad \mathbf{d}' = \mathbf{x}' - \mathbf{v}$$

Note that this formulation is valid if $\mathbf{v}$ is finite.

The required estimates $\hat{\mathbf{x}}$ and $\hat{\mathbf{x}}'$ are the orthogonal projections of the points $\mathbf{x}$ and $\mathbf{x}'$ onto the line $\mathbf{l}$:

$$\hat{\mathbf{x}} = \begin{pmatrix} l_y(\mathbf{x} \cdot \mathtt{Fl}) - l_x l_w \\ -l_x(\mathbf{x} \cdot \mathtt{Fl}) - l_y l_w \\ l_x^2 + l_y^2 \end{pmatrix}, \quad \hat{\mathbf{x}}' = \begin{pmatrix} l_y(\mathbf{x}' \cdot \mathtt{Fl}) - l_x l_w \\ -l_x(\mathbf{x}' \cdot \mathtt{Fl}) - l_y l_w \\ l_x^2 + l_y^2 \end{pmatrix} \tag{B.1}$$

with $\mathtt{F} = \begin{bmatrix} 0 & 1 & 0 \\ -1 & 0 & 0 \end{bmatrix}$.

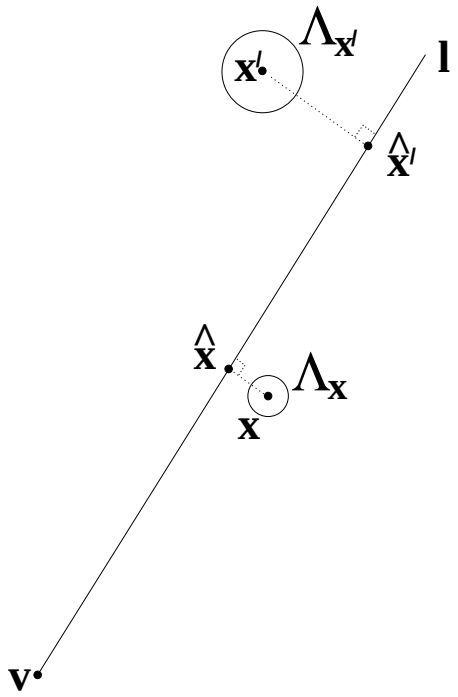

Figure B.1: **Maximum likelihood estimation** of the location of two points subject to the alignment constraint. The uncertainty of the input points $\mathbf{x}$ and $\mathbf{x}'$ is Gaussian and isotropic. The points $\hat{\mathbf{x}}$ and $\hat{\mathbf{x}}'$ are the ML estimates.

The points $\hat{\mathbf{x}}$ and $\hat{\mathbf{x}}'$ obtained above are used to provide an initial solution in the general non-isotropic covariance case, for which closed form solution does not exist. In the general case the non-isotropic covariance matrices $\Lambda_{\mathbf{x}}$ and $\Lambda_{\mathbf{x}'}$ are approximated with isotropic ones with radius

$$r = |\det(\Lambda_{\mathbf{x}})|^{1/4} \quad r' = |\det(\Lambda_{\mathbf{x}'})|^{1/4}$$

then (B.1) is applied and the solution end points are refined by using a Levenberg-Marquardt numerical algorithm to minimize the cost function (5.21) while satisfying the alignment constraint (5.22).

Appendix C

Single view metrology, variance of distance between planes

C.1 Covariance of MLE end points

In Appendix B we have shown how to estimate the MLE points $\hat{\mathbf{x}}$ and $\hat{\mathbf{x}}'$ given two end points $\mathbf{x}$ and $\mathbf{x}'$ characterized by non-isotropic uncertainties. This section demonstrates how to compute the 4×4 covariance matrix of the MLE 4-vector $\hat{\boldsymbol{\zeta}} = \begin{pmatrix} \hat{\mathbf{x}}^\top & \hat{\mathbf{x}}'^\top \end{pmatrix}^\top$ from the covariances of the input points $\mathbf{x}$ and $\mathbf{x}'$ and the covariance of the projection matrix.

In order to simplify the following formulae we define the points: $\mathbf{b} = \mathbf{x}$ (referred to as *base point*) on the plane π; and $\mathbf{t} = \mathbf{x}'$ (referred to as *top point*) on the plane π' corresponding to $\mathbf{x}$.

It can be shown that the 4×4 covariance matrix $\Lambda_{\hat{\boldsymbol{\zeta}}}$ of the vector $\hat{\boldsymbol{\zeta}} = \begin{pmatrix} \hat{b}_x & \hat{b}_y & \hat{t}_x & \hat{t}_y \end{pmatrix}^\top$ (MLE top and base points, see section (5.4.2)) can be computed by using the *implicit function theorem* [20, 36] as:

$$\Lambda_{\hat{\boldsymbol{\zeta}}} = \mathtt{A}^{-1}\mathtt{B}\Lambda_{\boldsymbol{\zeta}}\mathtt{B}^\top\mathtt{A}^{-\top} \tag{C.1}$$

where $\boldsymbol{\zeta} = \begin{pmatrix} b_x & b_y & t_x & t_y & p_{13} & p_{23} & p_{33} \end{pmatrix}^\top$ and

$$\Lambda_{\boldsymbol{\zeta}} = \begin{bmatrix} \Lambda_{\mathbf{b}} & 0 & 0 \\ 0 & \Lambda_{\mathbf{t}} & 0 \\ 0 & 0 & \Lambda_{\mathbf{p}_3} \end{bmatrix} \tag{C.2}$$

$\Lambda_{\mathbf{b}}$ and $\Lambda_{\mathbf{t}}$ are the 2×2 covariance matrices of the image points $\mathbf{b}$ and $\mathbf{t}$ respectively and $\Lambda_{\mathbf{p}_3}$ is the 3×3 covariance matrix of the vector $\mathbf{p}_3 = \alpha\mathbf{v}$ defined in (5.3). The assumption of statistical independence in (C.2) is a valid one.

The matrix $\mathtt{A}$ in (C.1) is the following 4×4 matrix

$$\mathtt{A} = \begin{bmatrix} -\mathbf{e}_1^{\mathbf{b}} \cdot \boldsymbol{\delta}_t & -\mathbf{e}_2^{\mathbf{b}} \cdot \boldsymbol{\delta}_t & -\lambda p_{33}\delta_{t_y} & \lambda p_{33}\delta_{t_x} \\ \delta_{e_x}\delta_{b_y} & \delta_{e_y}\delta_{b_y} - \tau\lambda p_{33} & -\tau e_{11}^t - \lambda p_{33}\delta_{b_y} & -\tau e_{12}^t - \lambda p_{33}\delta_{b_y} \\ \tau\lambda p_{33} - \delta_{e_x}\delta_{b_x} & -\delta_{e_y}\delta_{b_x} & -\tau e_{12}^t + \lambda p_{33}\delta_{b_x} & -\tau e_{22}^t + \lambda p_{33}\delta_{b_x} \\ -\tau\delta_{t_y} & \tau\delta_{t_x} & \tau\delta_{b_y} & -\tau\delta_{b_x} \end{bmatrix}$$

where we have defined:

- $\mathtt{E}_{\mathbf{t}} = \mathtt{\Lambda}_{\mathbf{t}}^{-1}$ and $e_{ij}^{\mathbf{t}}$ its element in (i,j) position;
- $\mathtt{E}_{\mathbf{b}} = \mathtt{\Lambda}_{\mathbf{b}}^{-1}$ and $\mathbf{e}_1^{\mathbf{b}}$ and $\mathbf{e}_2^{\mathbf{b}}$ respectively its first and second row;
- $\mathbf{p} = (p_{13}, p_{23})^\top, \quad \boldsymbol{\delta}_{\mathbf{t}} = p_{33}\hat{\mathbf{t}} - \mathbf{p}, \quad \boldsymbol{\delta}_{\mathbf{b}} = p_{33}\hat{\mathbf{b}} - \mathbf{p}, \quad \boldsymbol{\delta}_{\mathbf{e}} = \mathbf{e}_2^{\mathbf{b}} - \mathbf{e}_1^{\mathbf{b}}$;
- $\tau = (\mathbf{p}_3 \times \hat{\mathbf{t}})_y - (\mathbf{p}_3 \times \hat{\mathbf{t}})_x, \quad \lambda = \frac{\boldsymbol{\delta}_{\mathbf{e}} \cdot (\mathbf{b} - \hat{\mathbf{b}})}{\tau}$;

The matrix $\mathtt{B}$ in (C.1) is the following 4×7 matrix:

$$\mathtt{B} = \begin{bmatrix} \mathbf{e}_1^{\mathbf{b}} \cdot \boldsymbol{\delta}_t & \mathbf{e}_2^{\mathbf{b}} \cdot \boldsymbol{\delta}_t & 0 & 0 & \lambda\delta_{t_y} & -\lambda\delta_{t_x} & -\lambda\nu_1 \\ -\delta_{e_x}\delta_{b_y} & -\delta_{e_y}\delta_{b_y} & \tau e_{11}^t & \tau e_{12}^t & -\lambda\delta_{b_y} & -\lambda(\tau + \delta_{b_y}) & \lambda\nu_2 \\ \delta_{e_x}\delta_{b_x} & \delta_{e_y}\delta_{b_x} & \tau e_{12}^t & \tau e_{22}^t & \lambda(\tau + \delta_{b_x}) & \lambda\delta_{b_x} & -\lambda\nu_3 \\ 0 & 0 & 0 & 0 & \tau(\hat{t}_y - \hat{b}_y) & \tau(\hat{b}_x - \hat{t}_x) & \tau\nu_4 \end{bmatrix}$$

where we have defined

$$\nu_1 = \hat{t}_y(p_{23}\hat{t}_x - p_{13}\hat{t}_y), \quad \nu_2 = \hat{b}_y(p_{13} + p_{23}) - p_{23}(\hat{t}_x + \hat{t}_y)$$

$$\nu_3 = \hat{b}_x(p_{13} + p_{23}) - p_{13}(\hat{t}_x + \hat{t}_y), \quad \nu_4 = \hat{t}_x\hat{b}_y - \hat{t}_y\hat{b}_x$$

If the vanishing point is noise-free then $\mathtt{\Lambda}_{\hat{\boldsymbol{\zeta}}}$ has rank 3 as expected because of the alignment constraint.

C.2 Variance of the distance measurement, σ_Z^2

As seen in section 5.4.2 and 5.4.2 the components of the vector $\hat{\boldsymbol{\zeta}}$ are used to compute the distance Z from (5.6) rewritten here as:

$$Z = -\frac{||\hat{\mathbf{b}} \times \hat{\mathbf{t}}||}{(\mathbf{p}_4 \cdot \hat{\mathbf{b}})||\mathbf{p}_3 \times \hat{\mathbf{t}}||}$$

with the MLE points $\hat{\mathbf{b}}$, $\hat{\mathbf{t}}$ homogeneous with unit third coordinate.

The variance σ_Z^2 of the measurement Z depends on the covariance of the $\hat{\boldsymbol{\zeta}}$ vector and the covariance of the 6-vector $\mathbf{p} = \begin{pmatrix} \mathbf{p}_3^\top & \mathbf{p}_4^\top \end{pmatrix}^\top$ computed in section 5.4.1. If $\hat{\boldsymbol{\zeta}}$ and $\mathbf{p}$ are statistically independent, then from first order error analysis

$$\sigma_Z^2 = \boldsymbol{\nabla}_Z \begin{pmatrix} \Lambda_{\hat{\boldsymbol{\zeta}}} & 0 \\ 0 & \Lambda_{\mathbf{p}} \end{pmatrix} \boldsymbol{\nabla}_Z{}^\top \tag{C.3}$$

the 1×10 Jacobian $\boldsymbol{\nabla}_Z$ is:

$$\boldsymbol{\nabla}_Z = Z \begin{pmatrix} \mathtt{F}\left(\frac{(\hat{\mathbf{t}}\times\hat{\mathbf{b}})\times\hat{\mathbf{t}}}{\beta^2} - \frac{p_4}{\rho}\right) \\ \mathtt{F}\left(\frac{(\hat{\mathbf{b}}\times\hat{\mathbf{t}})\times\hat{\mathbf{b}}}{\beta^2} - \frac{(\mathbf{p}_3\times\hat{\mathbf{t}})\times\mathbf{p}_3}{\gamma^2}\right) \\ \frac{(\mathbf{p}_3\times\hat{\mathbf{t}})\times\hat{\mathbf{t}}}{\gamma^2} \\ -\frac{\hat{\mathbf{b}}}{\rho} \end{pmatrix}^\top$$

where we have defined $\beta = ||\hat{\mathbf{b}} \times \hat{\mathbf{t}}||$, $\gamma = ||\mathbf{p}_3 \times \hat{\mathbf{t}}||$, $\rho = \mathbf{p}_4 \cdot \hat{\mathbf{b}}$ and $\mathtt{F} = \begin{bmatrix} 1 & 0 & 0 \\ 0 & 1 & 0 \end{bmatrix}$. Note that the assumption of statistical independence in (C.3) is an approximation.

Appendix D

Single view metrology, variance of the affine parameter α

In section 5.3.1 the affine parameter α is obtained by computing the eigenvector $\mathbf{s}$ with smallest eigenvalue of the matrix $\mathtt{A}^\top\mathtt{A}$ (5.6). If the measured reference points are noise-free, or $n = 1$, then $\mathbf{s} = \mathrm{Null}(\mathtt{A})$ and in general we can assume that for $\mathbf{s}$ the residual error $\mathbf{s}^\top\mathtt{A}^\top\mathtt{A}\mathbf{s} = \lambda \approx 0$.

As in appendix A we now use matrix perturbation theory [47, 115, 128] to compute the covariance $\Lambda_{\mathbf{s}}$ of the solution vector $\mathbf{s}$ based on this zero approximation.

Note that the i^{th} row of the matrix $\mathtt{A}$ depends on the normalized vanishing line $\mathbf{l}$, on the vanishing point $\mathbf{v}$, on the reference end points $\mathbf{b}_i, \mathbf{t}_i$ and on reference distances Z_i. Uncertainty in any of those elements induces an uncertainty in the matrix $\mathtt{A}$ and therefore uncertainty in the final solution $\mathbf{s}$. Let us define the input vector

$$\boldsymbol{\eta} = (l_x\, l_y\, l_w\, v_x\, v_y\, v_w\, Z_1\, t_{1_x}\, t_{1_y}\, b_{1_x}\, b_{1_y}\, Z_n\, t_{n_x}\, t_{n_y}\, b_{n_x}\, b_{n_y})^\top$$

which contains the plane vanishing line, the vanishing point and the $5n$ components of the n references. Because of noise we have:

$$\begin{aligned}\boldsymbol{\eta} &= \tilde{\boldsymbol{\eta}} + \delta\boldsymbol{\eta} = (\tilde{l}_x\, \tilde{l}_y\, \tilde{l}_w\, \tilde{v}_x\, \tilde{v}_y\, \tilde{v}_w\, \tilde{Z}_1\, \tilde{t}_{1_x}\, \tilde{t}_{1_y}\, \tilde{b}_{1_x}\, \tilde{b}_{1_y}\, \tilde{Z}_n\, \tilde{t}_{n_x}\, \tilde{t}_{n_y}\, \tilde{b}_{n_x}\, \tilde{b}_{n_y})^\top + \\ & (\delta l_x\, \delta l_y\, \delta l_w\, \delta v_x\, \delta v_y\, \delta v_w\, \delta Z_1\, \delta t_{1_x}\, \delta t_{1_y} \delta Z_n\, \delta t_{n_x}\, \delta t_{n_y}\, \delta b_{n_x}\, \delta b_{n_y})^\top\end{aligned}$$

where the $\tilde{}$ indicates noiseless quantities.

We assume that the noise is Gaussian with zero mean and also that different reference distances are uncorrelated. However, the rows of the $\mathtt{A}$ matrix are correlated by the presence of $\mathbf{v}$ and $\mathbf{l}$ in each of them.

The 1×2 row-vector of the design matrix $\mathtt{A}$ is (see section 5.3.1)

$$\mathbf{a}_i = \begin{pmatrix} Z_i\rho_i\gamma_i & \beta_i \end{pmatrix}$$

with $i = 1 \cdots n$. Because of the noise $\mathbf{a}_i = \tilde{\mathbf{a}}_i + \delta\mathbf{a}_i$ and

$$\delta\mathbf{a}_i = \begin{pmatrix} \rho_i\gamma_i\delta Z_i + Z_i\gamma_i\delta\rho_i + Z_i\rho_i\delta\gamma_i & \delta\beta_i \end{pmatrix}$$

It can be shown that $\delta\rho_i$, $\delta\gamma_i$ and $\delta\beta_i$ can be computed as functions of $\delta\boldsymbol{\eta}$ and therefore, taking account of the statistical dependence of the rows of the $\mathtt{A}$ matrix, the 2×2 matrices $\mathtt{E}_{ij} = \mathrm{E}(\delta\mathbf{a}_\mathrm{i}^\top \delta\mathbf{a}_\mathrm{j})$ $\forall i, j = 1 \cdots n$ can be computed.

Furthermore if we define the matrix $\mathtt{M} = \mathtt{A}^\top\mathtt{A}$ then

$$\mathtt{M} = (\tilde{\mathtt{A}} + \delta\mathtt{A})^\top(\tilde{\mathtt{A}} + \delta\mathtt{A}) = \tilde{\mathtt{A}}^\top\tilde{\mathtt{A}} + \delta\mathtt{A}^\top\tilde{\mathtt{A}} + \tilde{\mathtt{A}}^\top\delta\mathtt{A} + \delta\mathtt{A}^\top\delta\mathtt{A}$$

Thus $\mathtt{M} = \tilde{\mathtt{M}} + \delta\mathtt{M}$ and for the first order approximation $\delta\mathtt{M} = \delta\mathtt{A}^\top\tilde{\mathtt{A}} + \tilde{\mathtt{A}}^\top\delta\mathtt{A}$.

As said the vector $\mathbf{s}$ is the eigenvector corresponding to the null eigenvalue of the matrix $\tilde{\mathtt{M}}$; the other eigensolution is: $\tilde{\mathtt{M}}\tilde{\mathbf{u}} = \tilde{\lambda}_2\tilde{\mathbf{u}}$ with $\tilde{\mathbf{u}}$ the second eigenvector of the $\mathtt{A}^\top\mathtt{A}$ matrix and $\tilde{\lambda}_2$ the corresponding eigenvalue.

It is proved in [47, 103] that the variation of the solutions is related to the noise of the matrix $\mathtt{M}$ as:

$$\delta\mathbf{s} = -\frac{\tilde{\mathbf{u}}\tilde{\mathbf{u}}^\top}{\tilde{\lambda}_2}\delta\mathtt{M}\tilde{\mathbf{s}}$$

but since $\delta\mathtt{M}\tilde{\mathbf{s}} = \delta\mathtt{A}^\top\tilde{\mathtt{A}}\tilde{\mathbf{s}} + \tilde{\mathtt{A}}^\top\delta\mathtt{A}\tilde{\mathbf{s}}$ and $\tilde{\mathtt{A}}\tilde{\mathbf{s}} = 0$ then $\delta\mathtt{M}\tilde{\mathbf{s}} = \tilde{\mathtt{A}}^\top\delta\mathtt{A}\tilde{\mathbf{s}}$ and thus

$$\delta\mathbf{s} = \tilde{\mathtt{J}}\tilde{\mathtt{A}}^\top\delta\mathtt{A}\tilde{\mathbf{s}}$$

where $\tilde{\mathtt{J}}$ is

$$\tilde{\mathtt{J}} = -\frac{\tilde{\mathbf{u}}\tilde{\mathbf{u}}^\top}{\tilde{\lambda}_2}$$

Therefore:

$$\begin{aligned}\Lambda_{\mathbf{s}} &= \mathrm{E}\left[\delta\mathbf{s}\delta\mathbf{s}^{\top}\right] = \tilde{\mathtt{J}}\mathrm{E}\left[\tilde{\mathtt{A}}^{\top}\delta\mathtt{A}\tilde{\mathbf{s}}\tilde{\mathbf{s}}^{\top}\delta\mathtt{A}^{\top}\tilde{\mathtt{A}}\right]\tilde{\mathtt{J}}^{\top} = \tilde{\mathtt{J}}\mathrm{E}\left[\sum_{\mathrm{i}=1}^{\mathrm{n}}\tilde{\mathbf{a}}_{\mathrm{i}}^{\top}\left(\delta\tilde{\mathbf{a}}_{\mathrm{i}}\cdot\tilde{\mathbf{s}}\right)\sum_{\mathrm{j}=1}^{\mathrm{n}}\tilde{\mathbf{a}}_{\mathrm{j}}(\delta\tilde{\mathbf{a}}_{\mathrm{j}}\cdot\tilde{\mathbf{s}})\right]\tilde{\mathtt{J}}^{\top} \quad \text{(D.1)}\\ &= \tilde{\mathtt{J}}\mathrm{E}\left[\sum_{\mathrm{i}=1}^{\mathrm{n}}\tilde{\mathbf{a}}_{\mathrm{i}}^{\top}\left(\sum_{\mathrm{j}=1}^{\mathrm{n}}\tilde{\mathbf{a}}_{\mathrm{j}}\tilde{\mathbf{s}}^{\top}(\delta\tilde{\mathbf{a}}_{\mathrm{i}}^{\top}\delta\tilde{\mathbf{a}}_{\mathrm{j}})\tilde{\mathbf{s}}\right)\right]\tilde{\mathtt{J}}^{\top} = \tilde{\mathtt{J}}\left[\sum_{\mathrm{i}=1}^{\mathrm{n}}\tilde{\mathbf{a}}_{\mathrm{i}}^{\top}\left(\sum_{\mathrm{j}=1}^{\mathrm{n}}\tilde{\mathbf{a}}_{\mathrm{j}}\tilde{\mathbf{s}}^{\top}\mathrm{E}(\delta\tilde{\mathbf{a}}_{\mathrm{i}}^{\top}\delta\tilde{\mathbf{a}}_{\mathrm{j}})\tilde{\mathbf{s}}\right)\right]\tilde{\mathtt{J}}^{\top}\end{aligned}$$

having used that

$$(\delta\tilde{\mathbf{a}}_i\cdot\tilde{\mathbf{s}})(\delta\tilde{\mathbf{a}}_j\cdot\tilde{\mathbf{s}}) = \tilde{\mathbf{s}}^{\top}(\delta\tilde{\mathbf{a}}_i^{\top}\delta\tilde{\mathbf{a}}_j)\tilde{\mathbf{s}}$$

Now considering that $\tilde{\mathtt{J}}$ is a symmetric matrix ($\tilde{\mathtt{J}}^{\top} = \tilde{\mathtt{J}}$) eq. (D.1) can be written as

$$\Lambda_{\mathbf{s}} = \tilde{\mathtt{J}}\tilde{\mathtt{S}}\tilde{\mathtt{J}}$$

where $\tilde{\mathtt{S}}$ is the following 2×2 matrix:

$$\tilde{\mathtt{S}} = \sum_{i=1}^{n}\tilde{\mathbf{a}}_i^{\top}\left(\sum_{j=1}^{n}\tilde{\mathbf{a}}_j\tilde{\mathbf{s}}^{\top}\tilde{\mathtt{E}}_{ij}\tilde{\mathbf{s}}\right)$$

with.

Note that many of the above equations require the true noise-free quantities, which in general are not available. As in Appendix A if one writes, for instance, $\tilde{\mathtt{A}} = \mathtt{A} - \delta\mathtt{A}$ and substitutes this in the relevant equations, the term in $\delta\mathtt{A}$ disappears in the first order expression, allowing $\tilde{\mathtt{A}}$ to be simply interchanged with $\mathtt{A}$, and so on. Therefore the 2×2 covariance matrix $\Lambda_{\mathbf{s}}$ is simply

$$\Lambda_{\mathbf{s}} = \mathtt{JSJ} \quad \text{(D.2)}$$

where $\mathtt{J} = -\frac{\mathbf{u}\mathbf{u}^{\top}}{\lambda_2}$. The 2×2 matrix $\mathtt{S}$ is:

$$\mathtt{S} = \sum_{i=1}^{n}\mathbf{a}_i^{\top}\left(\sum_{j=1}^{n}\mathbf{a}_j\mathbf{s}^{\top}\mathtt{E}_{ij}\mathbf{s}\right) \quad \text{(D.3)}$$

with $\mathbf{a}_i$ the i^{th} 1×2 row-vector of the design matrix $\mathtt{A}$ and n the number of references.

The 2×2 covariance matrix $\Lambda_{\mathbf{s}}$ of the vector $\mathbf{s}$ is therefore computed.

Noise-free $\mathbf{v}$ and $\mathbf{l}$. In the case $\Lambda_{\mathbf{l}} = 0$ and $\Lambda_{\mathbf{v}} = 0$ then (D.3) simply becomes:

$$\mathtt{S} = \sum_{i=1}^{n} \mathbf{a}_i^{\top} \mathbf{a}_i \mathbf{s}^{\top} \mathtt{E}_{ii} \mathbf{s} \tag{D.4}$$

in fact the rows of the $\mathtt{A}$ matrix are all statistically independent.

Variance of α. It is easy to convert the 2×2 homogeneous covariance matrix $\Lambda_{\mathbf{s}}$ in eq. (D.2) into inhomogeneous coordinates. In fact, since $\mathbf{s} = \begin{pmatrix} s(1) & s(2) \end{pmatrix}^{\top}$ and $\alpha = \frac{s(1)}{s(2)}$ for a first order error analysis the variance of the affine parameter α is

$$\sigma_{\alpha}^2 = \boldsymbol{\nabla}\alpha \Lambda_{\mathbf{s}} \boldsymbol{\nabla}\alpha^{\top} \tag{D.5}$$

with $\boldsymbol{\nabla}\alpha$ the 1×2 Jacobian matrix

$$\boldsymbol{\nabla}\alpha = \frac{1}{s(2)^2} \begin{pmatrix} s(2) & -s(1) \end{pmatrix}$$

Appendix E

Metrology from planar parallax, derivations

E.1 Computing the motion constraints

In this section we derive some of the motion constraints described in chapter 6. Extensive use is made of the lemma given in figure E.1.

Equation 6.1 (motion constraints):

$$A_{\mathbf{p}_1\mathbf{p}_2\mathbf{x}_2} A_{\mathbf{q}_1\mathbf{q}_2\mathbf{x}_1} = A_{\mathbf{p}_1\mathbf{p}_2\mathbf{x}_1} A_{\mathbf{q}_1\mathbf{q}_2\mathbf{x}_2}$$

Proof. Applying the lemma to figure 6.3 (substituting $\mathbf{e} \rightarrow \mathbf{e}_{12}$, $\mathbf{a} \rightarrow \mathbf{p}_1$, $\mathbf{b} \rightarrow \mathbf{p}_2$, $\mathbf{c} \rightarrow \mathbf{q}_1$, $\mathbf{d} \rightarrow \mathbf{x}_1$) we can write

$$\frac{A_{\mathbf{x}_2\mathbf{p}_1\mathbf{p}_2}}{A_{\mathbf{x}_1\mathbf{p}_1\mathbf{p}_2}} = \frac{A_{\mathbf{e}_{12}\mathbf{x}_2\mathbf{p}_1}}{A_{\mathbf{e}_{12}\mathbf{x}_1\mathbf{p}_1}}, \quad \frac{A_{\mathbf{x}_2\mathbf{q}_1\mathbf{q}_2}}{A_{\mathbf{x}_1\mathbf{q}_1\mathbf{q}_2}} = \frac{A_{\mathbf{e}_{12}\mathbf{x}_2\mathbf{q}_1}}{A_{\mathbf{e}_{12}\mathbf{x}_1\mathbf{q}_1}}$$

Also from the lemma

$$\frac{A_{\mathbf{e}_{12}\mathbf{x}_2\mathbf{p}_1}}{A_{\mathbf{e}_{12}\mathbf{x}_2\mathbf{q}_1}} = \frac{A_{\mathbf{e}_{12}\mathbf{x}_1\mathbf{p}_1}}{A_{\mathbf{e}_{12}\mathbf{x}_1\mathbf{q}_1}}$$

Combining the above yields:

$$A_{\mathbf{p}_1\mathbf{p}_2\mathbf{x}_2} A_{\mathbf{q}_1\mathbf{q}_2\mathbf{x}_1} = A_{\mathbf{p}_1\mathbf{p}_2\mathbf{x}_1} A_{\mathbf{q}_1\mathbf{q}_2\mathbf{x}_2}$$

□

Equation 6.4 (motion constraints):

$$A_{\mathbf{p}_1\mathbf{p}_2\mathbf{x}_1} A_{\mathbf{q}_1\mathbf{q}_2\mathbf{p}_1} A_{\mathbf{x}_1\mathbf{x}_2\mathbf{q}_1} = A_{\mathbf{p}_1\mathbf{p}_2\mathbf{q}_1} A_{\mathbf{q}_1\mathbf{q}_2\mathbf{x}_1} A_{\mathbf{x}_1\mathbf{x}_2\mathbf{p}_1}$$

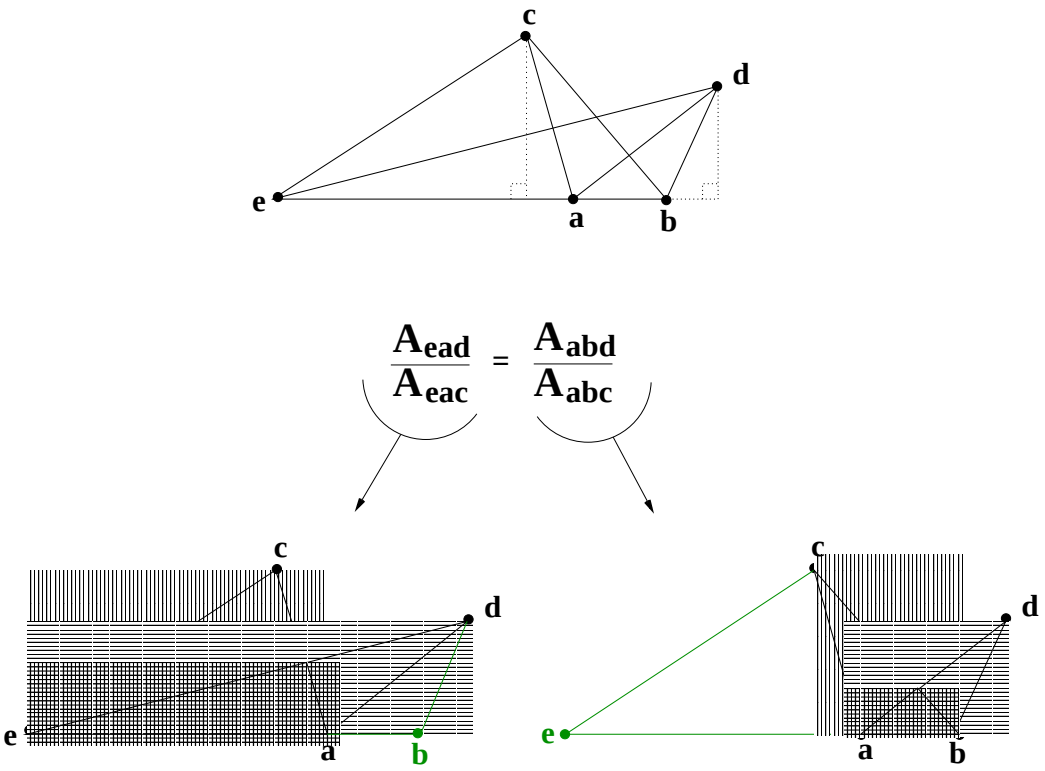

Figure E.1: **Lemma:** The equality of the area ratios is easily seen by considering the relative heights and base lengths of the triangles.

Proof. In figure 6.3 clearly we have

$$\frac{A_{\mathbf{e}_{12}\mathbf{p}_1\mathbf{x}_1}}{A_{\mathbf{e}_{12}\mathbf{p}_1\mathbf{q}_1}} = \frac{A_{\mathbf{e}_{12}\mathbf{q}_1\mathbf{x}_1}}{A_{\mathbf{e}_{12}\mathbf{p}_1\mathbf{q}_1}} \frac{A_{\mathbf{e}_{12}\mathbf{p}_1\mathbf{x}_1}}{A_{\mathbf{e}_{12}\mathbf{q}_1\mathbf{x}_1}}$$

However by the lemma

$$\frac{A_{\mathbf{e}_{12}\mathbf{p}_1\mathbf{x}_1}}{A_{\mathbf{e}_{12}\mathbf{p}_1\mathbf{q}_1}} = \frac{A_{\mathbf{p}_1\mathbf{p}_2\mathbf{x}_1}}{A_{\mathbf{p}_1\mathbf{p}_2\mathbf{q}_1}}, \quad \frac{A_{\mathbf{e}_{12}\mathbf{q}_1\mathbf{x}_1}}{A_{\mathbf{e}_{12}\mathbf{q}_1\mathbf{p}_1}} = \frac{A_{\mathbf{q}_1\mathbf{q}_2\mathbf{x}_1}}{A_{\mathbf{q}_1\mathbf{q}_2\mathbf{p}_1}}, \quad \frac{A_{\mathbf{e}_{12}\mathbf{p}_1\mathbf{x}_1}}{A_{\mathbf{e}_{12}\mathbf{q}_1\mathbf{x}_1}} = \frac{A_{\mathbf{p}_1\mathbf{x}_1\mathbf{x}_2}}{A_{\mathbf{q}_1\mathbf{x}_1\mathbf{x}_2}}$$

Hence combining the identities above we obtain the desired result.

$$A_{\mathbf{p}_1\mathbf{p}_2\mathbf{x}_1} A_{\mathbf{q}_1\mathbf{q}_2\mathbf{p}_1} A_{\mathbf{x}_1\mathbf{x}_2\mathbf{q}_1} = A_{\mathbf{p}_1\mathbf{p}_2\mathbf{q}_1} A_{\mathbf{q}_1\mathbf{q}_2\mathbf{x}_1} A_{\mathbf{x}_1\mathbf{x}_2\mathbf{p}_1}$$

□

E.2 Computing distances of points from planes directly in the images

In this section we show how from (6.38) we obtain (6.39).

First of all we need to compute the relationship between the area of a triangle on the distinguished plane an the area of its image.

Areas of triangles on the images

For a generic triangle on the reference plane, the relation between its area and the area of its image on the first image can be computed as follow.

Let us assume that $\mathtt{H}_1$ and $\mathtt{H}_2$ are the image-to-world homographies for the first and second image respectively, such that:

$$\mathbf{X} = \mathtt{H}_1\mathbf{x} \quad \mathbf{X} = \mathtt{H}_2\mathbf{x}'$$

for every point $\mathbf{X}$ on the distinguished plane $\boldsymbol{\pi}$. Consequently $\mathbf{x} = \mathtt{H}\mathbf{x}'$ where $\mathtt{H} = \mathtt{H}_1^{-1}\mathtt{H}_2$ is the inter-image homography.

Then for the triangle of vertices $\mathbf{p}_1, \mathbf{p}_2, \mathbf{x}_1$ on the world plane we have:

$$A_{\mathbf{p}_1\mathbf{p}_2\mathbf{x}_1} = \frac{|\mathtt{H}_1\mathbf{p} \;\; \mathtt{H}_2\mathbf{p}' \;\; \mathtt{H}_1\mathbf{x}|}{(\mathbf{l}\cdot\mathbf{p})(\mathbf{l}'\cdot\mathbf{p}')(\mathbf{l}\cdot\mathbf{x})} = \frac{|\mathtt{H}_1|}{(\mathbf{l}\cdot\mathbf{p})(\mathbf{l}'\cdot\mathbf{p}')(\mathbf{l}\cdot\mathbf{x})}|\mathbf{p} \;\; \mathtt{H}\mathbf{p}' \;\; \mathbf{x}| = \frac{|\mathtt{H}_1|}{(\mathbf{l}\cdot\mathbf{p})(\mathbf{l}'\cdot\mathbf{p}')(\mathbf{l}\cdot\mathbf{x})}A_{\mathbf{p}\dot{\mathbf{p}}\mathbf{x}} \tag{E.1}$$

with $\dot{\mathbf{p}} = \mathtt{H}\mathbf{p}'$. The area of the corresponding triangle on the first image is $A_{\mathbf{p}\dot{\mathbf{p}}\mathbf{x}}$.

Distances of points and cameras from the distinguished plane

The distance of a point $\mathbf{X}$ from the plane can be computed if both image-to-world homographies are known by applying (6.38); but it can also be computed directly in the images if the inter-image homography $\mathtt{H}$ is known and the plane vanishing line $\mathbf{l}$ in either image are known. By applying (E.1) to (6.38) obtaining (6.39) is straightforward.

Similar procedure can be applied to compute the distance of the cameras in (6.35) from (6.34).

Appendix F

Metrology from planar parallax, variance of distances

As seen in section 6.5.2 the variance on the distance Z_x of a point $\mathbf{X}$ from a plane can be computed employing the plane-plus-parallax approach as:

$$\sigma^2_{Z_x} = \boldsymbol{\nabla}_{Z_x} \Lambda \boldsymbol{\nabla}^\top_{Z_x}$$

In this section we compute the 1×32 Jacobian $\boldsymbol{\nabla}_{Z_x}$.

F.1 Definitions

Equation (6.39) can be rewritten as;

$$Z_x = Z_p Z_q \frac{N}{D}$$

where we define

- $N = N_1 - N_2$; $N_1 = \rho_q A_{\mathbf{x}\dot{\mathbf{x}}\dot{\mathbf{q}}} A_{\mathbf{p}\dot{\mathbf{p}}\dot{\mathbf{x}}}$; $N_2 = \rho_p A_{\mathbf{q}\dot{\mathbf{q}}\dot{\mathbf{x}}} A_{\mathbf{x}\dot{\mathbf{x}}\dot{\mathbf{p}}}$;
- $D = Zq D_1 + Z_p D_2$;
- $D_1 = A_{\mathbf{p}\dot{\mathbf{p}}\dot{\mathbf{x}}}(\rho_q A_{\mathbf{x}\dot{\mathbf{x}}\dot{\mathbf{q}}} - \rho_r A_{\mathbf{q}\dot{\mathbf{q}}\dot{\mathbf{x}}})$;
- $D_2 = A_{\mathbf{q}\dot{\mathbf{q}}\dot{\mathbf{x}}}(\rho_r A_{\mathbf{p}\dot{\mathbf{p}}\dot{\mathbf{x}}} - \rho_p A_{\mathbf{x}\dot{\mathbf{x}}\dot{\mathbf{p}}})$;
- $\rho_p = \mathbf{l} \cdot \mathbf{p}$; $\rho_q = \mathbf{l} \cdot \mathbf{q}$; $\rho_r = \mathbf{l} \cdot \mathbf{x}$;

for a generic triplet of points $\mathbf{a}, \mathbf{b}, \mathbf{c}$ we define: the determinant $D_{\mathbf{abc}} = \det \begin{bmatrix} \mathbf{a} & \mathbf{b} & \mathbf{c} \end{bmatrix}$; the area $A_{\mathbf{abc}} = |D_{\mathbf{abc}}|$; the sign $S_{\mathbf{abc}} = \frac{D_{\mathbf{abc}}}{A_{\mathbf{abc}}}$.

Uncertainty is assumed on: the inter-image homography $\mathtt{H}$; the plane vanishing line $\mathbf{l}$; the two input references, their world distance and the position of the image points Z_p, $\mathbf{p}$, $\mathbf{p}'$, Z_q, $\mathbf{q}$, $\mathbf{q}'$; the input image points $\mathbf{x}$, $\mathbf{x}'$.

F.2 Computing the Jacobian ∇_{Z_x}

Firstly we compute

$$\begin{aligned} \frac{\partial Z_x}{\partial Z_p} &= Z_q^2 \frac{N D_1}{D^2} \\ \frac{\partial Z_x}{\partial Z_q} &= Z_p^2 \frac{N D_2}{D^2} \end{aligned}$$

Furthermore for a generic vector $\mathbf{v}$ we have

$$\frac{\partial Z_x}{\partial \mathbf{v}} = \frac{Z_p Z_q}{D^2} \left(\frac{\partial N}{\partial \mathbf{v}} D - N \left(Z_q \frac{\partial D_1}{\partial \mathbf{v}} + Z_p \frac{\partial D_2}{\partial \mathbf{v}} \right) \right)$$

where $\mathbf{v}$ can be $\mathbf{v} = \mathbf{l}, \mathbf{h}, \mathbf{p}, \mathbf{p}', \mathbf{q}, \mathbf{q}', \mathbf{x}, \mathbf{x}'$.

- Since $D_1 = A_{\mathbf{p}\dot{\mathbf{p}}\dot{\mathbf{x}}} (\rho_q A_{\mathbf{x}\dot{\mathbf{x}}\dot{\mathbf{q}}} - \rho_r A_{\mathbf{q}\dot{\mathbf{q}}\dot{\mathbf{x}}})$ we have

$$\begin{aligned} \frac{\partial D_1}{\partial \mathbf{l}} &= A_{\mathbf{p}\dot{\mathbf{p}}\dot{\mathbf{x}}} \left(A_{\mathbf{x}\dot{\mathbf{x}}\dot{\mathbf{q}}} \mathbf{q} - A_{\mathbf{q}\dot{\mathbf{q}}\dot{\mathbf{x}}} \mathbf{x} \right) \\ \frac{\partial D_1}{\partial \mathbf{h}} &= \frac{\partial A_{\mathbf{p}\dot{\mathbf{p}}\dot{\mathbf{x}}}}{\partial \mathbf{h}} \left(\rho_q A_{\mathbf{x}\dot{\mathbf{x}}\dot{\mathbf{q}}} - \rho_r A_{\mathbf{q}\dot{\mathbf{q}}\dot{\mathbf{x}}} \right) + A_{\mathbf{p}\dot{\mathbf{p}}\dot{\mathbf{x}}} \left(\rho_q \frac{\partial A_{\mathbf{x}\dot{\mathbf{x}}\dot{\mathbf{q}}}}{\partial \mathbf{h}} - \rho_r \frac{\partial A_{\mathbf{q}\dot{\mathbf{q}}\dot{\mathbf{x}}}}{\partial \mathbf{h}} \right) \\ \frac{\partial D_1}{\partial \mathbf{p}} &= \frac{D_1}{D_{\mathbf{p}\dot{\mathbf{p}}\dot{\mathbf{x}}}} (\dot{\mathbf{p}} \times \dot{\mathbf{x}})^\top \\ \frac{\partial D_1}{\partial \mathbf{p}'} &= \frac{D_1}{D_{\mathbf{p}\dot{\mathbf{p}}\dot{\mathbf{x}}}} (\dot{\mathbf{x}} \times \mathbf{p})^\top \mathtt{H} \\ \frac{\partial D_1}{\partial \mathbf{q}} &= A_{\mathbf{p}\dot{\mathbf{p}}\dot{\mathbf{x}}} \left(A_{\mathbf{x}\dot{\mathbf{x}}\dot{\mathbf{q}}} \mathbf{l}^\top - \rho_r S_{\mathbf{q}\dot{\mathbf{q}}\dot{\mathbf{x}}} (\dot{\mathbf{q}} \times \dot{\mathbf{x}})^\top \right) \\ \frac{\partial D_1}{\partial \mathbf{q}'} &= A_{\mathbf{p}\dot{\mathbf{p}}\dot{\mathbf{x}}} \left(\rho_q S_{\mathbf{x}\dot{\mathbf{x}}\dot{\mathbf{q}}} (\mathbf{x} \times \dot{\mathbf{x}})^\top - \rho_r S_{\mathbf{q}\dot{\mathbf{q}}\dot{\mathbf{x}}} (\dot{\mathbf{x}} \times \mathbf{q})^\top \right) \mathtt{H} \\ \frac{\partial D_1}{\partial \mathbf{x}} &= A_{\mathbf{p}\dot{\mathbf{p}}\dot{\mathbf{x}}} \left(\rho_q S_{\mathbf{x}\dot{\mathbf{x}}\dot{\mathbf{q}}} (\dot{\mathbf{x}} \times \dot{\mathbf{q}})^\top - A_{\mathbf{q}\dot{\mathbf{q}}\dot{\mathbf{x}}} \mathbf{l}^\top \right) \end{aligned}$$

$$\frac{\partial D_1}{\partial \mathbf{x}'} = \left(\frac{D_1}{D_{\mathbf{p}\dot{\mathbf{p}}\dot{\mathbf{x}}}} (\mathbf{p} \times \dot{\mathbf{p}})^\top + A_{\mathbf{p}\dot{\mathbf{p}}\dot{\mathbf{x}}} \left(\rho_q S_{\mathbf{x}\dot{\mathbf{x}}\dot{\mathbf{q}}} (\dot{\mathbf{q}} \times \mathbf{x})^\top - \rho_r S_{\mathbf{q}\dot{\mathbf{q}}\dot{\mathbf{x}}} (\mathbf{q} \times \dot{\mathbf{q}})^\top \right) \right) \mathtt{H}$$

- And since $D_2 = A_{\mathbf{q}\dot{\mathbf{q}}\dot{\mathbf{x}}} (\rho_r A_{\mathbf{p}\dot{\mathbf{p}}\dot{\mathbf{x}}} - \rho_p A_{\mathbf{x}\dot{\mathbf{x}}\dot{\mathbf{p}}})$ we have

$$\begin{aligned}
\frac{\partial D_2}{\partial \mathbf{l}} &= A_{\mathbf{q}\dot{\mathbf{q}}\dot{\mathbf{x}}} \left(A_{\mathbf{p}\dot{\mathbf{p}}\dot{\mathbf{x}}} \mathbf{x} - A_{\mathbf{x}\dot{\mathbf{x}}\dot{\mathbf{p}}} \mathbf{p} \right) \\
\frac{\partial D_2}{\partial \mathbf{h}} &= \frac{\partial A_{\mathbf{q}\dot{\mathbf{q}}\dot{\mathbf{x}}}}{\partial \mathbf{h}} \left(\rho_r A_{\mathbf{p}\dot{\mathbf{p}}\dot{\mathbf{x}}} - \rho_p A_{\mathbf{x}\dot{\mathbf{x}}\dot{\mathbf{p}}} \right) + A_{\mathbf{q}\dot{\mathbf{q}}\dot{\mathbf{x}}} \left(\rho_r \frac{\partial A_{\mathbf{p}\dot{\mathbf{p}}\dot{\mathbf{x}}}}{\partial \mathbf{h}} - \rho_p \frac{\partial A_{\mathbf{x}\dot{\mathbf{x}}\dot{\mathbf{p}}}}{\partial \mathbf{h}} \right) \\
\frac{\partial D_2}{\partial \mathbf{p}} &= A_{\mathbf{q}\dot{\mathbf{q}}\dot{\mathbf{x}}} \left(\rho_r S_{\mathbf{p}\dot{\mathbf{p}}\dot{\mathbf{x}}} (\dot{\mathbf{p}} \times \dot{\mathbf{x}})^\top - A_{\mathbf{x}\dot{\mathbf{x}}\dot{\mathbf{p}}} \mathbf{l}^\top \right) \\
\frac{\partial D_2}{\partial \mathbf{p}'} &= A_{\mathbf{q}\dot{\mathbf{q}}\dot{\mathbf{x}}} \left(\rho_r S_{\mathbf{p}\dot{\mathbf{p}}\dot{\mathbf{x}}} (\dot{\mathbf{x}} \times \mathbf{p})^\top - \rho_p S_{\mathbf{x}\dot{\mathbf{x}}\dot{\mathbf{p}}} (\mathbf{x} \times \dot{\mathbf{x}})^\top \right) \mathtt{H} \\
\frac{\partial D_2}{\partial \mathbf{q}} &= \frac{D_2}{D_{\mathbf{q}\dot{\mathbf{q}}\dot{\mathbf{x}}}} (\dot{\mathbf{q}} \times \dot{\mathbf{x}})^\top \\
\frac{\partial D_2}{\partial \mathbf{q}'} &= \frac{D_2}{D_{\mathbf{q}\dot{\mathbf{q}}\dot{\mathbf{x}}}} (\dot{\mathbf{x}} \times \mathbf{q})^\top \mathtt{H} \\
\frac{\partial D_2}{\partial \mathbf{x}} &= A_{\mathbf{q}\dot{\mathbf{q}}\dot{\mathbf{x}}} \left(A_{\mathbf{p}\dot{\mathbf{p}}\dot{\mathbf{x}}} \mathbf{l}^\top - \rho_p S_{\mathbf{x}\dot{\mathbf{x}}\dot{\mathbf{p}}} (\dot{\mathbf{x}} \times \dot{\mathbf{p}})^\top \right) \\
\frac{\partial D_2}{\partial \mathbf{x}'} &= \left(\frac{D_2}{D_{\mathbf{q}\dot{\mathbf{q}}\dot{\mathbf{x}}}} (\mathbf{q} \times \dot{\mathbf{q}})^\top + A_{\mathbf{q}\dot{\mathbf{q}}\dot{\mathbf{x}}} \left(\rho_r S_{\mathbf{p}\dot{\mathbf{p}}\dot{\mathbf{x}}} (\mathbf{p} \times \dot{\mathbf{p}})^\top - \rho_p S_{\mathbf{x}\dot{\mathbf{x}}\dot{\mathbf{p}}} (\dot{\mathbf{p}} \times \mathbf{x})^\top \right) \right) \mathtt{H}
\end{aligned}$$

- Furthermore since $N = \rho_q A_{\mathbf{x}\dot{\mathbf{x}}\dot{\mathbf{q}}} A_{\mathbf{p}\dot{\mathbf{p}}\dot{\mathbf{x}}} - \rho_p A_{\mathbf{q}\dot{\mathbf{q}}\dot{\mathbf{x}}} A_{\mathbf{x}\dot{\mathbf{x}}\dot{\mathbf{p}}}$ we have

$$\begin{aligned}
\frac{\partial N}{\partial \mathbf{l}} &= A_{\mathbf{x}\dot{\mathbf{x}}\dot{\mathbf{q}}} A_{\mathbf{p}\dot{\mathbf{p}}\dot{\mathbf{x}}} \mathbf{q} - A_{\mathbf{q}\dot{\mathbf{q}}\dot{\mathbf{x}}} A_{\mathbf{x}\dot{\mathbf{x}}\dot{\mathbf{p}}} \mathbf{p} \\
\frac{\partial N}{\partial \mathbf{h}} &= \rho_q \left(A_{\mathbf{p}\dot{\mathbf{p}}\dot{\mathbf{x}}} \frac{\partial A_{\mathbf{x}\dot{\mathbf{x}}\dot{\mathbf{q}}}}{\partial \mathbf{h}} + A_{\mathbf{x}\dot{\mathbf{x}}\dot{\mathbf{q}}} \frac{\partial A_{\mathbf{p}\dot{\mathbf{p}}\dot{\mathbf{x}}}}{\partial \mathbf{h}} \right) - \rho_p \left(A_{\mathbf{x}\dot{\mathbf{x}}\dot{\mathbf{p}}} \frac{\partial A_{\mathbf{q}\dot{\mathbf{q}}\dot{\mathbf{x}}}}{\partial \mathbf{h}} + A_{\mathbf{q}\dot{\mathbf{q}}\dot{\mathbf{x}}} \frac{\partial A_{\mathbf{x}\dot{\mathbf{x}}\dot{\mathbf{p}}}}{\partial \mathbf{h}} \right) \\
\frac{\partial N}{\partial \mathbf{p}} &= \frac{N_1}{D_{\mathbf{p}\dot{\mathbf{p}}\dot{\mathbf{x}}}} (\dot{\mathbf{p}} \times \dot{\mathbf{x}})^\top - \frac{N_2}{\rho_p} \mathbf{l}^\top \\
\frac{\partial N}{\partial \mathbf{p}'} &= \left(\frac{N_1}{D_{\mathbf{p}\dot{\mathbf{p}}\dot{\mathbf{x}}}} (\dot{\mathbf{x}} \times \mathbf{p})^\top - \frac{N_2}{D_{\mathbf{x}\dot{\mathbf{x}}\dot{\mathbf{p}}}} (\mathbf{x} \times \dot{\mathbf{x}})^\top \right) \mathtt{H} \\
\frac{\partial N}{\partial \mathbf{q}} &= \frac{N_1}{\rho_q} \mathbf{l}^\top - \frac{N_2}{D_{\mathbf{q}\dot{\mathbf{q}}\dot{\mathbf{x}}}} (\dot{\mathbf{q}} \times \dot{\mathbf{x}})^\top \\
\frac{\partial N}{\partial \mathbf{q}'} &= \left(\frac{N_1}{D_{\mathbf{x}\dot{\mathbf{x}}\dot{\mathbf{q}}}} (\mathbf{x} \times \dot{\mathbf{x}})^\top - \frac{N_2}{D_{\mathbf{q}\dot{\mathbf{q}}\dot{\mathbf{x}}}} (\dot{\mathbf{x}} \times \mathbf{q})^\top \right) \mathtt{H} \\
\frac{\partial N}{\partial \mathbf{x}} &= \frac{N_1}{D_{\mathbf{x}\dot{\mathbf{x}}\dot{\mathbf{q}}}} (\dot{\mathbf{x}} \times \dot{\mathbf{q}})^\top - \frac{N_2}{D_{\mathbf{x}\dot{\mathbf{x}}\dot{\mathbf{p}}}} (\dot{\mathbf{x}} \times \dot{\mathbf{p}})^\top
\end{aligned}$$

$$\frac{\partial N}{\partial \mathbf{x}'} = \left(\frac{N_1}{D_{\mathbf{x}\dot{\mathbf{x}}\dot{\mathbf{q}}}} (\dot{\mathbf{q}} \times \mathbf{x})^\top + \frac{N_1}{D_{\mathbf{p}\dot{\mathbf{p}}\dot{\mathbf{x}}}} (\mathbf{p} \times \dot{\mathbf{p}})^\top - \frac{N_2}{D_{\mathbf{q}\dot{\mathbf{q}}\dot{\mathbf{x}}}} (\mathbf{q} \times \dot{\mathbf{q}})^\top - \frac{N_2}{D_{\mathbf{x}\dot{\mathbf{x}}\dot{\mathbf{p}}}} (\dot{\mathbf{p}} \times \mathbf{x})^\top \right) \mathtt{H}$$

Finally

$$\begin{aligned}
\frac{\partial A_{\mathbf{x}\dot{\mathbf{x}}\dot{\mathbf{p}}}}{\partial \mathbf{h}} &= S_{\mathbf{x}\dot{\mathbf{x}}\dot{\mathbf{p}}} \left((\dot{\mathbf{p}} \times \mathbf{x})^\top \mathtt{B}_{r'} + (\mathbf{x} \times \dot{\mathbf{x}})^\top \mathtt{B}_{p'} \right) \\
\frac{\partial A_{\mathbf{x}\dot{\mathbf{x}}\dot{\mathbf{q}}}}{\partial \mathbf{h}} &= S_{\mathbf{x}\dot{\mathbf{x}}\dot{\mathbf{q}}} \left((\dot{\mathbf{q}} \times \mathbf{x})^\top \mathtt{B}_{r'} + (\mathbf{x} \times \dot{\mathbf{x}})^\top \mathtt{B}_{q'} \right) \\
\frac{\partial A_{\mathbf{p}\dot{\mathbf{p}}\dot{\mathbf{x}}}}{\partial \mathbf{h}} &= S_{\mathbf{p}\dot{\mathbf{p}}\dot{\mathbf{x}}} \left((\dot{\mathbf{x}} \times \mathbf{p})^\top \mathtt{B}_{p'} + (\mathbf{p} \times \dot{\mathbf{p}})^\top \mathtt{B}_{r'} \right) \\
\frac{\partial A_{\mathbf{q}\dot{\mathbf{q}}\dot{\mathbf{x}}}}{\partial \mathbf{h}} &= S_{\mathbf{q}\dot{\mathbf{q}}\dot{\mathbf{x}}} \left((\dot{\mathbf{x}} \times \mathbf{q})^\top \mathtt{B}_{q'} + (\mathbf{q} \times \dot{\mathbf{q}})^\top \mathtt{B}_{r'} \right)
\end{aligned}$$

where for a generic point $\mathbf{x}$

$$\mathtt{B}_x = \begin{bmatrix} \mathbf{x}^\top & \mathbf{0} & \mathbf{0} \\ \mathbf{0} & \mathbf{x}^\top & \mathbf{0} \\ \mathbf{0} & \mathbf{0} & \mathbf{x}^\top \end{bmatrix}$$

The Jacobian $\boldsymbol{\nabla}_{Z_x}$ is thus computed as:

$$\boldsymbol{\nabla}_{Z_x} = \begin{pmatrix} \frac{\partial Z_x}{\partial \mathbf{l}} & \frac{\partial Z_x}{\partial \mathbf{h}} & \frac{\partial Z_x}{\partial Z_p} & \frac{\partial Z_x}{\partial \mathbf{p}} & \frac{\partial Z_x}{\partial \mathbf{p}'} & \frac{\partial Z_x}{\partial Z_q} & \frac{\partial Z_x}{\partial \mathbf{q}} & \frac{\partial Z_x}{\partial \mathbf{q}'} & \frac{\partial Z_x}{\partial \mathbf{x}} & \frac{\partial Z_x}{\partial \mathbf{x}'} \end{pmatrix}$$

.